

REFERENCE ONLY



2809287755

UNIVERSITY OF LONDON THESIS

Degree *phd*

Year *2007*

Name of Author *KRISTINA GISELLE*

HINDS

COPYRIGHT

This is a thesis accepted for a Higher Degree of the University of London. It is an unpublished typescript and the copyright is held by the author. All persons consulting the thesis must read and abide by the Copyright Declaration below.

COPYRIGHT DECLARATION

I recognise that the copyright of the above-described thesis rests with the author and that no quotation from it or information derived from it may be published without the prior written consent of the author.

LOAN

Theses may not be lent to individuals, but the University Library may lend a copy to approved libraries within the United Kingdom, for consultation solely on the premises of those libraries. Application should be made to: The Theses Section, University of London Library, Senate House, Malet Street, London WC1E 7HU.

REPRODUCTION

University of London theses may not be reproduced without explicit written permission from the University of London Library. Enquiries should be addressed to the Theses Section of the Library. Regulations concerning reproduction vary according to the date of acceptance of the thesis and are listed below as guidelines.

- A. Before 1962. Permission granted only upon the prior written consent of the author. (The University Library will provide addresses where possible).
- B. 1962 - 1974. In many cases the author has agreed to permit copying upon completion of a Copyright Declaration.
- C. 1975 - 1988. Most theses may be copied upon completion of a Copyright Declaration.
- D. 1989 onwards. Most theses may be copied.

This thesis comes within category D.

☐

This copy has been deposited in the Library of

~~*Le*~~

☐

This copy has been deposited in the University of London Library, Senate House, Malet Street, London WC1E 7HU.

Surf zone vortices near piecewise flat topography

Alan Karl Hinds

DEPARTMENT OF MATHEMATICS
UNIVERSITY COLLEGE LONDON
UNIVERSITY OF LONDON

A THESIS SUBMITTED FOR THE DEGREE OF
DOCTOR OF PHILOSOPHY

SUPERVISORS

Dr. N. R. McDonald & Prof. E.R. Johnson

NOVEMBER 2006

UMI Number: U591320

All rights reserved

INFORMATION TO ALL USERS

The quality of this reproduction is dependent upon the quality of the copy submitted.

In the unlikely event that the author did not send a complete manuscript and there are missing pages, these will be noted. Also, if material had to be removed, a note will indicate the deletion.



UMI U591320

Published by ProQuest LLC 2013. Copyright in the Dissertation held by the Author.
Microform Edition © ProQuest LLC.

All rights reserved. This work is protected against
unauthorized copying under Title 17, United States Code.



ProQuest LLC
789 East Eisenhower Parkway
P.O. Box 1346
Ann Arbor, MI 48106-1346

Abstract

The motion of ideal shallow water vortices near piecewise flat topography is studied without background rotation for two choices of bottom topography. First, topography is chosen in the form of a rectilinear step change in depth. Finite area monopolar vortices which propagate steadily, without change in shape, parallel to the step are computed numerically. Next, the general motion of a pair of point vortices of arbitrary circulation near an escarpment is found explicitly using Hamiltonian techniques. Some vortex paths are periodic and for specific initial conditions each vortex comprising the pair translates parallel to the step. Comparisons to point vortex trajectories are made with vortex patch trajectories computed using contour dynamics. Agreement between the two trajectories is close provided a vortex patch is sufficiently away from the escarpment. Then, the scattering at a rectilinear step change in depth of a shallow water vortex pair consisting of two patches of equal, but oppositely signed vorticity is studied. Using the constants of motion an explicit relationship is derived relating the angle of incidence to the refracted angle after crossing. It is found that for certain initial conditions a pair can be totally internally reflected by the escarpment. For large depth changes numerical computations show the coherence of the vortex pair is lost on encountering the escarpment.

The second part of this work concerns the dynamics of shallow water vortices near circular topography. Finite area monopolar vortices which translate without change in shape around the topography are computed near a seamount or well including the limiting cases of each: an island or deep well. The behaviour of a vortex pair propagating toward circular topography is examined. Using Hamiltonian techniques, trajectories of point vortices exterior to the topography are found and are compared to trajectories of vortex patches computed using contour dynamics. Point vortex trajectories can be periodic and, for specific initial conditions, each vortex orbits the topography with the same frequency.

Finally, laboratory experiments are performed to find the behaviour of a dipole propagating toward a step change in height. Dipoles approaching the step from either deep or shallow water at normal and oblique incidence are considered. Qualitative observations agree well with theoretical predictions: a dipole increases its separation when crossing from deep water and decreases for a dipole crossing from shallow water. Furthermore, for dipoles approaching from shallow water with a sufficiently large incident angle the dipole was observed to perform total internal reflection.

Acknowledgements

I would like to express my sincere and heartfelt appreciation to my supervisors, Ted Johnson and Robb McDonald for their guidance, encouragement and help. It has been a pleasure to work with them and to learn from their expertise. A special acknowledgement is made to Robb McDonald who has been my mentor throughout my University education and without whom I would not have considered undertaking this period of study.

I am extremely grateful to Ian Eames (for his wise supervision throughout my time in the laboratory), the Mechanical Engineering Fluid Dynamics Group (in particular, Mark Landeryou and Andre Nicolle for writing the software used in the experimental setup and Jacob Snellings for his help in the laboratory), Terry Dyer along with all the technicians who gave suggestions in improving the apparatus) and Ed Green (for his help in designing the apparatus) for their contribution in making the laboratory experiments a success.

I am indebted to Engineering and Physical Sciences Research Council for financial support along with the Central Research Grant (University of London), Grad School (UCL) and the Mathematical Department (UCL) for their contributions to the laboratory experiments and to publicise this work at conference.

I also appreciate the numerous acts of assistance of the academic staff, support staff and post-graduate students of the mathematics department at UCL. I would especially like to thank the Geophysical Fluid Dynamics group for their helpful conversations and suggestions.

Lastly, I wish to warmly acknowledge the support of my friends and family. Most importantly, I would like to thank my parents, John and Jane for their patience and encouragement and my girlfriend, Caroline, for her unwavering kindness, devotion and belief.

Contents

1	Introduction	1
2	Fundamental Equations, Conservation Laws and Numerical Method	12
2.1	Model formulation and equations	12
2.1.1	Integral invariants of a vorticity distribution	14
2.2	Contour Dynamics	15
3	Steadily Translating Vortices near Step Topography	18
3.1	Introduction	18
3.2	Preliminary equations	20
3.3	Steadily-Propagating Finite Area Vortices: V-States	23
3.4	Analytical Approximations For V-States	27
3.5	V-States In Time-Dependent Flows	31
3.5.1	Flow initialized from a computed V-state	31
3.5.2	Flow initialized from a circular patch	32
3.6	Conclusions	34
4	Interactions of Two Vortices with Step Topography	36
4.1	Introduction	36
4.2	Preliminary equations and Hamiltonian formation	38
4.3	Trajectories of point vortices	42
4.3.1	Trajectories of point vortex pairs with like signed circulation	43
4.3.2	Trajectories of oppositely signed point vortex pairs	48
4.4	Vortex patch motion	54
4.4.1	Like signed vortex patches	55
4.4.2	Oppositely signed vortex patches	57

4.5	Two-patch equilibrium states	60
4.6	Discussion	62
5	Vortex Scattering from Step Topography	68
5.1	Introduction	68
5.2	Mathematical formulation	69
5.3	Numerical computation of vortex-pair scattering	77
5.3.1	Refraction at step topography	77
5.3.2	The critical angle and total internal reflection	80
5.3.3	The debris region	81
5.4	Conclusions	82
6	Trapped Vortices in Steady Rotation about Circular Topog- raphy	84
6.1	Introduction	84
6.2	Preliminary Equations And Conserved Quantities	87
6.3	An Alternative Approach To Determine Velocities	88
6.3.1	Image System Green's functions	90
6.3.2	Circular topography, an example	92
6.4	Equilibrium States For Vortex Patches Around Circular To- pography	94
6.4.1	V-states near finite height topography	95
6.4.2	Limiting cases for finite height circular topography	99
6.5	V-States In Time-dependent Flows	101
6.5.1	Using a computed V-state to initialize flow	101
6.5.2	Using a circular patch to initialize the flow	103
6.6	Conclusions	106
7	Interactions of Vortex Pairs with Circular Topography	108
7.1	Equations and Hamiltonian structure	110
7.2	Trajectories of point vortex pairs	111
7.2.1	Point vortex pair approaching a seamount, $\gamma < 1$	113
7.2.2	Point vortex pair approaching a well, $\gamma > 1$	117
7.3	Computed vortex patch trajectories	120
7.3.1	Vortex patch pair evolving toward a seamount, $\gamma > 1$	122
7.3.2	Vortex patch pair evolving toward a well, $\gamma < 1$	124
7.4	Two-Vortex Patch Equilibrium States	131

7.5	Conclusions	134
8	Laboratory Experiments on Dipolar Vortices Colliding with Step Topography	136
8.1	Apparatus and experimental arrangement	139
8.2	Qualitative observations	141
8.2.1	Dipoles approaching from deep water: $\gamma < 1$	142
8.2.2	Dipoles approaching from shallow water: $\gamma > 1$	144
8.3	Quantitative results	147
8.3.1	Two-dimensional vortex entrainment	147
8.3.2	Vorticity decay	152
8.3.3	Experimental results and inviscid theory: a comparison	154
8.4	Conclusions	157
9	Conclusions and Future Work	160
	Appendices	
A	V-State Centres Of Vorticity And Propagation Speeds	164
B	Analytical Approximation to V-States near Rectilinear Topography	165
C	Straddling V-State Model	168
D	Point Vortex Trajectories near Step Topography: detailed point vortex trajectories	172
E	Calculating Two-Vortex Equilibrium States for Rectilinear Topography	177
F	Energy of a Vortex Patch near Step Topography	179
G	Numerical Method For Calculating V-States near Circular Topography	182
H	Computing the Velocity near the Origin of a Circular Domain	184
I	V-state Centres of Vorticity and Initial Mean Radius	186

J	Calculating Two-Vortex Equilibrium States for Circular Topography	188
K	Experimental Data Analysis	190
	K.1 MatPIV	190
	K.2 Dipole trajectories	192
	K.3 Dipole area	194
	K.4 Incident and transmitted angle	195
L	Technical Drawings of Experiment Apparatus	196
	Bibliography	235

Chapter 1

Introduction

The surf-zone can be thought of as the region of wind generated breaking waves incident to the shoreline where many important environmental processes act including, for example, the transport of sediments and pollutants. The region is dynamic and is frequently characterized by a non-uniform wave train propagating toward the beach, breaking as they enter shallow water. As these waves break, they lose energy and transfer momentum into the anomalous fluid, thus generating various fluid motions over a wide range of scales. These include low frequency wave motions known as ‘surf-beat’ (Munk, 1949), resulting from two distinct wave train sets approaching the shore at the same time, currents flowing parallel (along-shore) and perpendicular (rip currents) to the shoreline, and, intense localised swirling currents, commonly known as eddies or vortices.

Considerable progress has been made in the understanding of surf-zone dynamics since the theoretical study by Longuet-Higgins & Stewart (1964). They demonstrated that a uniform, obliquely incident wave train on a sloping beach gives rise to an along-shore current. They coined the term ‘radiation stress’ to describe the excess flow of momentum due to the presence

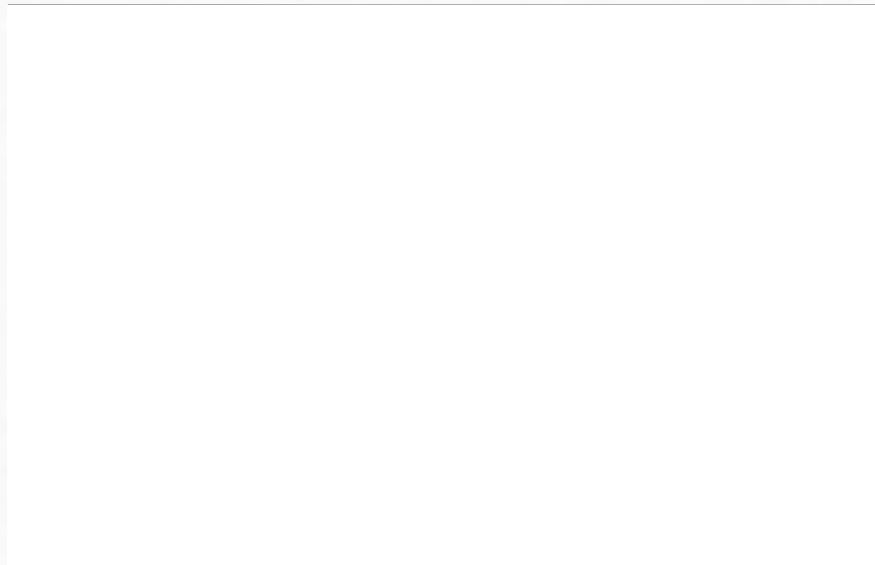


Figure 1.1: Rip currents as observed on Rosarita Beach, Baja California Mexico, October 1956 (from Peregrine, 1998).

of waves. Further theoretical work (Longuet-Higgins, 1970*a,b*) clarified the way in which the along-shore component of the incoming momentum flux acts to drive the along-shore current.

Perhaps more infamous than along-shore currents are riptides or rip currents which are relatively narrow strong currents reaching up to 2 m/s flowing roughly perpendicular to the shore and are observed frequently - see figure 1.1. Understanding the frequency and occurrence of rip currents is important since they are hazardous to bathers and have occasionally resulted in drowning when swimmers are swept offshore. Furthermore, they are often observed to carry debris and sediment (giving the current a distinctive colour to the surrounding fluid) out into the offshore region making them a key transport mechanism.

Shepard, Emery & La Fond (1941) gave the first qualitative description of rip currents and the process was divided into three main parts (see figure

Figure 1.2: A schematic of a rip current starting as a feeder region the current moves into a neck which spreads into the head from Shepard *et al.* (1941).

1.2). First the current is formed in the feeder region where flows are close to the beach and roughly parallel to the shore. The feeder current then flows outward into the narrow neck region where the current is fastest. Flows in the neck are thought to extend through the whole fluid depth since along the path of the neck a channel is often found carved out of an otherwise uniform bar in the bottom topography (formed by breaking waves in deep water). Beyond the breaking waves the current dissipates into the head where quasi-two dimensional eddies are observed.

Peregrine (1998) presents a theoretical study into the generation of vorticity (by breaking waves) with direction perpendicular to the plane of the

Figure 1.3: Schematic of a pair of eddies generated by, (a) gap in a pair of breaking waves and (b) from a single breaking wave incident to a beach. Vorticity is indicated by circular arrows, (from Peregrine, 1999).

waters surface. That is, the resulting eddying motion rotates in a two-dimensional fluid column over the entire depth of the fluid. A measure of the vorticity generated by breaking waves is found by considering the circulation around a circuit that cuts the edge of a breaking wave once. It follows that the rate of change of circulation due to an intersecting wave is proportional to the rate of change of energy dissipation. It is also argued that the generation of rip currents could be the result of an eddy couple translating away from the shore. The significant result of this work is the generation of vorticity which is manifested by vortical structures in the surf-zone which can ‘pair-up’ to mutually self advect off shore.

Peregrine (1999) further discusses vorticity generation in the surf-zone and gives schematic arguments on how such eddy pairs could form (see figure 1.3a). Here a gap in an otherwise homogeneous wave front, which is a common feature at beaches, results in an eddy pair. In the leftmost snapshot

a breaking wave starts to approach the beach. Vorticity is then generated at the edges of each of the waves. As the breaking waves translate closer to the shore the vorticity rolls up forming an eddy, which in turn, influences the dynamics of the waves. After the breaking wave has ceased there exists in the wake a pair of vortices which translate away from the shore. Peregrine (1999) shows another mechanism for eddy generation, where a pair translates toward the shoreline - see figure 1.3(b). Here an incident wave propagates toward the shore and starts to break. As before vorticity is generated at the edges of the wave. When the breaking wave has dissipated it leaves behind a pair of vortices this time translating toward the beach.

Observations and field experiments have verified the existence of rip currents and vortical structures. Smith & Largier (1995) examined, using sonar, the currents off a pier at the Scripps Institution, California. Rip currents were observed to occur in an episodic manner in unpredictable locations with a frequency of one to four rip currents per hour. These currents were quasi-two-dimensional and observed to be rich in sediments and bubbles confirming their importance for surf-zone mixing and transport. Individual eddies associated with the rip current were also observed, with a vortex pair often detaching from the initial 'rip' and carrying patches of surf-zone water offshore.

Field experiments observing other 'transient' rip currents have also been carried out. Johnson & Pattiaratchi (2004) used drifters and wave recorders to investigate the currents around a uniformly sloping beach in Leighton beach, Perth, Western Australia. These 'rips' behaved initially like a jet which flows offshore into a spreading head region around 20-30m away from the shoreline. Rip currents were observed along with dipolar and monopolar vortex structures suggesting the ubiquity of vortices in the surf-zone.

Considerable advances in computing have led to several studies simulating complex three-dimensional free surface wave breaking in the surf-zone. Slinn, Allen, Newberger & Holman (1998) solve the nonlinear shallow water equations with additional terms for bottom friction and forcing representing dispersion and momentum input in the along-shore direction for obliquely incident breaking waves. Periodic boundary conditions are used with barred beach topography without a rip channel. Computations show that shear instabilities in the alongshore current give rise to a ‘turbulent-sea’ of quasi two-dimensional vortex structures. In fact, vortices are shown to exist readily in the surf-zone with vortices often pair up to form dipoles which propagate offshore up to distances of $700m$. Monopoles are also observed to translate at a (nearly) constant speed parallel to the shore, occasionally overtaking one another.

Özkan-Haller & Kirby (1999) also use numerical techniques to simulate the surf-zone again using the non-linear shallow water equations with additional terms to account for forcing and damping effects. A uniform, obliquely incident wave train over barred beach was used to simulate an actual barred beach at Duck, North Carolina. The subsequent computations again show the ubiquitous nature of vortices in the surf-zone, with eddies often ejected out of the near-shore region and are advected over $100m$ offshore where they weaken due to viscous effects.

Chen, Dalrymple, Kirby, Kennedy & Haller (1999) used the nonlinear Boussinesq equations to investigate the surf-zone. This method allows the coupling of wave/current interactions. The beach topography is barred, but includes a rip channel with two separate simulations are made, one based on an actual beach the other on an idealized rip channel. Using a uniform normally incident wave train results show that for both beaches

strong vortices of opposite-sign are generated at the edges of the rip channel. Eddies then pair up and propagate away from the shoreline, translating beyond the breaking region in a perpendicular direction to the incoming waves before changing direction (due to instabilities in the rip current) and then propagating almost parallel to the shoreline.

Boussinesq modelling has also been used to study the generation and evolution of transient rip currents by Johnson & Pattiaratchi (2006). Here a random, directionally spread wave field was used so that no along-shore current was formed. Both monopolar and dipolar vortex structures were associated with rip currents with the latter often propagating offshore. Rip currents were found in the surf-zone with rip activity increasing with shallower beach slopes. It was suggested that a ‘rip index’ warning based on the sea state and slope of the beach could help lifeguards.

Bühler & Jacobson (2001) study the effects of breaking waves on a barred beach. Here the incoming waves are not uniform in the along-shore direction, but have finite length which lead to strong dipolar structures. Using the conservation of potential vorticity, the evolution of these vortices is found over the varying bottom topography. Then, a wave-mean theory is proposed for the surf-zone where alongshore currents interact with the dipolar structures generated by the finite length wave train. A numerical procedure is used to demonstrate these energetic dipolar structures propagate perpendicularly to the shoreline.

The above observational and numerical studies clearly demonstrate the common occurrence of vortices, both monopoles and dipoles, in the shallow water surf-zone. Such surf-zone regions are characterized by the presence of variable topography (i.e. sloping beaches, sand bars etc) which, in turn, play an important role in the dynamics of surf-zone vortices. This has

lead to several recent theoretical studies of shallow water vortices in the presence of variable topography. These studies are distinct from the large body of work on the dynamics of shallow water oceanic vortices in the rapidly rotating limit i.e. small Rossby number ($R_o = U/fl$). Instead, the following work considers the less well known dynamics of shallow water vortices over variable topography without rotation, i.e. $R_o = \infty$. This can be justified since the length scales associated with surf-zone vortices is small compared to geophysical scales such that the Coriolis force arising from planetary rotation can be neglected.

It is a well known phenomenon that a vortex near a solid wall will translate as if under the influence of a vortex of opposite-sign circulation located at the optical reflection in the wall. Known as the method of images, this technique has proved extremely powerful to determine fluid motion where boundaries with simple geometries exist. It is perhaps less well known that image methods can be used for other topographic configurations. Surf-zone vortices over a uniformly sloping beach may be considered to be a sector of a vortex ring and therefore have the ability to self-propagate (Peregrine, 1998; Johnson, 1978). Exploiting this idea Thorpe & Centurioni (2000) consider a wedge of inviscid fluid and use the method of images to determine the evolution of vortices and for jets parallel to the edge of the wedge. These jets are used to model the development of instability of the alongshore current using an axisymmetric jet as its image system. Previous results on jets carry over immediately, with instabilities in jets leading to two dimensional vortex structures. They conclude that vortices are common features in disturbances in alongshore flows.

Richardson (2000) considered the motion of shallow water vortices at zero Froude number (i.e. the rigid lid approximation) with variable topog-

raphy. In the limit of small vortex radius compared to the characteristic length scale for variations in depth, it is found that, to leading order, a vortex moves along contours of depth at a speed proportional to the local gradient in the logarithm of the depth. The resulting formula were solved for two vortices on beaches whose depth varied in one dimension only. First, using an exponential depth profile an exact solution for the Green's function is found enabling trajectories for point vortices to be found explicitly. The trajectories show a vortex pair initially in shallow water translates into deeper water with decreasing separation. Second, a numerical procedure was used to compute the trajectories of a vortex pair near a smooth step. As the pair translated from deep to shallow water the individual vortices were advected closer together. It was also noted that an obliquely incident dipole pair translating in shallow water could be reflected by the topography.

In another recent study, Johnson & McDonald (2004) investigate the motion of a vortex in a non-rotating homogeneous fluid with zero Froude number near a step change in depth. It is found that owing to the presence of the step a vortex in relatively deep water is under the action of 'partial' image of opposite-sign circulation and with reduced strength. Furthermore, a vortex in relatively shallow water is influenced by an 'partial' image of same-sign circulation. Note that these images are virtual and do not actually exist; they merely represent the effect of the boundary conditions at the step. An example is given of a vortex patch pair impinging on the step with normal incidence. Explicit knowledge of the Green's function allowed a computational method to evaluate the time dependent evolution of finite area vortex patches. The resulting trajectories of a vortex patch pair were compared to the trajectories of idealized point vortex motion (which cannot cross the escarpment) which were derived from Hamiltonian techniques. The

two sets of trajectories compared favourably provided the vortex patches were well spaced. Like Richardson (2000), it was found that vortices moving from deep water into shallow water had increased separation and larger cross-sectional area from mass conservation. Likewise, vortices translating from shallow to deep water had smaller separations after crossing the step and therefore translated quicker.

This thesis is concerned by the dynamics and evolution of two dimensional beach vortices near piecewise flat topography. Like the studies of Thorpe & Centurioni (2000), Richardson (2000) and Johnson & McDonald (2004) the complex problem of breaking waves in the surf-zone is divorced from the two-dimensional dynamics. Throughout this thesis, a rigid-lid or zero Froude number is assumed and vortices are taken to be two-dimensional. The consideration of piecewise flat topography is clearly an approximation to a smoothly varying beach profile. However, it does enable exact Hamiltonian methods to be used for point vortices and highly accurate numerical method to compute vortex patch motion.

The following work is broadly divided into two main sections according to the choice of topography. First, vortex evolution is found near an infinitely long step change in depth. Chapter 2 describes the fundamental equations of used in this research and their associated conservation laws. A brief description of the numerical method of contour dynamics used extensively in this research is also given. Chapter 3 forms the basis of a recent publication in *Phys. Fluids*, (Johnson, Hinds & McDonald, 2005), which computes steadily translating monopoles without deviation in shape, V-states near an escarpment. Using asymptotic techniques the V-state shape is found in the limit of large distance away from the escarpment and simple model is found to simulate the speed of a vortex when it straddles the escarpment.

Chapter 4 considers the general problem of two interacting vortices near a step using both Hamiltonian and numerical techniques. Chapter 5 recently been published in *J. Fluid Mech.* (Hinds, Johnson & McDonald, 2007), where a vortex patch pair with oblique incidence to a step is studied in detail. An analytical result is found which explicitly relates the incident angle to the transmitted angle in terms of the depth ratio of the topography and the centroid separation. Vortex patch pairs will always attempt to cross the escarpment except for certain initial conditions for a dipole approaching the step from shallow water where, interestingly, it is found that a pair will be reflected by the step.

The second part of this work considers isolated topography in the form of a circular step change in depth. Chapter 6 computes monopolar V-states which translate with constant angular frequency. Both shallow water interior and exterior to the topography are considered as well as computing V-states for the limiting cases of finite height topography: an island and an infinitely deep well. Chapter 7 then calculates the trajectories of a vortex pair, having equal and opposite-signed circulation impinging on the circular topography. Two cases are examined in detail, first when the dipole interacts with a seamount and second when the dipole is incident to a well. A critical trajectory is found which separates possible point vortex motion into different families. Comparisons with vortex patch motion are made with good agreement.

Laboratory experiments are described in chapter 8, in which dipolar vortices impinge on a escarpment. Comparisons are made with analytical results in previous chapters. Finally conclusions are presented in chapter 9.

Chapter 2

Fundamental Equations, Conservation Laws and Numerical Method

This chapter is used to state the main principles and assumptions frequently used in this thesis. Furthermore, the fundamental equations which govern the dynamics of the fluid are stated as well as giving a brief overview of the numerical techniques used.

2.1 Model formulation and equations

The surf-zone is characterized by continuous wave breaking which leads to vigorous fluid mixing and yields various rapidly flowing quasi two-dimensional currents and jets which interact on small (compared to the Earth's) length scales. Following previous analytical studies of Richardson (2000); Johnson & McDonald (2004) and Thorpe & Centurioni (2000) this thesis neglects the complex wave mean-flow interaction problem and

instead considers an idealized surf-zone modelled by a two-dimensional, homogeneous, inviscid, non-rotating fluid which is governed by the shallow water equations

$$\frac{D\mathbf{u}}{Dt} = -\nabla p, \quad (2.1a)$$

$$\frac{\partial H}{\partial t} + \nabla \cdot (H\mathbf{u}) = 0, \quad (2.1b)$$

where $D/Dt = \partial_t + \mathbf{u} \cdot \nabla$ is the material derivative, $\mathbf{u} = (u, v)$ is the two-dimensional velocity, p is the pressure owing changes in depth $H = h - h_B$ where h is the height at the fluid surface and h_B is the height of the bottom topography (for a detailed description see Pedlosky, 1987). Note the effect of the Earth's rotation has been neglected in (2.1a). This is justified since the Rossby number U/fL (where $f \sim 10^{-4}$ is the Coriolis parameter) is typically very large for these vortices since $L \sim 1 - 10m$ and $U \sim 1m/s$. Taking the curl (2.1a), and defining the vertical component of vorticity as $\omega = (\nabla \times \mathbf{u}) \cdot \mathbf{k} = v_x - u_y$ gives

$$\frac{\partial \omega}{\partial t} + u \frac{\partial \omega}{\partial x} + v \frac{\partial \omega}{\partial y} + \omega \left(\frac{\partial u}{\partial x} + \frac{\partial v}{\partial y} \right) = 0, \quad (2.2)$$

or, upon using (2.1b)

$$\frac{Dq}{Dt} = 0, \quad (2.3)$$

where $q = \omega/H$ is the potential vorticity, a conserved quantity governing the dynamics of the fluid. Equation (2.3) is of pivotal importance to this study and is central to many geophysical fluid processes. It states that following fluid particles q is conserved. That is, if particle passes into a different depth H , its vorticity ω is adjusted accordingly, e.g. passing into deeper water, its vorticity increases.

Consider a fluid in which the free surface is flat, such that the Froude

number is zero, commonly referred as the rigid lid approximation. Then equation (2.1b) allows the introduction of a volume flux stream function ψ (since H is constant in time)

$$(u, v) = H^{-1}(-\psi_y, \psi_x), \quad (2.4)$$

such that the instantaneous distribution of q determines the velocity field through (2.4) and the inversion of the vorticity-streamfunction relation

$$\nabla \cdot (H^{-1} \nabla \psi) = \omega. \quad (2.5)$$

Assume a piecewise constant vorticity distribution that vanishes at sufficiently large distances. Then assuming constant H (2.5) can be inverted using Green's functions such that

$$\psi(x, y) = \iint \omega(x', y') G(x, y, x', y') dx' dy', \quad (2.6)$$

where

$$\nabla^2 G = \delta(x - x') \delta(y - y'). \quad (2.7)$$

2.1.1 Integral invariants of a vorticity distribution

By mass conservation the volume

$$\mathcal{V} = \int H dx dy, \quad (2.8)$$

gives a second constant of motion (where here and below the integral is taken over the compact support of the vorticity). The circulation

$$\Gamma = \int q H dx dy, \quad (2.9)$$

yields a third constant of motion since

$$\frac{d\Gamma}{dt} = \int \omega_t dx dy = - \int \nabla \cdot (\mathbf{u}\omega) dx dy = 0. \quad (2.10)$$

The remaining constant of motion above arbitrary bottom topography is the kinetic energy, \mathcal{E}

$$\mathcal{E} = \frac{1}{2} \int \omega \psi dx dy. \quad (2.11)$$

For topography that varies in one dimension only it can be shown that the linear impulse,

$$\mathcal{I} = \int q H^2 dx dy, \quad (2.12)$$

gives another constant of motion, details of which are given in the next chapter.

2.2 Contour Dynamics

In general to follow the motion of a distribution of vorticity it is necessary to invert (2.5) numerically and use the resultant velocity field in (2.4) to advect the potential vorticity. For piecewise-constant patches of potential vorticity, contour dynamics is a particularly efficient and accurate method to achieve this. This section briefly details the method which was originally pioneered by Deem & Zabusky (1978) and enhanced by Dritschel (1988) whose algorithm is the basis of the numerical computations in this work.

For an infinitely large two-dimensional plane the Green's function for (2.7) is given by

$$G[(x - x'), (y - y')] = \frac{1}{2\pi} \log |(x - x')^2 + (y - y')^2|^{\frac{1}{2}} = \frac{1}{2\pi} \log r. \quad (2.13)$$

For piecewise constant H , the form of G will be given later in this thesis.

The velocity can be written from (2.4)

$$(u, v) = -\frac{1}{2\pi} \iint \omega(x', y') \left[-\frac{\partial G}{\partial y}, \frac{\partial G}{\partial x} \right] dx' dy'. \quad (2.14)$$

Suppose that the potential vorticity distribution can be divided into N distinct, piecewise constant patches of potential vorticity q_j in regions D_j , $j = 1, \dots, N$ to obtain N integrals

$$\begin{aligned} (u, v) &= -\frac{1}{2\pi} \sum_j \omega_j \iint_{D_j} \left[-\frac{y-y'}{r}, \frac{x-x'}{r} \right] dx' dy', \\ &= -\frac{1}{2\pi} \sum_j \omega_j \iint_{D_j} \left[\frac{\partial G}{\partial y'}, -\frac{\partial G}{\partial x'} \right] dx' dy' \end{aligned} \quad (2.15)$$

then by applying Green's theorem

$$\iint_D \left(\frac{\partial R}{\partial x} - \frac{\partial P}{\partial y} \right) dx dy = \oint_C (P dx + R dy), \quad (2.16)$$

where C is the boundary of the region D . For u set $P = -G$ and $R = 0$ and $R = -G$ and $P = 0$ for v , giving

$$(u, v) = \frac{1}{2\pi} \sum_j \Delta\omega_j \oint_{C_j} G(r_j) (dx', dy'). \quad (2.17)$$

where C_j is the boundary of region D_j , (x_j, y_j) is a point on C_j and $r_j^2 = (x - x_j)^2 + (y - y_j)^2$. Importantly $\Delta\omega_j$ is defined as the jump in vorticity across a contour C_j . Each C_j encloses a jump in vorticity with no mass flux crossing a contour.

Equation (2.17) forms the basis of contour dynamics and shows how the velocity field arising from a distribution of piecewise constant potential vorticity can be evaluated by a summation of line integrals. Usually this is

more efficient and accurate than using finite difference or spectral methods. The evolution of patches in time can then be found using, for example, a fourth order Runge-Kutta algorithm on (2.17) to update the position of the contour given the velocity points around the patch.

In implementing contour dynamics the total number of nodes, is in general, not constant, owing to the material deformation of the patch. As the patch stretches there is an increase in finer scales which need to be properly accounted for. This is based on the creation or deletion of nodes locally in order to achieve a distribution in which the local node spacing lies within a prescribed resolution. Node distribution around the contour is based on cubic interpolation between neighbouring nodes and is implemented at each Δt .

Contour dynamics was adapted by Dritschel (1988) to allow contours to break or merge known in a process he called contour surgery. This aspect of the algorithm also permits the removal of long thin filaments which are smaller than a predefined scale. This procedure lightens the computational load since very thin contours are dynamically insignificant flow features (since they have small circulation owing to their small area) and require a large number nodes to model their evolution (for further details see Pullin, 1992).

The basis of the computational work in this thesis uses the contour surgery algorithm based on the original 1988 code kindly provided by Prof. D. Dritschel. This has subsequently been modified to account for the piecewise constant topography (see Johnson & McDonald, 2004).

Chapter 3

Steadily Translating Vortices near Step Topography

3.1 Introduction

As discussed in Chapter 1 the shallow water associated with the surf zone on a beach is known to support two-dimensional eddy structures. Recently, Johnson & McDonald (2004) found the Green's function for a point vortex in a shallow, inviscid fluid near a step of finite depth ratio separating half spaces of constant depth. They noted that a point vortex propagates parallel to the step at a speed dependent on the depth ratio, the distance of the vortex from the step and the strength of the vortex. The explicit form for the Green's function enabled the time-dependent behaviour of finite-area patches of constant vorticity to be studied using an adaption of the numerical method of contour surgery (Dritschel, 1988). The collision of finite area vortex pairs of equal and opposite vorticity with the step was analysed and it was shown that finite area vortices approaching at normal incidence always cross whereas a point vortex never does. It was argued that this

followed from the fact that the along-step speed of a point vortex increases without limit as the vortex approaches a step whereas the along-step speed of a finite area vortex had a finite maximum. No computations or models were however presented to support this conjecture and it is one of the purposes of this chapter to present relevant computations and a simple predictive model for monopolar patches of uniform potential vorticity translating steadily parallel to a step. If such structures exist and, further, if they are stable, then they are likely to play an important role in transport processes in the surf zone.

In the absence of topography, the calculation of two-dimensional distributions of patches of constant vorticity governed by the Euler equations in steady translation or rotation—V-states—have been the subject of much research (see Deem & Zabusky, 1978; Pierrehumbert, 1980; Saffman & Tanveer, 1982; Wu, Overman & Zabusky, 1984; Dritschel, 1995). Indeed, the computation of such steady solutions was one of the original uses for the now well-established numerical method of contour dynamics. Typically, translating V-states have been found (Pierrehumbert, 1980; Saffman & Tanveer, 1982; Deem & Zabusky, 1978), which consist of a pair of symmetric, but oppositely signed patches of vorticity. Equivalently Wu *et al.* (1984) found monopolar V-states near a wall. In the context of the present work in which topography is present, the limit in which the depth on one side of the step vanishes is equivalent to this classic V-state problem. It is shown by direct computation here, however, that for arbitrary depth changes a monopolar vortex patch, which may, or may not, straddle the step, propagates steadily parallel to the step with finite speed.

Section 3.2 describes the governing equations and the properties of a point vortex near an escarpment. Section 3.3 gives the numerical method

and also describes the form of the steadily propagating solutions. Section 3.4 notes analytical approximations to the solutions and give a model for predicting vortex speeds. The robustness of the computed steady solutions is tested in section 3.5 using time-dependent contour dynamics, first by tracking the evolution of a flow initialized with a V-state and, second, by following a circular patch and computing its evolution toward a V-state. Conclusions are given in section 3.6.

3.2 Preliminary equations

It has been shown already that the motion is governed by the conservation of potential vorticity, viz. (2.3)

$$q_t + \mathbf{u} \cdot \nabla q = 0$$

where $q = \omega/H$ is the potential vorticity for $\omega = v_x - u_y$ the vertical component of vorticity. Consider a vorticity distribution that vanishes at sufficiently large distances. It has been shown that the energy and circulation are constants of motion above arbitrary bottom topography. Now consider topography independent of x and introduce

$$Y(y) = \int^y H(y') dy', \quad \mathcal{I} = \int Y \omega dx dy. \quad (3.1)$$

Then, with the area element $dx dy$ understood,

$$\frac{d\mathcal{I}}{dt} = \int Y \omega_t = - \int Y \nabla \cdot (\mathbf{u} \omega) = - \int \nabla \cdot (\mathbf{u} \omega Y) + \int \omega \mathbf{u} \cdot \nabla Y. \quad (3.2)$$

The first integral vanishes as $\omega \rightarrow 0$ at large distances and the second gives

$$\frac{d\mathcal{I}}{dt} = \int \omega v H = \int (v_x - u_y) v H = \int [(\frac{1}{2} v^2 H)_x - (u v H)_y + (v H)_y u]. \quad (3.3)$$

The first two terms vanish as the velocity decreases at large distances and so by continuity

$$\frac{d\mathcal{I}}{dt} = - \int (u H)_x u = - \int (\frac{1}{2} u^2 H)_x = 0. \quad (3.4)$$

Hence the quantity \mathcal{I} , the impulse of the vorticity distribution, is conserved throughout the motion.

Since the depth H cannot vanish in the interior of the flow, Y is a strictly monotonically increasing function of y . Thus

$$Y(y_{min})\Gamma < \mathcal{I} < Y(y_{max})\Gamma, \quad (3.5)$$

where y_{min} and y_{max} are the minimum and maximum extents of the vortex distribution in the y -direction. Since $Y(y)$ is monotone, this implies that with given \mathcal{I} and Γ there can be associated a unique value of y , y_c say, given by

$$Y(y_c) = \frac{\mathcal{I}}{\Gamma}, \quad (3.6)$$

with $y_{min} < y_c < y_{max}$ and this quantity remains constant throughout the motion. Thus with any vortex distribution there can be associated a unique centre of vorticity, above x -independent topography, (x_c, y_c) where x_c is the usual x -mean,

$$x_c = \frac{\int x \omega dx dy}{\Gamma}, \quad (3.7)$$

and y_c is the conserved quantity given by (3.6), lying within the extremes

of the vorticity distribution in the y -direction.

For topography consisting of a single step along $y = 0$ between flat regions in $y < 0$ and $y > 0$,

$$H(x, y) = \begin{cases} H^+ & y > 0, \\ H^- & y < 0, \end{cases} \quad (3.8)$$

for H^+ and H^- constant, Y can be taken to be $Y = Hy$. Then

$$\Gamma = \int q H dx dy, \quad \mathcal{I} = \int q H^2 y dx dy, \quad y_c = \mathcal{I}/(\Gamma H_0), \quad (3.9)$$

where $H_0 = H(\text{sgn}[\mathcal{I}/\Gamma])$. The centre of vorticity coincides with the centroid of the vorticity distribution for vortices located entirely on one side of the step, but differs for distributions with vorticity on both sides of the step and thus, in particular, for vortices straddling the step.

For the step topography (3.8) the Green's function can be determined from requiring pressure and mass flux to be continuous across the escarpment. This yields continuity conditions on G and $1/H \partial G / \partial n$ where n is the normal to the discontinuity in depth. Thus the streamfunction due to a point potential vortex $q = Q \delta(x - x_0) \delta(y - y_0)$ is

$$\Psi(z) = \begin{cases} -(Q/2\pi) H(y_0) [\log |z - z_0| + \alpha \log |z - \bar{z}_0| \text{sgn } y], & y_0 y > 0, \\ -(Q/2\pi) \beta \log |z - z_0|, & y_0 y < 0, \end{cases} \quad (3.10)$$

for complex $z = x + iy$, $z_0 = x_0 + iy_0$,

$$\alpha = \frac{\gamma - 1}{\gamma + 1}, \quad \beta = \frac{2H^+ \gamma}{\gamma + 1}, \quad (3.11)$$

and $\gamma = H^-/H^+$ with a similar form for the streamfunction found by Bidlot

& Stern (1994) and Richardson (2000). Here α gives the strength of the image of the vortex in the step and β the shielded strength of the original vortex on the opposite side of the step. For a vortex in deep water (e.g. $\gamma < 1$ and $y_0 > 0$), the flow in $y > 0$ is driven by an additional, oppositely signed image (of strength $\alpha < 0$) at $-y_0 < 0$. The flow in $y < 0$ is driven simply by the original vortex, but with reduced strength β . A vortex in shallow water ($y_0 < 0$, $\gamma < 1$), has an image of same-sign circulation with strength α and a shielded strength β in deep water ($y > 0$).

The image strength α and the shielded vortex strength β have ranges $-1 < \alpha < 1$, $0 < \beta < 2H^+$, with extreme values corresponding to a wall ($\gamma = 0$) and an infinitely deep drop-off ($\gamma \rightarrow \infty$) respectively. A vortex in deep water has a usual image, with opposite-sign circulation as the step is ‘wall-like’, whereas a vortex in shallow water has an image with same-sign circulation as the step acts as an ‘anti-wall’. It follows that a point vortex thus propagates parallel to the step under the influence of its image with velocity

$$(u, v) = \left(\frac{QH_0\alpha}{4\pi y_0}, 0 \right). \quad (3.12)$$

3.3 Steadily-Propagating Finite Area Vortices: V-States

Propagating finite area vortices can be constructed using the Green’s function (3.10) and the algorithm for two-dimensional vortices in the Euler equations based on previous work by Wu *et al.* (1984). Essentially V-states are found by evaluating the streamfunction found by immersing a circular monopolar vortex in a constant velocity field i.e. Uy . Starting with an initially circular contour of constant potential vorticity, velocity components

are computed at N nodes along the vortex boundary which is parameterized with angle θ such that the radial distance from a fixed point inside the vortex (of free choice) is given by $R(\theta)$. Then

$$\Psi(R, \theta) + Uy = \text{const}, \quad (3.13)$$

is required, where Ψ is the streamfunction of the vortex only. Differentiating with respect to θ gives

$$\frac{\partial \Psi}{\partial x} \frac{\partial x}{\partial \theta} + \frac{\partial \Psi}{\partial y} \frac{\partial y}{\partial \theta} + U \frac{\partial y}{\partial \theta} = 0, \quad (3.14)$$

or discretizing for N nodes

$$\bar{v}_i \Delta x_i + (U - \bar{u}_i) \Delta y_i = 0, \quad (3.15)$$

where $\bar{\mathbf{u}}_i$ is the mean value of the velocity between adjacent nodes. Δx and Δy are functions of R and θ , therefore by considering the i^{th} and $(i+1)^{th}$ node it is possible to construct a tridiagonal system which can be inverted to evaluate $R(\theta_i)$ simultaneously. Repeating this process iteratively, it is possible for a V-state to be converged upon i.e. until the translational velocity has converged to six significant figures on using 4704 nodes for a patch with unit radius. If the vortex straddles the step, the sections of the vortex on each side are treated separately with the area and relative vorticity adjusting to conserve potential vorticity and volume.

Figure 3.1 shows V-states for varying y_c for $\gamma = 1/2, 1/3, 1/5$ with volume chosen, without loss of generality, as πH^+ so each V-state has unit mean radius in deep water, $y > 0$ (note here and below deep water always resides in $y > 0$). Each frame of Figure 3.1 is a steady, monopolar V-state,

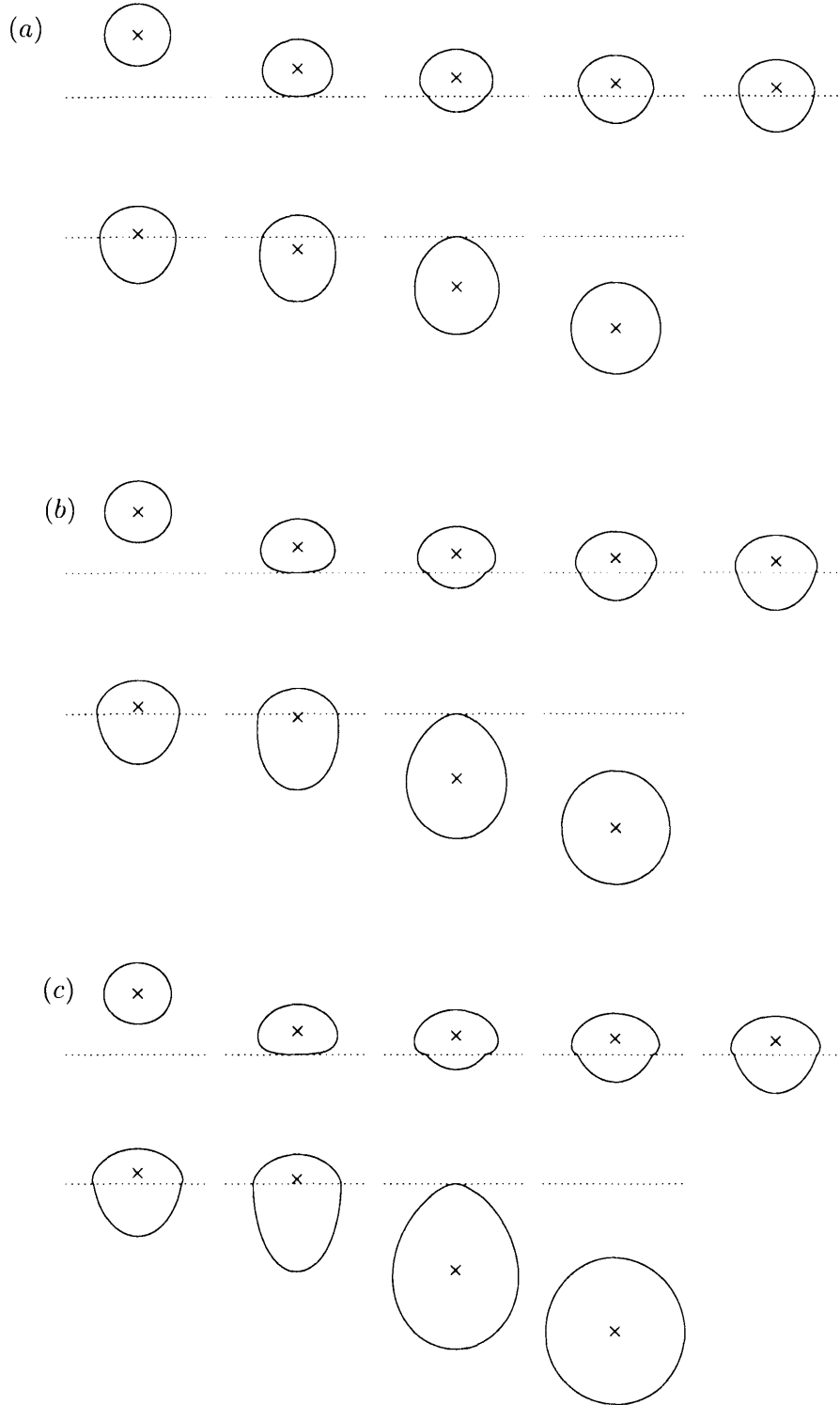


Figure 3.1: V-states at nine centre of vorticity positions for depth ratios $\gamma = H^-/H^+$. (a) $\gamma = 1/2$, (b) $\gamma = 1/3$, (c) $\gamma = 1/5$. The dotted line gives the escarpment dividing deep water in $y > 0$ from shallow water in $y < 0$. The corresponding centre of vorticity positions and translational velocities are given in table A.

translating parallel to the step. Table A gives the corresponding centre of vorticity positions and translational velocities.

The form of a V-state can be anticipated from an analogy with equilibrium states of self-gravitating bodies (Johnson, 1978). A monopole in deep water ($y > 0$) has in shallow water ($y < 0$) a repulsive image of strength proportional to the depth ratio. A V-state with centroid position far from the escarpment is influenced only slightly by this image and remains almost circular. A V-state with centre of vorticity closer to the escarpment is more strongly influenced by its image and is repelled and elongates along the escarpment, flattening on the side closest to the escarpment to resemble two-dimensional Euler vortices near vertical walls, (Pierrehumbert, 1980; Wu *et al.*, 1984; Saffman & Tanveer, 1982). This becomes more pronounced as γ decreases so the flow is shallower on the far side of the step.

A monopole in shallow water ($y < 0$) has in deep water ($y > 0$) an attractive image. A V-state with centre of vorticity position close to the escarpment is attracted by its image and stretches toward the escarpment, narrowing parallel to the escarpment. V-states wholly in $y < 0$ the contour are ‘tear-like’, with average radius increased to $\sqrt{1/\gamma}$ to conserve volume. They resemble a single vortex forming half of a same-signed two-dimensional Euler vortex pair, cf. Dritschel (1995), although there the pair rotates and here the single vortex translates rectilinearly. V-states straddling the escarpment are attracted in $y > 0$ and repelled in $y < 0$. Large depth contrasts, i.e. for small γ , the boundary curves significantly where it crosses the escarpment.

3.4 Analytical Approximations For V-States

Appendix B notes that the boundary of a vortex patch of unit average radius in deep water can be written in polar coordinates with origin at the centre of vorticity as

$$R(\theta) = 1 + \frac{\epsilon^2 \alpha}{4} \cos 2\theta - \frac{\epsilon^3 \alpha}{16} \sin 3\theta + \mathcal{O}(\epsilon^4), \quad (3.16)$$

where $\epsilon^{-1} \gg 1$ is the distance from the step to the centre of vorticity, with a similar expression for patches in shallow water. Figure 3.2 shows for $\gamma = 1/3$ a comparison between a numerically computed V-state contour and the V-state from (3.16) when the V-states are touching the step (i.e. the value of ϵ is equal to the distance from the step). Even in this most extreme case ($\epsilon = 1.15$ for a V-state in deep water and $\epsilon = 0.514$ for shallow water) expansion (3.16) agrees well with the computed V-states. In deep water the approximate V-state flattens along the side closest to the step and in shallow water the V-state stretches towards the escarpment. Figure 3.3 compares the aspect ratio Δ of a V-state, defined as the ratio of the longest y -direction chord of the V-state to the longest x -direction chord, from (3.16) with numerical results for $\gamma = 1/3$. They agree closely until the V-state touches the escarpment (straddling occurring for $-2.02 < y_c < 0.811$), the limit of validity of the analytical model. From deep water, the aspect ratio decreases as the centre of vorticity of the V-state approaches the escarpment, with Δ a minimum when the V-state touches the escarpment, and then increases rapidly as y_c decreases for V-states over the step. A maximum aspect ratio is reached before decreasing to unity once the V-state is away from the step in shallow water.

This analysis does not apply to vortices straddling the step and a dif-

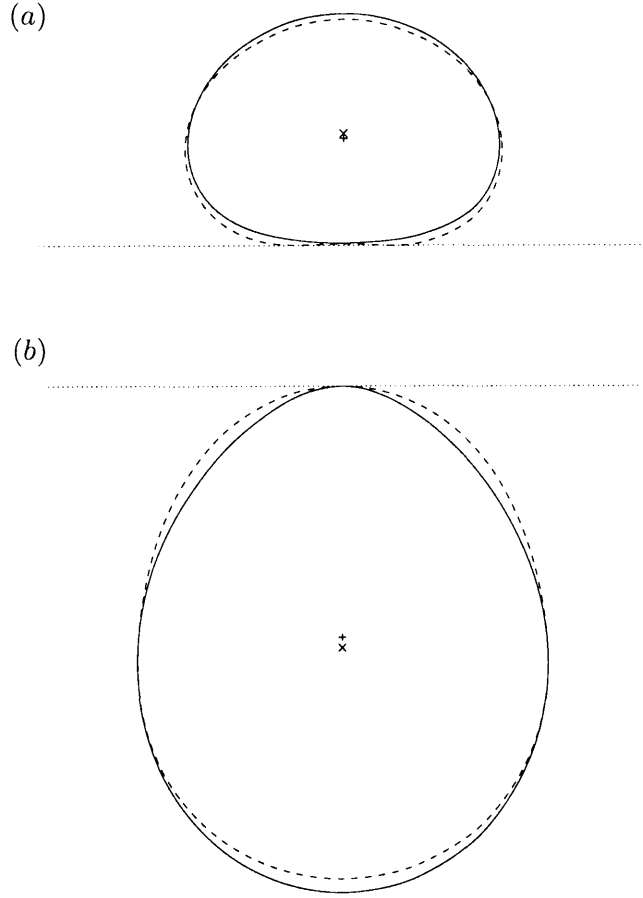


Figure 3.2: A comparison between the analytical V-state boundary for $\gamma = 1/3$ when ϵ is taken so that the contour is just touching the escarpment (dashed line with centroid $+$) and a numerically computed V-state when the V-state is just touching the escarpment (solid line with centroid \times). (a) A deep water ($y > 0$) V-state. (b) A shallow water ($y < 0$) V-state.

ferent model is described in Appendix C for this case. The sections of the V-state on either side of the escarpment are taken to be segments of ellipses. The aspect ratios of each segment are precisely those determined by the analytical approximation (3.16) when the V-state touches the escarpment and the volume associated with the V-state is held constant. This determines the approximate V-state uniquely and provides a continuous transition be-

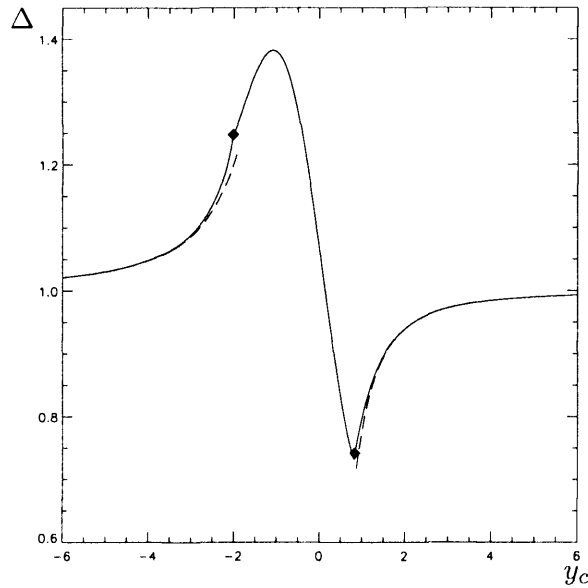


Figure 3.3: The aspect ratio, Δ , of a family of V-states with depth ratio $\gamma = 1/3$ as a function of the centre of vorticity y_c . The solid line is the numerical value and the dashed line the aspect ratio from (3.16). The dashed line stops when the approximate V-state touches the escarpment and the diamonds on the solid curve show where the numerically computed V-state first touches the step.

tween the solutions for V-states touching the escarpment in deep and shallow water.

Figure 3.4 compares translational speeds from this model with those from the numerical solutions at various depth ratios γ . Away from the step point vortex speeds closely matches V-state speeds, but closer to the step the V-state travels more slowly compared to a point vortex. This deviation occurs earlier with smaller γ as the larger depth ratio distorts the V-state more strongly from circular. The V-state has a unique maximum, finite, translational velocity which increases with decreasing γ . The value of y_c where the maximum is attained is well predicted by the elliptical segment model although the magnitude is slightly over estimated. All V-states have

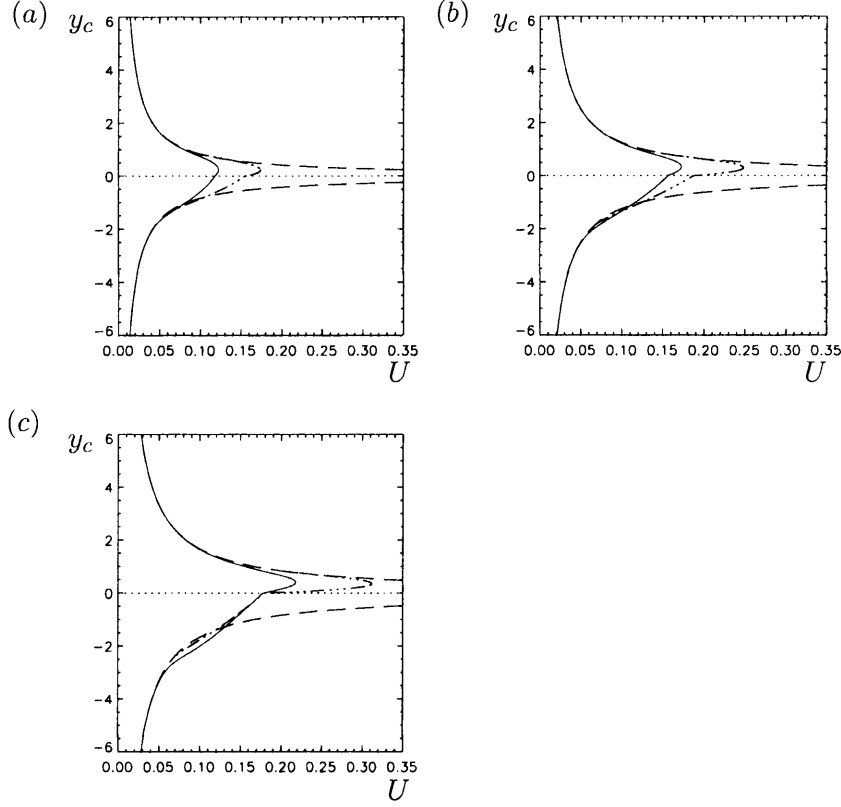


Figure 3.4: The translational velocity, U , as a function of the centre of vorticity y_c : the numerical result (solid line), a point vortex of equivalent circulation (dashed line) and the V-state model as described in Appendix C (dashed-dotted line). (a) $\gamma = 1/2$. (b) $\gamma = 1/3$. (c) $\gamma = 1/5$.

finite translation speed unlike point vortices whose translational velocity becomes unbounded in the limit $y_0 \rightarrow 0$ (as in (3.12)). This is captured by the elliptical segment model (in Appendix C) and shows that it is the finite separation of the centroid position of each segment patch forming the straddling V-state that limits the translational velocity.

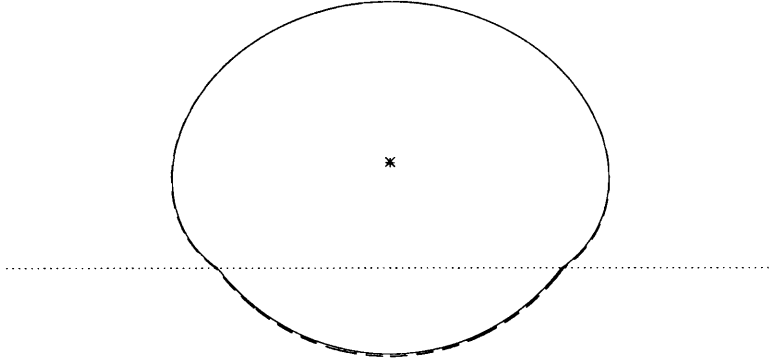


Figure 3.5: A comparison between the initial and final states of a flow started from a V-state. Here the depth ratio is $\gamma = 1/2$. The solid line is the initial V-state (with the centre of vorticity marked by +) and the dashed line the contour after 25 turnover times (with centre of vorticity marked by \times).

3.5 V-States In Time-Dependent Flows

3.5.1 Flow initialized from a computed V-state

To test the robustness of the computed V-states, the time-dependent equations of motion were integrated using a fourth order in time Runge-Kutta scheme. The flow was initialized with a computed V-state above a doubling of depth ($\gamma = 1/2$) and figure 3.5 compares the initial computed V-state against the shape of the patch after 25 eddy turnover times (during which time it has propagated over 38 radius lengths). There is minimal vorticity shedding throughout the evolution (after 10 turnover times approximately 0.283% of patch volume has been lost and even after 25 turnover times only 0.676% of the volume is lost) caused by the finite resolution of the time-dependent code and subsequent vortex surgery. The removal of small filaments generated during the motion also causes the centre of vorticity to be displaced slightly. Both these effects are remarkably small given the long duration (in space and time) of the integration. This and other integrations, not shown here, show that the computed V-states appear stable in the sense

that their shape remains coherent and relatively invariant over long times. Although V-states have a weak tendency to shed vorticity, particularly over large depth contrasts, they propagate large distances with little change in form.

3.5.2 Flow initialized from a circular patch

A further set of time dependent numerical integrations have been performed to find whether computed V-states act as attractors to the flow, i.e. whether a vortex patch that is not an exact V-state will evolve to approach a V-state. Figure 3.6 shows the evolution of an initially circular patch for $\gamma = 1/3$ with the area of the initial vortex being split equally between the deep and shallow side of the step and for $\gamma = 1/5$ with the ratio of the area on the deep to shallow side being 1 : 3. Each evolution is followed for 25 turnover times while the vortices propagate over 75 radius lengths. The last frame in each series shows the V-state with the same volume and centre of vorticity as the final frame of the patch evolution. The strong similarity of each of these final pairs of frames shows that V-states can indeed act as attractors to the flow. For $\gamma = 1/3$ there is little vortex shedding and y_c is approximately constant for the main vortex patch. However for the larger depth contrast of $\gamma = 1/5$ vortex shedding is significant with 4.83% of the initial patch volume lost from the main patch. This means that although the centre of vorticity y_c remains constant when calculated over all space (including filaments) as required, but y_c for the main patch changes as vorticity is shed. Further integrations, not shown here, show that vortices of arbitrary shape above a step shed vorticity through filamentation and tend towards a V-state. The depth contrast strongly affects the rate of convergence to a V-state. For the same initial configuration (with equal areas in deep and shallow

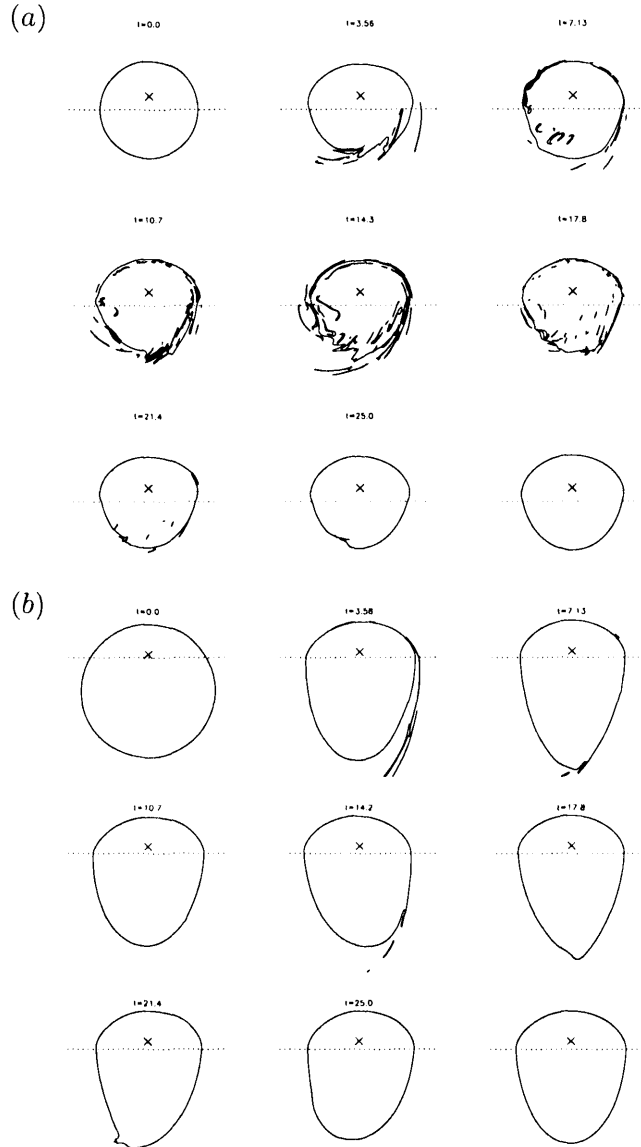


Figure 3.6: The evolution of a vortex that is initially circular and directly over an escarpment. Frame are at equal intervals of time t , scaled on the eddy turnover time. (a) $\gamma = 1/3$, (b) $\gamma = 1/5$. The last frame in each series is the V-state with the same centre of vorticity as the penultimate frame.

water) convergence when $\gamma = 1/3$ is relatively quick – after 5 turnover times the volume of the main patch is within 0.844% of the final volume of the main patch whereas for $\gamma = 1/5$ similar convergence takes approximately 15

turnover times.

3.6 Conclusions

Self-propagating, monopolar V-states, consisting of a single patch of constant vorticity near an infinitely long step of constant height ratio have been obtained numerically and described analytically for non-rotating, inviscid flow in the limit of zero Froude number. It has been shown that the fundamental conserved quantity for rectilinear topography, in addition to the energy, is the centre of vorticity, y_c , and that this differs from the vortex centroid. General trends of the properties of the V-states are given as functions of y_c and the depth contrast $\gamma = H^-/H^+$. V-states in shallow water are ‘tear’ shaped with the vortex stretched towards the escarpment by an attracting image in deep water. V-states in deep water flatten along the side closest to the escarpment, with flattening becoming more pronounced as the V-state approaches the escarpment as in Euler equation V-states near walls, (Wu *et al.*, 1984; Saffman & Tanveer, 1982; Pierrehumbert, 1980; Deem & Zabusky, 1978). V-states have been derived analytically for $y_c \gg 1$ and with an elliptical segment model for V-state straddling an escarpment, allowing a qualitative prediction of the finite translation speed of the vortices.

Time-dependent flows initialized with a V-state showed little change in vortex shape even after 25 turnover times and the vortex had propagated over 75 radius lengths, showing that V-states are robust features of the flow. V-states were also shown to act as attractors to the flow in that initially circular patches above a step shed vorticity to approach a V-state. The combination of these properties means that V-states should be observable in both the surf-zone and the laboratory. They are likely to be important transport mechanisms in the surf-zone with their ability to capture and

transport anomalous fluid over large distances parallel to isobaths (or depth contours).

Chapter 4

Interactions of Two Vortices with Step Topography

4.1 Introduction

Chapter 3 examined the interaction of a single vortex with an infinitely long escarpment. The principal aim of this chapter is to understand the general dynamics of two arbitrary vortices interacting with topography.

In the absence of topography it is a classical result by Kirchoff (1876) and developed further by Lin (1941) that the equations of motion for an N point vortex system in an arbitrary domain are Hamiltonian. The Hamiltonian structure has been exploited in many studies of point vortices (see for example Aref & Stremler, 1999; Aref, 1978).

The motion of a point vortex pair near a wall has been studied in detail (e.g Saffman, 1992). This is a special case of four vortex motion where two image vortices (having opposite-sign circulation to the vortices) are used to account for the presence of the wall. Typically the motion for two vortices having same-sign circulation near a wall is either; *orbiting*, where both

vortices rotate about their centre of vorticity, or *leap-frogging*, where one vortex overtakes the other and is then overtaken itself. Motion of vortices having opposite-sign circulation is also characterized by orbiting (without leap-frogging) and *pairing-off*, where vortices translate parallel to the wall toward each other and then pair-up to translate away in a direction perpendicular to the wall.

Love (1894) found that two point vortex pairs existing in two-dimensional inviscid fluid can exist in a stable leap-frogging trajectory along an axis of symmetry, or equivalently, a point vortex pair near a wall leap-frog parallel to the impermeable barrier. More recently, this analytical work has been verified computationally by Acheson (2000) and experimentally by Yamada & Matsui (1978), where three-dimensional vortex rings (whose motion is used as an analog for two point vortex pairs) ‘mutually slip’ through each other before becoming unstable.

The motion of two vortex patches near a wall has been studied by Overman & Zabusky (1982) over a wide range of parameters. Using contour dynamics, initially distant vortex patches having opposite-sign were allowed to approach each other. Several numerical experiments where vortices have opposite-sign are described: a distant pair (with equal and oppositely signed circulation, but unequal area) translated mainly under the influence of their image in the wall until they become close. They then ‘exchange’ into an asymmetric quasi-steady configuration travelling away from the wall. The trajectories in the remaining experiments could be categorized as orbiting where patches passed around a fixed point until the contributions from their images were strong enough for the vortices to break the orbit and translate parallel to the wall. Other experiments used vortices of the same-sign, but different magnitude circulation where one vortex was allowed to catch up

with the other. Although the patches deformed severely, the trajectories could be categorized as orbiting (since there was no repeated overtaking, i.e. leap-frogging).

Motivated by these results, the aim for the present work is to classify the possible motions of two vortices near topography in the form of an infinitely long step. Even with this simple choice of topography the problem yields a large number of parameters namely; depth ratio, the initial positions of the vortices, the circulations of each vortex and, for vortex patches, their volume. These parameters determine the conserved quantities of linear impulse, energy and circulation. For brevity, focus is given here to motions with varying impulse, energy and the sign of each vortex.

After stating the preliminary equations section 4.2 continues by deriving the motion of point vortices, casting their dynamics in Hamiltonian form. Section 4.3 gives examples of possible motion for two point vortices, with examples given for vortex pairs having the same and opposite-sign circulation. Section 4.4 uses contour dynamics to compute the motion of two vortex patches of constant potential vorticity and their trajectories are compared to point vortex motion for equivalent constants of motion. Section 4.5 computes a special trajectory where two vortex patches translate parallel to the step. A brief discussion of results is given in section 4.6.

4.2 Preliminary equations and Hamiltonian formation

As in chapter 3, a two-dimensional, non-rotating, ideal fluid in the limit of zero Froude number is assumed and the topography is taken to be a finite step change in height (where the fluid has depth H^+ in $y > 0$ and H^- in

$y < 0$). Fluid motion is governed by the conservation of potential vorticity $q = \omega/H$ and the total kinetic energy

$$\mathcal{E} = \frac{1}{2} \int \psi \omega \, dx dy, \quad (4.1)$$

is a constant of the motion and recalling ψ as a volume flux streamfunction giving velocity components $(u, v) = H^{-1}(-\psi_y, \psi_x)$. Here and below, ω is taken to decay sufficiently rapidly at infinity to give convergent integrals. For topography that varies in one direction only (the y direction, say), the linear impulse

$$\mathcal{I} = \int Y(y) \omega \, dx dy, \quad (4.2)$$

where $Y(y) = \int^y H(y') dy'$ gives a second constant of the motion, where the circulation

$$\Gamma = \int \omega \, dx dy, \quad (4.3)$$

gives the third constant of motion. However, for vortex patches only, a fourth constant, the volume

$$\mathcal{V} = \int H(y) \, dx dy, \quad (4.4)$$

of each patch (with the integral taken over the support of either patch) remains constant by mass conservation. Conservation of q and \mathcal{V} together imply the circulation of each vortex patch is individually conserved.

Consider N point vortices situated near unbounded stepped topography each having potential vorticities Q_0, \dots, Q_N and positions z_0, \dots, z_N where $z_1 = x_1 + iy_1, \dots, z_N = x_N + iy_N$, with each unique z_j with $y_j \neq 0, j =$

$1, \dots, N$. Then the complex potential, w , at the point z has the form,

$$\Im[w] = \sum_{j=1}^N Q_j H_j G(z; z_j) = \psi. \quad (4.5)$$

It follows (see, for example, Saffman, 1992) that differentiating (4.5) with respect to z at $z = z_j$ gives

$$Q_j H_j (u_j - iv_j) = \sum_{k=1}^N Q_j H_j Q_k H(z_k) \frac{\partial}{\partial z_j} G(z_j, z_k) + Q_j^2 H_j^2 \frac{\partial}{\partial z} g(z; z_j) \Big|_{z=z_j}, \quad (4.6)$$

where $H(z_j)$ is the height of fluid depth at point z_j and $g(z, z_j) = G(z, z_j) + \frac{1}{2}\pi \log |z - z_j|$ is differentiable everywhere H is (Johnson & McDonald, 2004). Further, g is the contribution to the streamfunction at z due to vortex j and can be regarded as the image system of vortex j owing to topography. Define

$$\mathcal{H}(z_1, \dots, z_N) = \frac{1}{2} \sum_{j=1}^N \sum_{k=j+1}^N Q_j H_j Q_k H(z_k) G(z_j, z_k) + \frac{1}{2} \sum_{j=1}^N Q_j^2 H_j^2 g(z_j, z_j), \quad (4.7)$$

then it follows that

$$Q_j H_j (u_j - iv_j) = \frac{\partial \mathcal{H}}{\partial z_j} = \frac{\partial \mathcal{H}}{\partial y_j} + i \frac{\partial \mathcal{H}}{\partial x_j}. \quad (4.8)$$

Hence by (4.8) \mathcal{H} is of Hamiltonian form and the co-ordinates of the vortices follow curves of constant \mathcal{H} .

For $N = 1$ using the Green's function for a point vortex near an escarpment, (3.10), a point vortex can only exist in deep water or shallow water. Then the double sum in (4.7) vanishes and the vortex follows constant curves of $\frac{1}{2}(Q_1 H_1)^2 g(z_1, z_1) = \text{constant}$, or $\Im[z_1] = \text{constant}$. For two vortices with arbitrary circulations there are four possible point vortex configurations and

three independent Hamiltonians. These are from (4.7),

(i) Both vortices exist in deep water, [deep, deep] :

$$\mathcal{H}_{d,d} = -\frac{1}{2\pi} \left\{ Q_1 Q_2 (H^+)^3 (\log |z_1 - z_2| + \alpha \log |z_1 - \bar{z}_2|) + \frac{1}{2} \alpha Q_1^2 (H^+)^3 \log |2y_1| + \frac{1}{2} \alpha Q_2^2 (H^+)^3 \log |2y_2| \right\}. \quad (4.9)$$

(ii) One vortex is in deep water the other is in shallow, [deep, shallow] :

$$\mathcal{H}_{d,s} = -\frac{1}{2\pi} \left\{ \beta Q_1 Q_2 H^+ H^- \log |z_1 - z_2| + \frac{1}{2} \alpha Q_1^2 (H^+)^3 \log |2y_1| - \frac{1}{2} \alpha Q_2^2 (H^-)^3 \log |2y_2| \right\}. \quad (4.10)$$

(iii) Both vortices exist in shallow water, [shallow, shallow] :

$$\mathcal{H}_{s,s} = -\frac{1}{2\pi} \left\{ Q_1 Q_2 (H^-)^3 (\log |z_1 - z_2| + \alpha \log |z_1 - \bar{z}_2|) - \frac{1}{2} \alpha Q_1^2 (H^-)^3 \log |2y_1| - \frac{1}{2} \alpha Q_2^2 (H^-)^3 \log |2y_2| \right\}, \quad (4.11)$$

with subscripts 1 and 2 describing the position of each vortex. The fourth vortex configuration (the opposite of (ii)), where vortex 1 is in shallow water and vortex 2 is in deep water, [shallow, deep] has Hamiltonian of the same form as [deep, shallow] with subscripts 1, 2 interchanged.

For a given depth ratio, γ , the dynamics of point vortex motion is constrained by the constants of motion, namely the circulation $\Gamma = QH$, the energy \mathcal{E} (given by the Hamiltonian) and for topography that varies in one dimension the impulse \mathcal{I}

$$\mathcal{I} = \sum_i Q_i H_i^2 y_i. \quad (4.12)$$

It is this set of parameters which uniquely defines the trajectories of point vortices near stepped topography. Equivalently, point vortex motion can be uniquely defined in terms of the parameter set $(\mathcal{I}, \Gamma, \mathcal{E})$. For two vortices with like sign circulation (of different magnitude) it is useful to introduce

the new variables

$$\xi = x_1 - x_2, \quad \eta = y_1 - y_2. \quad (4.13)$$

This allows the y position of each vortex, using (4.12), to be written in terms of the impulse and η i.e.

$$y_1 = \frac{\mathcal{I} + Q_2 H_2^2 \eta}{Q_2 H_2^2 + Q_1 H_1^2}, \quad y_2 = \frac{\mathcal{I} - Q_1 H_1^2 \eta}{Q_2 H_2^2 + Q_1 H_1^2}. \quad (4.14)$$

For a specified depth ratio, γ , impulse and circulation, the Hamiltonian can only vary in the relative x positions of the vortices i.e. vary as a function of $\xi = x_1 - x_2$ only. It follows that identical trajectories exist when the vortices are translated in the x -plane. Thus it is not necessary to specifically define the actual x -positions of the vortices, but only their relative distance. This implies that knowing the system location in (ξ, η) -space uniquely defines the (x, y) positions of the vortices (up to translations in the x -plane). By contouring the Hamiltonian in (ξ, η) -space, all possible vortex trajectories with parameters $\mathcal{E}, \mathcal{I}, \Gamma$ can be drawn at once. In what follows, without loss of generality, $x_1 < x_2$ (i.e. vortex 1 is to the left of vortex 2) and in *all* figures the depth ratio $\gamma < 1$ (such that deep water exists in $y > 0$).

4.3 Trajectories of point vortices

There is a wide range of possible trajectories for two vortices near stepped topography. Here they are split into two groups: when both vortices have the same-sign circulation and when they have oppositely signed circulation. This is motivated by the contrasting trajectories of point vortices near a wall by changing the sign of one vortex (see for example Aref, 1983a; Saffman, 1992). Each vortex configuration is described in terms of the depth ratio

$\gamma = H^-/H^+$ and its conserved quantities: impulse, energy and circulation.

4.3.1 Trajectories of point vortex pairs with like signed circulation

As noted in chapter 3, a point vortex cannot cross the escarpment. It follows that there are limits on possible η for a two vortex system, which can be written in terms of \mathcal{I} , from (4.12)

$$\mathcal{I} = Q_1 H_1^2 y_1 + Q_2 H_2^2 y_2. \quad (4.15)$$

First, assume both vortices are in deep water (i.e. [deep,deep] configuration) and assume for now $\mathcal{I} > 0$ (such that $Q_{1,2} > 0$). The maximum value of $\eta = y_1 - y_2$ occurs when $y_2 = 0$, that is when vortex 2 approaches the escarpment. It follows that at maximum y separation, $\eta = \mathcal{I}/Q_1 H_1^2$. Similarly the minimum value of η is given by $\eta = -\mathcal{I}/Q_2 H_2^2$, when vortex 1 is close to the step. Thus since a point vortex cannot cross the escarpment the bounds of realizable vortex motion for [deep,deep] configuration are

$$-\frac{\mathcal{I}}{Q_2 H_2^2} < \eta < \frac{\mathcal{I}}{Q_1 H_1^2}. \quad (4.16)$$

If $\mathcal{I} < 0$ it is not possible for both vortices to translate in deep water, since it would require $y_{1,2} < 0$, however, it is possible for both vortices to translate in shallow water [shallow,shallow]. Similar arguments to the above yield the following bounds, on the other possible configurations:

- (i) [deep, shallow]: For $\mathcal{I} > 0$, η has a lower bound with no upper bound
i.e.

$$\eta > \frac{\mathcal{I}}{Q_1 H_1^2}. \quad (4.17)$$

The direction of inequality is reversed for $\mathcal{I} < 0$.

- (ii) [shallow, deep]: For $\mathcal{I} > 0$, η has an upper bound with no lower bound i.e.

$$\eta < \frac{\mathcal{I}}{Q_2 H_2^2}. \quad (4.18)$$

For $\mathcal{I} < 0$ the direction of inequality is reversed.

- (iii) [shallow, shallow]: For $\mathcal{I} < 0$ bounds for realizable trajectories satisfy

$$-\frac{\mathcal{I}}{Q_2 H_2^2} < \eta < \frac{\mathcal{I}}{Q_1 H_1^2}, \quad (4.19)$$

with no motion allowed for $\mathcal{I} > 0$ since this would require both vortices existing in deep water (this is the converse of the initial example given).

4.3.1.1 Trajectories of vortex pairs with like sign circulation and positive impulse

Figure 4.1 gives typical trajectories obtained by contouring the appropriate Hamiltonian for each depth configuration, for two vortices with positive impulse in (ξ, η) -space.

For large η figure 4.1 shows the configuration is such that vortex 1 is in deep water and vortex 2 is in shallow water [deep, shallow] with a typical trajectory given by figure 4.1(a). In this regime the motion of each vortex is dominated by its topographic image, only when $\xi \rightarrow 0$ do the vortices interact strongly, forcing each other away from the step. After reaching maximum y separation, i.e. maximum η , the pair separate and interact only weakly. Further, the shallow water vortex is forced closer to the escarpment until it is arbitrarily close and propagates parallel to the step with increasing speed whereas the deep water vortex translates closer to its lower bound,

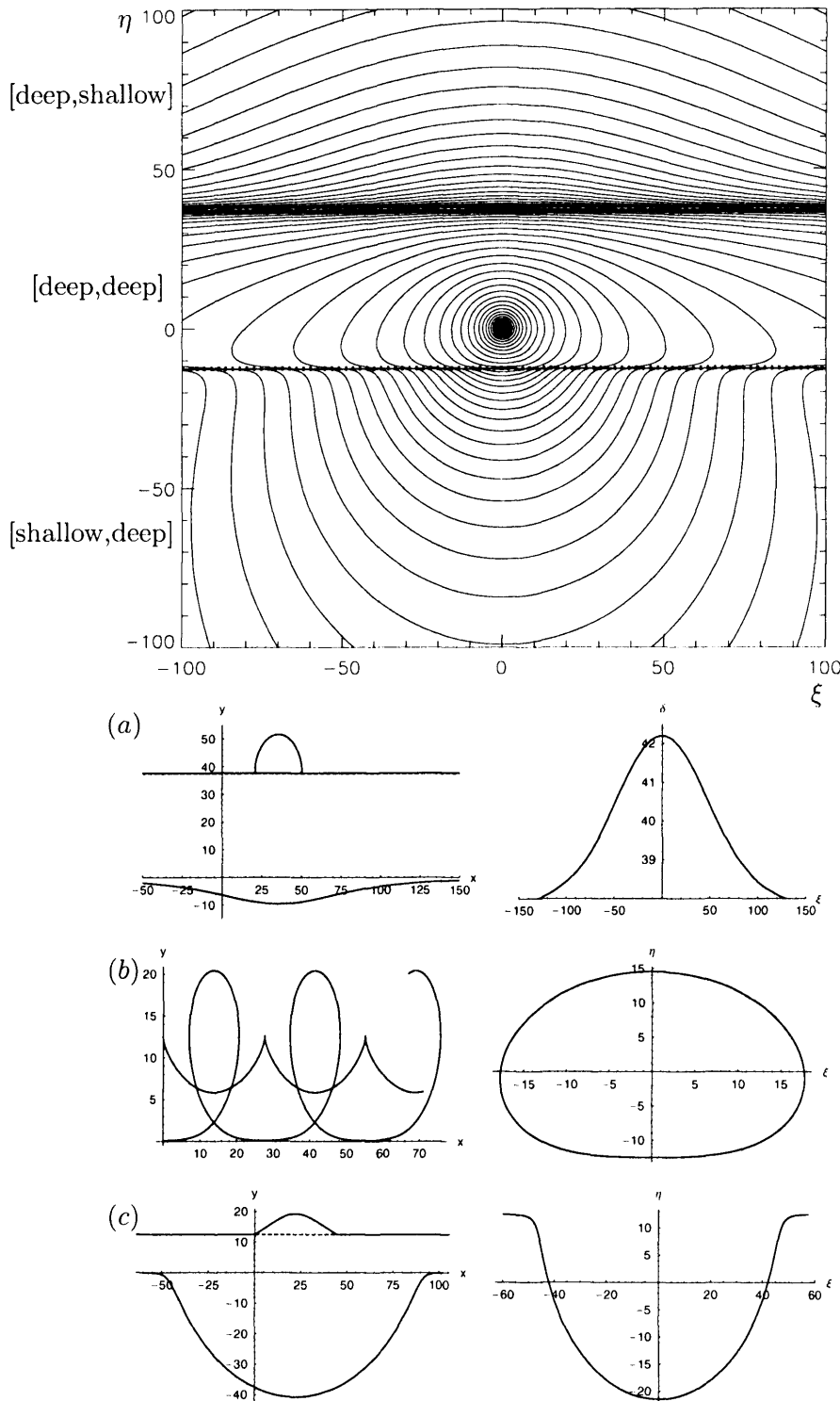


Figure 4.1: Possible (ξ, η) -space trajectories for two point vortices with same-sign circulation near stepped topography with depth ratio $\gamma = 1/2$ and impulse $\mathcal{I} = 75\pi$, $Q_1 H_1 = \pi$ and $Q_2 H_2 = 3\pi$. Dotted lines separate the possible regimes of flow and indicate where its partnering point vortex approaches the escarpment. The remaining figures represent typical trajectories in (x, y) space and (ξ, η) space for (a) [deep, shallow], (b) [deep, deep] and (c) [shallow, deep] flow. Here and below dotted lines, where shown, indicate the appropriate bound to vortex motion determined from the impulse.

given by (4.17) (i.e. $y_1 = \mathcal{I}/Q_1 H^+$ marked here and below on the figure by a dotted line) and also translates parallel to the step albeit at a much slower rate.

Typical trajectories for the [deep,deep] configuration are closed in (ξ, η) -space which represents leap frogging vortices in (x, y) -space, as shown in figure 4.1(b). As such, the trajectories are similar to those of like signed vortices near a wall (Aref & Stremler, 1999; Saffman, 1992). Trajectories in (ξ, η) -space become more circular when the vortices are closer together, as the topography has a lesser effect on the dynamics of the motion and the vortices act like two signed vortices orbiting each other.

In the final configuration, [shallow, deep], trajectories in (ξ, η) and (x, y) spaces have similar properties to [deep, shallow] motion. For large η the vortex motion is dominated by their respective images. Similar to [deep, shallow]; as the vortices interact strongly the shallow and deep water vortices are advected away from the step. After reaching maximum η both vortices are forced closer to the step and separate: the shallow water vortex approaches the escarpment and translates quickly, and the deep water vortex approaches its bound found from (4.18).

4.3.1.2 Trajectories of vortex pairs with like sign circulation and negative impulse

Figure 4.2 show contours of the Hamiltonian in (ξ, η) -space for $\gamma = 1/2$ and negative impulse. Again, the trajectories fall into three regimes.

For the [deep,shallow] configuration, vortex motion is periodic with typical trajectories given by figure 4.2(a). For [shallow,shallow] it is not the case that all trajectories are closed (as in [deep, deep] configuration in the previous example). However, two separatrices exist in (ξ, η) -space which dis-

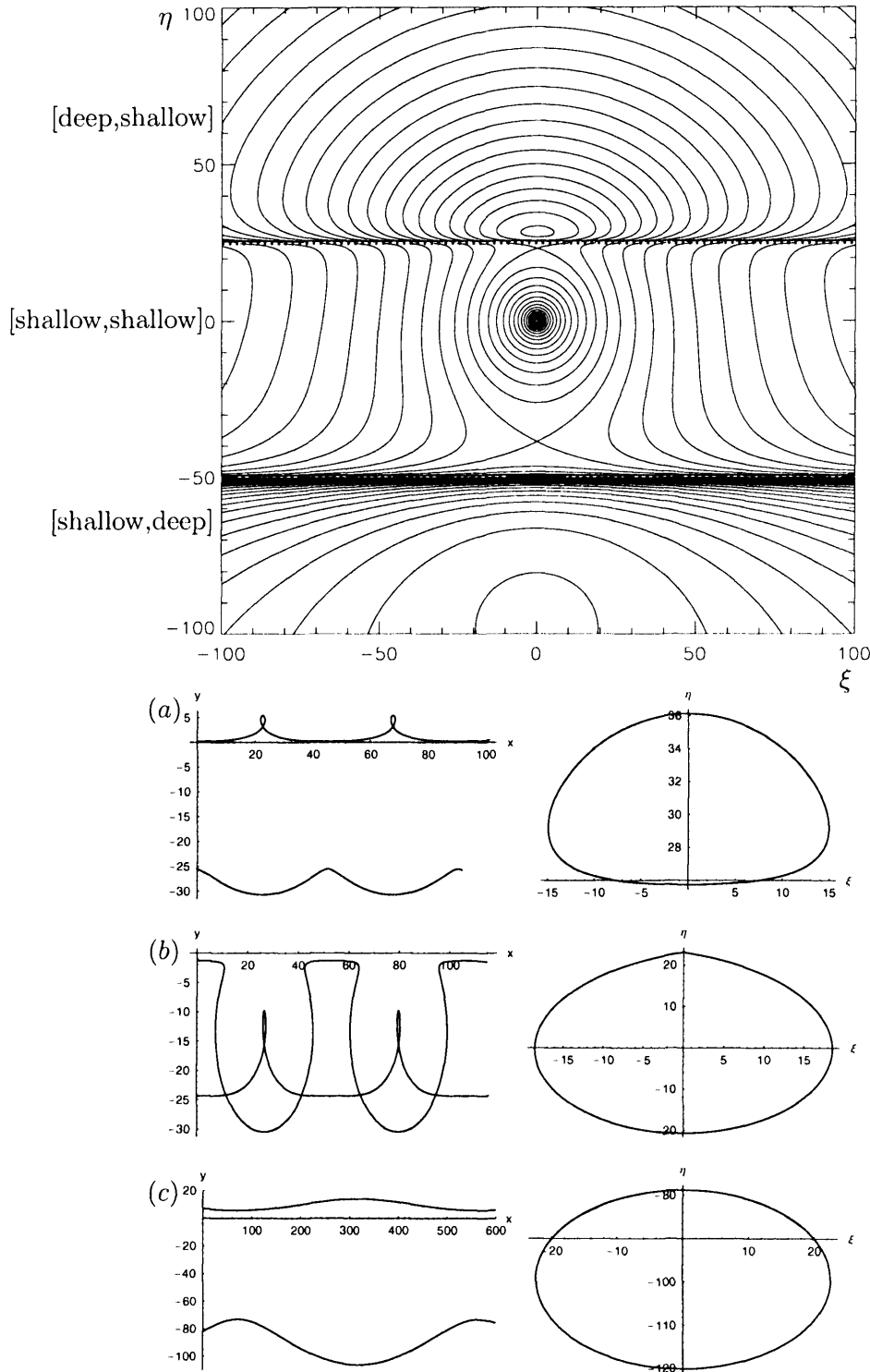


Figure 4.2: Possible (η, ξ) -space trajectories for two point vortices with same-sign circulation near stepped topography with depth ratio $\gamma = 1/2$ and $\mathcal{I} = -50\pi$, $Q_1 H_1 = \pi$ and $Q_2 H_2 = 2\pi$. Dotted lines separate the three regimes and indicate where a point vortex approaches the escarpment. The remaining figures represent typical trajectories in (x, y) -space and (ξ, η) -space for (a) [deep, shallow], (b) [shallow, shallow] and (c) [shallow, deep] configurations.

tinguish between periodic motion in (x, y) -space (i.e. closed loops in (ξ, δ) -space), and trajectories which are aperiodic. As the pair translates in shallow water each vortex will experience an image of the same-sign circulation. When the partnering vortex in the pair dominates over the partial image, trajectories are periodic (with example trajectories shown in figure 4.2b). If the partial image dominates over the partnering vortex, periodic motion does not occur and one vortex will approach the step, eventually becoming arbitrarily close to the escarpment (see Appendix D, figure D.1). It follows there exists stationary point in (ξ, η) space where the relative distance between the vortices remains constant and the vortices translate steadily together parallel to the step. These points and the resulting separatrices separate periodic motion which form closed loops in (ξ, η) -space and motion where a vortex will approach the escarpment. These two-vortex equilibrium states can be found easily by equating the velocity parallel to the escarpment of each vortex and solving for $y_{1,2}$ positions when $\xi = 0$ (see Appendix E).

The last regime in figure 4.2 is [shallow, deep]. Here trajectories are closed loops in (ξ, η) -space, but do not represent orbiting or leap-frogging. In this configuration the vortices move in tandem along the step, but on opposite sides of the escarpment executing small amplitude oscillations.

4.3.2 Trajectories of oppositely signed point vortex pairs

For oppositely signed vortices introduce (ξ, δ) -space where

$$\delta = y_1 + y_2, \quad (4.20)$$

such that $y_{1,2}$ can now be written in terms of \mathcal{I} and δ i.e.

$$y_1 = \frac{|Q_2|H_2^2\delta\mathcal{I} + \mathcal{I}}{|Q_1|H_1^2 + |Q_2|H_2^2}, \quad y_2 = \frac{|Q_1|H_1^2\delta - \mathcal{I}}{|Q_1|H_1^2 + |Q_2|H_2^2}. \quad (4.21)$$

The Hamiltonian (4.9), for each depth regime is the same as for like-signed vortices, but the bounds for realizable motion are subtly different. Consider the [deep,deep] configuration for example: a positive impulse with $Q_1H_1 > 0$ and $Q_2H_2 < 0$ (i.e. \mathcal{I} has the same-sign as Q_1H_1) gives,

$$\mathcal{I} = |Q_1|H_1^2y_1 - |Q_2|H_2^2y_2, \quad (4.22)$$

where $y_{1,2} > 0$. There is no upper bound on δ , however there is a lower bound when y_2 approaches the escarpment, given by,

$$\delta > \frac{\mathcal{I}}{|Q_1|H_1^2}. \quad (4.23)$$

When \mathcal{I} has the same-sign as Q_2H_2 the same argument applies yielding (4.23) with subscripts 1,2 swapped. For the other regimes:

- (i) [deep,shallow]: When the impulse has the same-sign as Q_1H_1 then realizable trajectories exist for δ such that,

$$-\frac{\mathcal{I}}{|Q_2|H_2^2} < \delta < \frac{\mathcal{I}}{|Q_1|H_1^2}. \quad (4.24)$$

It is therefore possible for either vortex 1 or vortex 2 to approach the step. However, when \mathcal{I} has the same-sign as Q_2H_2 , there are no realizable trajectories.

- (ii) [shallow,deep]: This configuration is constrained in a similar way to

[deep shallow]; when \mathcal{I} has the same-sign as Q_2H_2 , δ is bounded by

$$-\frac{\mathcal{I}}{|Q_1|H_1^2} < \delta < \frac{\mathcal{I}}{|Q_2|H_2^2}, \quad (4.25)$$

so that both vortices can get close to the step. When \mathcal{I} has the same-sign as Q_1H_1 there are no possible trajectories.

(iii) [shallow,shallow]: Similar to the [deep,deep] case; when \mathcal{I} has the same-sign as Q_1H_1 there is no lower bound on δ , but an upper bound exists:

$$\delta < -\frac{\mathcal{I}}{|Q_2|H_2^2}. \quad (4.26)$$

When \mathcal{I} has the same-sign as Q_2H_2 , the same inequality applies with vortex subscripts swapped. Therefore only the vortex with the same-sign as \mathcal{I} can approach the step.

4.3.2.1 Trajectories of vortex pairs with opposite-sign circulation and positive impulse

Example trajectories (obtained by contouring the appropriate Hamiltonian) of point vortices with positive impulse and depth ratio $\gamma = 1/2$ are given in figure 4.3.

For large δ both point vortices propagate in deep water (i.e. [deep,deep]) and trajectories are analogous to a pair near a wall. Trajectories which are closed in (ξ, δ) -space correspond to a pair orbiting periodically about a fixed (with respect to the y axis) point. However, figure 4.3(a) shows an example of an open trajectory in (ξ, δ) -space together with the corresponding trajectory in the physical plane. A separatrix divides these differing types of motion with the hyperbolic point representing a two-vortex equilibrium

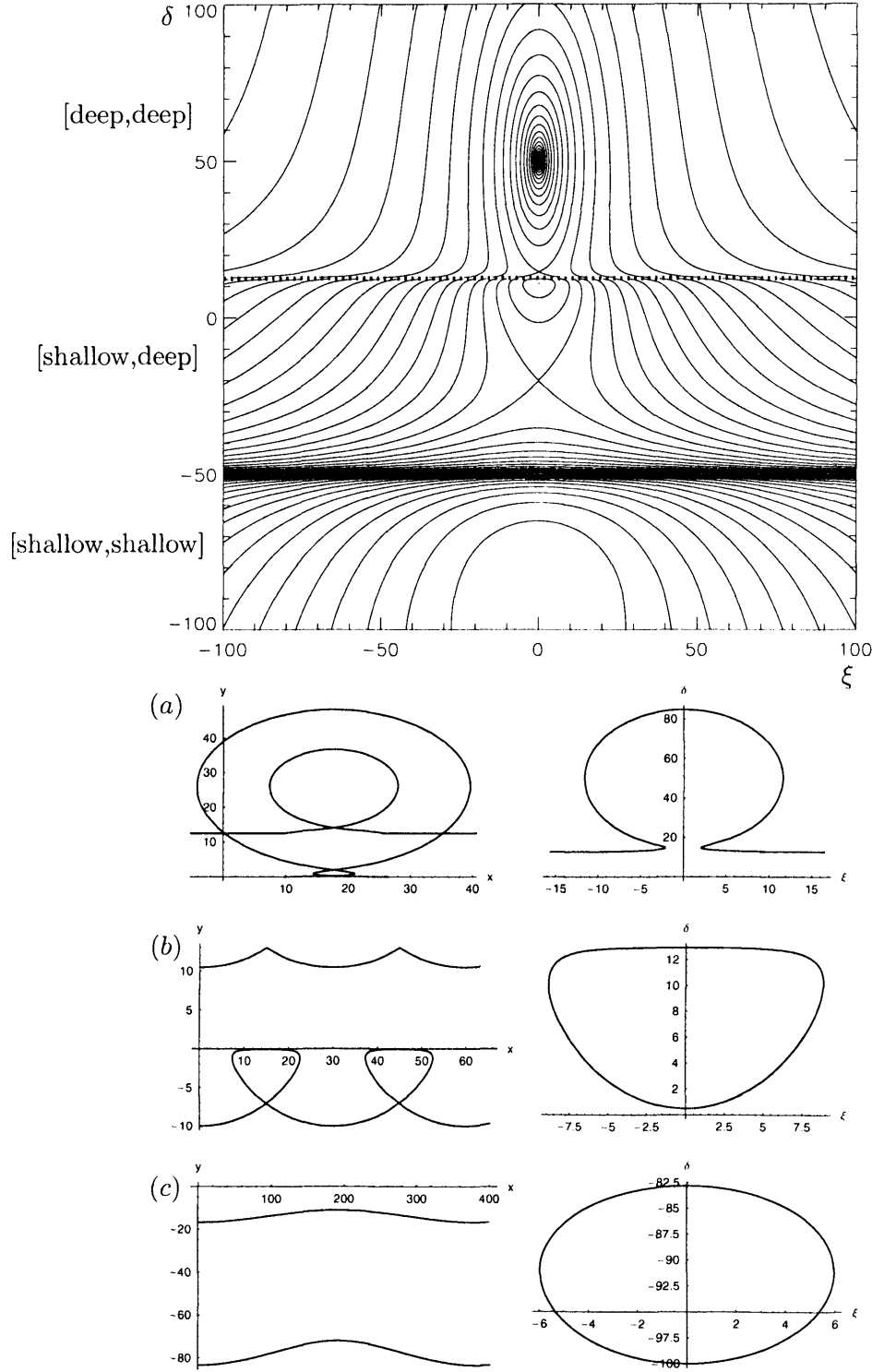


Figure 4.3: Possible (η, δ) -space trajectories for two point vortices with oppositely signed circulation near stepped topography with depth ratio $\gamma = 1/2$ and $\mathcal{I} = 50\pi$, $Q_1 H_1 = -\pi$ and $Q_2 H_2 = 2\pi$. Dotted lines separate the possible regimes of flow and indicate where a point vortex would come close to the escarpment. The remaining figures represent typical trajectories in (x, y) space and (ξ, η) space for (a) [deep,deep], (b) [shallow,deep] and (c) [shallow,shallow] flow.

state, discussed in more detail in Appendix E. Perturbations to this state either result in a vortex being advected close to the step (open trajectories in (ξ, δ) -space), or for the vortices to orbit each other with a large time period (closed trajectories in (ξ, δ) -space). A full list of the different types of trajectories for this [deep,deep] regime is given in Appendix D, figure D.2. In the [shallow,deep] configuration, there are two equilibrium states for two vortices: one located at a centre in (ξ, δ) -space where perturbations from this point are shown in figure 4.3b and the other at a hyperbolic point. As expected, small perturbations from a the hyperbolic point will lead to one vortex approaching the escarpment or translating periodically with large time period. In contrast, small perturbations from the centre lead to periodic motion such that both vortices translate almost parallel to the step. A detailed classification of the types of trajectories are given in Appendix D, figure D.3.

In the final regime, [shallow, shallow], a single two-vortex equilibrium state exists at a center in (ξ, δ) -space. Therefore all other trajectories in this regime are periodic which represent sinusoidal-like oscillations in (x, y) -space, typically given by figure 4.3(c).

4.3.2.2 Trajectories of vortex pairs with opposite-sign circulation and negative impulse

Figure 4.4 gives an example of point vortex trajectories for $\gamma = 1/2$ and negative impulse. For the [deep, deep] configuration a typical trajectory is shown in figure 4.4(a). For large separation the vortices are dominated by their respective partial images and translate parallel to the step. As they approach each other they do not move in an orbiting trajectory (in contrast to [deep,deep] for positive impulse), instead after reaching maximum δ the

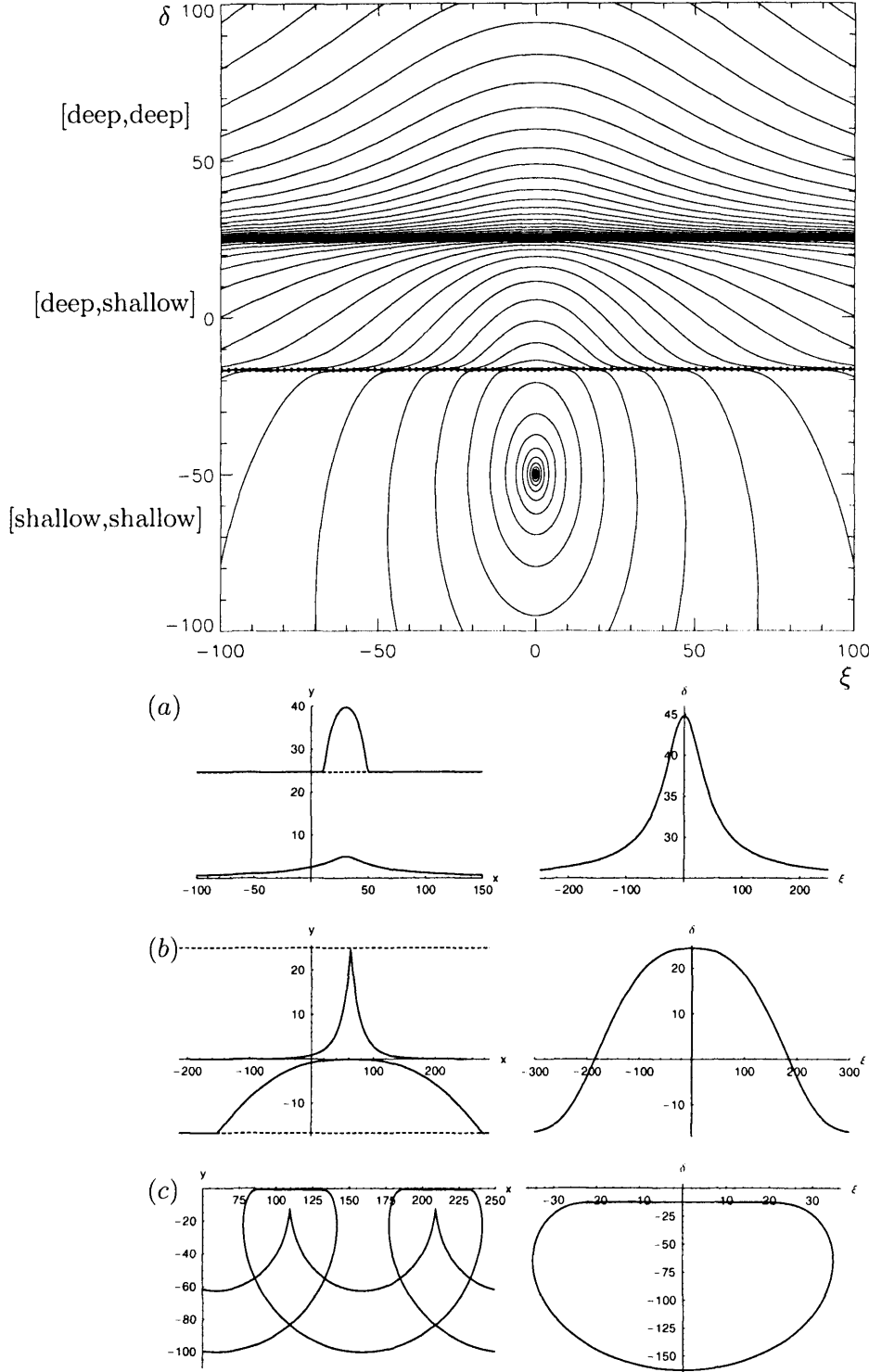


Figure 4.4: Possible (ξ, δ) -space trajectories for two point vortices with oppositely signed circulation near stepped topography with depth ratio $\gamma = 1/2$ and $\mathcal{I} = -50\pi$, $Q_1 H_1 = -\pi$ and $Q_2 H_2 = 3\pi$. Dotted lines separate the possible regimes of flow and indicate where a point vortex would come close to the escarpment. The remaining figures represent typical trajectories in (x, y) space and (ξ, η) space for (a) [deep,deep], (b) [deep,shallow] and (c) [shallow,shallow] flow.

vortex closest to the step approaches the escarpment translating quickly as it does so. Whereas the vortex further away from the step approaches its bound given by (4.23) and translates parallel to the step, but more slowly owing to its distance from the step.

For [deep,shallow] configuration similar trajectories (typically given by figure 4.4*b*) in (ξ, δ) -space arise except that the vortices are located on opposite sides of the step. For the [shallow,shallow] configuration trajectories in (ξ, δ) -space are closed loops representing leap-frogging motion in the physical plane (figure 4.4*c*).

4.4 Vortex patch motion

Using the modified contour dynamics algorithm described in chapter 3, the interaction of two vortex patches near an escarpment is studied. Comparison to the point vortex trajectories discussed earlier in this chapter is made whenever possible, bearing in mind that vortex patches unlike point vortices are able to cross the step.

It has been shown for constant-depth flow (Johnson & McDonald, 2004*b*) that provided vortex patches remain circular, their centroids are constrained to follow the paths of singular vortices with equivalent circulation and energy. This argument has been extended by Johnson & McDonald (2004) to piecewise-constant depth profiles for any vortex that is not straddling a discontinuity in H . It was established that provided patches remain coherent and close to circular after crossing, the energy associated with the pair remains constant (see Appendix F). Along with the circulation (which is sufficient for normally incident vortices), the energy of the vortex patch is then used as the matching condition enabling point vortex and vortex patch trajectories to be compared even when a patch crosses the step. This

procedure is used in this chapter, with the impulse acting as the additional constraint required to recover the y positions of both vortices.

4.4.1 Like signed vortex patches

Two examples are given of vortex patches with like sign circulation. First, figure 4.5 gives an example of two vortices initially in a [shallow, deep] configuration with $\gamma = 1/2$. Vortices are initialized such that $\mathcal{I} = 65\pi$ with $Q_1 H_1 = \pi/2$ and $Q_2 H_2 = 2\pi$.

Comparisons of the trajectories pair of point vortices and of vortex patch centroids is excellent, as indicated by the plot in (ξ, η) -space where trajectories of centroid positions are plotted for each point vortices and vortex patches and the trajectories are shown to be almost identical. In (x, y) -space the motion is characterized by the weaker, shallow water vortex (vortex 1) being advected toward the escarpment by the stronger, deep water vortex (vortex 2). The weaker vortex then accelerates under the influence of its like signed image and translates almost parallel to the step. Unlike a point vortex, the weaker vortex patch then crosses the step and the regime switches to the [deep, deep] configuration. The vortices then leap-frog before the patch crosses the escarpment once more. This periodic motion corresponds in (ξ, η) -space to a closed circuit straddling the escarpment where the weaker vortex crosses the step.

The second example involving like signed vortex patches is given in figure 4.6. Here the circulations are given by $Q_1 H_1 = 2\pi$ and $Q_2 H_2 = \pi$ with $\mathcal{I} = -50\pi$. Motion is initialized with both vortices in shallow water (i.e. [shallow, shallow]), with the weaker vortex (vortex 2) being advected toward the escarpment by its topographic image. Again the comparison between vortex patches and point vortices is excellent with the trajectories being vir-

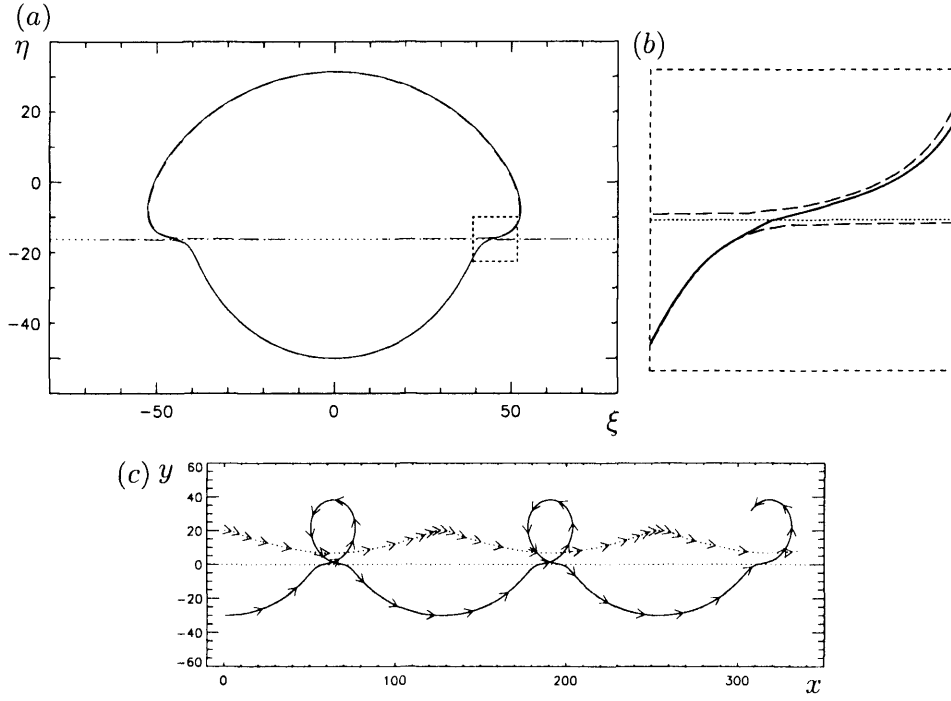


Figure 4.5: A comparison between the trajectories of the centroid positions of vortex patches and point vortex trajectories in (a) (ξ, η) -space with (b), an exploded view of the dotted region and (c) real (x, y) -space. The circulation of vortex 1 is $\pi/2$ and the circulation of vortex 2 is 2π with $\mathcal{I} = 65\pi$. Long dashed lines in (a) indicate the path of a point vortices with equivalent configurations in phase space and short dashed lines indicate where the trajectory encounter the escarpment. Dashed lines in (c) indicate the path of vortex 2 and the solid line shows the path of vortex 1, arrows are drawn at equal time intervals to indicate the speed of propagation. The horizontal dashed line shows the location of the escarpment.

tually indistinguishable in (ξ, η) -space. After crossing, leap frogging motion occurs with the weaker vortex in deep water and the stronger vortex (vortex 1) takes to cycloid-like trajectories. This periodic motion corresponds in (ξ, η) -space as a closed trajectory straddling where the weaker vortex crosses the step.

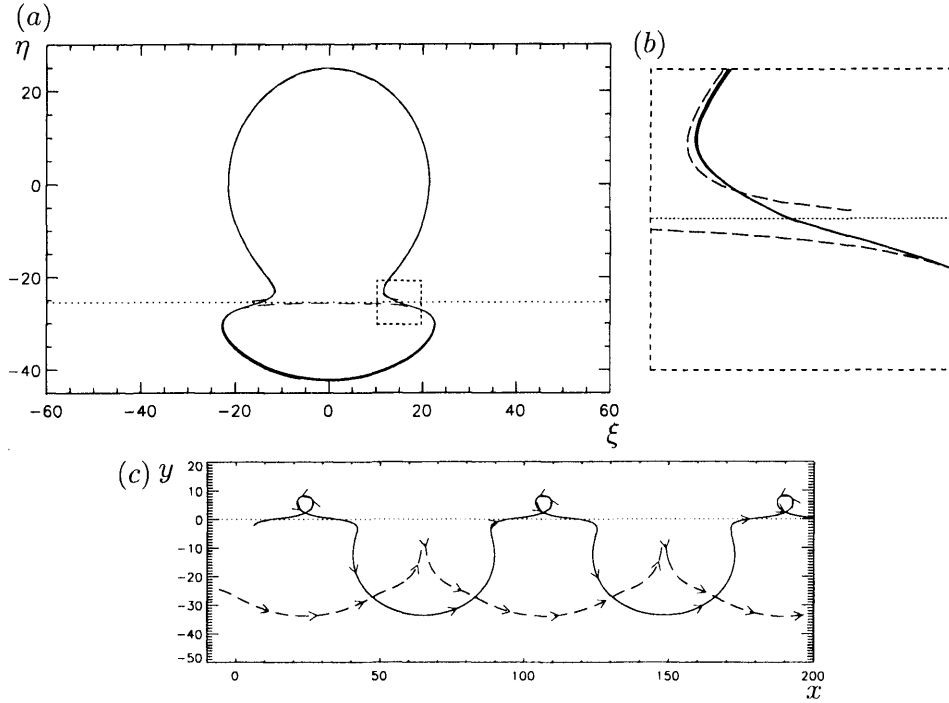


Figure 4.6: A comparison between the trajectories of the centroid positions of vortex patches and point vortex trajectories in (a) (ξ, η) -space (b), an exploded view of the dotted region and (c) real (x, y) -space. The circulation of vortex 1 is 2π and the circulation of vortex 2 is π with $\mathcal{I} = -50\pi$. Dash conventions are given in the previous figure apart from vortex 1 in (c) is shown by a dashed line.

4.4.2 Oppositely signed vortex patches

Figure 4.7 shows the trajectories of two vortex patches with $Q_1 H_1 = 3\pi$, $Q_2 H_2 = -\pi/2$, $\mathcal{I} = -55\pi$ and $\gamma = 1/2$. Motion is started in the [deep, shallow] configuration with both vortices initially orbiting each other. The weaker vortex then approaches and subsequently crosses the step so that the patches assume the [deep, deep] configuration and again undergo orbiting motion, this time in deep water. After reaching their maximum y separation the vortices mutually self advect toward the step. The weaker vortex crosses the step (i.e. to [deep, shallow]), with the stronger vortex accelerating as

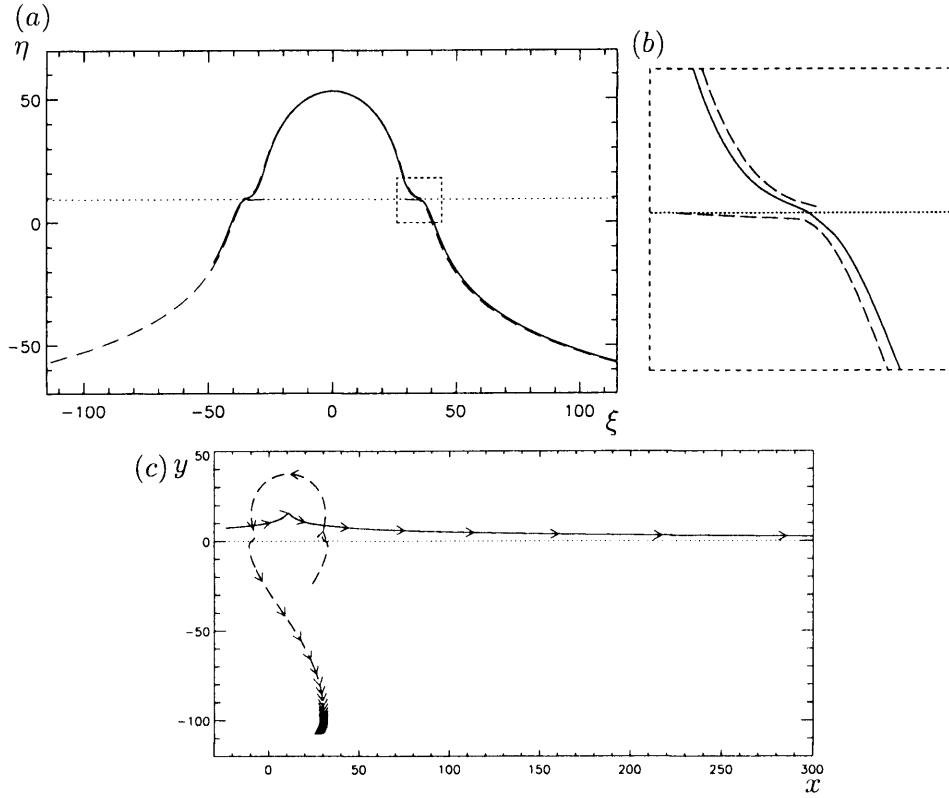


Figure 4.7: Comparison between point vortex trajectories and vortex patch centroid trajectories for oppositely signed vortices in (a) η, δ space (b), an exploded view of the dotted region and (c) real (x, y) space with $Q_1 H_1 = 4\pi$ and $Q_2 H_2 = -\pi$, here $\mathcal{I} = 50\pi$. Dashed conventions are the same as in previous figures with a solid line indicating vortex 1 in (c).

it approaches the escarpment and leaves the vicinity of its partner owing to ‘pairing-off’ (or exchanging) with its image. As the separation of the vortices increases the dynamics of each vortex is dominated by its respective image. Consequently their y positions remain relatively constant so that in (ξ, δ) -space the trajectory tends toward $\delta = \text{constant}$. After sufficiently long time (notice the arrow separation in the shallow water vortex) the stronger vortex will eventually cross the escarpment resulting in a [shallow, shallow] configuration (not shown) and the vortices will (very slowly owing to their large separation) orbit about their center of vorticity. The pair will

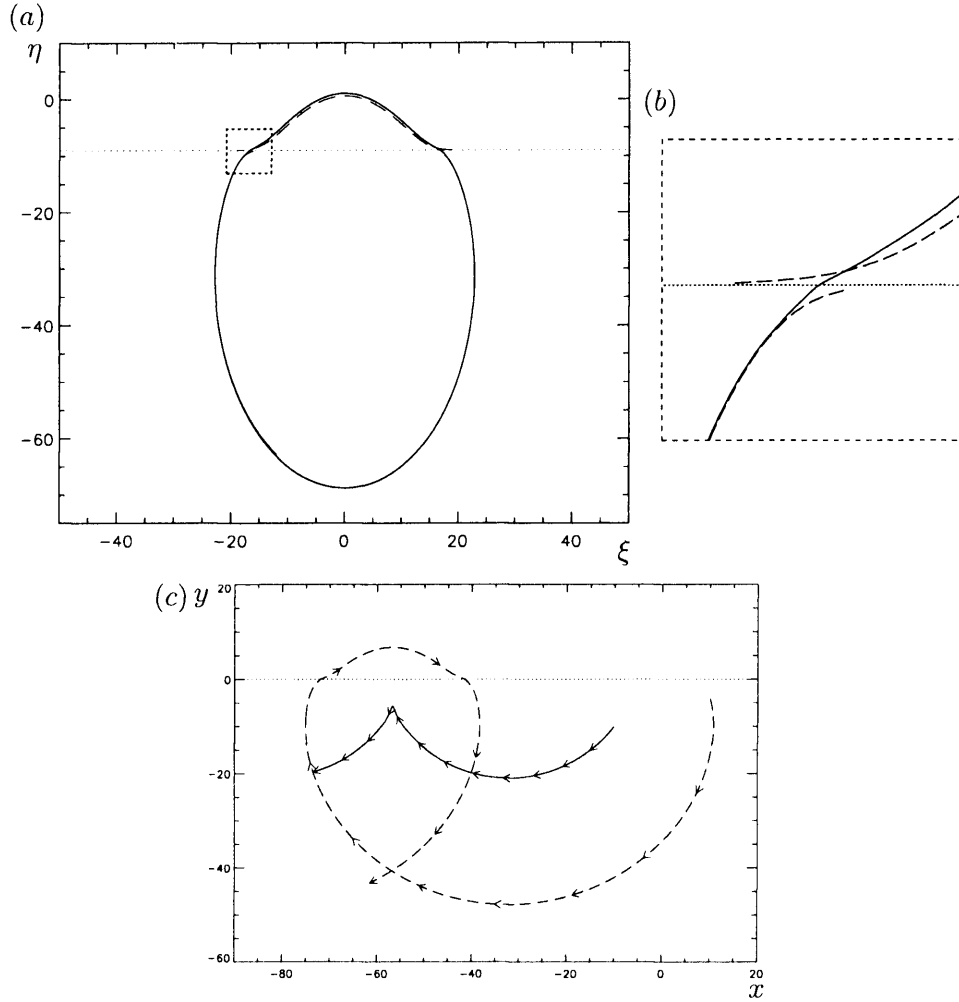


Figure 4.8: Comparison between point vortex trajectories and vortex patch centroid trajectories for oppositely signed vortices in (a) η, δ space (b), an exploded view of the dotted region and (c) real (x, y) space with $Q_1 H_1 = -4\pi$ and $Q_2 H_2 = \pi$, here $\mathcal{I} = 36\pi$. Dashed conventions are the same as in previous figures with a solid line indicating vortex 1 in (c).

eventually cross into the [shallow, deep] regime and the above motion will repeat.

Figure 4.8 gives another example of trajectories for oppositely signed vortex patches. The initial configuration is [shallow, shallow] and begins with both vortices orbiting about their center of vorticity. The weaker vortex then

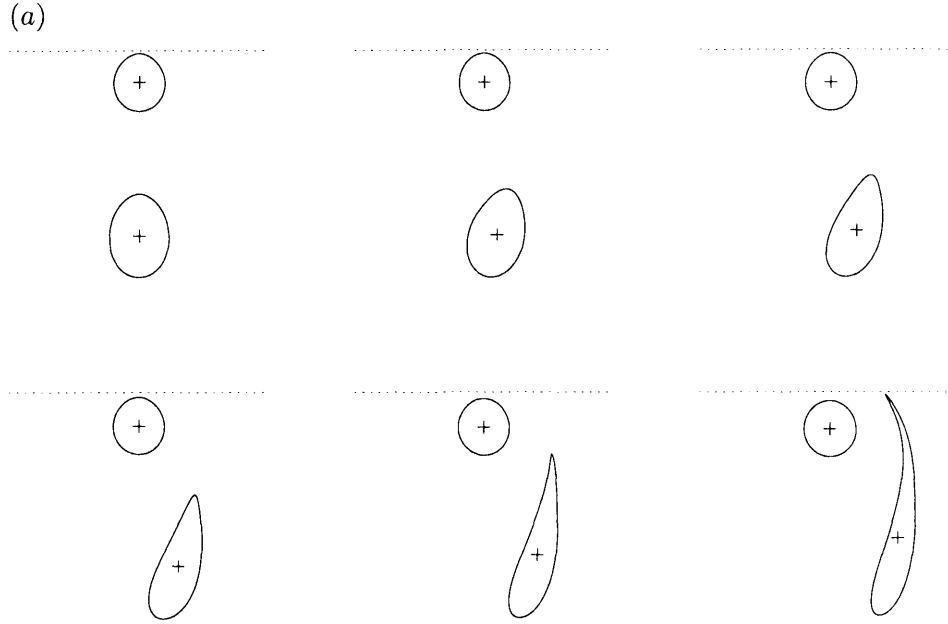


Figure 4.9: (a) a two-patch equilibrium state where both vortices exist wholly in shallow water and have the same-sign and the depth ratio $\gamma = 1/2$. The remaining figures show the subsequent evolution of the patches. Here $Q_1 H_1 = 0.108$ and $Q_2 H_2 = 0.00687$ with $\mathcal{I} = -0.165$. A cross indicates the center of vorticity of each vortex patch.

crosses the escarpment changing the regime to [deep,shallow]. After reaching maximum y separation the stronger vortex is forced away from the step with the weaker vortex crossing the step and the motion is repeated.

4.5 Two-patch equilibrium states

Motivated by the existence two-vortex equilibrium states for point vortices (as described by section 4.3), such equilibrium states for vortex patches are sought numerically, using the method described to find monopolar V-states near step topography in chapter 3, section 3.3. Figure 4.9(a) shows an example of a two-vortex equilibrium state with the remaining frames showing the (unstable) evolution of a two-vortex patch equilibrium state where both

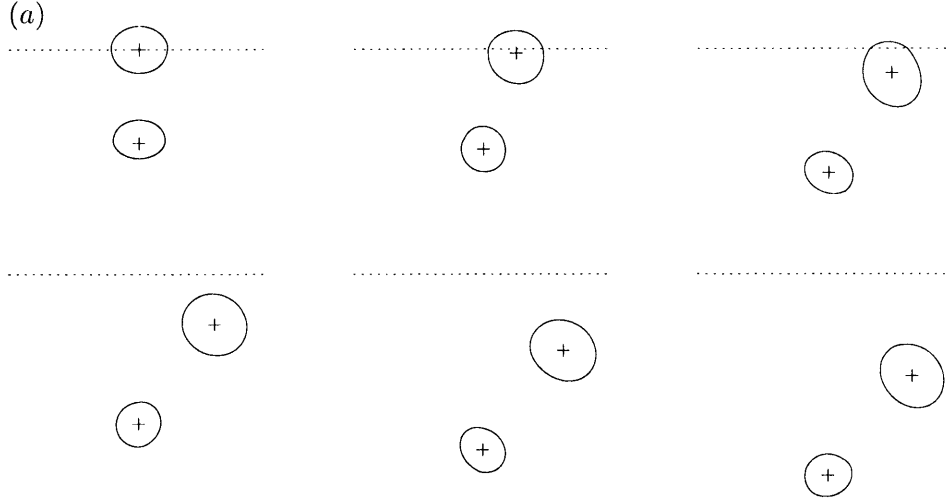


Figure 4.10: (a) a vortex patch equilibrium state where one vortex straddles the escarpment with vortices having opposite-sign and $\gamma = 1/2$. The remaining figures show the subsequent evolution of the patches. Here $Q_1 H_1 = 0.223$ and $Q_2 H_2 = -0.223$ with $\mathcal{I} = 0.855$. A cross indicates the centre of vorticity of each vortex patch.

vortices exist wholly in shallow water and have the same-sign such that the vortices translate without change in shape parallel to the step. To the author's knowledge the first known example of two-patch equilibrium state where both patches have the same-sign circulation. As expected, from earlier work with point vortices in shallow water (section 4.3), this configuration is unstable with the weaker vortex being severely distorted by the stronger vortex. Subsequent evolution (not shown) shows the weaker vortex splitting and eventually become insignificant to the dynamics of its partnering vortex. Figure 4.10(a) shows an example of a patch equilibrium state (with vortices having opposite-sign) where one vortex straddles the escarpment with the remaining plots show the subsequent evolution of the patches. This specific configuration is also found to be unstable with each vortex not translating parallel to the step. Section 4.3.2 stated that two-vortex equilibrium states existed for point vortices having opposite-sign (and $\mathcal{I} > 0$) at a center

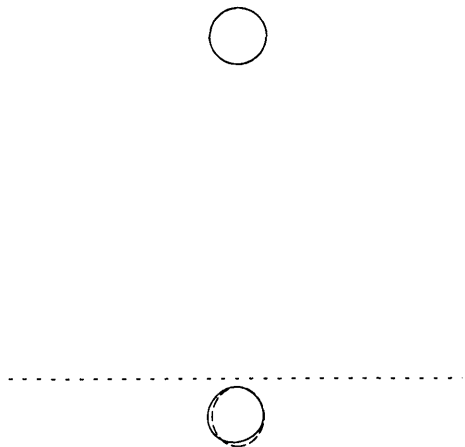


Figure 4.11: A vortex patch equilibrium state with each vortex existing on opposite sides of the step having opposite-sign and $\gamma = 1/2$ (dashed line). The solid curve shows the evolved equilibrium state after 5 turnover times (of the deep water vortex). Here $Q_1 H_1 = -0.593$ and $Q_2 H_2 = 0.2233$ with $\mathcal{I} = -1.84$.

in (ξ, δ) -space. Motivated by this observation an equivalent vortex patch equilibrium state is sought. Figure 4.11(a) gives an example of such a configuration. In contrast to the previous examples this configuration is stable, since the patches translate (virtually) parallel to the step.

4.6 Discussion

Trajectories for two interacting point vortices near step topography have been found which has been written explicitly in terms of the Hamiltonian and conserved quantities, $(\Gamma, \mathcal{I}, \mathcal{E})$. Trajectories were divided into four regimes depending on the placement of vortices in either deep or shallow water. It was found that point vortex trajectories are either periodic or aperiodic (where one vortex would approach the escarpment). Periodic trajectories can be classified in the following way; (i) orbit about each other, (ii) leap frog, (iii) translate in a sinusoidal-like way or (iv) exist as a steadily propa-

gating configuration – a two-vortex equilibrium state. The latter configuration exists at a hyperbolic point on the separatrix of the contoured Hamiltonian in (ξ, η) -space for like signed vortices, or at a centre of the Hamiltonian in (ξ, δ) -space for oppositely signed vortices. Although analysis of their stability is not given here, it is predicted that perturbations to a two-vortex equilibrium state configuration at the hyperbolic point is unstable, while a perturbation to a two-vortex equilibrium state about a centre would be stable and lead to small amplitude periodic motion. In addition to point vortex equilibrium states, vortex patch equilibrium states were found numerically. Configurations where both vortices exist wholly in shallow water having the same-sign and a state where a vortex straddles the step having opposite-sign were found to be unstable shown using time dependent integrations. A two-patch equilibrium configuration which existed at a centre in phase-space was found and this state was robust to time integrations confirming the stability of equilibrium states about centres. A detailed investigation of the stability of two-vortex equilibrium states is not given here and requires further research.

Trajectories of two vortex patches found using an adapted contour dynamics algorithm, compared well to point vortex trajectories for equivalent values of energy, impulse and circulation. Examples displaying periodic motion (with one vortex patch crossing the escarpment) were given for both like signed and oppositely signed vortices. In making comparisons, point vortex trajectories with equivalent circulation, energy and impulse were assigned to vortex patch trajectories. When a vortex patch crosses the escarpment a new point vortex trajectory must be assigned to the vortex patch trajectory. It is important to emphasize that there is no free choice in this assignment. Considering a vortex patch pair not only does the energy depend on patch

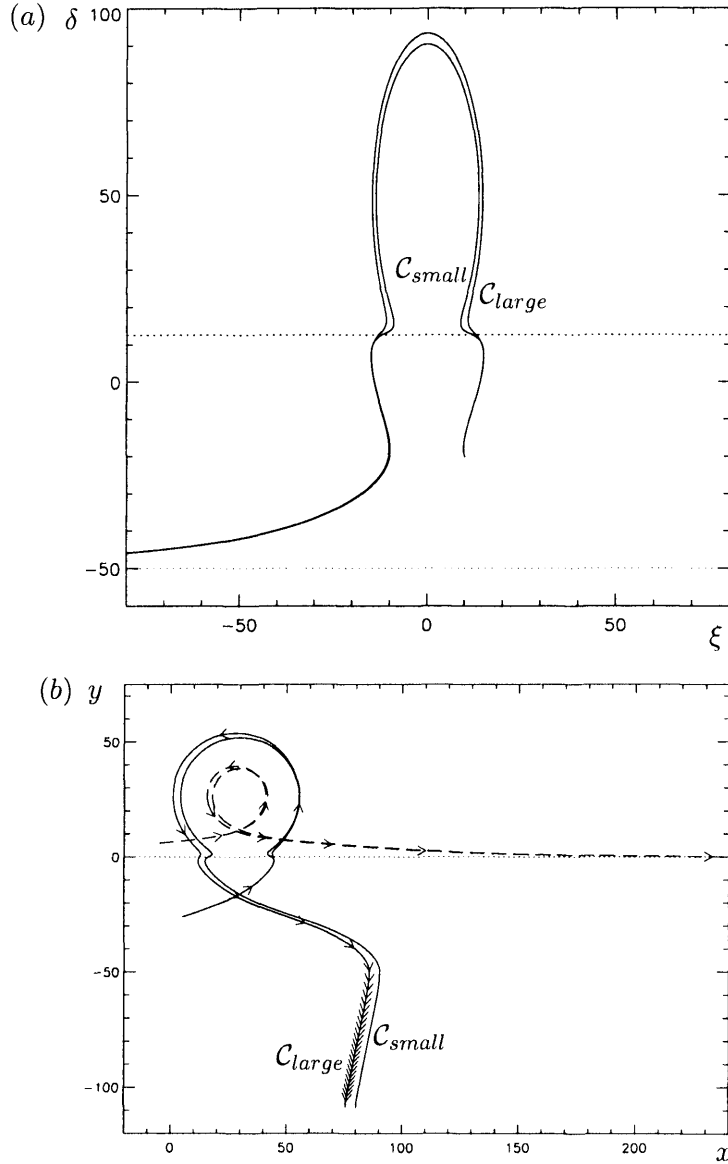


Figure 4.12: Two numerical simulations of a dipolar vortex patches, both simulations have $Q_1 H_1 = -\pi$, $Q_2 H_2 = 2\pi$ with $\mathcal{I} = 50\pi$. However in one case vortex 2 has the same volume (2π) as vortex 1 where the second run has vortex 2 having volume 6π with vortex 1 having volume 2π . (a) (ξ, δ) -space trajectories, the larger volume computation being the trajectory which experiences a larger position in (ξ, δ) -space, (b) Real (x, y) -space, arrows are given to the larger volume simulation, all other line conventions are the same as used previously.

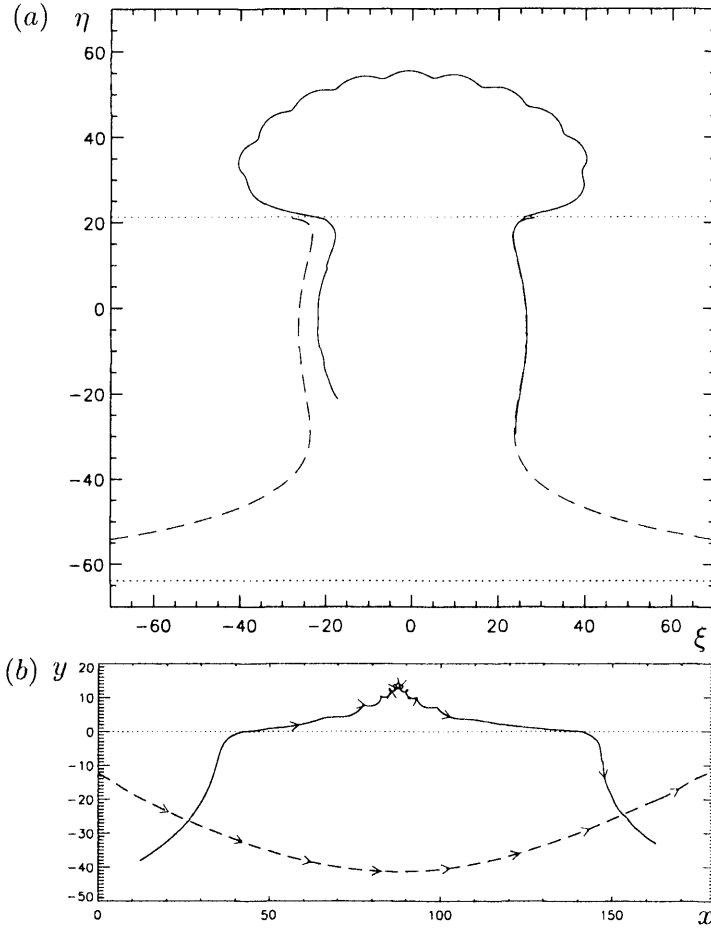


Figure 4.13: (a) (ξ, η) -space motion for an initial vortex pair with $Q_1 H_1 = \pi$, $Q_2 H_2 = 3\pi$ and $\mathcal{I} = -65\pi$ here $\gamma = 1/5$. The dashed line is a comparison with a point vortex system with an equivalent configuration. (b) Real space trajectories, the interaction of vortex 2 with the third vortex is clearly observable.

separation, but also the size of each patch (Appendix F derives the appropriate expression for the energy). Thus changing the size of a patch (with fixed circulation) defines a new energy and thus trajectory. Figure 4.12 compares the different trajectories that occur for patches with different volumes.

In particular, the two simulations are initialized in the [shallow, deep] configuration with the same parameters with the exception that in the sec-

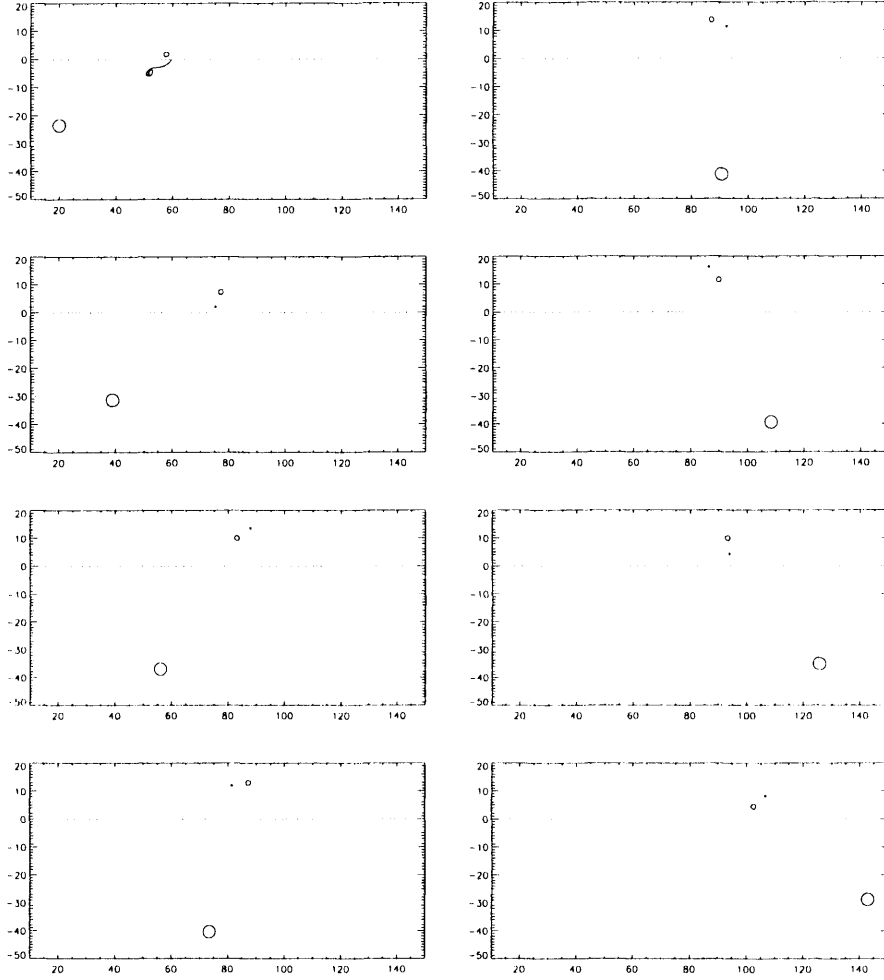


Figure 4.14: Evolution of the vortex pair from figure 4.13. Time increases down the page from left to right. The third vortex formed by the collision from vortex 2 and the subsequent orbiting around vortex 2 is clearly visible.

ond computation, \mathcal{C}_{large} , the volume of the shallow water vortex is three times as large as the shallow water vortex in the first computation \mathcal{C}_{small} . Starting at the same point the two different simulations are comparable to one another until the shallow water vortex is close to the escarpment. In \mathcal{C}_{large} the shallow water vortex will impinge upon the step earlier than the smaller shallow water vortex in \mathcal{C}_{small} , and hence realize a different trajectory in the [deep,deep] regime (similarly if the vortex was smaller then it

would impinge the escarpment later giving rise to another trajectory).

Comparison between trajectories of patches and point vortices is excellent provided the patches remain coherent. It is possible for a patch to deform and possibly split in to two or more separate vortices. This is especially the case for patches encountering large changes in depth.

An example of a vortex pair colliding with a large depth contrast depth ratio is given in figures 4.13, 4.14. Here the configuration is initially [shallow, shallow] with $Q_1 H_1 = \pi$, $Q_2 H_2 = 3\pi$, $\mathcal{I} = -65\pi$ and $\gamma = 1/5$. Up until vortex 2 is forced into deep water the motion compares well to point vortex motion as shown by the dashed line. As vortex 2 crosses there is a large amount of shedding and results in a tertiary vortex, vortex 3 as shown in figure 4.14. Although relatively small (about 11% of the original size of vortex 2) this third vortex plays a significant role in the dynamics. In (ξ, δ) -space this is shown in figure 4.13 by the ‘wobble’ in [shallow, deep] configuration. Once this third vortex has formed comparing with a pair of point vortices is no longer sensible since the two vortex assumption which leads to the derivation of the Hamiltonian is no longer valid.

Chapter 5

Vortex Scattering from Step Topography

5.1 Introduction

Chapter 4 studied the interaction of two vortices with step topography. It was found that distant vortices of opposite-sign can translate parallel to the step and ‘pair-off’ into a pair which translates away from the step. This phenomenon has been studied with vortex patches having unequal area near a wall by Overman & Zabusky (1982) where patches paired-off to translate at a constant angle of incidence and for a vortex patch pair having normal incidence to a step change in depth by Johnson & McDonald (2004).

Motivated by these observations the present chapter considers the dynamics of a vortex patch pair of opposite-sign with same magnitude translating at an arbitrary angle of incidence to rectilinear step (figure 5.1). Fluid is modelled as in the previous chapters by a two dimensional, non-rotating, ideal fluid in the limit of zero Froude number and the topography is taken to be a finite step change in depth (where the fluid has depth H^+ in $y > 0$

and H^- in $y < 0$). Further, chapter 4, section 4.2 shows (provided there is minimal shedding and shape of each patch remains close to circular) that from the conservation of energy, circulation, volume and linear impulse a trajectory of a pair can be determined including the case where the vortices cross the escarpment.

Section 5.2 outlines the mathematical formulation of the problem and derives an explicit relationship determining the angle of reflection given the initial separation of the pair, the angle of incidence and the size of the vortex patches comprising the pair. In section 5.3, the evolution of such pairs is computed numerically using an adapted contour surgery algorithm based on Dritschel (1988), for various angles of incidence from both shallow and deep water. These computations results are then compared to that predicted by the relationship of section 5.2. Section 5.4 presents conclusions.

5.2 Mathematical formulation

The energy of a vortex pair consisting of two finite area, equal volume, circular patches of uniform vorticity, centred at (x_1, y_1) and (x_2, y_2) near a finite escarpment with depth H^+ in $y > 0$ and H^- in $y < 0$ when the pair translates in deeper water is (Johnson & McDonald, 2004)

$$\mathcal{E}_{d,d} = \frac{\Gamma^2 H^+}{2\pi} \left\{ \log \left(\frac{r}{a} \left| \frac{2(y_1 y_2)^{1/2}}{r'} \right|^\alpha \right) + \frac{1}{4} \right\}, \quad (5.1)$$

where $\gamma = H^-/H^+$ is the depth ratio, $\alpha = (\gamma - 1)/(\gamma + 1)$ the image strength due to the topography, a the patch radius, r the vortex pair centroid separation and $r' = [(x_1 - x_2)^2 + (y_1 + y_2)^2]^{1/2}$. The depth ratio lies in the range $0 \leq \gamma < \infty$ so the image strength satisfies $-1 \leq \alpha \leq 1$. For a pair far from escarpment, the topographic image terms are negligible,

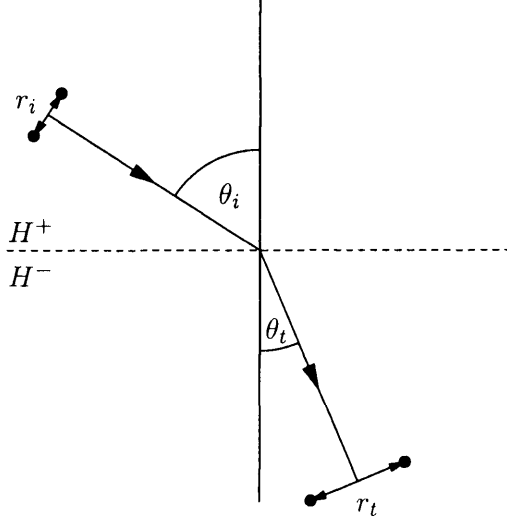


Figure 5.1: Sketch of a vortex pair crossing a step (along $y = 0$, indicated by the dashed line). The subscripts i and t denote the quantities before and after crossing the step i.e. ‘incident’ and ‘transmitted’. The centroid separation is denoted r with the normal angle to the step θ .

thus $(y_1 y_2)^{1/2} \approx y$ and $r' \approx 2y$, where y is the normal distance from the escarpment to the centre of vorticity of the vortex pair. Then the energy of a pair in deep water ($y > 0$) is

$$\mathcal{E} = \frac{\Gamma^2 H^+}{2\pi} \left(\log \chi + \frac{1}{4} \right), \quad (5.2)$$

for $\chi = r/a$, the ratio of centroid separation to patch radius. Conservation of circulation, with (5.2) and its equivalent form in $y < 0$ where H^- replaces H^+ , gives the relation between pair separation either side of the step

$$\chi_t = \chi_i^{1/\gamma} \exp[(1/\gamma - 1)/4], \quad (5.3)$$

where subscript i denotes a quantity incident on the step and t denotes the transmitted quantity, assuming the pair has crossed the escarpment. For $\gamma < 1$ (i.e. a pair crossing from deep to shallow water), the patch separation increases after crossing and for $\gamma > 1$, the separation decreases. The vortices are assumed to remain circular after crossing the step so the centroid separation must be at least twice the radius of the vortices comprising the pair, i.e. $\chi_t \geq 2$. For each χ_i , there is a sufficiently large increase in depth for which $\chi_t = 2$. This critical depth ratio $\gamma_d > 1$ (where subscript d denotes *debris*) follows from (5.3) as

$$\gamma_d = \frac{\log \chi_i + 1/4}{\log 2 + 1/4}. \quad (5.4)$$

For depth ratios larger than γ_d , the numerical integrations (in §5.3 and Johnson & McDonald 2004) show that the vortices are pulled so close together that they shed vorticity. This region of parameter space is described here as the ‘*debris region*’ (Figure 5.2). Constancy of \mathcal{V} , from (4.4), gives $2H^+ \pi a_i^2 = 2H^- \pi a_t^2$, and so the incident and transmitted radii are related by

$$a_i = \sqrt{\gamma} a_t. \quad (5.5)$$

Conservation of linear impulse, \mathcal{I} , gives

$$\mathcal{I} = \Gamma H^+ (-y_{1i} + y_{2i}) = \Gamma H^- (-y_{1t} + y_{2t}), \quad (5.6)$$

relating the vortex separation perpendicular to the step before and after crossing. In terms of the quantities $r_{i,t}$ and $\theta_{i,t}$ defined in figure 5.1, (5.6) becomes

$$r_i \sin \theta_i = \gamma r_t \sin \theta_t. \quad (5.7)$$

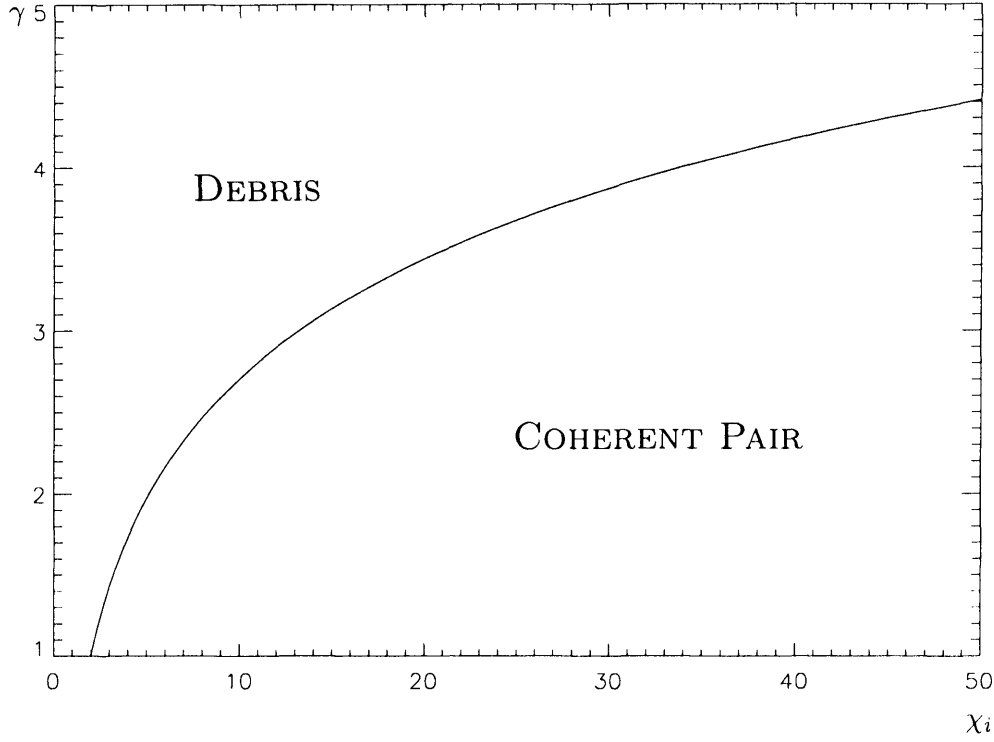


Figure 5.2: The evolution regimes determined by the depth ratio γ and the initial vortex separation χ_i . ‘Coherent pair’: a pair incident to a step will cross with the vortices in the pair remaining coherent. ‘Debris’: where significant vortex shedding will occur upon crossing. The dividing curve is the critical depth ratio γ_d , from (5.4).

Combining (5.3), (5.5) and (5.7),

$$\frac{\sin \theta_i}{\sin \theta_t} = \chi_i^{1/\gamma-1} \sqrt{\gamma} \exp [(1/\gamma - 1)/4], \quad (5.8)$$

an explicit relation between the incident and transmitted angles in terms of the depth ratio γ and the incident vortex separation χ_i . An immediate consequence of (5.8) is that $\theta_t = \theta_i$ for two values of depth ratio. First the trivial case when there is no change in depth ($H^+ = H^-$, and $\gamma = 1$), and when

$$\frac{\gamma \log \gamma}{2(\gamma - 1)} = \log \chi_i + 1/4. \quad (5.9)$$

Furthermore there is a depth ratio, γ_{max} , where the refracted angle after crossing is a maximum, $\gamma_{max} = 2(\log \chi_i + 1/4)$. Since $\gamma_{max} > \gamma_d$, a pair crossing from shallow water to deep water at any incident angle cannot reach its maximum refracted angle and importantly never refracts *towards* the normal since if $\gamma = \gamma_{max} + \epsilon$ then we would expect $\theta_t < \theta_{max}$. Eventually for a sufficiently large $\gamma = \hat{\gamma}$ say, $\theta_t < \theta_i$ but since $\gamma_{max} > \gamma_d$ then $\hat{\gamma} > \gamma_d$. Therefore a pair cannot be refracted towards the normal crossing from shallow water.

Figure 5.3 shows the transmitted angle θ_t as a function of the depth ratio γ for fixed incident angle, θ_i and incident vortex separation, χ_i . The depth ratio γ lies in the range $0 \leq \gamma < \infty$, corresponding to a pair incident on a wall ($\gamma = 0$) and a pair incident on a infinitely deep drop-off ($\gamma \rightarrow \infty$). If $\gamma < 1$ (so that the pair crosses into relatively shallow water), the pair is refracted *towards* the normal of the topography (i.e. $\theta_t < \theta_i$). As $\gamma \rightarrow 0$ (so that the topography becomes more ‘wall-like’), $\theta_t \rightarrow 0$ for all non-zero θ_i . In this limit, the vortices forming the pair separate as they approach the step. They subsequently propagate far along the wall as monopoles before crossing where they translate with large separation almost perpendicularly away from the escarpment in shallow water (cf. Johnson & McDonald, 2004). When $\gamma > 1$ (so the pair would cross from shallow water into relatively deep water), an incident pair would be refracted away from the normal (as could be deduced from time reversal with the results just noted). However for certain incident angles, the transmitted angle can be equal to $\pi/2$. This corresponds to the pair translating parallel to the step after it has crossed. Let this critical incident angle be θ_c , so

$$\sin \theta_c = \chi_i^{1/\gamma-1} \sqrt{\gamma} \exp [(1/\gamma - 1)/4]. \quad (5.10)$$

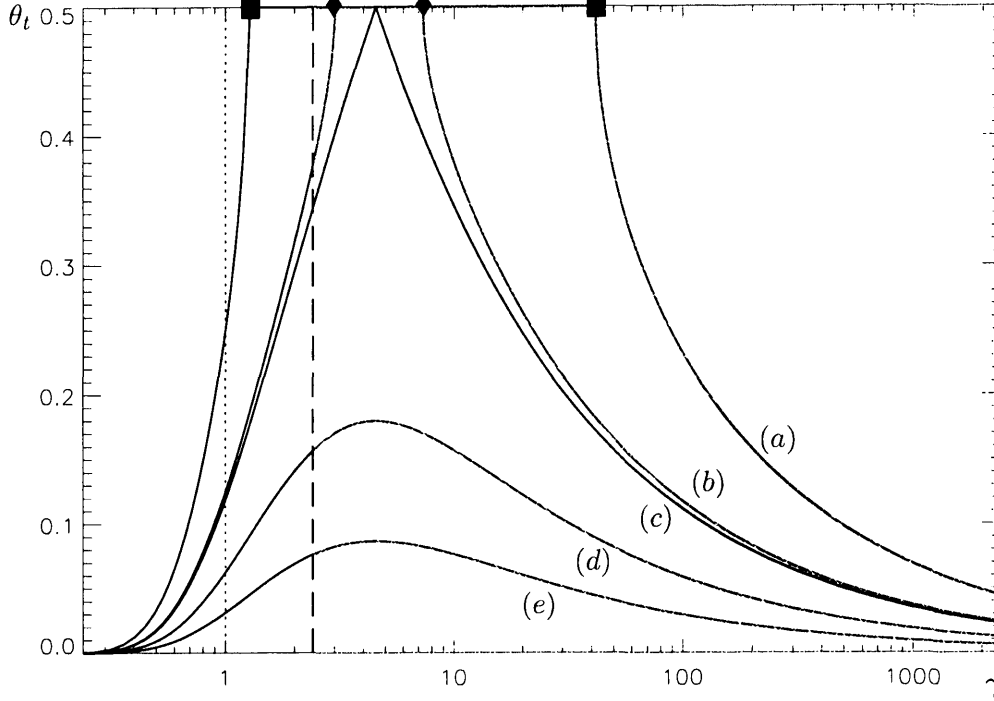


Figure 5.3: The refracted angle (in units of π), θ_t as a function of depth ratio γ for vortex separation $\chi_i = 7.5$ at varying angles of incidence θ_i , (a) $\theta_i = \pi/4$, (b) $\theta_i = \pi/8$, (c) $\theta_i = 0.119\pi$, (d) $\theta_i = \pi/16$, (e) $\theta_i = \pi/32$. The short dashed line is where the step is absent, $\gamma = 1$ and $\theta_i = \theta_t$. The line $\gamma = \gamma_d$ is shown long-dashed with the debris region, $\gamma > \gamma_d$ hatched. Solid marks show the range of depth ratios where the incident pair can be totally internally reflected.

For incident angles greater than θ_c , with all other parameters fixed, the vortex pair undergoes *total internal reflection* (TIR): it does not cross the step, but is instead reflected and translates away from the step at its incident angle. Total internal reflection here is analogous to Snell's law for refraction of a light ray as it enters a medium with a different refractive index. The angle of incidence (measured relative to the normal to the interface) decreases when light passes into a medium of higher refractive index and increases passing into a medium of lower refractive index, with deeper water corresponding to a lower refractive index in the present work.

It has been established that a pair crossing the step with depth ratio greater than γ_d , given by (5.4), will shed vorticity as it crosses the step. This debris region is cross-hatched in figure 5.3 and here the pair does not have a well-defined transmitted angle. However, for $\gamma > \gamma_d$, the pair can still undergo TIR, as on curve (b) in figure 5.3. Here there is a range of depth ratios, γ (delimited by solid diamonds in figure 3) where a pair undergoes TIR and remains coherent despite lying inside the debris region. Similarly for curve (a) in figure 3, solid squares mark out where a pair with incident angle $\theta_i = \pi/4$ will perform total internal reflection. For larger depth ratios, a translating pair could exist in the debris region, reflecting without shedding. However, for depth ratios greater than the right-hand diamond, an incident pair is unable to undergo reflection and instead crosses the step and, being in the debris region, undergoes significant vortex shedding.

Figure 5.4 shows the transmitted angle, θ_t as a function of incident angle, θ_i for different depth ratios for two cases; (a) $\chi_i = 3$ and (b) $\chi_i = 7.5$. The dash-dotted line shows where $\theta_t = \theta_i$ and $\gamma = 1$ when there is no change of depth. The marked region on each figure shows the debris region for depth ratios up to γ_{max} , shown with a dotted line, which is the value of γ where the largest θ_t occurs for a given θ_i . This region is split into two further regions. In the shaded region shedding occurs unless the depth ratio is large enough so that $\theta_i > \theta_c$ and the pair undergoes TIR. In the cross-hatched region, the pair crosses leading to vortex shedding.

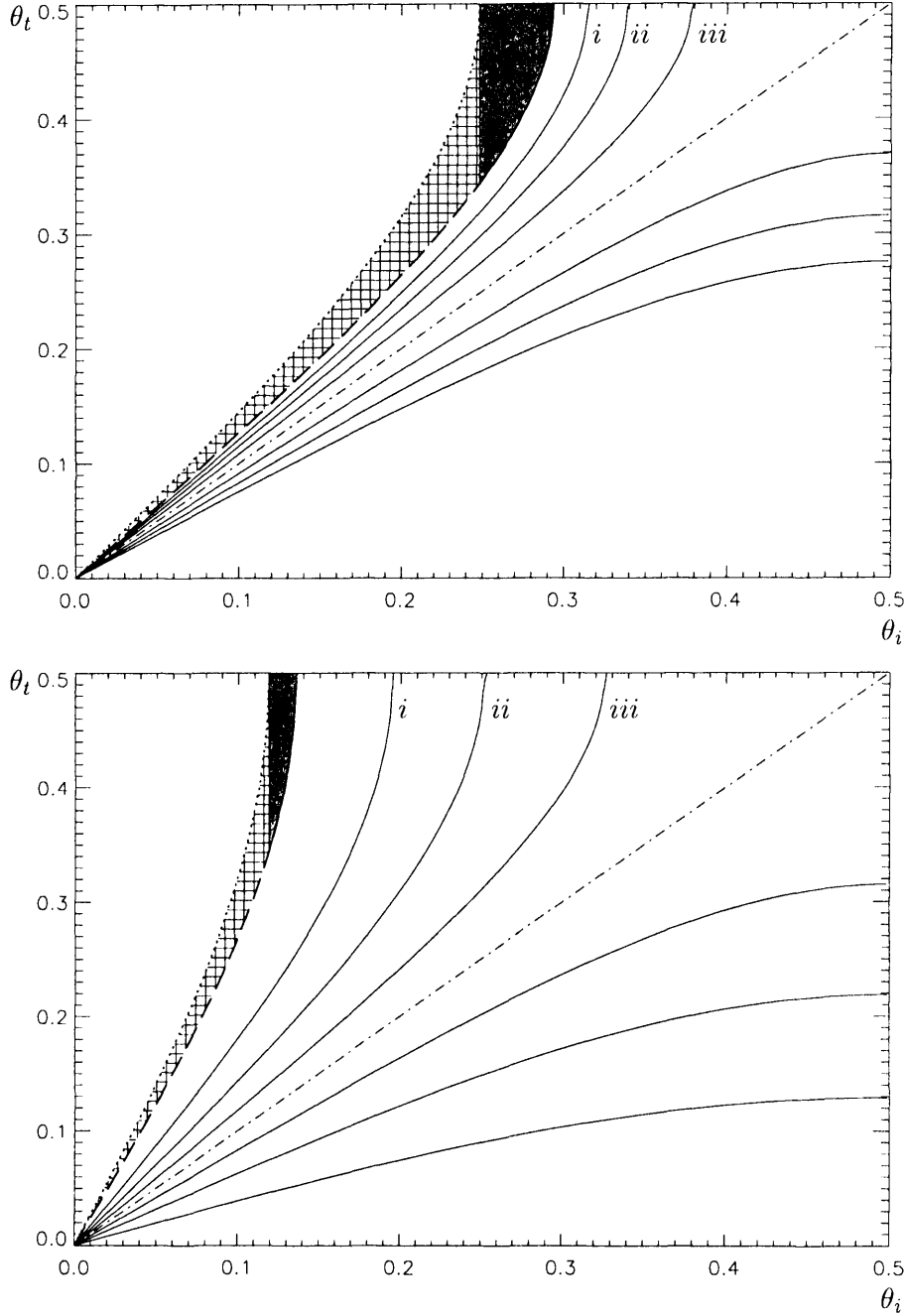


Figure 5.4: The refracted angle, θ_t as a function of incident angle, θ_i (both in units of π) with incident separation (a) $\chi_i = 3$ for different depth ratios, (i) $\gamma = 1.3$, (ii) $\gamma = 1.2$, (iii) $\gamma = 1.1$ and (b) $\chi_i = 7.5$ for depth ratios (i) $\gamma = 1.5$, (ii) $\gamma = 1.25$, (iii) $\gamma = 1.1$. The dash-dotted line shows where $\theta_t = \theta_i$, or $\gamma = 1$. The marked region shows the debris regime for values of γ between γ_d , shown by a long dashed line, up to γ_{max} shown with a dotted line. The shaded region shows where a pair may undergo TIR if the depth ratio is sufficiently large. In the cross-hatched region, the pair always crosses the step shedding vorticity. The contours below the dash-dotted line are the reciprocals of the contours for $\gamma > 1$.

5.3 Numerical computation of vortex-pair scattering

The instantaneous velocity field for a given vorticity distribution ω follows from inverting

$$\nabla \cdot (H^{-1} \nabla \psi) = \omega, \quad (5.11)$$

to obtain the streamfunction ψ . For piecewise constant ω , contour surgery (Dritschel, 1988) gives a particularly accurate and efficient numerical algorithm for this inversion, allowing contours of potential vorticity to split and merge as dictated by the flow and removing filaments which form during the integrations provided they are dynamically insignificant.

Details of the specific algorithm used here, which takes into account finite-height topography and the possibility of a vortex straddling the escarpment can be found in Johnson & McDonald (2004) and Johnson *et al.* (2005). The computations here use a resolution with, on average, 150 nodes around a vortex patch (of unit radius), initialized sufficiently far from the step that the effect of the partial images owing to the topography is small (here $r'/2y \leq 1$, cf. (5.2)). The total decrease in vortex patch volume through surgery is less than 1% unless stated.

5.3.1 Refraction at step topography

Figure 5.5 compares the theoretical prediction (5.8) for θ_t with numerical results for a vortex pair colliding with a step for various incident angles θ_i for $\chi_i = 20$ and $\gamma = 2$. The solid line is that predicted by (5.8) for a pair being refracted as they cross the step and the dashed line shows where the pair is reflected, i.e. $\theta_i > \theta_c$. The marked data points give the incident and refracted angles for a given numerical computation. The agreement between

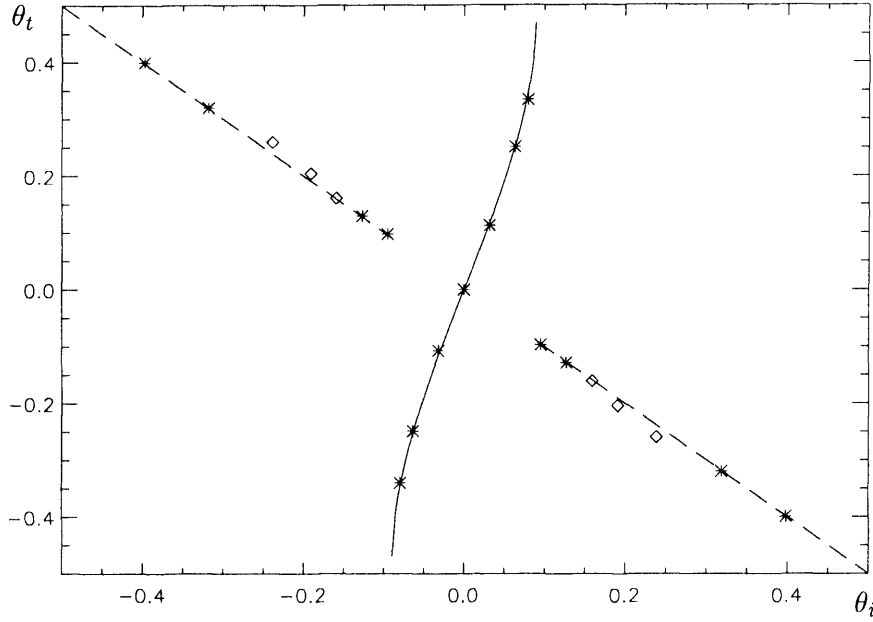


Figure 5.5: Comparison between analytical and numerical results for a vortex patch pair colliding with a step. The transmitted angle θ_t is given as a function of the incident angle θ_i (in units of π) over a step which doubles in depth, $\gamma = 2$ and an initial separation $\chi_i = 20$. The solid line shows where the pair is refracted and the long dashed line shows where the pair undergoes TIR. Vertical dotted lines show where $\theta_i = \theta_c$. Each marked point plots the incident and refractive angles for a single computation with asterisks showing where shedding is $\leq 1\%$ of the pair's volume, and diamonds showing where vortex shedding is $\geq 1\%$.

the theoretical and computational angles is remarkable when shedding is negligible ($\leq 1\%$ of the pair volume), as indicated by an asterisk. In this case, there is only a brief time where each vortex of the pair straddles the escarpment, where shedding occurs. Diamonds show where shedding is more significant ($\geq 1\%$, but still small compared with the size of the vortex). Here, vortices spend several rotation periods over the step, where shedding is at a maximum and the agreement, although not as close as for the non-shedding case, is still excellent.

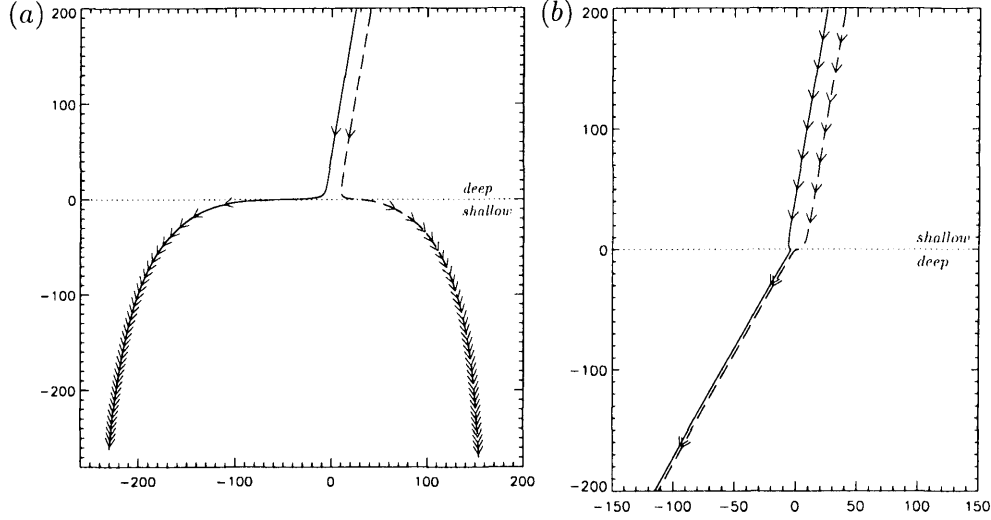


Figure 5.6: Trajectories of patch centroid positions when a pair is refracted by step topography. The initial conditions are the same for each computation, $\theta_i = 0.222$, with arrows drawn here and hereinafter at equal time intervals. (a) The depth halves and (initially in deep water) the pair cross the step and translates in shallow water with increased separation and $\theta_t = 0.0162$. (b) The depth doubles and the pair initially in shallow water cross the step with decreased separation and $\theta_t = 0.684$

Figure 5.6(a) shows centroid paths for each patch of a pair propagating from deep to shallow water with $\gamma = 1/2$ and $(\theta_i, \theta_t) = (0.222, 0.0162)$. The pair is refracted toward the normal after crossing the escarpment into shallow water. As the pair crosses the step, the separation distance between vortex centroids increases under the influence of the oppositely signed images in the step. Figure 5.6(b) shows a pair propagating from shallow to deep water with $(\theta_i, \theta_t) = (0.222, 0.684)$. In this case, the separation between vortex centroids decreases under the influence of same-signed images in the step, which now acts as an ‘anti-wall’ (Johnson & McDonald, 2004).

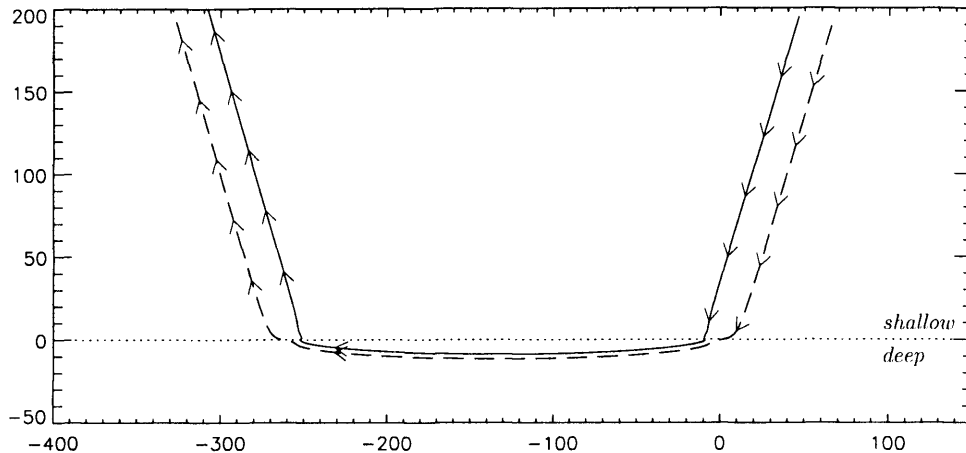


Figure 5.7: Patch centroid trajectories for an incident vortex pair at the critical angle. Weak vortex shedding at the step means one vortex is stronger than the other and the pair eventually recrosses the escarpment, after propagating 300 radius lengths parallel to the step.

5.3.2 The critical angle and total internal reflection

Figure 5.7 shows patch centroid trajectories for a vortex pair propagating from shallow to deep water at the critical angle of incidence so the pair is refracted parallel to the step. In the absence of vortex shedding, the pair would propagate parallel to the step on the deep side. A small amount of vortex shedding as the pair crosses the escarpment means that the vortices no longer have precisely equal and opposite circulation. The path thus eventually curves back toward the escarpment and the pair cross back into shallow water. The effect is extremely small: the pair travels nearly 300 radius lengths parallel to the step before it recrosses the escarpment. A similar phenomenon called the Goos-Hähnchen effect occurs in optics: a light beam undergoing TIR propagates a few wavelengths parallel to the interface between different media before being reflected (Yeh, 1998).

Figure 5.8(a) shows a trajectory for $\theta_i > \theta_c$, so the pair undergoes TIR. At no stage do the vortex patches straddle the escarpment and so shedding

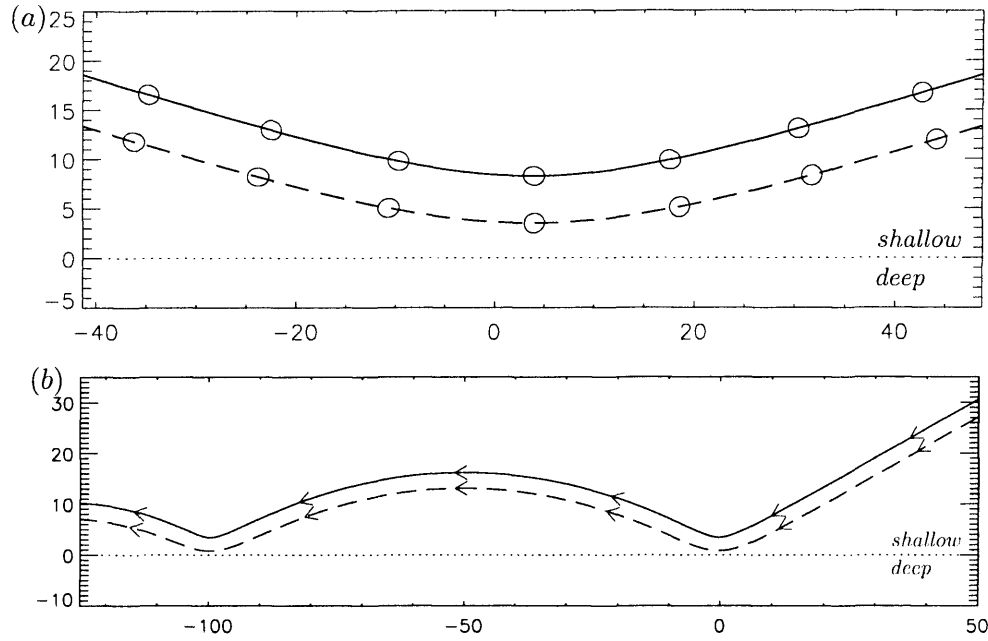


Figure 5.8: Trajectories of patch centroids for a vortex pair incident from shallow water. (a) $\theta_i > \theta_c$, the angle of incidence is greater than the critical angle and the pair is reflected. (b) $\theta_i \sim \theta_c$, one vortex momentarily straddles the escarpment, shedding vorticity and the pair is captured in relatively shallow water.

is minimal. Figure 5.8(b) shows another case of TIR, but with $\theta_i \gtrsim \theta_c$, so that one of the vortex patches comprising the pair momentarily straddles the escarpment. Since this vortex sheds some vorticity, the vortex pair is no longer comprised of patches with equal and opposite circulation and subsequently the pair ‘bounces’ along the escarpment.

5.3.3 The debris region

Figure 5.9 gives an example where the depth ratio is greater than γ_d , so the trajectories lie in the debris region. The incident angle is chosen so the pair neither reflects nor crosses the escarpment coherently to translate away at a constant transmitted angle. On approaching the step, the pair is forced

closer together under the influence of the partial images present from the step. The pair crosses the step and, since $\gamma > \gamma_d$ so $\chi_t < 2$, the pair sheds vorticity leaving one patch with larger (in magnitude) circulation than the other. The subsequent pair trajectory, figure 5.9(a), is almost circular and the pair eventually recrosses the step and, in the shallow region, the pair follows a curved path with much larger radius (figure 5.9b). The pair cross the step for the third time into deeper water where, after more shedding, the paths follow tighter circular paths, with a drift parallel to the escarpment.

5.4 Conclusions

The conservation of potential vorticity, energy, linear impulse and mass give an explicit relation for the angle of refraction and separation of vortex centroids for a vortex pair colliding with a rectilinear step, providing the vortex patches remain close to circular.

A pair initially translating in deep water with depth ratio $\gamma = H^-/H^+ < 1$, always crosses the escarpment and is refracted toward the normal to the step and cannot undergo TIR. The evolution of a vortex pair initially in shallow water, $\gamma > 1$, depends on the size of the angle of incidence θ_i compared to the critical angle θ_c which is determined by the height of the escarpment and the initial separation of the pair (see (5.10)). If $\theta_i < \theta_c$, the pair refracts away from the normal. If $\theta_i = \theta_c$, the pair translates along the escarpment and if $\theta_i > \theta_c$, the pair undergoes total internal reflection.

If the depth ratio is greater than a critical value γ_d (determined from (5.4)) then vorticity is shed by the patches when $\theta_i < \theta_c$, and subsequent paths are curved.

Numerical integrations of the full equations of motion supported the analysis with results for the angle of refraction agreeing closely with pre-

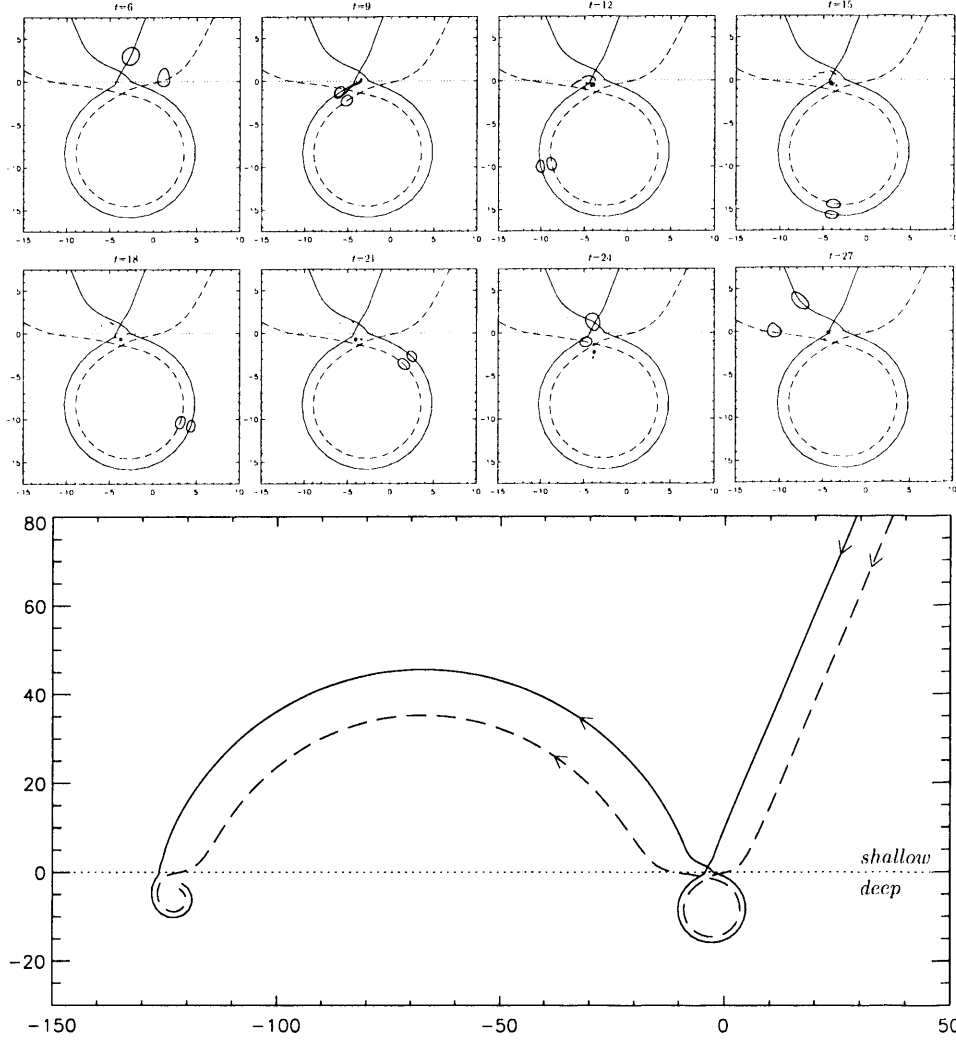


Figure 5.9: Trajectories and the evolution of a vortex pair with initial separation $\chi_i = 7.5$. The large depth increase, $\gamma = 2.5 > 2.4 = \gamma_d$ means the trajectory lies in the debris region. (a) Crossing and recrossing, (b) the subsequent evolution over a much larger time.

dictions provided vortex shedding was small. They also showed that for $\theta_i \gtrsim \theta_c$, it is possible for the pair to be captured at the escarpment and ‘bounce’ along the step.

Chapter 6

Trapped Vortices in Steady Rotation about Circular Topography

6.1 Introduction

Geophysical vortices ranging in size from surf-zone vortices to large-scale ocean eddies are characterized by their long life times. Given this, it is likely that these vortices will encounter topographic obstacles. For example, observations in the Canary Basin by Richardson & Tychensky (1993-1995) have shown that Mediterranean salt lenses, or more commonly known as meddies, interact strongly with seamounts in the North Atlantic. Meddies are subsurface eddies which do not extend throughout the fluid depth but do, however, interact with seamounts as if they were islands such that Meddies are able to pass around the seamount, occasionally bifurcating in so doing. Field observations by Fratantoni & Johns (1995) describe North Brazil Current Rings hundreds of kilometers in diameter colliding with islands in the

Caribbean.

Motivated by this work, a recent paper by Johnson & McDonald (2004*b*) consider the motion of vortex patches and point vortices around two impermeable unconnected circular cylinders. Using conformal mapping techniques it was possible to find the Hamiltonian governing point vortex motion which preserved the zero normal flow condition around the cylinder. A critical path for a point vortex was found which divides the class of solutions which orbit one or both cylinders. Paths of vortex patch centroids obtained using a modified contour dynamics routine were compared with this separatrix vortex with good agreement even though the patch is able to deform from its initial circular shape. For the limiting case where one of the cylinders has large curvature so that it can be considered a straight wall, an incoming patch (propagated by its image in the wall) could bifurcate with portions of vorticity passing around different sides of the cylinder. A more general approach to point vortex motion around multiple cylinders of arbitrary size has been carried out recently by Crowdy & Marshall (2005). Here the point vortex Hamiltonian around a finite number of circular boundaries of arbitrary size is obtained analytically.

Dewar (2002) considered the scattering of baroclinic eddies by circular topography. Here a ‘cloud’ of vortices in a three-layer model is used as an analog to baroclinic eddies. Interactions with the topography can be gauged by the resulting redistribution of the point vortices. It was found that upon collision with the topography, the vortices comprising the eddy underwent significant dispersion leading to the conclusion that a continuous baroclinic eddy might split after impact with the seamount. Further, Stern (1999) studied the interaction of baroclinic vortices near circular topography using shielded (with zero-net circulation) vortices.

The principal aim of this chapter is to find V-states around finite height circular topography including the limiting case where the cylinder passes through the whole of the fluid depth (island) or when a vortex is trapped in a circular domain (infinitely deep well). Although circular obstacles are not common features in the surf-zone, they will occasionally be present, and they represent an idealization for any isolated topographic features. Moreover, for completeness and in complement to chapter 3, it will be interesting to investigate the properties of V-states near finite height circular topography.

The main problem involves solving for the appropriate Green's function from the equation representing conservation of potential vorticity with pressure and normal mass flux continuous across the escarpment. Unlike previous studies involving contour dynamics in the presence of boundaries (e.g. Johnson & McDonald, 2004*b*) where the streamfunction was found by first ignoring the boundaries and then adding an irrotational flow such that the normal velocity was zero at the boundaries, here a different method is presented which avoids these extra computations.

After stating the preliminary equations section in section 6.2, section 6.3 details the new computational method based on Green's functions. Section 6.4 presents results for V-states with steady angular velocity about the topography. The robustness of the computed steady solutions is tested in section 6.5, using time-dependent contour dynamics, first by tracking the evolution of a flow initialized with a V-state and, second, by following a circular patch and computing its evolution toward a V-state. Conclusions are given in section 6.6.

6.2 Preliminary Equations And Conserved Quantities

Section 2.1 shows that fluid is governed by the conservation of potential vorticity $q = \omega/H$, where ω is the vertical component of vorticity ($\omega = v_x - u_y$). From this it is shown that circulation, Γ and kinetic energy \mathcal{E} are invariants. Further, for topography that varies in one dimension only section 3.2 shows that the linear impulse \mathcal{I} is also conserved. In this case of circular topography, a conservation law is now found where the fluid depth H is a function of r alone. With polar coordinates (r, θ) introduce the quantity

$$R(r) = \int^r H(r')r' dr', \quad (6.1)$$

and consider the angular impulse of a vortex patch with uniform vorticity ω

$$\mathcal{J} = \int R\omega r dr d\theta, \quad (6.2)$$

where the integration is taken over the support of ω . Then, using analogous manipulations to those from section 3.2, it can be shown that \mathcal{J} is a constant of the motion. Further, since R is a monotonically increasing function of r , a centre of vorticity (r_{cv}, θ_{cv}) can be associated with any bounded vorticity distribution ω where

$$R(r_{cv}) = \frac{\mathcal{J}}{\Gamma}, \quad (6.3)$$

and θ_{cv} is the usual θ -mean

$$\theta_{cv} = \frac{\int \theta \omega r dr d\theta}{\Gamma}. \quad (6.4)$$

Since R is a monotonically increasing function r_{cv} lies within the extremes of the vorticity distribution in the r -direction. An equivalent vortex patch for a given distribution q is thus given by a point vortex with the same circulation, Γ , lying at the centre of vorticity.

For circular topography consisting of a single step at $r = 1$ between flat regions of depth H^- in $r < 1$ and depth H^+ in $r > 1$, R can be defined as

$$R(r) = \begin{cases} \frac{1}{2}H^-r^2 & \text{if } r < 1, \\ \frac{1}{2}H^+(r^2 - 1) + \frac{1}{2}H^- & \text{if } r > 1. \end{cases} \quad (6.5)$$

As for rectilinear step topography, the centre of vorticity of a patch corresponds to the usual vorticity centroid for patches located entirely on one side or other of the step at $r = 1$, but differs for distributions with vorticity located on both sides i.e. for vortex patches straddling $r = 1$.

6.3 An Alternative Approach To Determine Velocities

Since Deem & Zabusky (1978) formulated contour dynamics it has been highly successful in investigating of the evolution of piecewise-constant vorticity. This method has however proved difficult to implement and expensive in the presence of boundaries other than semi-infinite domains bounded by a single planar wall or channels with two parallel rectilinear walls (Haynes *et al.*, 1978). Recently several studies, (Johnson & McDonald, 2004*a,b*), have presented a method for incorporating boundaries using contour dynamics. First, solve the problem using contour dynamics by ignoring the boundaries. Then find the exact irrotational solution typically using conformal mapping that cancels the flow along the boundaries. The two solutions

are then superposed to give the total velocity.

A different approach is presented here that avoids these extra computations by modifying the Green's function in the contour dynamics integrations. This method applies to flows with finite depth changes and also extends to free-surface flows where the governing equation is the homogeneous Helmholtz equation instead of Poisson's equation considered here.

Let the Green's function giving the streamfunction, $\psi(x, y)$ be $G(x, y, x_0, y_0)$ so for some distribution of vorticity $\omega(x, y)$.

$$\psi(x, y) = \iint_{\mathcal{R}} \omega(x_0, y_0) G(x, y, x_0, y_0) dx_0 dy_0, \quad (6.6)$$

where $\nabla^2 G = \delta(x - x')\delta(y - y')$ and the integral is taken over all regions with non-zero vorticity, $\omega(x_0, y_0)$. Now suppose that the partial derivatives of G are related to those of some function \hat{G} through

$$\frac{\partial G}{\partial x} = g_{11}(x, y) \frac{\partial \hat{G}}{\partial x_0} + g_{12}(x, y) \frac{\partial \hat{G}}{\partial y_0}, \quad (6.7a)$$

$$\frac{\partial G}{\partial y} = g_{21}(x, y) \frac{\partial \hat{G}}{\partial x_0} + g_{22}(x, y) \frac{\partial \hat{G}}{\partial y_0}. \quad (6.7b)$$

Then the horizontal velocities components are

$$\begin{aligned} u + iv &= -\frac{\partial \psi}{\partial y} + i \frac{\partial \psi}{\partial x} = \iint_{\mathcal{R}} \omega_0 \left(-\frac{\partial G}{\partial y} + i \frac{\partial G}{\partial x} \right) dx_0 dy_0 \\ &= (g_{22} - ig_{12}) \oint \omega_0 \hat{G} dx_0 - (g_{21} - ig_{11}) \oint \omega_0 \hat{G} dy_0, \end{aligned} \quad (6.8)$$

by Green's theorem with the integral taken anticlockwise around $\partial \mathcal{R}$, the boundary of \mathcal{R} . Writing $z = x + iy$, $z_0 = x_0 + iy_0$ shows that (6.8) reduces

to the usual unbounded domain expression (Saffman, 1992),

$$u + iv = \oint_{\partial\mathcal{R}} \omega_0 G dz_0, \quad (6.9)$$

when G depends on the distance $|z - z_0|$ alone so \hat{G} can be identified with G , giving $g_{11} = -1$, $g_{12} = 0$, $g_{21} = 0$, $g_{22} = -1$.

6.3.1 Image System Green's functions

A useful application of (6.8) follows for a Green's function where boundary effects can be represented by a finite system of image vortices. Let a vortex at z_0 have N images $Z_k(z_0) = X_k(z_0) + iY_k(z_0)$, ($k = 1, \dots, N$) and thus the Green's function has the form

$$G(x, y, x_0, y_0) = \sum G_k(|z - Z_k(z_0)|^2), \quad (6.10)$$

where the sum is taken over $k = 0, \dots, N$ with $Z_0(z) = z_0$, the identity, giving the vortex itself. The Green's function depends solely on the distances from the observation point z to the vortex and its images. By symmetry between the reference z_0 point and the observation point z of the Green's function

$$G(x, y, x_0, y_0) = G(x_0, y_0, x, y) = \sum G_k(|z_0 - Z_k(z)|^2). \quad (6.11)$$

Differentiating (6.11) with respect to x gives

$$\begin{aligned} & \frac{\partial G}{\partial x}(x, y, x_0, y_0) \\ &= -2 \sum G'_k(|z_0 - Z_k(z)|^2) \left\{ [x_0 - X_k(x, y)] \frac{\partial X_k}{\partial x} + [y_0 - Y_k(x, y)] \frac{\partial Y_k}{\partial x} \right\}, \\ &= - \sum \left\{ \frac{\partial G_k}{\partial x_0}(|z_0 - Z_k(z)|^2) \frac{\partial X_k}{\partial x}(x, y) + \frac{\partial G_k}{\partial y_0}(|z_0 - Z_k(z)|^2) \frac{\partial Y_k}{\partial x}(x, y) \right\}, \end{aligned} \quad (6.12)$$

and $\frac{\partial G}{\partial y}$ similarly. These are of the required form, (6.7a), to apply to (6.8) giving

$$u + iv = i \sum \left\{ \left(\frac{\partial Y_k}{\partial x} + i \frac{\partial Y_k}{\partial y} \right) u_k - \left(\frac{\partial X_k}{\partial x} + i \frac{\partial X_k}{\partial y} \right) v_k \right\}, \quad (6.13)$$

where

$$u_k + iv_k = \oint_{\partial \mathcal{R}} \omega_k G_k(|z_0 - Z_k(z)|^2) dz_0, \quad (6.14)$$

the velocity induced by the vortex z_0 at the k^{th} image $Z_k(z)$ of the observation point z . The velocity at the observation point z is simply the sum of multiples of the velocity induced at each of the n image point of z , found simply by integrating the Green's functions G_k around $\partial \mathcal{R}$ alone. This is particularly efficient when using contour dynamics since no additional calculations are required to determine the boundary effects. When the images are absent (6.13) reduces to (6.9) as expected.

6.3.2 Circular topography, an example

Consider axisymmetric topography as described earlier. The Green's function has been derived by Johnson (1978) and is given here in complex form

$$G(z, z_0) = -\frac{1}{2\pi} \begin{cases} H^+ [\log |z - z_0| + \alpha \log |1 - 1/(z\bar{z}_0)|], & |z| > 1, |z_0| > 1, \\ H^+ [\beta \log |z - z_0| - \alpha \log |z_0|], & |z| < 1, |z_0| > 1, \\ H^+ [\beta \log |z - z_0| - \alpha \log |z|], & |z| > 1, |z_0| < 1, \\ H^- [\log |z - z_0| - \alpha \log |1 - z\bar{z}_0|], & |z| < 1, |z_0| < 1, \end{cases} \quad (6.15)$$

where \bar{z} denotes the conjugate of z and

$$\alpha = \frac{\gamma - 1}{\gamma + 1}, \quad \beta = 1 + \alpha, \quad (6.16)$$

which are derived from the boundary conditions of continuous mass flux and normal pressure continuous across the escarpment. Here the depth ratio is defined as $\gamma = H^-/H^+$. The Green's function G is continuous across the escarpment at $|z| = 1$ and is symmetric with respect to z and z_0 , as required. Moreover in the neighbourhood of the vortex at z_0 ,

$$G(z, z_0) \rightarrow -(H(z_0)/2\pi) \log |z - z_0|, \quad \text{as } z \rightarrow z_0, \quad (6.17)$$

as required. Now G is of the form (6.10) with $Z_1(z) = 1/\bar{z}$ so the complex velocity, using (6.13), is (assuming unit vorticity)

$$u+iv = \frac{1}{2\pi} \begin{cases} H^+[(u_0 + iv_0) + \alpha(u_1 - iv_1)/\bar{z}^2], & |z| > 1, |z_0| > 1, \\ H^+\beta(u_0 + iv_0), & |z| < 1, |z_0| > 1, \\ H^+[\beta(u_0 + iv_0) - i\alpha H^+ \mathcal{A}/\bar{z}], & |z| > 1, |z_0| < 1, \\ H^-[(u_0 + iv_0) - \alpha(u_1 - iv_1)/\bar{z}^2 - i\alpha \mathcal{A}/\bar{z}], & |z| < 1, |z_0| < 1, \end{cases} \quad (6.18)$$

where \mathcal{A} is the area of the patch in $|z_0| < 1$ arising from (6.6) and the subscripts 0, 1 represent contributions from the vortex and its image point respectively.

From (6.18), for the case of $|z| < 1, |z_0| < 1$, two singularities of equal and opposite strength exist at $z = 0$. Appendix H gives an alternate formulation, valid for all $|z| < 1, |z_0| < 1$, but particularly accurate near the origin.

Using (6.18) to calculate the velocity field, the usual image vorticity analogs no longer hold. For example, a point vortex in relative deep water outside the topography ($\gamma < 1$ and $r_0 > 1$) the usual way to find the velocity is to consider two image vortices of strength α ; one positioned at $z = 1/\bar{z}_0$ with oppositely signed circulation and one at the origin with the same-signed circulation (see, for example, Milne-Thomson, 1955). In the above formulation the same point is advected by a single (image) point vortex at $z = 1/\bar{z}_0$ with modified strength by a factor $1/\bar{z}^2$, from the first line of (6.18) (henceforth this is what is meant by modified image vortex). The flow inside the cylinder is driven by a vortex outside the cylinder modified by the factor β (second line of (6.18)). A vortex inside the cylinder in shallow water, a the vortex is advected by a modified image at $z = 1/\bar{z}_0$ with strength $-\alpha$ and a image vortex at the origin with strength $-\alpha$ (last line of (6.18)). Flow

outside the cylinder when the vortex is inside the cylinder is driven by the vortex with strength β and a image vortex of strength $-\alpha$ (third line of (6.18)). Similarly to rectilinear topography (see 3.2) the image strength α and the residual vortex strength β have ranges $-1 < \alpha < 1$, $0 < \beta < 2$ with extreme values corresponding to a circular wall ($\gamma = 0$) and a deep well, $\gamma \rightarrow \infty$ respectively.

6.4 Equilibrium States For Vortex Patches Around Circular Topography

Finite area vortices which rotate around the circular topography at constant angular velocity without change in form (equilibrium states or V-states) can be constructed numerically using an algorithm which ensures the vortex boundary is a streamline. The necessary velocity field along the vortex boundary is computed using contour dynamics with Green's function (6.15). Details of the algorithm are given in Appendix G and closely follow previous work by Wu *et al.* (1984). That is, starting with an initially circular contour, velocity components are computed at N nodes along the vortex boundary using contour dynamics. The nodal positions are then adjusted iteratively so that the boundary is parallel to the local velocity by satisfying a $N \times N$ tri-diagonal system of algebraic equations at each iteration. This iterative process of using contour dynamics to find the velocity at each node and then adjusting the boundary by solving the tri-diagonal system of equations is repeated until a tolerance, ϵ (equal to 10^{-6}), for the steady angular velocity, Ω , is met after typically 50 – 60 iterations using a resolution of 4704 nodes around a circular patch of unit radius. For vortices straddling the topography, contributions to the velocity field owing to vorticity distributions on

each side of the step are computed separately.

6.4.1 V-states near finite height topography

In contrast to rectilinear topography, circular topography has an additional length scale: the radius of the topography, ϱ . Therefore, unlike chapter 3, the volume and centre of vorticity are insufficient to give a unique V-state, and here, the radius of the cylinder must also be specified. Figure 6.1 gives examples of V-states near finite height circular topography with unit radius for two examples of depth ratio: figure 6.1(a) describes V-states for $\gamma = 1/2$ with deep water *outside* the cylinder and figure 6.1(b) gives examples of V-states for $\gamma = 2$ with deep water *inside* the cylinder.

Figure 6.1 shows examples of V-states near circular topography including the case where the V-state straddles the step. As mentioned earlier, to uniquely define a V-state near circular topography it is sufficient to specify the volume and center of vorticity and the radius of the circular topography. The radius here is fixed at $\varrho = 1$, and several V-states are drawn to highlight the different shapes attained with different volumes.

Figure 6.1(a) gives V-states near a seamount with $\gamma = 1/2$. V-states with centroids near the center of the topography will have a quasi-circular shape since the contributions from its images points will be close to symmetric. Small (in comparison to ϱ , the radius of the topography) V-states which exist wholly outside or inside but close to the step have similar shapes to V-states near rectilinear topography existing in deep and shallow water respectively (chapter 3, section 3.3), where inside the topography V-states will be attracted by a positively signed image and outside repelled by an oppositely signed image. However straddling V-states and (if the volume of the V-state is sufficiently large) enveloping V-states (i.e. where the vortex

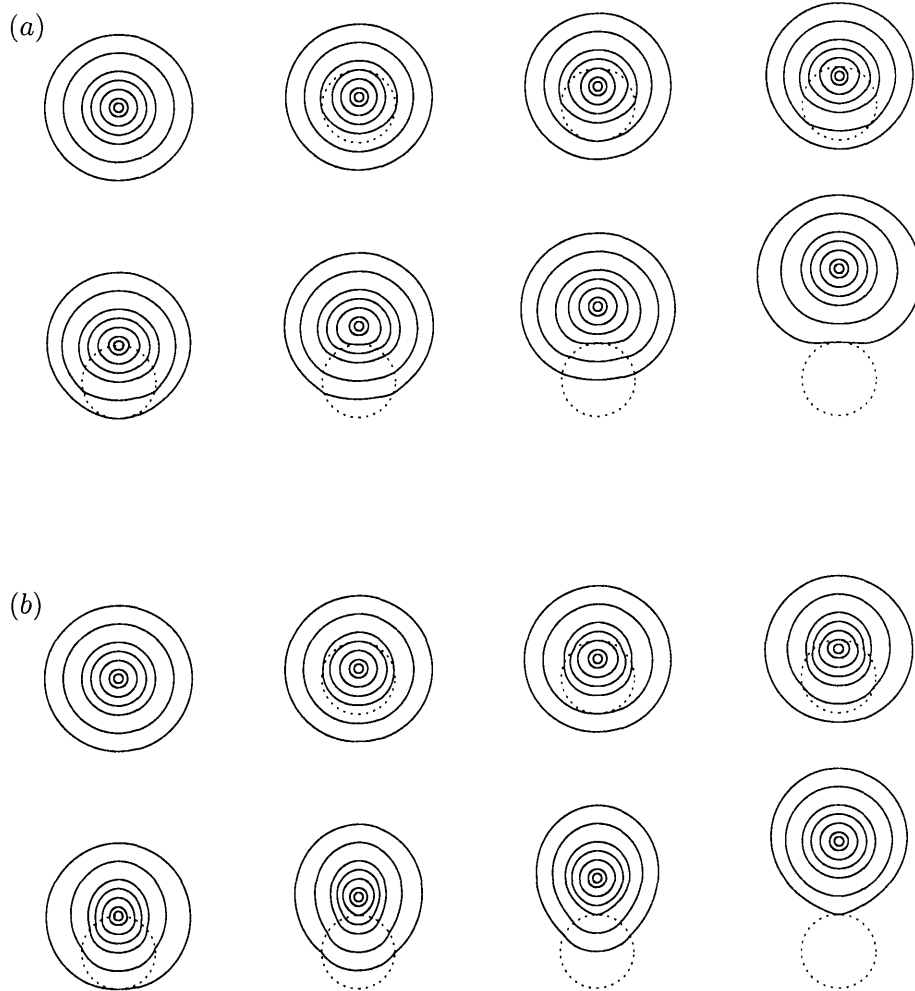


Figure 6.1: V-states near finite height topography, (a) depth ratio $\gamma = 1/2$ such that deep water is *outside* the cylinder and (b) $\gamma = 2$ with deep water *inside* the cylinder. Each frame shows seven V-states plotted on top of one another with collated vortices in each frame have mean radii $\frac{1}{8}, \frac{1}{4}, \frac{1}{2}, \frac{3}{4}, 1, 2, 3$ with one of the patches in each frame just touching the escarpment. The dotted line here represents the location of the finite height topography.

completely envelopes the topography such that the whole seamount exists inside the vortex) will, in general, have distorted shapes. The shape of off centre enveloping V-states is due to the asymmetric distribution of the im-

age points, where straddling V-states will have contributions by oppositely signed image points from deep water and same-signed image points from shallow water.

Figure 6.1(b) gives V-states near a well with $\gamma = 2$. In this case the shape of the V-states is different to the previous case (where $\gamma = 1/2$). However each shape can be explained in a similar way: vortices exterior to the well will have image points of the same-sign as the vortex, with vortices interior to the well have image points with opposite-sign to the vortex. Consequently vortices exterior to the well are stretched toward the topography with vortices interior to the well, flattening along the edge of the topography. Similarly to the previous example, straddling vortices will have two image contributions from deep water (the wells interior) and shallow water (the wells exterior).

Figure 6.2 compares the angular velocity (plotted as a function of r_{cv}) of a computed V-state with a point vortex having equivalent circulation (normalized to π) and centre of vorticity for two values of depth ratio; (a) $\gamma = 1/2$, (b) $\gamma = 2$. Each curve in each frame represents a different choice of patch volume; $\pi/16$, $\pi/4$ and π .

As expected for vortex patches having small volume the angular velocity agrees well with the angular velocity of a point vortex. This is especially true at large distances from the step where the patch is close to a circular shape (note also for small patches the profile of the angular velocity compares well to the rectilinear case see chapter 3, section 3.4, since the effect of the topographic curvature is small). For larger patches the comparison to a point vortex is less favourable since the shapes of these V-states are no longer circular. In fact for patches whose area is comparable to the area of the interior topography, comparisons with a point vortex is not expected

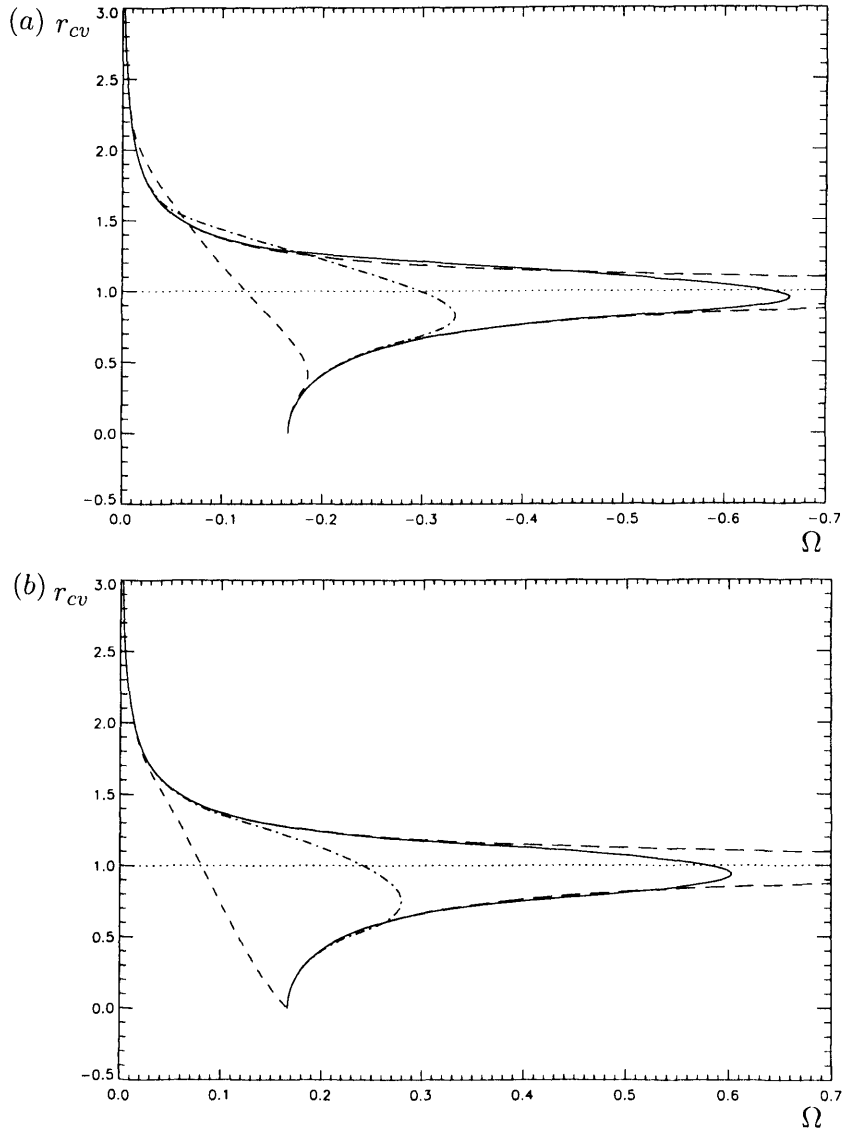


Figure 6.2: The angular velocity Ω of the V-state about the topography as a function of center of vorticity r_{cv} for (a) $\gamma = 1/2$ and (b) $\gamma = 2$. The long dashes represents an equivalent point vortex both interior and exterior to the topography with boundary given by the dotted line. A solid line shows the velocity of a patch with volume $\pi/16$ shorter dashes with volume $\pi/4$ and dash-dotted line π . The circulation of each patch and point vortex is normalized such that the circulation is π .

to have close agreement. Indeed, when the patch volume is π , for $\gamma = 1/2$ the boundary of the patch lies over the step. Any V-state with off centre centroid will straddle the topography. However, for larger patches exterior to the boundary a comparison to a point vortex is accurate since, as explained earlier, far away from the topography a patch will tend to a circular shape regardless of the size of the patch.

6.4.2 Limiting cases for finite height circular topography

For rectilinear topography the limiting case of the topography corresponds to the escarpment passing through the entire fluid depth i.e. a wall. This case where a vortex translates parallel to a wall has been subject to much research (see Deem & Zabusky, 1978; Wu *et al.*, 1984; Pierrehumbert, 1980; Saffman & Tanveer, 1982). For finite height circular topography there are two limiting cases for vortex motion: first when the vortex translates exterior to the cylinder (cf. island) and second when the vortex is trapped inside a circle (cf. deep well) neither which have been previously studied. The Green's function for each case is given by (6.15) with $\alpha = \pm 1$ depending if the vortex is interior or exterior to the cylinder with the appropriate branch of the Green's function chosen (note there will be no contribution in (6.15) from terms involving $|z| < 1, |z_0| > 1$ or $|z| > 1, |z_0| < 1$).

Figure 6.3(a) gives examples of V-states trapped inside a well of unit radius, with 6.3(b) gives of V-states outside an island. The limiting V-state in each case does not touch the topography, but gets to within a distance of less than 1% of the boundary radius. Shapes of V-states in both cases may be anticipated from extreme cases of finite height topography: small vortices (compared to the cylinder radius) exterior or interior to the cylindrical wall near the solid boundary will resemble V-states near a rectilinear wall, (Deem

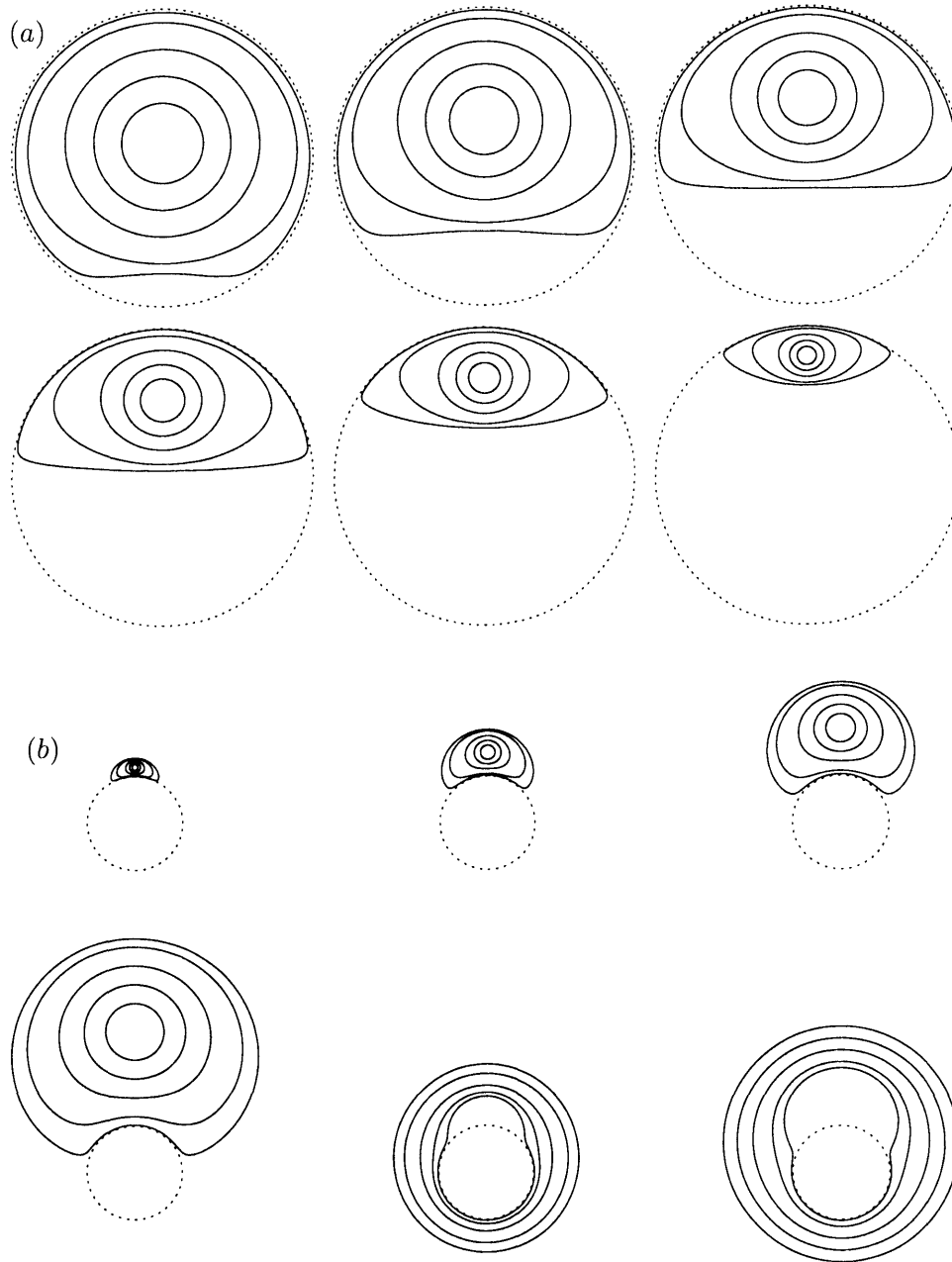


Figure 6.3: V-states for limiting cases of finite height topography which passes through the whole depth of the fluid. (a) $\gamma \rightarrow \infty$ and each V-state is trapped inside circular topography. (b) $\gamma = 0$ with V-states are trapped outside circular topography. The dotted line here represents the boundary of the topography. Locations and mean radii of the V-states are given in Appendix I

& Zabusky, 1978; Wu *et al.*, 1984; Pierrehumbert, 1980; Saffman & Tanveer, 1982). Whereas V-states away from the boundary will interact weakly with the topography and remain close to circular.

The angular velocity of the V-states as a function of r_{cv} in the case of limiting finite height circular topography (i.e. an island or deep well) is given in figure 6.4 for two different patch volumes; $\pi/16$ and $\pi/8$. A comparison to a point vortex with equivalent centre of vorticity and circulation is also given. There is good agreement between computed V-states and a point vortex where comparisons are possible. That is, each of these lines terminate where the patch is touching the boundary of the topography and so no V-states can be computed beyond this value of r_{cv} . However, the angular velocity of the V-state starts to deviate away from the point vortex when V-states are close to the boundary and are no longer circular in shape.

6.5 V-States In Time-dependent Flows

6.5.1 Using a computed V-state to initialize flow

Equilibrium states for vortex patches near variable height circular topography have been computed. As in the rectilinear case (see chapter 3, section 3.5) to investigate the robustness (i.e. stability) of these computed states, the time dependent equations of motion were integrated using a fourth-order Runge-Kutta scheme and contour surgery (Dritschel, 1988). In each case the flow was initialized with a computed V-state. Two examples of these integrations are given by figure 6.5. The first figure 6.5(a) has $\gamma = 1/2$ and shows the vortex patch after 25 eddy turnover times (equivalent to over two complete revolutions around the topography) together with the initial computed V-state as a comparison. Figure 6.5(b) shows the analogous case for

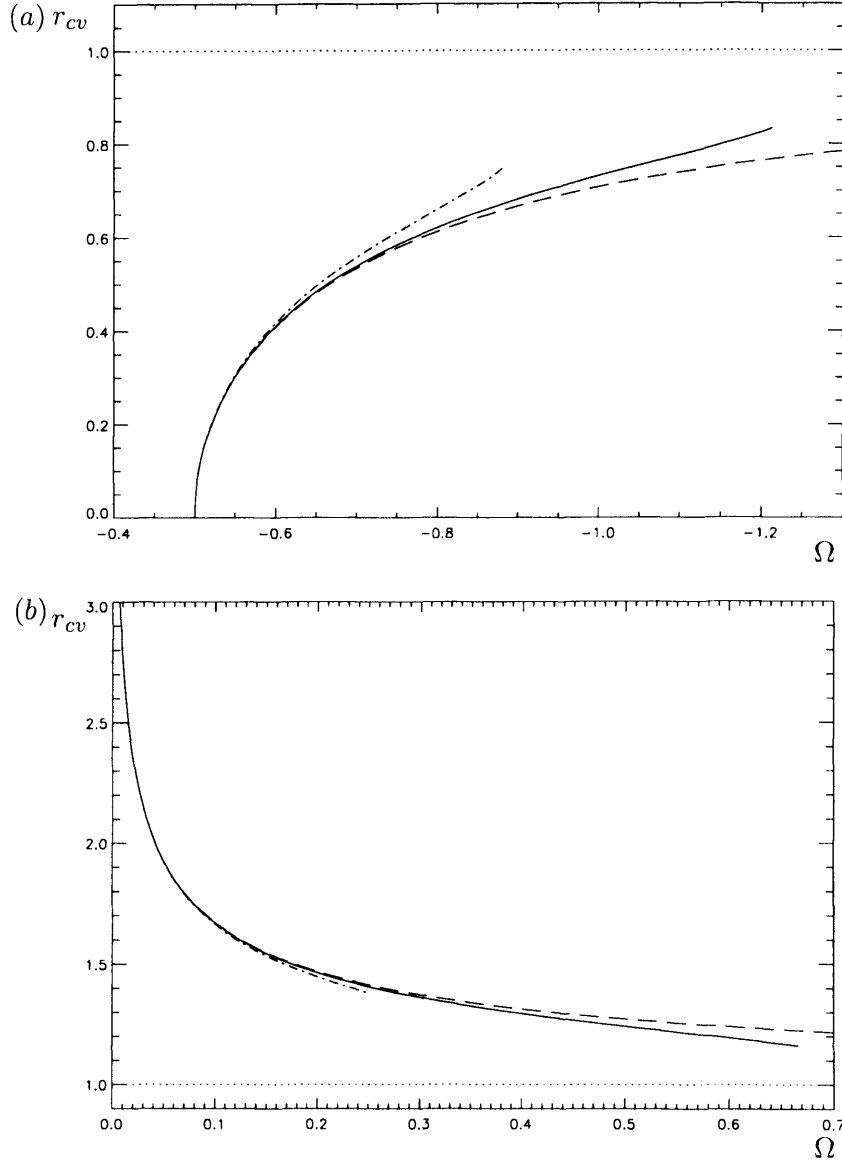


Figure 6.4: The angular velocity Ω as a function of center of vorticity r_{cv} for limiting cases of finite height topography (i.e. extending over the whole fluid column), (a) exterior to the cylinder and (b) interior to the cylinder. The long dashes represents an equivalent point vortex both interior and exterior to the topography with boundary given by the dotted line. A solid line shows the velocity of a patch with volume $\pi/16$ shorter dashes with volume $\pi/8$. Each of these lines terminate where the patch is touching the boundary of the topography and so no V-states can be computed beyond this value of r_{cv} . The circulation of each patch and point vortex is normalized such that it is equal to π .

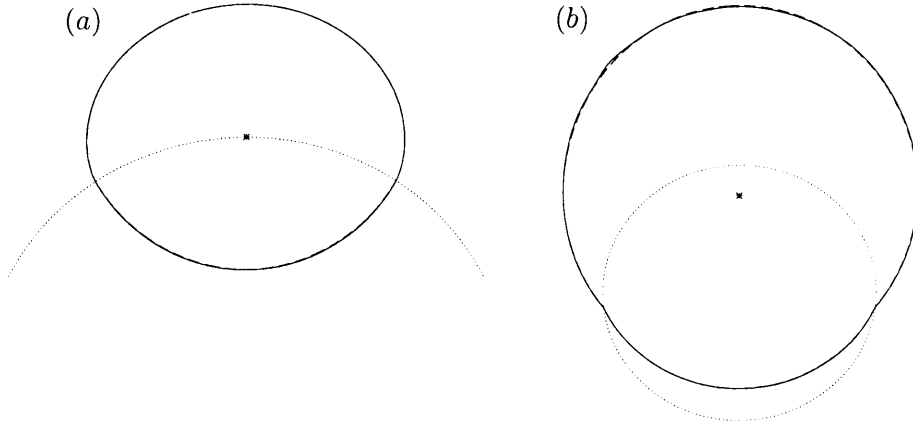


Figure 6.5: Comparison between the initial and final states of an evolved flow started from a computed V-state, (a) an example of a flow with $\gamma = 1/2$ and (b) with $\gamma = 2$. The dashed line represents the initial V-state (with the centre of vorticity marked by +) with the solid line the time evolved patch after 25 eddy turnover times (with centre of vorticity marked by \times). The dotted line here represents the escarpment for the circular topography.

$\gamma = 2$ (for clarity each evolved patch is rotated such that $\theta_{cv} = 0$).

The time evolved vortex patch and the original V-state for each depth ratio compare favourably, suggesting they are highly durable, stable structures. However, there is a small amount of vortex shedding during the integrations owing to the finite resolution of the time-dependent numerical algorithm (Dritschel, 1988). The removal of tiny filaments generated during the motion also causes the centre of vorticity to be displaced slightly. Both these effects are remarkably small given the long duration (in space and time) of the integration.

6.5.2 Using a circular patch to initialize the flow

Computed V-states have been tested for robustness by starting them in a time dependent flow. However it is of interest to ascertain whether arbitrar-

ily shaped patches can evolve towards equilibrium states. This issue was addressed for rectilinear topography (chapter 3, section 3.5.2) with the conclusion that there is a strong tendency for a vortex to shed vorticity in such a way that a V-state is approached. To answer this question time dependent integrations are executed using an initially circular vortex patch to initialize the flow. Figure 6.6 shows eight snapshots of the evolving flow for two cases: (a) $\gamma = 1/5$ and (b) $\gamma = 1/3$. In both cases the circular patch is initially straddling, in other integrations which are not shown here, the patch does not initially straddle the escarpment and no shedding occurs. The patch subsequently rotates about the circular topography in a similar fashion to that of a vortex patch near a wall or rectilinear escarpment, (chapter 3, section 3.5.2). Each set of integrations is run for 50 eddy turnover times.

Figure 6.6 suggests that circular patches will approach equilibrium states provided the patch is able to shed a non-negligible amount of vorticity. Further integrations, not shown here, show that larger depth contrasts increases the quantity of vortex shedding so that quasi-V-state shapes are found with fewer turnover times than for smaller depth ratios. Moreover, for small depth contrasts quasi-V-state shapes are found to form more slowly due to the minimal vortex shedding.

The ability of a vortex to shed vorticity is a vital mechanism for a patch to attract towards an equilibrium state however, too much shedding will cause the patch to lose coherency. Figure 6.7 contrasts the evolution of two identical patches with different depth ratios, $\gamma = 3$ and $\gamma = 2$. It is evident that the larger contrast in depth causes the patch to shed severely, whereas the smaller depth contrast the patch sheds vorticity only slightly resulting in the formation of a stable a quasi-V-state shape.

The mechanism which is responsible for this destructive shedding is ow-

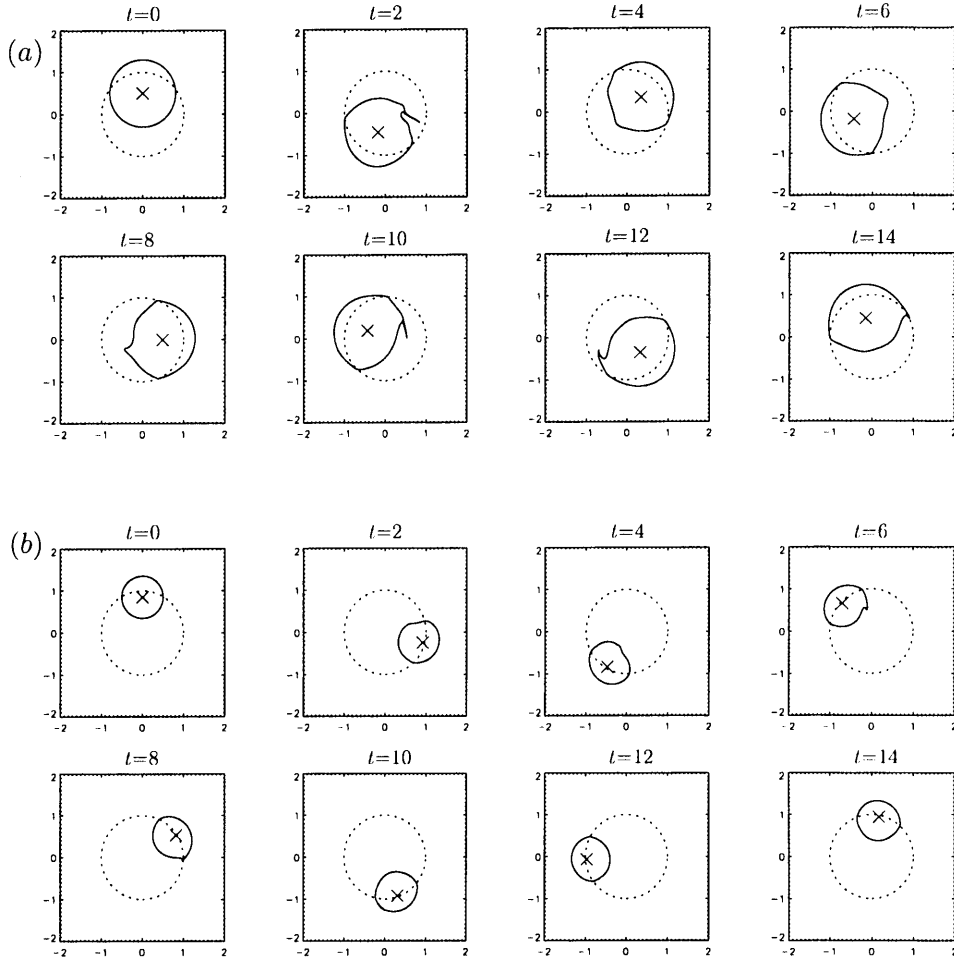


Figure 6.6: The evolution of a vortex that is initially circular and directly over the topography, (a) a patch evolved with $\gamma = 1/5$ and (b) $\gamma = 1/3$. Frames are at equal intervals showing the initial configuration up to 50 turnover times.

ing to the conservation of potential vorticity. For large depth contrasts, say $\gamma = \gamma_1 > 1$, filaments in deep water (here $r > 1$) have vorticity ω . If a filament is forced over the escarpment its vorticity increases to $\gamma_1\omega$, thereby having a strong impact on the flow. Whereas for smaller depth contrasts, $0 < \gamma = \gamma_2 < 1$, filaments in shallow water, inside the boundary will have vorticity $\gamma_2\omega$ and will have a weaker impact.

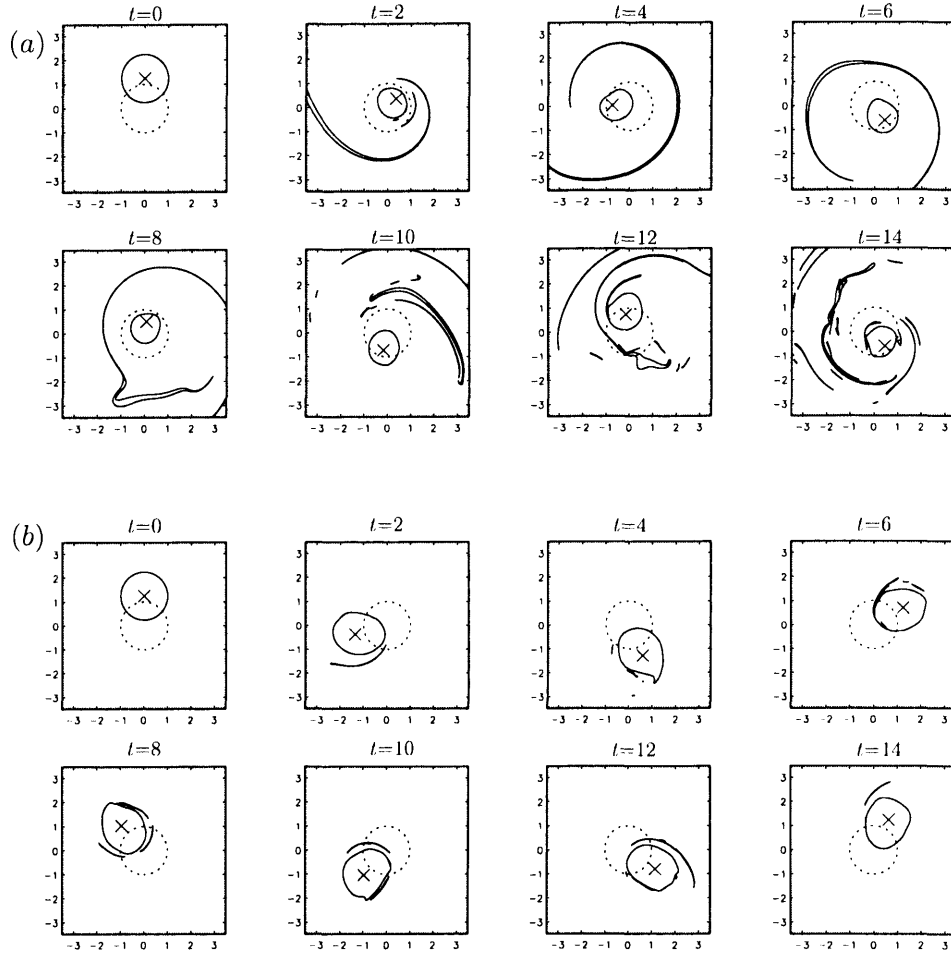


Figure 6.7: The evolution of a vortex that is initially circular and directly over the topography. Frames are at equal intervals showing the initial configuration up to 10 turnover times. The initial configurations are the same up to the depth ratio. (a) $\gamma = 3$ and (b) $\gamma = 2$.

6.6 Conclusions

A novel approach in computing the velocity field using contour dynamics, avoiding extra computations or modifications to the Green's function is presented and was used to find V-states around circular topography of arbitrary height. Similar to V-states near rectilinear topography (chapter 3, section 3.3), V-states for circular topography in shallow water are 'tear' shaped with

the vortex stretched towards the escarpment by an attracting image in deep water. V-states in deep water flatten along the side closest to the escarpment, with flattening becoming more pronounced as the V-state approaches the escarpment as in Euler equation V-states near walls (Wu *et al.*, 1984; Saffman & Tanveer, 1982; Pierrehumbert, 1980; Deem & Zabusky, 1978). The contrast in angular velocity between a computed V-state and a point vortex was found to be small provided the V-state remained close to circular. Importantly, unlike a point vortex, the angular velocity of a V-state is finite even when the V-state is straddling the topography.

Time-dependent flows initialized with a V-state showed little change in vortex shape even after 25 turnover times, showing that V-states are robust, stable structures. Further time dependent flows starting with circular patches propose that V-states act as attractors provided that a vortex is able to efficiently shed vorticity. It was found that non-straddling patches do not approach a V-state since there is minimal shedding. Vortices which straddle and have large depth changes the vortex will not remain coherent as in figure 6.7. The combination of these properties means they are likely to be important transport mechanisms around small islands and wells with their ability to capture and transport anomalous fluid.

Chapter 7

Interactions of Vortex Pairs with Circular Topography

In the absence of background currents or potential vorticity gradients (commonly provided by the variations in the Coriolis parameter, f , see for example McDonald, 1999), vortices are advected by other vortical structures and can often be found in pairs. Indeed, Peregrine (1998) shows that vortices frequently ‘pair-up’ forming dipoles which are robust vortical distributions with the ability to survive for several rotation periods, (Gorshkov, Ostrovsky & Soustova, 2000). Therefore, it will be likely that transient vortex pairs will encounter topography. The case of a vortex dipole approaching a solid cylinder which occupies the whole fluid depth has been studied both numerically and experimentally. Orlandi (1993) investigated the interactions of a Lamb dipole with a circular cylinder. In the inviscid case, dipoles were found, upon collision, to bifurcate and translate around the topography, meeting again as they translated away from the cylinder. With non-slip boundary conditions, a dipole impinged on a cylinder significantly smaller than the mean radius of the dipole, chosen to complement laboratory experiments

by Homa, Lucas & Rockwell (1988). Secondary vorticity was generated at the boundary, which in turn advected the primary vorticity away from the cylinder. Further laboratory experiments by Verzicco, Flór, van Heijst & Orlandi (1995) found that the diameter of the cylinder played a significant role in the generation of wall generated vorticity.

The aim of this chapter is to understand the interactions of vortex pairs near finite height topography. This is motivated from the little attention given to dipoles which approach circular topography ‘off-centre’, that is, with a trajectory not aligned along an axis of symmetry. Moreover, this is in complement to chapters 4 and 5 where the dynamics of vortex pairs near rectilinear topography was examined.

Section 7.1 considers a point vortex pair close to finite height circular topography. It is found that a pair can exist in four spatial configuration regimes and the motion for the pair is found by deriving the Hamiltonian for each configuration. Section 7.2 examines in detail the trajectories of distant point vortex pairs approaching the topography in the form of a circular seamount well both studied. It is found that the resulting trajectories can be divided into four classes: (i) an approaching pair can bifurcate with each vortex in the pair passing on opposite sides of the topography, (ii) an approaching pair does not bifurcate and passes the same side of the topography, (iii) each vortex is trapped in orbits about the topography with different frequencies and (iv) an equilibrium state where each vortex is trapped by the topography, having identical rotation frequencies. Section 7.3 computes the evolution of a vortex patch pair and the trajectories of the patches are compared to point vortex motion. Finally, conclusions are presented.

7.1 Equations and Hamiltonian structure

Attention here is confined to a vortex pair of equal and oppositely signed circulation with each vortex centred at (r_1, θ_1) and (r_2, θ_2) interacting with finite height circular topography consisting of a single circular step at $r = 1$ between flat regions of depth H^- in $r < 1$ and depth H^+ in $r > 1$, where r is the radial distance from the origin. The energy, \mathcal{E} and angular impulse, \mathcal{J} are as written in chapter 6, i.e.

$$\mathcal{E} = \int \omega \psi r dr d\theta, \quad \mathcal{J} = \int R \omega r dr d\theta, \quad (7.1)$$

where the integrals are taken over the support of the vorticity $\omega = r^{-1}(\partial_r(r u_\theta) - \partial_\theta u_r)$, ψ is a volume flux streamfunction and $R(r)$ is constrained to be a strictly monotonically increasing or decreasing function of r (see chapter 6, section 6.2). The circulation Γ , and for vortex patches, the volume, \mathcal{V} give the remaining constants of motion and are defined as in chapter 4 section 4.2 given by (4.3) and (4.4) respectively.

As discussed in chapter 4, vortex paths follow from the Kirchoff-Routh path or vortex Hamiltonian (without background flow) viz. (4.7),

$$\mathcal{H}(z_1, \dots, z_N) = \frac{1}{2} \sum_{j=1}^N \sum_{k=j+1}^N Q_j H_j Q_k H(z_k) G(z_j, z_k) + \frac{1}{2} \sum_{j=1}^N Q_j^2 H_j^2 g(z_j, z_j),$$

where $H(z_j)$ is the height of the fluid at point z_j and $g(z, z_j) = G(z, z_j) + 1/2\pi \log |z - z_j|$. As in the case of rectilinear topography (see chapter 4), a point vortex cannot cross the circular step, therefore, point vortex trajectories can be divided regimes depending on the location of vortices being exterior or interior to the circular topography. Using (4.7) and (6.15) the

four different regimes are

1. Both vortices are exterior to the circular topography, $r_1, r_2 > 1$, [ext,ext]:

$$\begin{aligned} \mathcal{H}_{ext,ext} = & -\frac{H^+}{4\pi} \left\{ \Gamma_1 \Gamma_2 \log[r_1^2 + r_2^2 - 2r_1 r_2 \cos(\theta_1 - \theta_2)] \right. \\ & + \Gamma_1 \Gamma_2 \alpha \log \left[\frac{r_1^2 r_2^2 - 2r_1 r_2 \cos(\theta_1 - \theta_2) + 1}{r_1^2 r_2^2} \right] \\ & \left. + \Gamma_1^2 \alpha \log \left[1 - \frac{1}{r_1^2} \right] + \Gamma_2^2 \alpha \log \left[1 - \frac{1}{r_2^2} \right] \right\}. \end{aligned} \quad (7.2a)$$

2. One vortex is interior the circular topography (call this, without loss of generality, vortex 1) with one vortex exterior (vortex 2), $r_1 > 1, r_2 < 1$, [ext,int]:

$$\begin{aligned} \mathcal{H}_{ext,int} = & -\frac{H^+}{4\pi} \left\{ \Gamma_1 \Gamma_2 \beta \log[r_1^2 + r_2^2 - 2r_1 r_2 \cos(\theta_1 - \theta_2)] - \Gamma_1 \Gamma_2 \alpha \log[r_1] \right. \\ & \left. - \Gamma_1^2 \alpha \log \left[1 - \frac{1}{r_1^2} \right] + \gamma \Gamma_2^2 \alpha \log[1 - r_2^2] \right\}. \end{aligned} \quad (7.2b)$$

3. Both vortices are inside the circular topography, $r_1, r_2 < 1$, [int,int]:

$$\begin{aligned} \mathcal{H}_{int,int} = & -\frac{\gamma H^+}{4\pi} \left\{ \Gamma_1 \Gamma_2 \log[r_1^2 + r_2^2 - 2r_1 r_2 \cos(\theta_1 - \theta_2)] \right. \\ & - \Gamma_1 \Gamma_2 \alpha \log \left[\frac{r_1^2 r_2^2 - 2r_1 r_2 \cos(\theta_1 - \theta_2) + 1}{r_1^2 r_2^2} \right] \\ & \left. - \Gamma_1^2 \alpha \log[1 - r_1^2] - \Gamma_2^2 \alpha \log[1 - r_2^2] \right\}. \end{aligned} \quad (7.2c)$$

The case where one vortex is interior to the topography while the other is exterior is closely related to [int,ext], with subscripts 1, 2 swapped.

7.2 Trajectories of point vortex pairs

Motivated by work where vortices encounter circular topography and occasionally bifurcate, (Stern, 1999; Richardson & Tychensky, 1993-1995), the

aim of the present work is to examine the trajectories of vortex pairs *exterior* to finite height circular topography for the cases of a seamount, $\gamma > 1$, and a well, $\gamma < 1$. This will include the limiting cases for each: a surface piercing island $\gamma = 0$, and a deep well $\gamma \rightarrow \infty$. Let $\Gamma = \Gamma_1 = -\Gamma_2$ and rewrite (7.2a) to give

$$\mathcal{H}_{ext,ext} = \frac{\Gamma^2 H^+}{4\pi} \log \left[\frac{(r_1^2 + r_2^2 - 2r_1 r_2 \cos \phi)(r_1^2 r_2^2 - 2r_1 r_2 \cos \phi + 1)^\alpha}{(r_1^2 - 1)^\alpha (r_2^2 - 1)^\alpha} \right]. \quad (7.3)$$

Chapter 4 showed that the trajectories of two point vortices near rectilinear topography can be explicitly stated in terms of the conserved quantities; circulation, Γ , energy \mathcal{E} and impulse, \mathcal{I} . For circular topography use the angular impulse

$$\mathcal{J} = \sum_j \Gamma_j H_j r_j^2, \quad (7.4)$$

and introduce new variables

$$\lambda = \frac{1}{2}(r_1 + r_2), \quad \phi = \theta_1 - \theta_2, \quad (7.5)$$

such that the radial distance for vortex pairs $r_{1,2}$ can be written,

$$r_1 = \lambda + \frac{\mathcal{J}}{2H^+ \lambda \Gamma}, \quad r_2 = \lambda - \frac{\mathcal{J}}{2H^+ \lambda \Gamma}. \quad (7.6)$$

Trajectories for the vortices can now be obtained from contours of the Hamiltonian, (7.3), in (λ, ϕ) -space. As previously mentioned, a point vortex cannot cross the step, therefore it follows that there is a minimum value of λ corresponding to when one vortex of the pair gets arbitrarily close the topography,

$$\lambda_{min} = \frac{1}{2} \left(1 + \sqrt{1 + \frac{2\mathcal{J}}{\Gamma H^+}} \right), \quad (7.7)$$

this lower bound is plotted in the following figures with a bold line, and the forbidden area, $\lambda < \lambda_{min}$, hatched.

7.2.1 Point vortex pair approaching a seamount, $\gamma < 1$

Trajectories for a point vortex pair approaching a seamount with $\gamma = 1/2$ are given in figure 7.1 and can be divided into four different families. First, consider the line shaded region in (λ, ϕ) -space with a typical trajectory given in 7.1(i). In this region the trajectories in (λ, ϕ) -space are not closed so, as expected, the trajectories in physical space are aperiodic. Assuming the pair far away from the topography (i.e. $\lambda \gg 1$), then as the pair approaches the seamount the influence of the partial images (of opposite-sign) slow the vortices and its path is deflected as the pair passes on the same side of the topography (i.e. the trajectory in (λ, ϕ) -space passes through $\phi = 0$), before eventually translating away from the seamount.

Second, consider the unshaded (λ, ϕ) -space. Again the trajectories in (λ, ϕ) -space are open, so, trajectories in (x, y) -space are not periodic. An initially distant pair, approaches the seamount and is slowed by the topographic partial images, but now, the vortex closest to the seamount ‘pairs-off’ with its partial image and translates rapidly around the seamount leaving its partnering vortex to translate more slowly around the topography. Hence the pair bifurcate and each constituent vortex passes on opposite sides of the seamount. This is characterized in (λ, ϕ) -space as a trajectory which passes through $\phi = \pi$. Soon after, the vortex closer to the seamount is advected away from the seamount by the other more slowly translating vortex. The pair then translate away from the seamount with the resulting trajectory in (x, y) -space being deflected considerably by the topography.

The third class of trajectories is represented in (λ, ϕ) -space by the solid

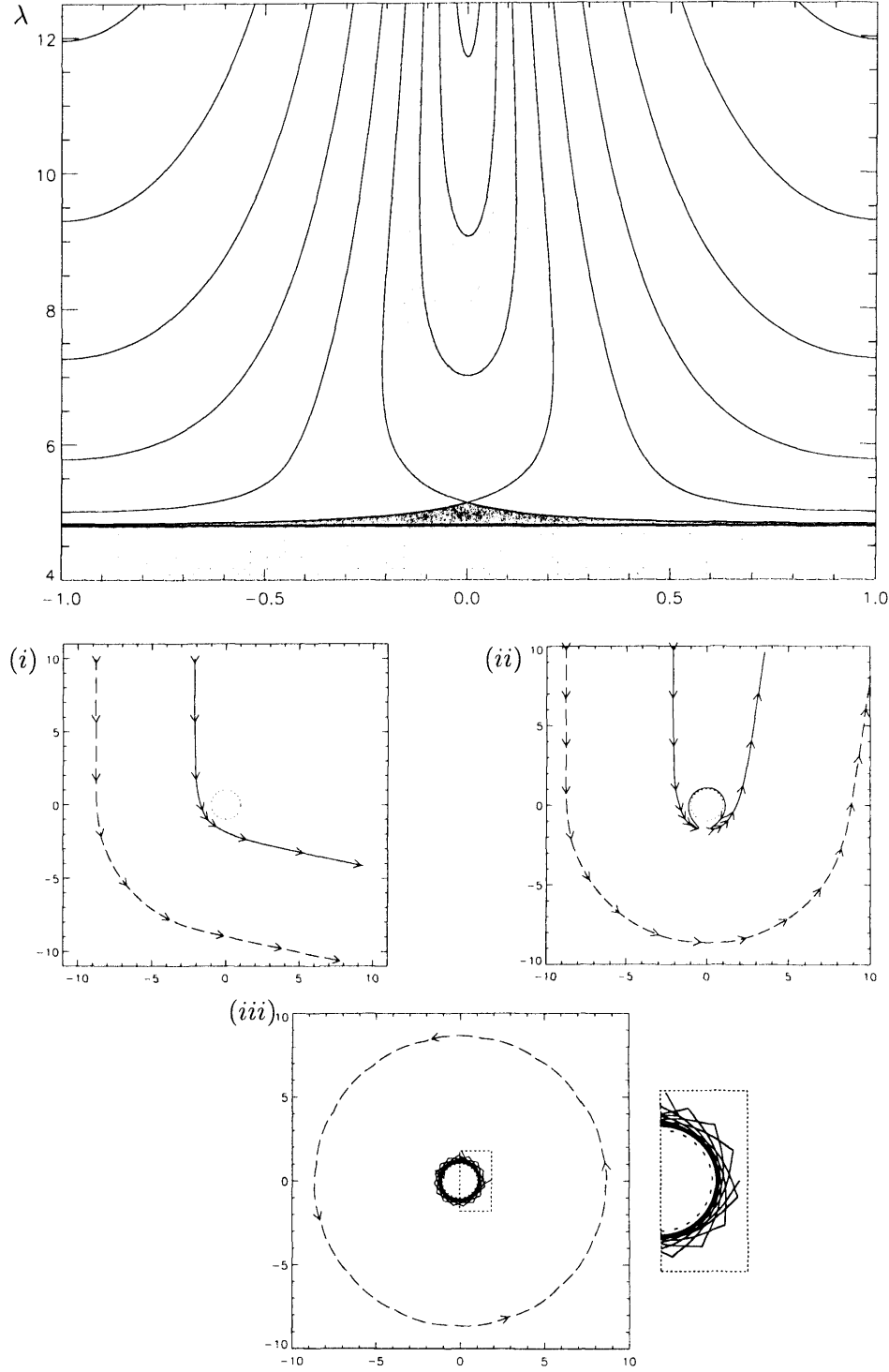


Figure 7.1: Trajectories of point vortices exterior to circular topography with $\gamma = 1/2$ and $\mathcal{J} \approx 228$. Shadings in (λ, ϕ) -space show the different families of trajectories with examples of each type of trajectory in (x, y) -space given by (i), (ii) and (iii) where the dotted box is enlarged. The cross hatched area, here and subsequently, shows the forbidden area where $\lambda < \lambda_{min}$ with arrows drawn at equal intervals.

shaded region in figure 7.1. Here (λ, ϕ) -space trajectories are closed (since (λ, ϕ) -space is periodic in the ϕ direction) indicating periodic motion in (x, y) -space, where the pair (having different rotation frequencies) is trapped about the seamount translating in different directions. Hence, when the pair interact strongly with each other (i.e. when $\phi \approx 0$), the distant vortex advects the closer vortex away from the seamount. But the vortex closer to the seamount is translating more quickly and overtakes the more distant vortex, such that the closer vortex is now advected back toward the seamount. Therefore the pair describe small amplitude leap-frogging motion. Figure 7.1(iii) gives a typical example.

The last class of trajectories is represented by the hyperbolic point in (λ, ϕ) -space. This point represents a two-vortex equilibrium state where both vortices are in steady rotation around the seamount with $\phi = 0$ such that they rotate on the same side of the topography. Although analysis is not shown here, it is expected that this state would be unstable being located at a hyperbolic point. Appendix J shows how such states are found.

Figure 7.2 shows the trajectories of a point vortex pair around an island occupying the entire depth of fluid ($\gamma = 0$), this being the limiting case of a seamount. The trajectories of the pair can be classified in the same way as those for a seamount ($\gamma < 1$): (a) the pair passing the topography on the same side (the lined region in figure 7.2 with an example trajectory given by figure 7.2i), (b) the pair bifurcating and passing on opposite sides (the unshaded region, figure 7.2ii), (c) the pair being trapped around the island (the coloured region, figure 7.2iii) and (d) a two-vortex equilibrium state located in (λ, ϕ) -space at the hyperbolic point. Similar to the case of a seamount ($\gamma < 1$), this dipole equilibrium state is located at $\phi = 0$ such that the pair rotates around the island on the same side (in this case the

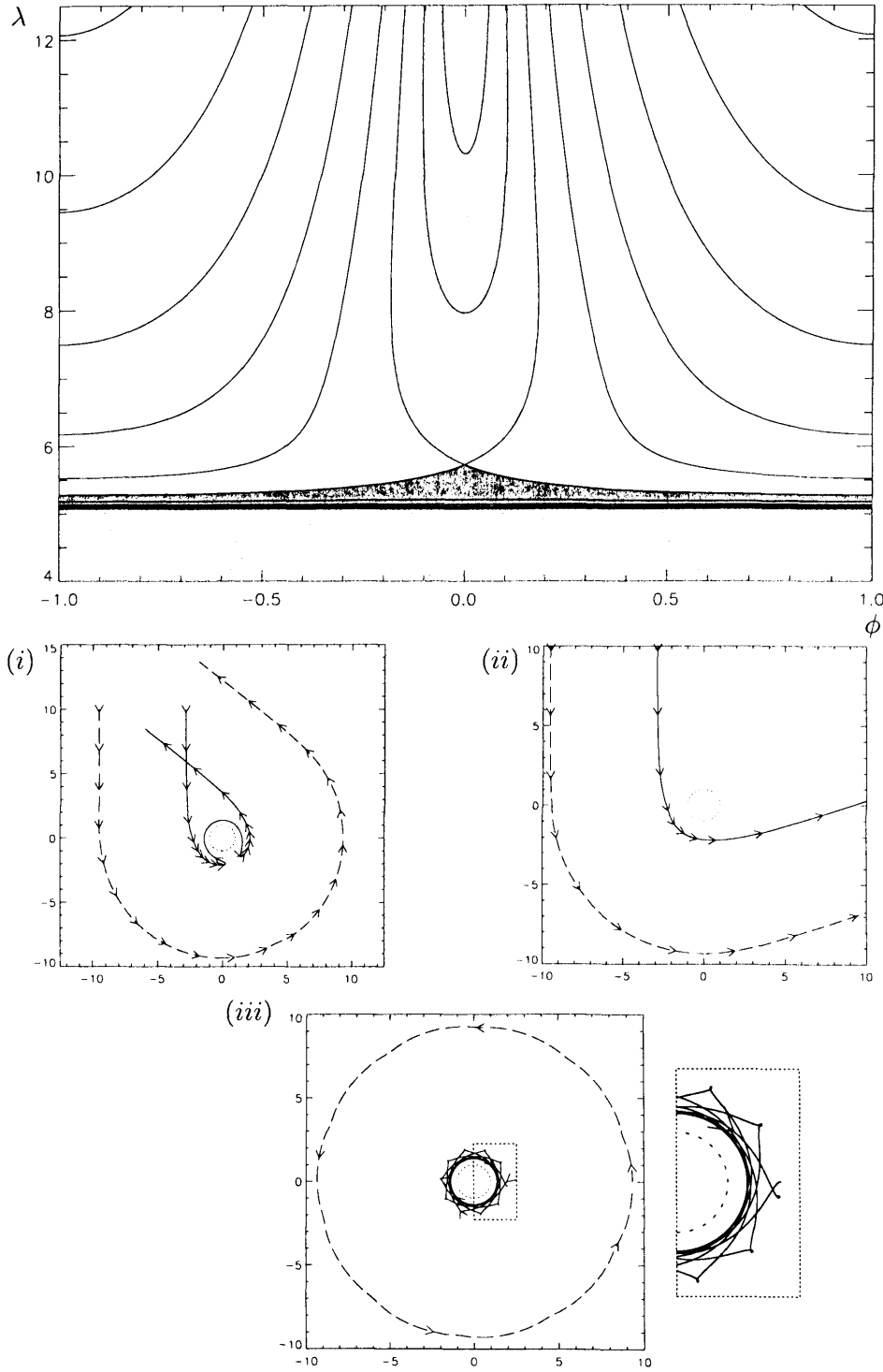


Figure 7.2: Trajectories of point vortices exterior to circular topography with $\gamma = 0$ and $\mathcal{J} \approx 130$. Shadings in (λ, ϕ) -space show the different families of trajectories with examples of each type of trajectory in (x, y) -space given by (i), (ii) and (iii) where the dotted box is enlarged.

leap-frogging motion is accentuated since the topographic images are of the same magnitude as each vortex).

7.2.2 Point vortex pair approaching a well, $\gamma > 1$

A vortex outside circular topography with $\gamma < 1$ (i.e. a well) will experience a topographic partial image of the same sign as the vortex. Consider the case where $\mathcal{J} = 0$ such that $r_1 = r_2 = \rho$ (say). As the pair approaches the well, each vortex will be advected closer to the topography. If the separation is not sufficiently large enough each vortex comprising the pair will ‘pair-off’ with its image in the well. Subsequently, each vortex will translate around the well translating in a direction approaching each other so that they are on a collision course. Eventually since they have identical radial distances, each vortex will meet at a point at the edge of the well. Therefore, there is a minimum separation, when the pair is far from the well, below which the pair will collide with the step.

To evaluate this separation first write (7.3) in terms of ρ with $\phi = \pi$, i.e.

$$\mathcal{E}|_{\phi=\pi} = 4\rho^2 \left(\frac{(\rho^2 + 1)}{(\rho^2 - 1)} \right)^{2\alpha}. \quad (7.8)$$

Computing the minimum value of (7.8) will lead to the minimum radial distance of the pair to just avoid colliding with the well which can be written explicitly as

$$\rho = \sqrt{2\alpha + \sqrt{4\alpha^2 + 1}}. \quad (7.9)$$

Using (7.3) the energy for this trajectory can be computed, thereby giving a minimum value of energy which, if reduced, will lead to an initially distant pair colliding with the topography. In (λ, ϕ) -space this will lead to trajectories existing in $\lambda < \lambda_{min}$.

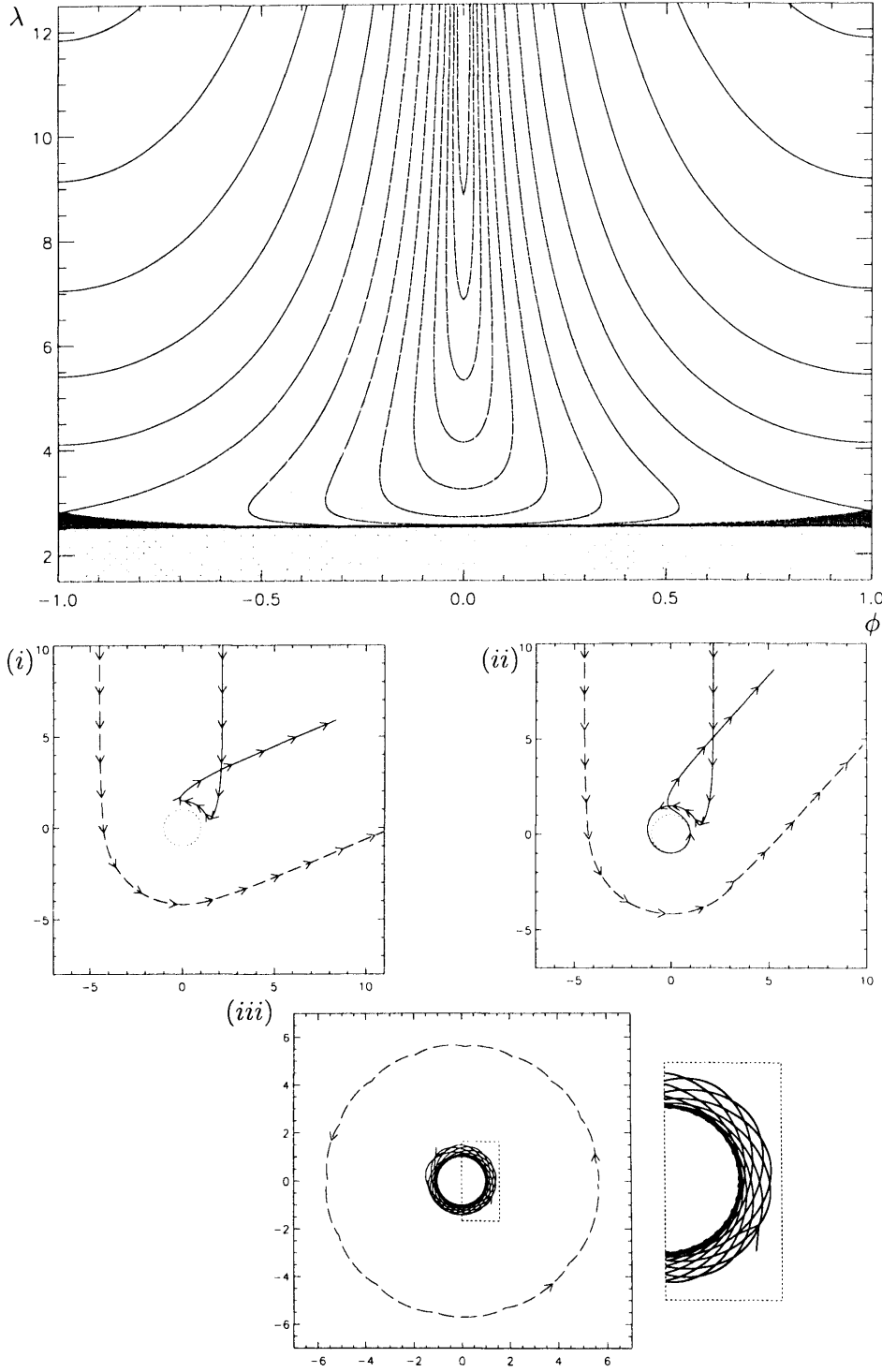


Figure 7.3: Trajectories of point vortices exterior to circular topography with $\gamma = 2$ and $\mathcal{J} \approx 12.1$. Shadings in (λ, ϕ) -space show the different families of trajectories with examples of each type of trajectory in (x, y) -space given by (i), (ii) and (iii) where the dotted box is enlarged.

Trajectories for a pair of point vortices with $\gamma = 2$ in (λ, ϕ) -space near a well with examples trajectories in (x, y) -space are given in figure 7.3. Similarly to the previous case where $\gamma < 1$, trajectories of a point vortex pair fall into four distinct families. However, the behaviour in each regime is subtly different. Consider the unshaded region in figure 7.3, with typical (x, y) -space trajectory given in figure 7.3(i). Here a distant point vortex pair approaches the well, while in the neighbourhood of the well each vortex experiences an image of the same-sign circulation. Then, the vortex nearer the well slows and ‘pairs-off’ with its image and starts to translate around the well, as does its partner, albeit at a slower rate (as it is further away from the well). A short time later, after the pair have passed through $\phi = \pi$, the vortex closest to the well leaves the vicinity of the topography as it re-pairs with the distant vortex. The pair then translate away from the topography such that, eventually, $\lambda \gg 1$.

The second class of trajectory is associated with the line-shaded region of figure 7.3, with a typical trajectory given by figure 7.3(ii). Like before, an initially distant pair approaches the well and is attracted by partial images of the same-sign. However in this case the vortex closest to the topography becomes almost trapped by the well such that in (λ, ϕ) -space the trajectory passes through $\phi = 0$. After this vortex makes one complete orbit in (x, y) -space it re-pairs with the other, more distant vortex and the pair translate away from the well. Note that although the vortex closer to the well makes a complete pass of the well, this does not constitute periodic motion in (λ, ϕ) -space since for this family, trajectories are open i.e. they are not periodic.

The third class of trajectory is when the pair is trapped by the well, given by the coloured region in figure 7.3, where the vortices orbit the well at different angular speeds. However, in contrast to when $\gamma < 1$, the pair

translate in the same direction. Therefore when the vortices interact with each other strongly, the closer vortex is forced toward the well and no leap-frogging motion occurs. A typical trajectory is given in (x, y) -space by figure 7.3(iii).

The last class of trajectories, as with the previous section, is located the hyperbolic point in (λ, ϕ) -space which divides previously described trajectories. This point represents a two-vortex equilibrium state where both vortices are motionless, held stationary by the topographic images with $\phi = \pi$ such that they exist on opposite sides of the topography. This is in contrast to when $\gamma < 1$ where the vortices orbit around the seamount.

Figure 7.4 gives trajectories of a point vortex pair near an infinitely deep well with $\gamma \rightarrow \infty$. Trajectories divide into the same regimes as when $\gamma = 2$ where the pair either; (a) be deflected by the well with vortices remaining on opposite side of the topography figure 7.4(i), (b) be deflected with one vortex being momentarily trapped by the well figure 7.4(ii), (c) where the pair is trapped by the well or figure 7.4(iii), (d) where the pair are stationary, existing in a two-vortex equilibrium state with $\phi = \pi$ (i.e. the vortices are on opposite sides of the well).

7.3 Computed vortex patch trajectories

The evolution of a vortex patch pair consisting of two finite area, equal volume, patches of oppositely signed uniform vorticity is found using an adaption of the contour dynamics algorithm, details of which have been given in chapter 6. Two topographic cases are examined: first when the pair translates toward topography with $\gamma < 1$ with both a seamount ($\gamma = 1/2$) and a surface piercing island ($\gamma = 0$) studied. Second, the trajectories of when the vortex patch pair translate toward topography with $\gamma > 1$ with

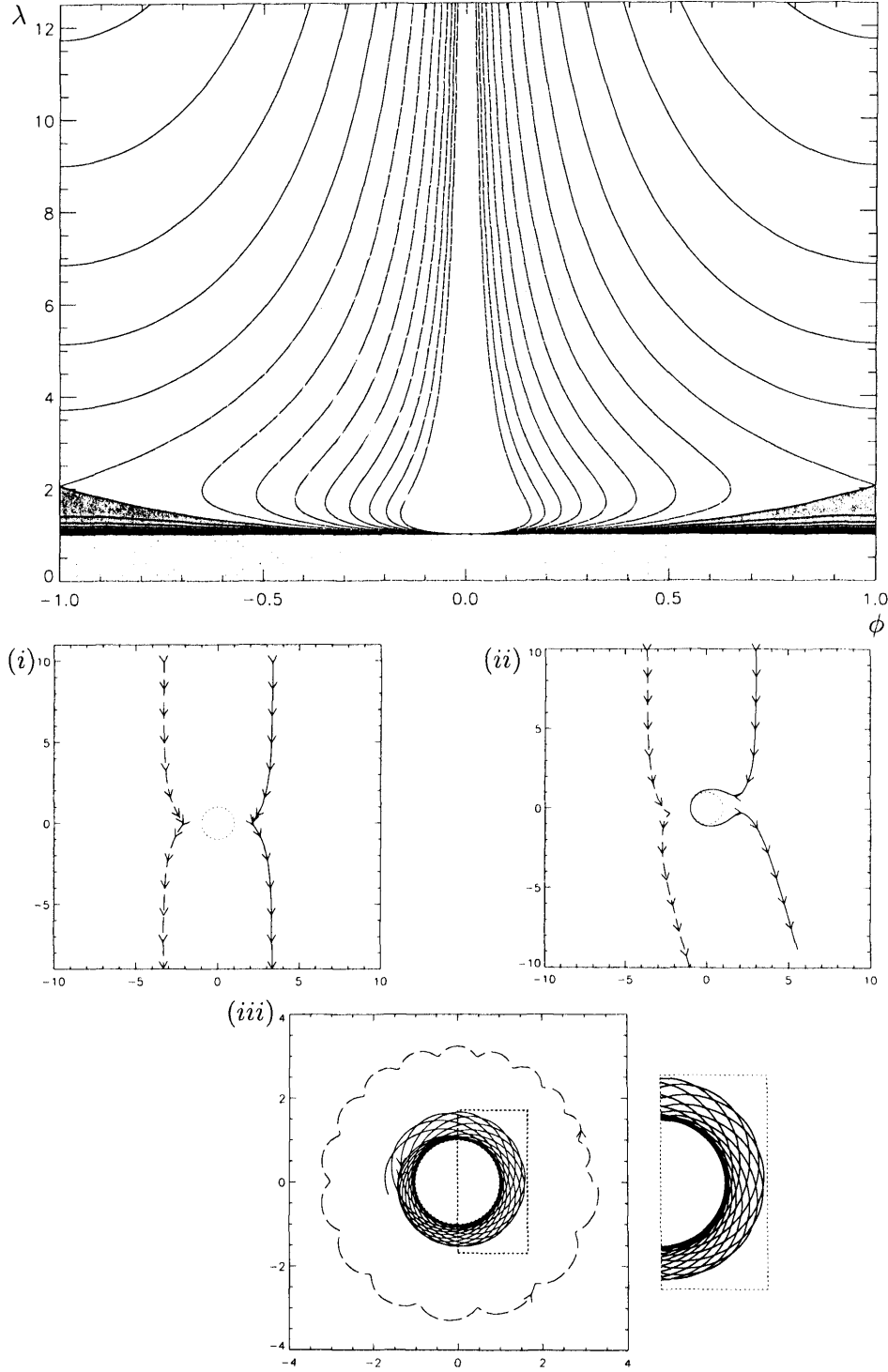


Figure 7.4: Trajectories of point vortices exterior to circular topography with $\gamma \rightarrow \infty$ and $\mathcal{J} \approx 9 \times 10^{-13}$. Shadings in (λ, ϕ) -space show the different families of trajectories with examples of each type of trajectory in (x, y) -space given by (i), (ii) and (iii) where the dotted box is enlarged.

both a well ($\gamma = 2$) and a deeper well ($\gamma = 7$) examined. The patches are initialized far from the circular topography such that initially, the effect of the ‘partial images’ is small. Furthermore, each patch is centred around a point vortex trajectory which has the energy and impulse of the trajectory which follows the separatrix in (λ, ϕ) -space. This choice is made so the most interesting patch trajectories can be observed.

In all computations the topography has unit radius and the initial separation of the pair is approximately 6.66 with each patch having area $\pi/2$. Each patch is discretized into 128 nodes around its boundary and is subjected to a loss of volume of $< 1\%$ unless stated otherwise.

7.3.1 Vortex patch pair evolving toward a seamount, $\gamma > 1$

Figure 7.5 shows three examples of the evolution of vortex patch trajectories with $\gamma = 1/2$, sketched in (x, y) -space and (λ, ϕ) -space where, an equivalent (in terms of its energy and impulse) point vortex pair is drawn for comparison in (λ, ϕ) -space only. Here and below, the three examples shown are initialized such that the pair has 1% less of the energy of a point vortex pair which passes through the separatrix, \mathcal{E}_s , precisely the energy of the separatrix and 1% more respectively.

As expected from chapter 4, the difference between the computed patch and an equivalent point vortex trajectories is small. In the example where the energy of the pair is less than \mathcal{E}_s , figure 7.5(a), the patches remain close to circular and do not touch the seamount, consequently, point vortex and vortex patch trajectories are virtually identical. The agreement is still excellent when the patches are initialized with energy equal to \mathcal{E}_s , figure 7.5(b). Here the patch closest to the seamount just touches the topography before translating away from the seamount. However, unlike its point vortex

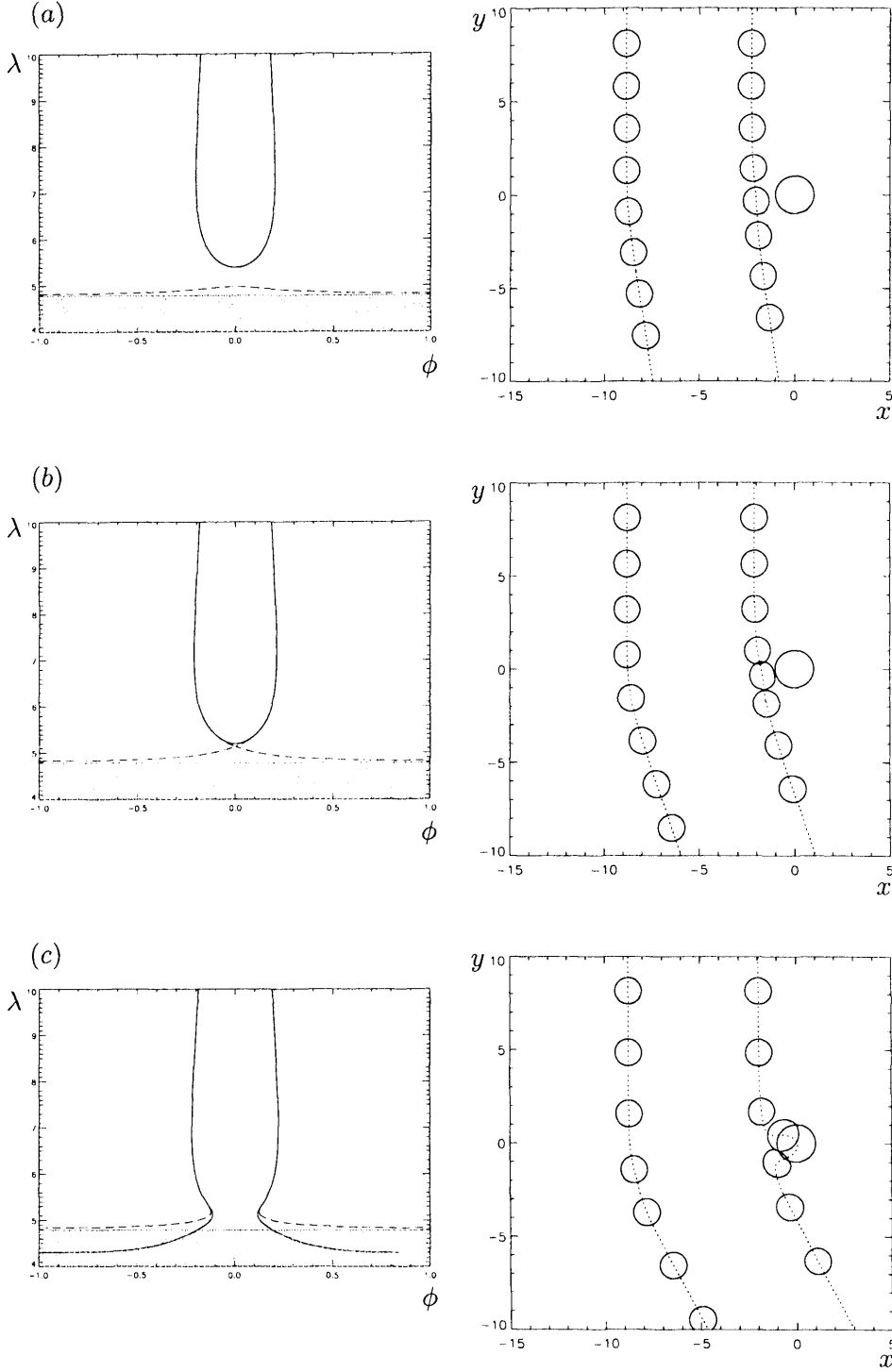


Figure 7.5: Vortex patch trajectories in (λ, ϕ) -space and (x, y) -space for a vortex pair (where here and subsequently, dotted lines show the path of each vortex centroid) approaching a seamount with $\gamma = 1/2$ for three different energy states: (a) less than \mathcal{E}_s , (b) equal to \mathcal{E}_s and (c) greater than \mathcal{E}_s . Trajectories in (λ, ϕ) -space are compared to equivalent point vortex pair (dashed lines, which are obscured by the solid line for the most part) and the region where $\lambda < \lambda_{min}$ is hatched.

equivalent, the pair does not bifurcate. When the patches are initialized with energy greater than \mathcal{E}_s , the comparison with a point vortex trajectory is less satisfactory since for this case one patch out of the pair straddles the seamount, allowing the trajectory to enter $\lambda < \lambda_{min}$.

Figure 7.6 shows three computed vortex patch trajectories with $\gamma = 0$ such that the topography is, in fact, an island. The first example, figure 7.6(a), shows when the patches are initialized with energy less than \mathcal{E}_s . In this case the resulting trajectory interacts only weakly with the island (therefore having its trajectory deflected only slightly) and the patches remain close to circular throughout its evolution and comparisons with trajectories for point vortex pairs is excellent. With energy equal to \mathcal{E}_s , the patches interact with the island more strongly, with the patch closest to the island slowing under the influence of its oppositely signed image. However, similar to the last case the pair does not bifurcate, but translates away from the island after being deflected from its original path. Lastly, figure 7.6(c) shows the case when the patches are initialized with energy greater than \mathcal{E}_s . Here the patches do bifurcate as they approach the island, with the vortex closer to the topography quickly orbiting the island before re-pairing with its partner shedding a small amount of vorticity as it does so.

7.3.2 Vortex patch pair evolving toward a well, $\gamma < 1$

As in section 7.3.2 three different energy states are examined, first when the patch pair are initialized with energy such that is it 1% less than \mathcal{E}_s – the energy of a point vortex pair whose trajectory passes through the separatrix. Second when the energy is equal to \mathcal{E}_s , and finally when the patch pair is initialized such that it has energy 1% more than \mathcal{E}_s .

Figure 7.7 shows the computed evolution of a vortex patch pair with

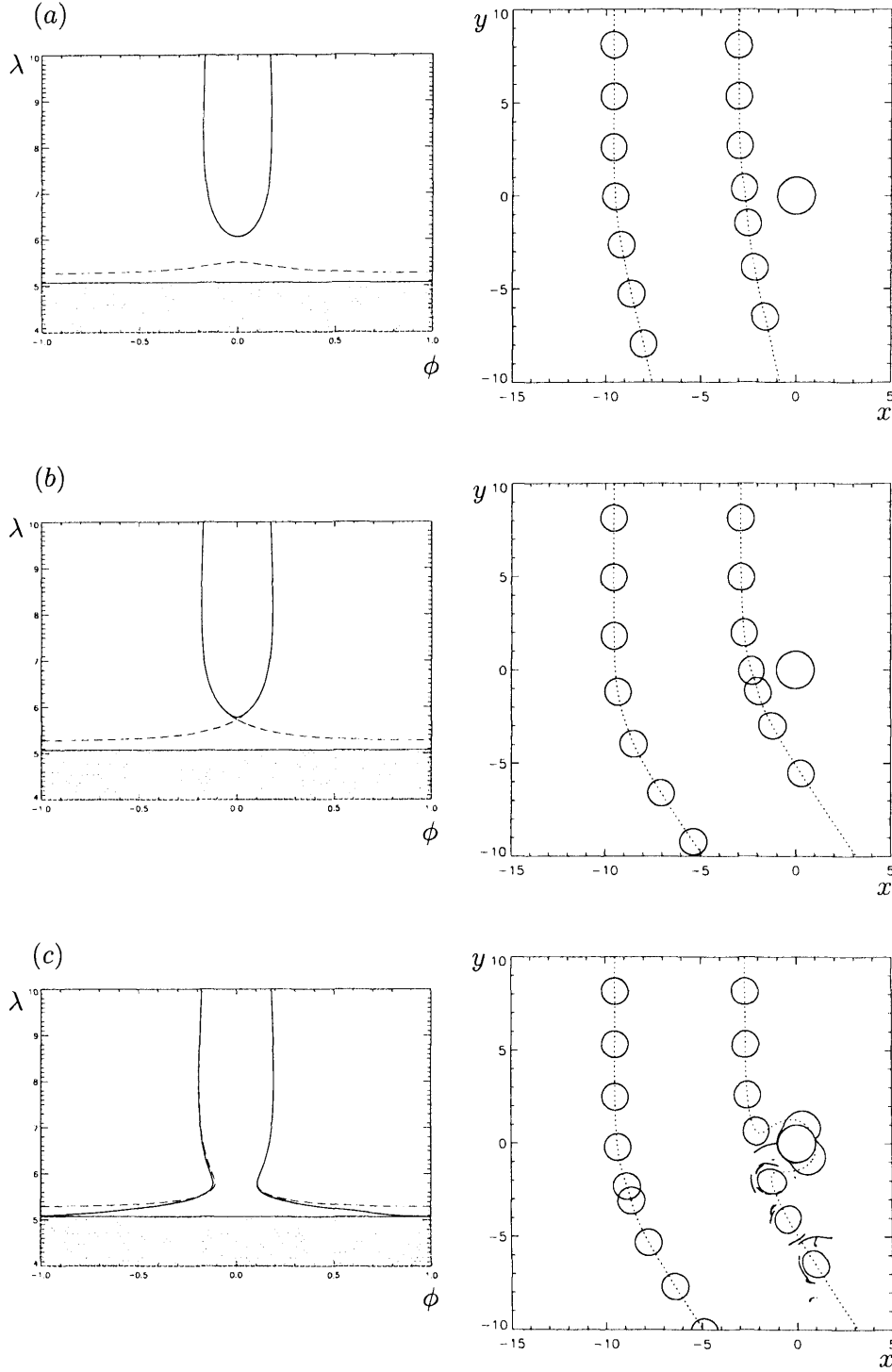


Figure 7.6: Vortex patch trajectories in (λ, ϕ) -space and (x, y) -space for a vortex pair approaching an island with $\gamma = 0$ for three different energy states: (a) less than \mathcal{E}_s , (b) equal to \mathcal{E}_s and (c) greater than \mathcal{E}_s . Trajectories in (λ, ϕ) -space are compared to an equivalent point vortex pair (dashed lines, obscured by the solid line for the most part) and the region where $\lambda < \lambda_{min}$ is hatched.

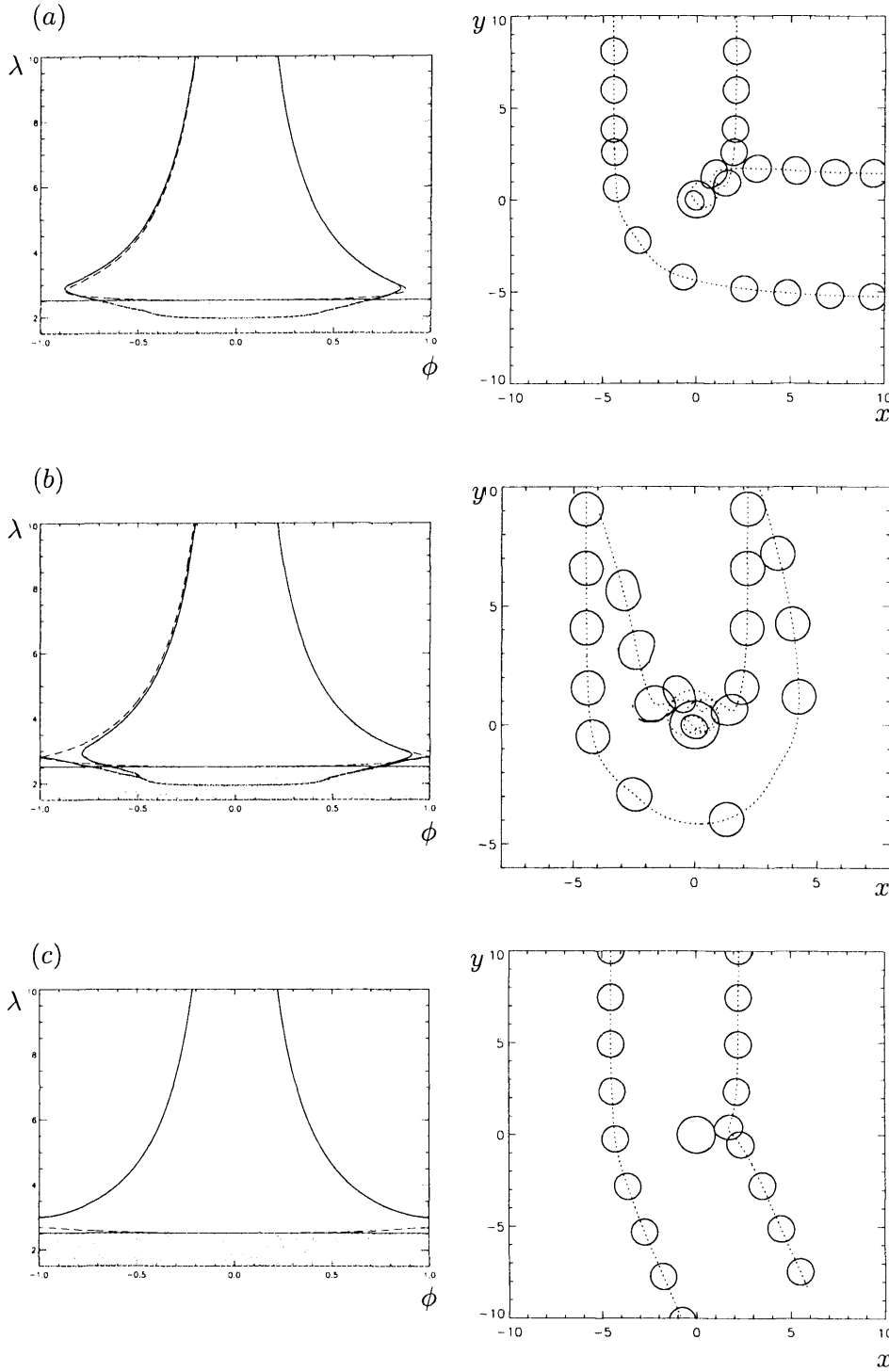


Figure 7.7: Vortex patch trajectories in (λ, ϕ) -space and (x, y) -space for a vortex pair approaching a well with $\gamma = 2$ for three different energy states: (a) less than \mathcal{E}_s , (b) equal to \mathcal{E}_s and (c) greater than \mathcal{E}_s . Trajectories in (λ, ϕ) -space are compared to equivalent point vortex pair (dashed lines, which are obscured by the solid line for the most part) and the region where $\lambda < \lambda_{min}$ is hatched.

$\gamma = 2$ such that the pair translates toward a well. The first example, figure 7.7(a), shows the motion of a patch pair with energy initialized such that it has energy less than \mathcal{E}_s . As the pair approaches the topography, each vortex is advected toward the well, soon after one vortex straddles the well and translates around the step before its partnering vortex advects the straddling vortex so that it exists wholly inside the well whereupon it subsequently translates about the well before leaving the well under the influence of its partnering vortex. This motion compares favourably to the equivalent point vortex motion apart from when the pair straddles the well where comparisons between the two can no longer be made. Figure 7.7(b) shows the trajectory of a vortex patch pair when the energy is equal to \mathcal{E}_s . Like the previous example, one vortex out of the pair straddles the well. However, on this occasion, the partnering vortex is allowed to almost translate around the well as the straddling vortex describes cycloid-like trajectories over the edge, shedding a small, but finite amount of vorticity as it does so. Eventually, the vortex breaks free of the topography (under the influence its partnering vortex) and translates away from the well. In the final example, figure 7.7(c), when the patches have energy greater than \mathcal{E}_s the patch and point vortex trajectories have excellent agreement. In this case one vortex just touches the well (before translating away), but does not straddle the topography.

Figures 7.8-7.10 shows vortex patch trajectories for a pair translating toward a deeper well with $\gamma = 7$. This choice is made as vortex patch motion with topography such that $\gamma \rightarrow \infty$ can not be computed effectively using contour surgery. Consider a pair translating toward topography with $\gamma \rightarrow \infty$. If the separation of the pair is sufficiently small, at least one vortex would straddle the well. However, to conserve mass this vortex would shrink to zero

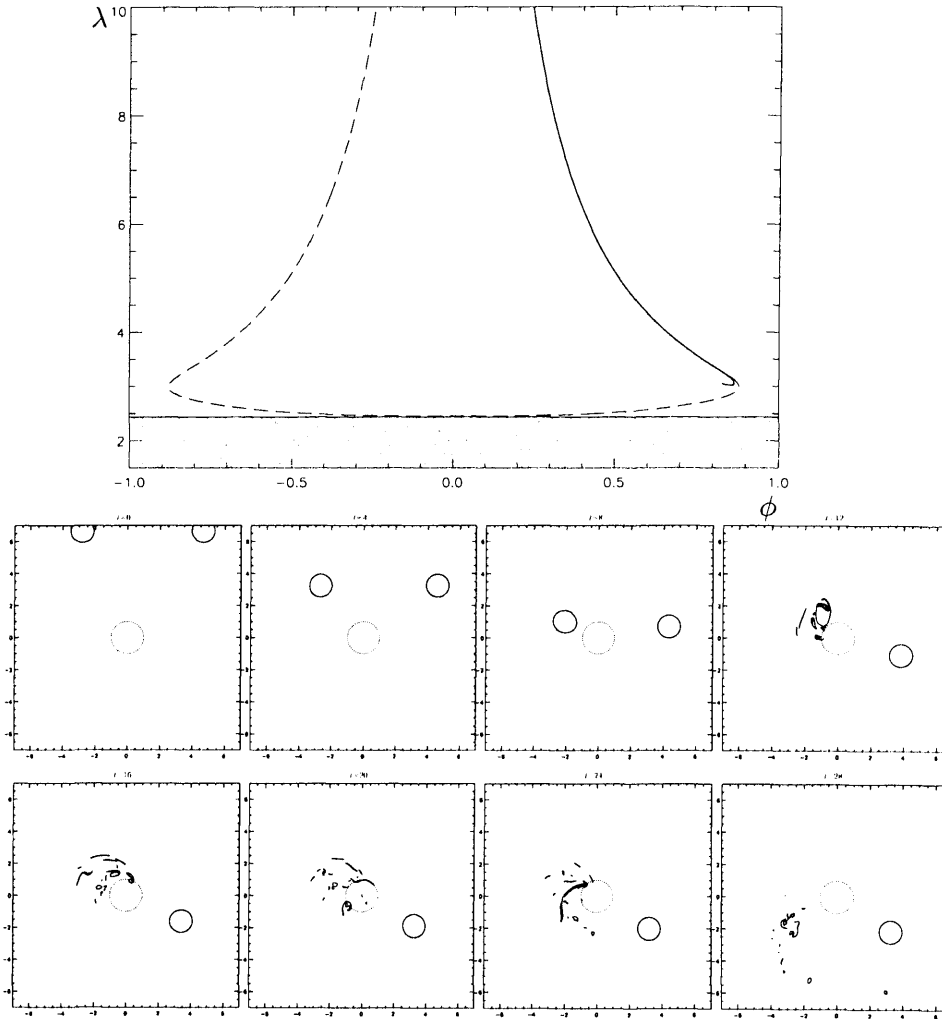


Figure 7.8: Vortex patch trajectories in (λ, ϕ) -space and (x, y) -space for a vortex pair approaching a well with $\gamma = 7$ having energy less than the that which follows the separatrix. Trajectories in (λ, ϕ) -space are compared to equivalent point vortex motion (with dashed lines) where each vortex remains coherent. With the onset of significant shedding comparisons can no longer be made. The region in $(\lambda - \phi)$ -space where $\lambda < \lambda_{min}$ is hatched.

size creating a vortex sheet. Using contour surgery this patch would become small enough for the algorithm to assume it has a minor dynamical effect and remove the patch using the surgery procedure. Despite this deficiency patches that do not straddle the well are still computed efficiently using

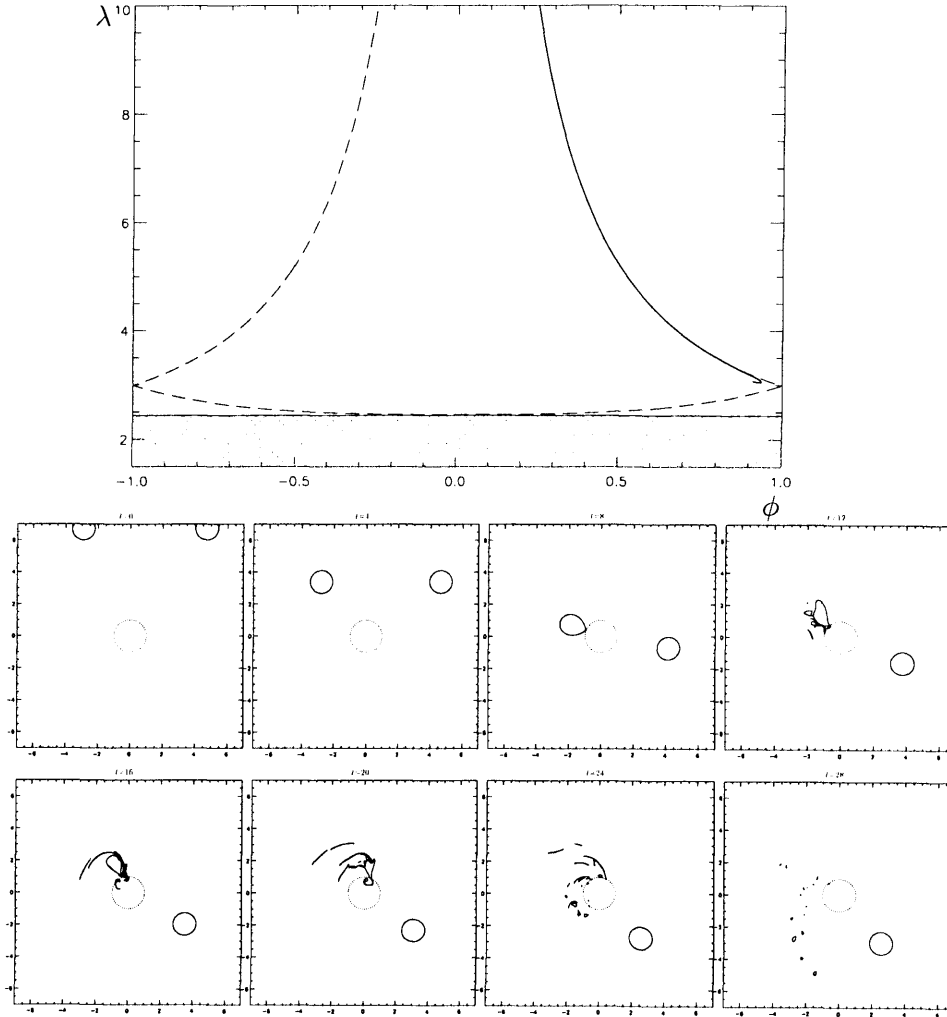


Figure 7.9: Vortex patch trajectories in (λ, ϕ) -space and (x, y) -space for a vortex pair approaching a well with $\gamma = 7$ having energy equal to that which follows the separatrix. Trajectories in (λ, ϕ) -space are compared to equivalent point vortex motion (with dashed lines) where each vortex remains coherent. With the onset of significant shedding comparisons can no longer be made. The region in $(\lambda - \phi)$ -space where $\lambda < \lambda_{min}$ is hatched.

contour surgery. Hence a well with $\gamma = 7$ is chosen to allow a straddling vortex to have finite area inside the well.

Figure 7.8 shows a distant vortex pair translating toward the deep well having energy less than \mathcal{E}_s . As the pair approaches the deep well each vortex

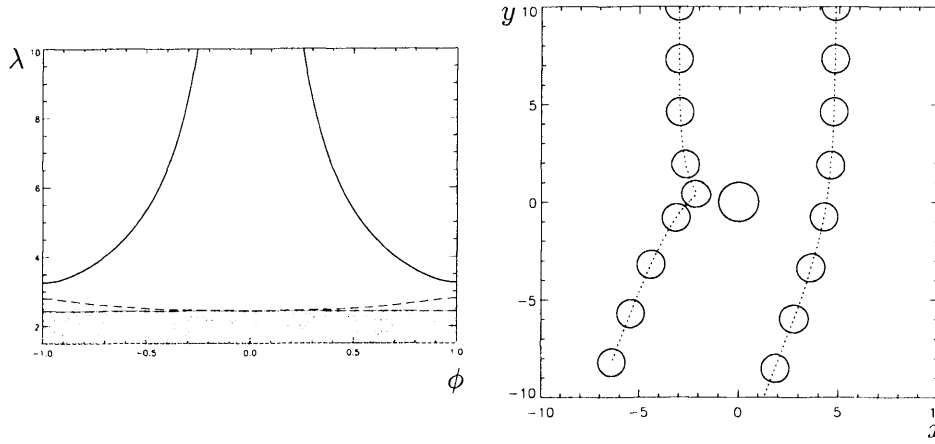


Figure 7.10: Vortex patch trajectories in (λ, ϕ) -space and (x, y) -space for a vortex pair approaching a well with $\gamma = 7$ having energy greater than that which follows the separatrix. Trajectories in (λ, ϕ) -space are compared to an equivalent energy point vortex pair (dashed lines) and the region where $\lambda < \lambda_{min}$ is hatched.

is advected toward the topography by the images. Soon after, one vortex approaches and eventually straddles the well, and due to the large contrast in depth this straddling vortex sheds vorticity. Vortex shedding continues as the patch translates around the edge of the well until the vortex can no longer be considered coherent. The other, more distant vortex, then orbits the well at a (reasonably) fixed distance from the centre of the well deviating slightly due to the effect of the small filaments. Figure 7.9 shows a vortex patch pair translating toward the well with energy equal to \mathcal{E}_s . The trajectories for this configuration are similar to the previous case. Approaching the well, one vortex comprising the pair straddles the well and sheds significant vorticity such that the vortex quickly becomes incoherent. The more distant vortex then translates about the well at an almost fixed distance from the centre, deviating slightly due to the effects from the small filaments. Figure 7.10 shows the vortex patch trajectories of a pair translating toward the well with energy greater than \mathcal{E}_s . In this example the pair is sufficiently far apart so

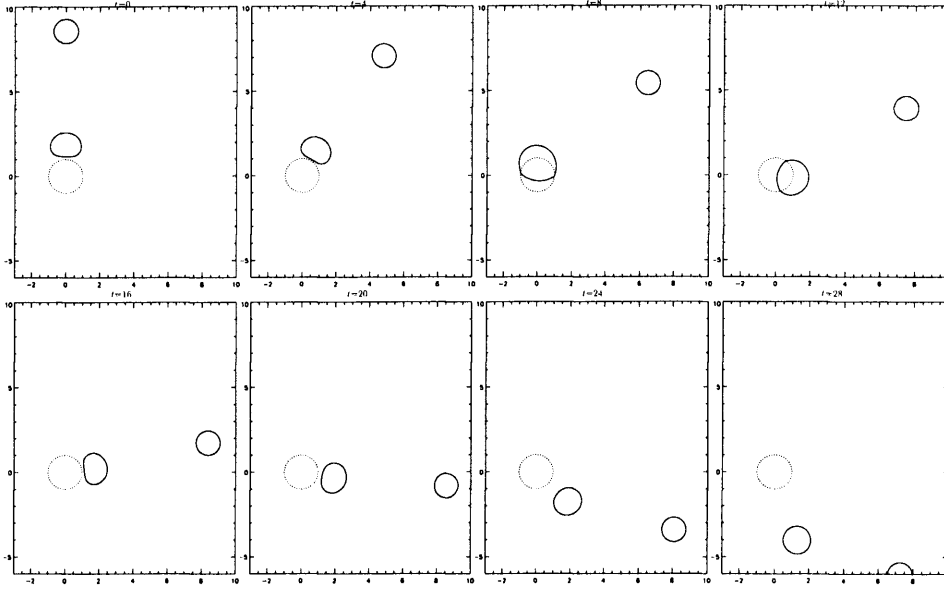


Figure 7.11: A two-vortex patch equilibrium state and its subsequent evolution near a seamount with $\gamma = 1/5$.

that neither vortex straddles the well. Consequently, there is no significant shedding and the pair translates away from the well with excellent agreement to point vortex trajectories.

7.4 Two-Vortex Patch Equilibrium States

Section 7.2 noted a special configuration of a point vortex pair corresponding to a stationary point in (λ, ϕ) -space. These points represent a point vortex pair orbiting the topography with identical angular speed for $\gamma > 1$, and a fixed pair for $\gamma < 1$. Motivated by these results for point vortices, in this section analogous states are computed for vortex patch pairs. The numerical method is the same as described for finding two-vortex patch equilibrium states for rectilinear topography (chapter 4, section 4.5), modified to account for the circular topography (Appendix G).

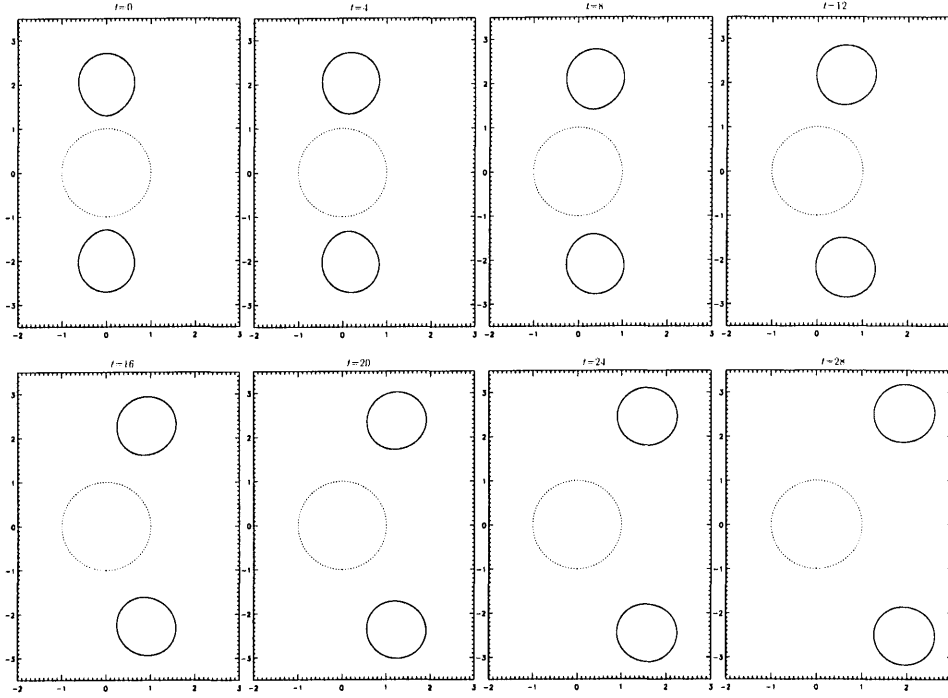


Figure 7.12: A two-vortex patch equilibrium state and its subsequent evolution near a well with $\gamma = 3$.

Figure 7.11 shows a two-vortex equilibrium state (first frame) with $\gamma = 1/5$ and the subsequent frames show the evolution of this configuration. As described by section 7.2, two-vortex equilibrium states exist (for a pair near circular topography at least) at hyperbolic points. Therefore it is not surprising that after being initialized as in figure 7.11, the pair breaks from its steady orbit and the pair eventually translates away from the topography. Figure 7.12 shows another two-vortex patch equilibrium state with $\gamma = 3$. As before, the evolution of the subsequent pair is shown. The pair is held stationary for less than half a rotation period by the topography. Therefore, the pair eventually translates away from the well, albeit at a much slower speed (i.e. more than 6 times slower) than if the topography were absent.

Figure 7.13 gives an example of a two-vortex patch equilibrium state

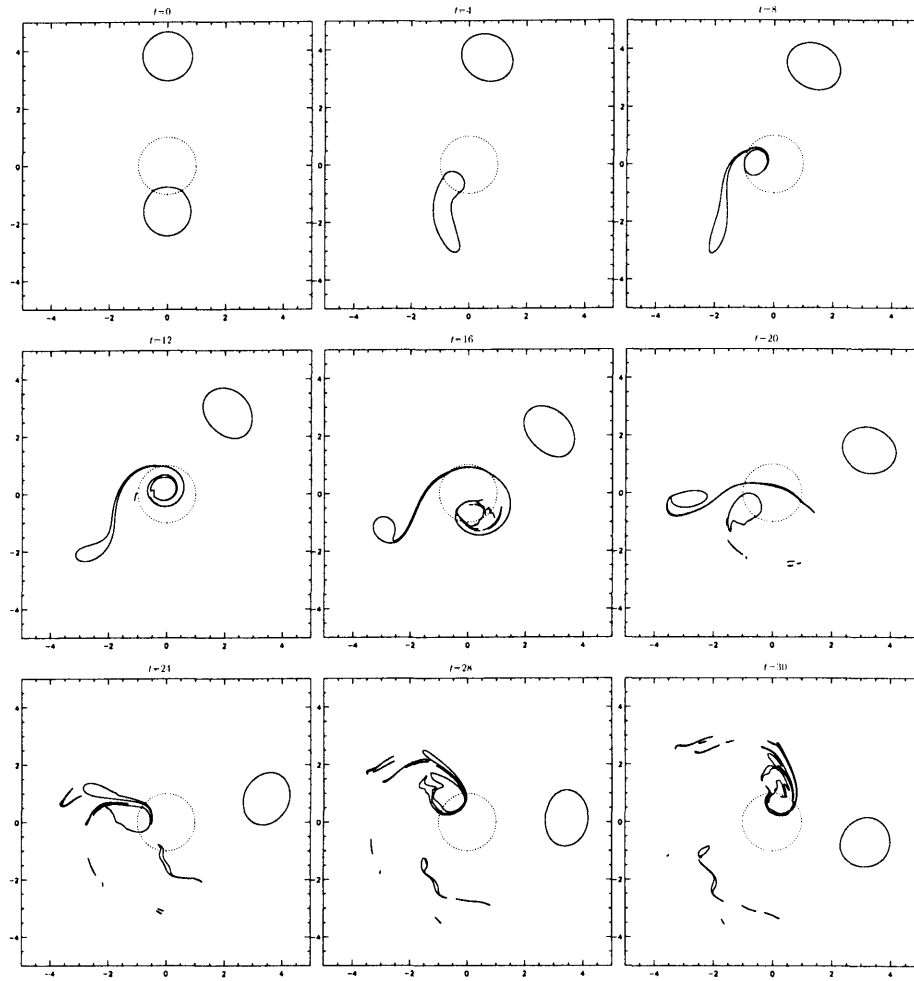


Figure 7.13: A two-vortex patch equilibrium state and its subsequent evolution near a well with $\gamma = 2$.

with for $\gamma = 2$ where both patches straddle the topography. Similar to the equilibrium states for rectilinear topography where a patch straddles the topography, this state for circular topography is extremely unstable. It very quickly breaks from its steady state and orbits the topography with one vortex shedding significantly.

7.5 Conclusions

The behaviour of a point vortex pair exterior to finite height circular topography has been found including the limiting cases of surfacing piercing topography (an island) and a deep well. The trajectories of point vortex pairs was derived explicitly from an appropriately derived Hamiltonian. For the topographic cases of $\gamma > 1$ and $\gamma < 1$ point vortex trajectories which approach the topography can be divided into four distinct categories: first when an a pair passes the topography such that the vortices pass on same side of the topography, second when the pair splits as it approaches the topography and passes on opposite sides, third when the pair is found trapped by the topography with each vortex in the pair having different frequency of rotation, and finally when each vortex in the pair is in a steady configuration such that for $\gamma > 1$ each vortex comprising the pair orbits with identical frequency, or each vortex is held stationary by the topography for $\gamma < 1$.

Vortex patch trajectories were computed using contour dynamics and comparisons were made with point vortex trajectories with examples given when $\gamma > 1$ and $\gamma < 1$. Provided the patches remained close to circular during their evolution, vortex patch trajectories compared extremely well to point vortex trajectories. Comparisons were less accurate when a patch straddled the topography. For the case where $\gamma \gtrsim 1$ it was observed that straddling patches could take to cycloid-like trajectories directly over the topography before departing locality of the well. Whereas, for $\gamma \gg 1$ it was observed that provided the vortices were sufficiently close to the deep well, vortex patch pairs could be trapped by the topography thereby changing from one class of trajectory to another. Finally, two-vortex patch equilibrium states were computed with examples given for an initially steady rotating pair near a seamount, a pair initially held stationary by a well and

a straddling pair near a well. Equilibrium states were found to be unstable (such points begin located at hyperbolic points in (λ, ϕ) -space), with the straddling equilibrium state found to be particularly unstable.

Chapter 8

Laboratory Experiments on Dipolar Vortices Colliding with Step Topography

Two-dimensional dipolar vortices in stratified shallow water have been studied extensively in laboratory experiments (see for example Flór & van Heijst, 1994; van Heijst & Flór, 1989*a*; Voropaev & Afanas'ev, 1992; Flór, van Heijst & Delfos, 1995). In these studies, vorticity is generated by disturbing an initially stationary fluid with a turbulent impulse (usually in the form of a horizontal jet) which is forced by a density stratification to collapse into quasi-two dimensional flows where a vortex dipole emerges. This phenomena, where larger structures form from smaller structures, is a characteristic feature of two-dimensional flows (see for example McWilliams, 1984) and is in contrast to three dimensional flows where turbulent flows cascade toward smaller and smaller scales (a cigarette plume for example). Velasco & van Heijst (1994) investigated the behaviour of dipolar vortices with background rotation on a topographic β plane with good agreement with theoretical pre-

dictions. Vortices were generated by towing a hollow cylinder through the tank and pulling it out of the fluid while maintaining its vertical axis. Dipolar vortex structures have also been generated in a thin layer of mercury by Nguyen Duc & Sommeria (1988) where turbulence was generated by a non-uniform magnetic field and by Couder & Basdevant (1986) where a soap film supported two dimensional vortex pairs.

There has been less attention given to the dynamics of dipolar structures in a non-rotating homogeneous fluid. In the absence of topography, Sous *et al.* (2005) describe dipolar vortices in a non-rotating, homogeneous, shallow water layer formed using a horizontal turbulent jet. The two-dimensional nature of the flow was found to depend on a dimensionless parameter $C = \sqrt{Q}t/H^2$ (where Q is the injected momentum flux, t is the injection duration and H is the fluid depth) known as the confinement number. For $C < 1$, the flow was typically three dimensional in nature, however for $C > 3$ (such that the fluid has small thickness), the initially turbulent flow collapses into two-dimensional eddy structures and a vortex dipole emerges.

Barker & Crow (1977) generated dipolar vortices by forcing fluid through a channel whose ends taper into a slit. Centurioni (2002) exploited this technique to investigate the dynamics of a vortex dipole propagating at normal incidence toward a planar sloping beach inclined at a constant angle to the horizontal. Vortices were observed to separate as they entered shallower water, eventually translating (almost) parallel to the shoreline in opposite directions. Observed vortex trajectories were compared to inviscid vortex ring trajectories with good agreement provided the vortices are initialized close to the topography and the Reynolds number, $Re > 1500$. In this study, unlike Centurioni (2002) dipoles at oblique incidence are considered, as are

both of cases of dipoles approaching the topography from shallow and deep water.

Johnson & McDonald (2004) examined the behaviour of a vortex pair impinging a rectilinear step change in depth at normal incidence. Upon collision with the step the pair's separation changed, increasing when crossing from deep into shallow water and decreasing when crossing from shallow into deeper water. This behaviour could be described in terms of the vortices interacting with 'partial images', owing to the presence of the step, which advected each vortex as the pair approached the escarpment. Chapter 5 considered the more general case of a vortex pair incident to an escarpment at oblique incidence. It was shown that a pair crossing from deep into shallow water always crossed the step and translated in shallow water with an angle refracted toward the normal of the step. Pairs approaching the step from shallow water would either cross the step and translate in deeper water at an angle refracted away from the normal, or, interestingly, not cross the step into deeper water, but instead be reflected at the escarpment and continue to translate in shallow water.

In this chapter, an experimental study of vortex dipoles interacting with topography is described to illustrate these theoretical predictions. Vortex pairs will be generated in a non-rotating homogeneous fluid and allowed to propagate (by mutual self-advection) toward an escarpment and interact with the step.

Section 8.1 describes the experimental setup and section 8.2 gives qualitative descriptions of experiments giving examples of experiments crossing from deep and shallow water. In section 8.3 experimental results are described quantitatively and are compared to those from inviscid predictions from previous chapters. Finally 8.4 presents conclusions.

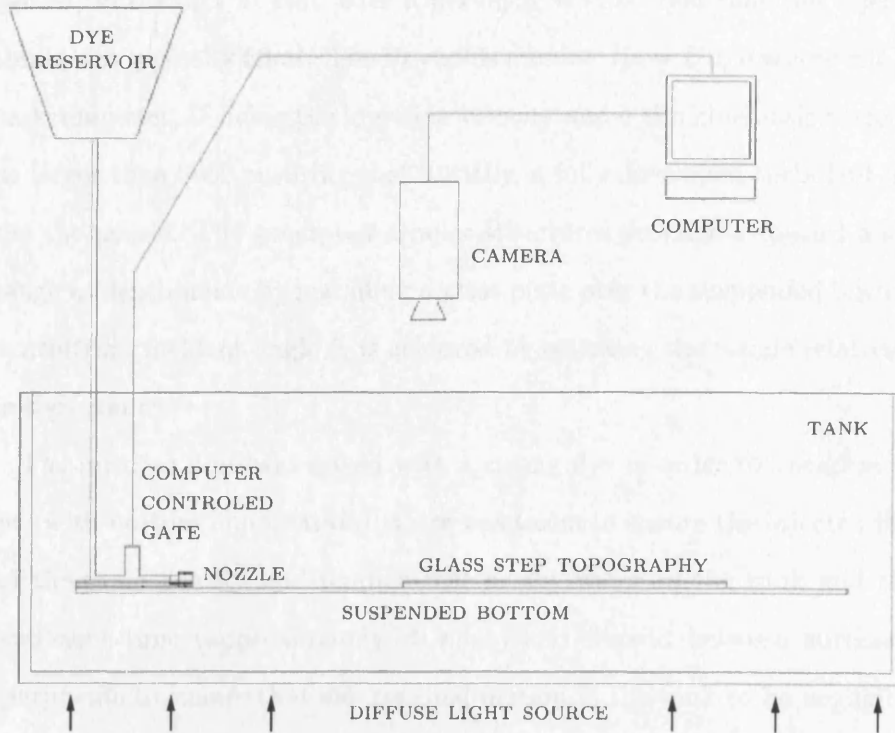


Figure 8.1: The experimental testing tank.

8.1 Apparatus and experimental arrangement

The following experiments were performed in a perspex tank having dimensions $1.5 \times 1.0 \times 0.5m$ (see figure 8.1). The vortical flows were confined to move over a suspended rigid glass plate (with dimensions $1.31 \times 0.81m$) to assure a constant depth throughout the flow (note, perspex is not used since it is known to buckle). The tank was filled with water of constant density to a working depth (above the glass plate) of $20 - 30mm$ which is sufficiently shallow to generate two-dimensional vortical structures. Vorticity was generated using an isolated turbulent jet as described by Sous *et al.* (2005). A computer controlled gate controlled the delivery of fluid at a constant pressure. The nozzle diameter ($1mm$) was directed at half depth. The fluid was

injected, into water at rest, over a period $t_i = 0.9s$ such that the injected volume was typically $50ml$. The Reynolds number $Re = Ud/\nu$ where d is the nozzle diameter, U being the injection velocity and ν the kinematic viscosity was larger than 5000 ensuring that initially, a fully developed turbulent flow exits the nozzle. The generated dipolar structures propagate toward a step change in depth made by installing a glass plate over the suspended bottom. An arbitrary incident angle θ_i is achieved by orienting the nozzle relative to the topography.

The injected fluid was mixed with a strong dye in order to visualize the flow (with bottom illumination). Care was taken to ensure the injected fluid had the same density and temperature as the water in the tank and that a sufficient time (approximately 20 mins) had elapsed between successive experiments to ensure that any residual motion in the tank to be negligible. The evolution of the flow was captured at a rate of $15Hz$ using a camera mounted above the tank with each image corrected for barrel distortion using Adobe Photoshop. Quantitative measurements of velocity and vorticity were made using the MATPIV software package (J. K. Sveen, University of Oslo). Experiments are divided by the choice of depth ratio $\gamma = H^-/H^+$, into two sections. First, a dipole approaches the step from deep water, $\gamma < 1$, and, second, a dipole approaches from shallow water, $\gamma > 1$. For each topographic case three different depth ratios are examined where for each depth ratio four different incident nozzle angles (relative to the normal of the topography) were tested, $\theta_i = 0, \pi/8, \pi/4, 3\pi/4$. The following results illustrate the observed general flow features.

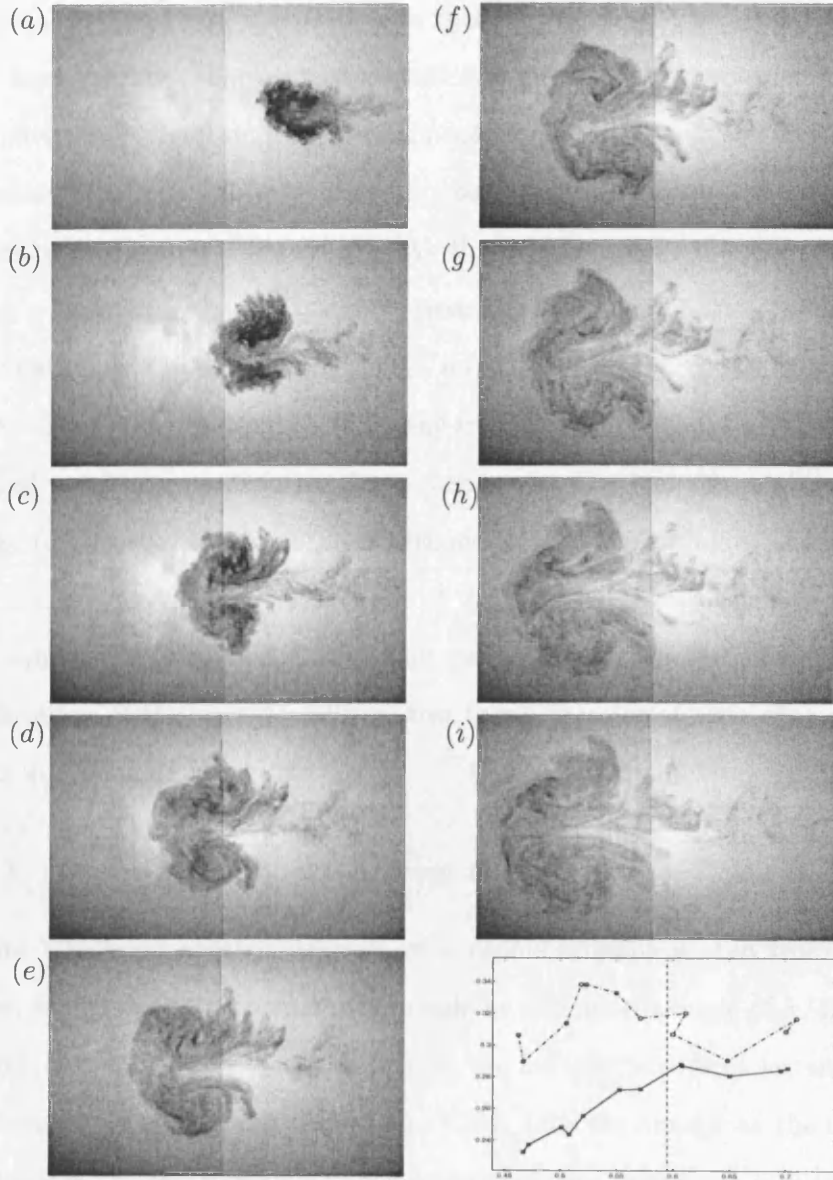


Figure 8.2: Snapshots taken at regular intervals of $1.87s$ for a dipole approaching a step at normal incidence with $\gamma = 4/5$ from relatively deep water. The last figure shows the computed trajectories of the vortex centroids with the points shown here (and below) taken at $1.33s$ intervals. The dashed line indicates the location of the step.

8.2 Qualitative observations

Figure 8.2 shows the evolution of a dipole at normal incidence to a step with depth ratio $\gamma = 4/5$. Frames are taken at $1.87s$ intervals. Initially (figure

8.2a) the injected flow is essentially a three-dimensional turbulent jet. The flow then quickly collapses into a quasi two-dimensional dipolar structure. By mutual self advection the eddies approach the step where their separation increases from the influence of the oppositely signed images owing to the presence of the step (figure 8.2b). As the dipole crosses the step (figures 8.2c-f), the area of the each patch increases by mass conservation (a detailed explanation of the topographic effect on the size of the dipole follows in 8.3.1). Then, the dipole translates away from the step with (approximately) normal incidence, as expected from chapter 5. The last figure shows the computed trajectories (from the experimental data) for each vortex centroid comprising the dipole. The position of the dipole (shown by either circles and squares) is computed at 1.33s intervals with the dashed line showing the location of the step. Details on how these trajectories were obtained is given in Appendix K.

8.2.1 Dipoles approaching from deep water: $\gamma < 1$

Figure 8.3 shows another example of a dipole crossing a step from deep water, with $\gamma = 7/10$, but with the nozzle at an incident angle of $\pi/4$. Figure 8.3(a) shows a dipole emerging from the initially turbulent jet and the pair propagate toward the step (figure 8.3b). Like previously, as the dipole approaches the escarpment its separation increases under the influence of the oppositely signed images in the step (figures 8.3c-d). The dipole then straddles and eventually crosses the step such that the dipole exists wholly in shallow water with a larger area as a consequence of mass conservation (figures 8.3d-i). Furthermore, since the dipole crosses from deep water at oblique incidence it is expected (from Chapter 5) that the dipole be refracted toward the normal. Using techniques described in Appendix K the

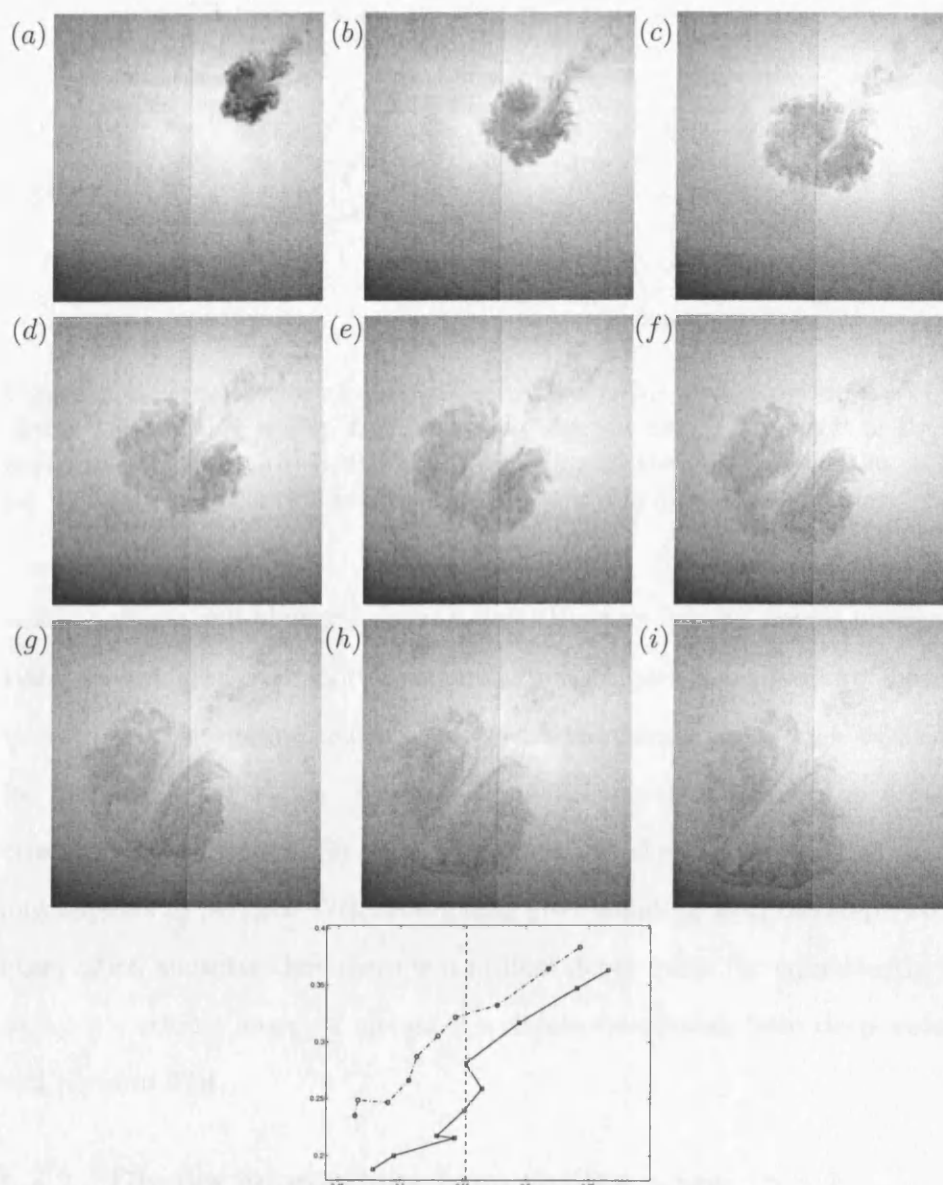


Figure 8.3: Snapshots taken at regular intervals of 1.87s for a dipole approaching a step with $\gamma = 7/10$ from relatively deep water at an angle of $\pi/4$ normal to the step.

dipole refracts through an angle of 0.178 which is within 4.36% of the angle predicted by (5.8).

The inviscid theory of chapter 5 predicts that approaching from deep

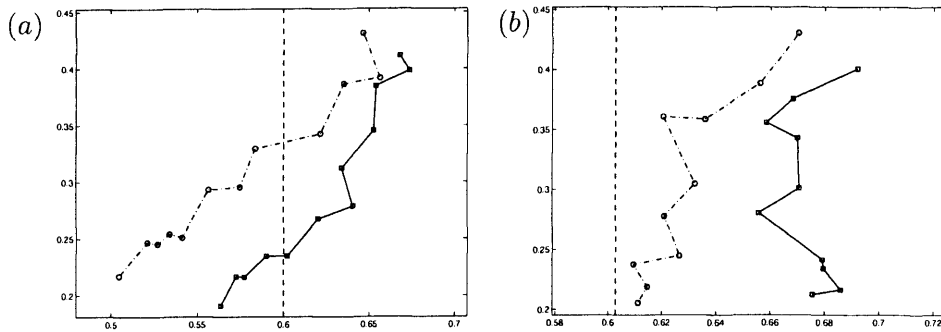


Figure 8.4: Trajectories of the vortex centroids for two experiments of a dipole approaching a step from relatively deep water at an angle of $3\pi/8$ normal to the step. (a) depth ratio $\gamma = 4/5$ and the pair crosses the step, (b) $\gamma = 7/10$ and the dipole does not cross and remains in deep water.

water a dipole will always cross the step. However, experimental observations do not always support this prediction. Figure 8.4 gives two dipole trajectories propagating toward a step with the nozzle at an angle of $3\pi/8$ for different depth ratios: figure 8.4(a) with $\gamma = 7/10$ where the dipole crosses the step, and 8.4(b) with $\gamma = 4/5$ where the dipole does not cross and appears to perform TIR, rebounding after colliding with the step. This observation suggests that there is a critical depth ratio (or equivalently if fixing γ a critical angle) if increased a dipole translating from deep water will perform TIR.

8.2.2 Dipoles approaching from shallow water: $\gamma > 1$

Figure 8.5 shows an example of a dipole initially translating in shallow water at an angle of $\pi/4$ toward a step with $\gamma = 6/5$, such that its separation decreases as it approaches the step. Away from the step, in shallow water, figure 8.5(a) shows the dipole emerge from the initial turbulence. Then, as the dipole approaches the step its separation decreases under the influence of topographic images of the same-sign circulation (figures 8.5b-c) such that its

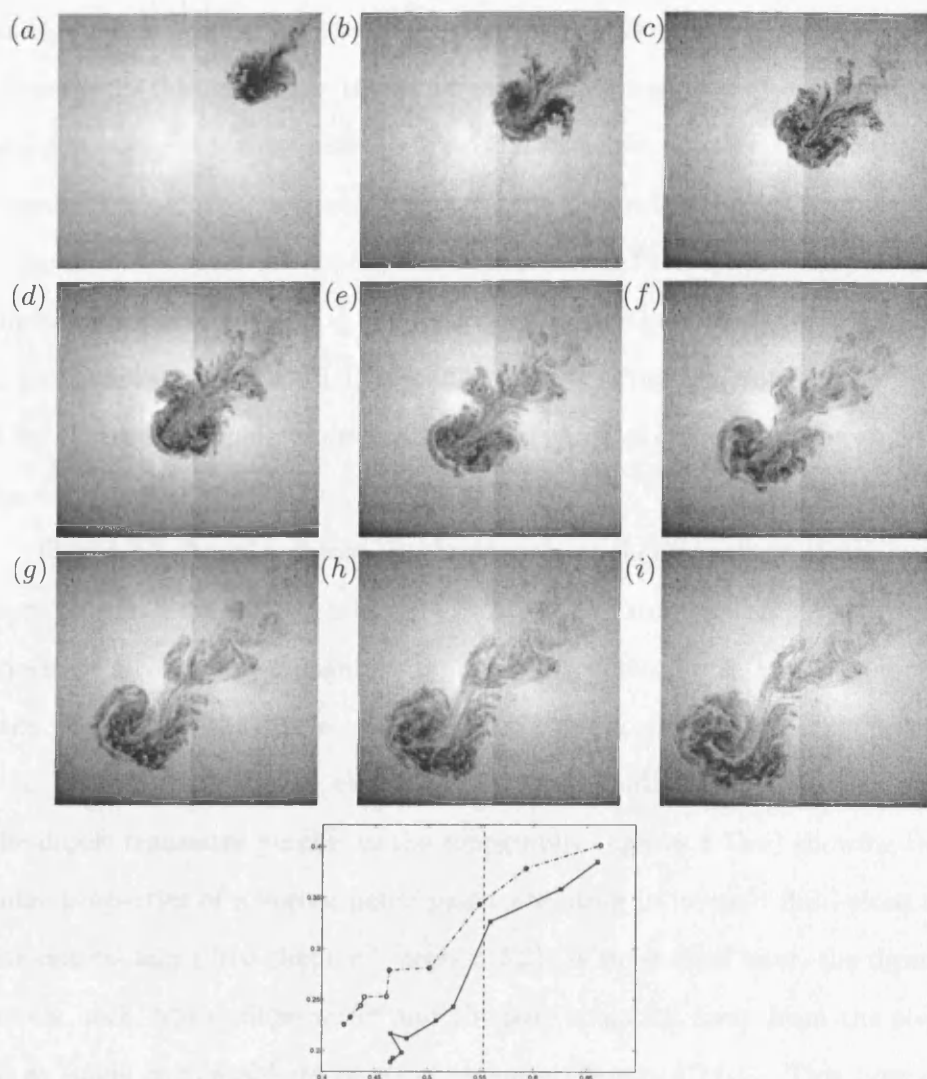


Figure 8.5: Snapshots taken at regular intervals of 1.47s for a dipole approaching a step with $\gamma = 6/5$ from relatively shallow water at an incident angle of $\pi/4$ normal to the step.

speed increases and it moves over the step relatively quickly (figures 8.5d-g). The dipole refracts away from the normal (figures 8.5h-i) through an angle of 0.427 which is an overestimate of the predicted refracted angle by 35.4%.

Figure 8.6 shows a dipole initially translating in shallow water toward a step with $\gamma = 3/2$ and at an angle of $\pi/4$. Similar to the previous example,

as the dipole approaches the step its separation decreases (figures 8.6*a-b*). However in this case, due to the larger step change in depth, the dipole is forced closer together than the previous example. In fact, as the dipole crosses the step each vortex comprising the dipole interferes destructively (figures 8.6*c-i*) and the dipole loses coherency. This is an example of a dipole approaching a step in the debris region (chapter 5 section 5.2). The critical depth ratio from (5.4) is found (from experimental data) to be $\gamma_d = 1.25$. Therefore, dipoles approaching the step in this configuration would be expected to lose coherency.

Figure 8.7 shows a dipole approaching from shallow water at $3\pi/8$ toward a step with depth ratio $\gamma = 3/2$. Away from the step the dipole moves at a constant propagation angle. Then, as the dipole approaches the step, the dipole does not cross, but instead performs total internal reflection, TIR. First, the patch closest to the step straddles the escarpment and the dipole translates parallel to the topography (figures 8.7*b-e*) showing the same properties of a vortex patch pair translating in inviscid fluid close to the critical angle (see chapter 5, section 5.2). A short time later, the dipole moves back into shallow water and the pair translate away from the step at an angle comparable to its incident angle (figures 8.7*f-i*). This type of trajectory (TIR) is to be expected since the critical angle for this configuration (calculated from (5.10)) is 1.16 compared to actual incident angle 1.33. Furthermore, with the incident angle being close to the critical angle the observation of the dipole straddling the escarpment is also expected (see figure 5.7).

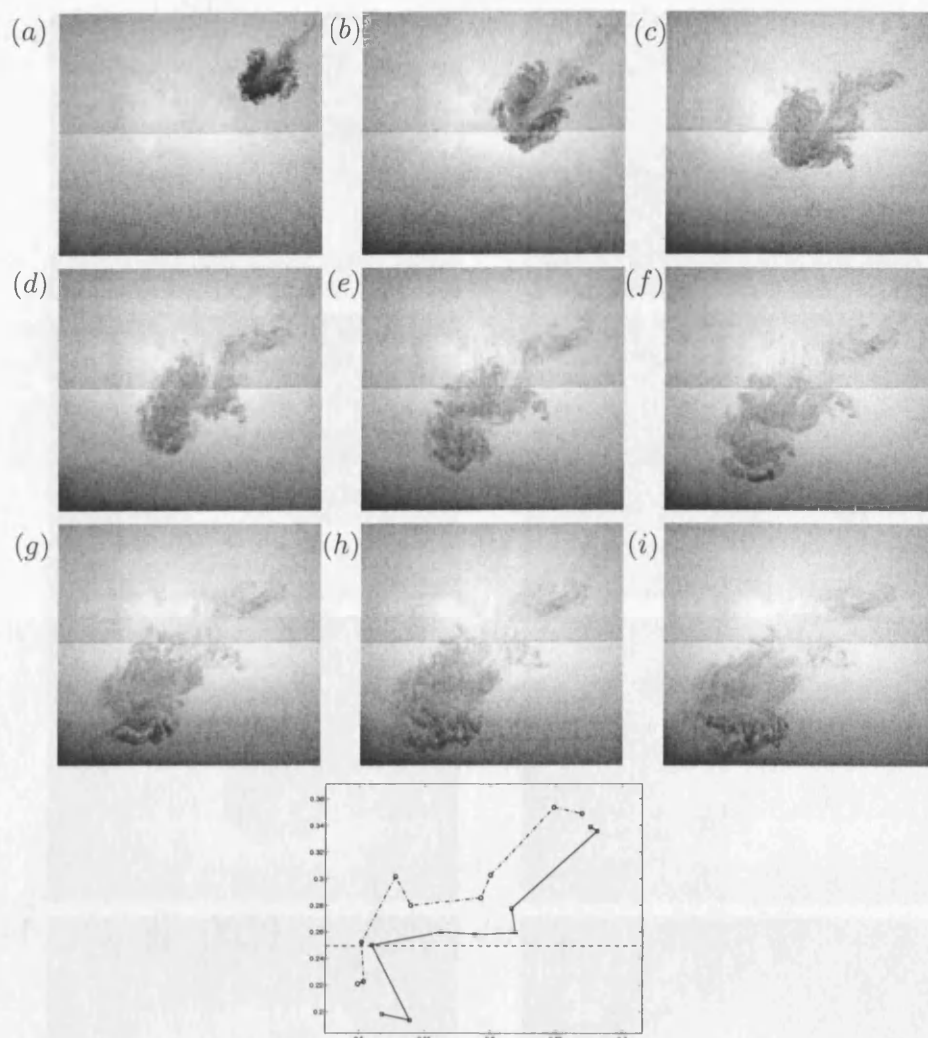


Figure 8.6: Snapshots taken at regular intervals of $2.27s$ for a dipole approaching a step with $\gamma = 3/2$ from relatively shallow water at an incident angle of $\pi/4$ normal to the step.

8.3 Quantitative results

8.3.1 Two-dimensional vortex entrainment

It has been observed experimentally that the area of a dipole increases with time by capturing anomalous fluid as it evolves, irrespective of topographic effects. This phenomenon, known as entrainment, is a common feature of

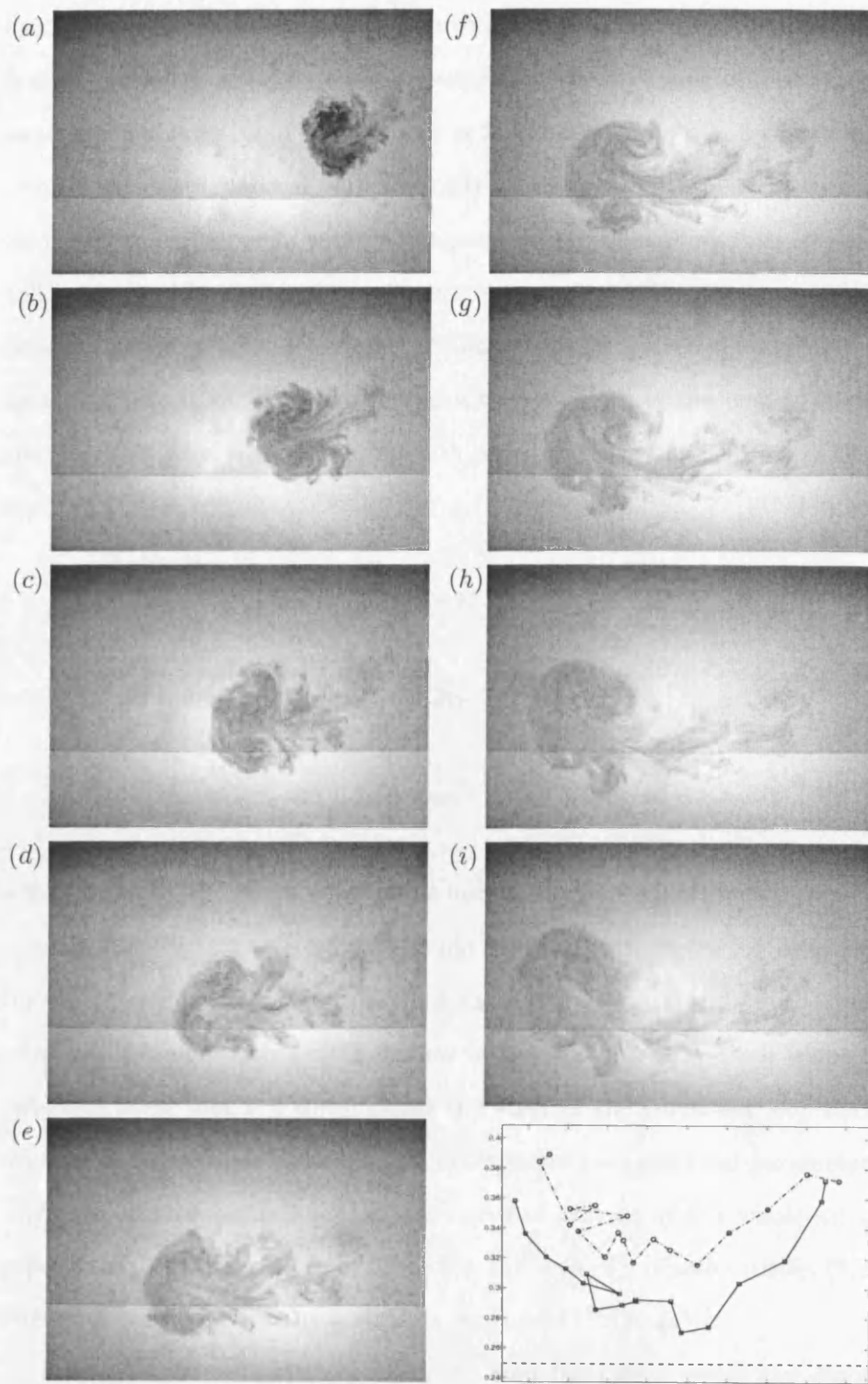


Figure 8.7: Snapshots taken at regular intervals of 2.93s for a dipole approaching a step with $\gamma = 7/10$ from relatively shallow water at an incident angle of $3\pi/8$ normal to the step where the dipole performs TIR.

fluid flows. The seminal paper by Morton, Taylor & Turner (1956) was the first to develop a theory on entrainment on a vertically rising plume. It was assumed that the rate of entrainment of fluid at any height is proportional to a characteristic vertical plume velocity at that height. Their theory was compared to experiments with good agreement. Here, a similar assumption will be applied to circular, two-dimensional vortices. First assume a rigid lid and consider a two-dimensional circular vortex with area \mathcal{A} and over flat bottom topography. The angular velocity $u_\theta = \frac{1}{2}\omega r$ is the characteristic velocity associated with the vortex with constant vorticity ω . But $\omega \sim \Gamma/\mathcal{A}$ and $r \sim \sqrt{\mathcal{A}/\pi}$, therefore

$$\frac{d\mathcal{A}}{dt} = \mathcal{K}u_\theta = \mathcal{K}\frac{\Gamma}{\sqrt{\pi}}\mathcal{A}^{-\frac{1}{2}}, \quad (8.1)$$

where \mathcal{K} is a constant of proportionality. It follows that,

$$\mathcal{A} = \kappa t^{2/3}, \quad (8.2)$$

where $\kappa = (\frac{3\mathcal{K}\Gamma}{4\sqrt{\pi}})^{2/3}$. Figure 8.8 shows how the area of experimental dipoles varies with time to the power two-thirds for two cases: figure 8.8(a), when the dipole approaches a step from deep water with $\gamma = 1/2$ and figure 8.8(b) when a dipole approaches from shallow water with $\gamma = 3/2$. Each frame is initialised such that $t = 0$ represents the start of the turbulent jet. Each coloured line describes an individual experiment with identical parameters where the dotted black line gives the curve of best fit of the whole set of experiments. As observed from figure 8.8, the area of a dipole satisfies (8.2) since each plot is essentially a straight line up to $t^{2/3} \approx 4s^{2/3}$.

It is expected that after crossing the step from deep water the dipole should increase its area by mass conservation (as well as entrainment) as

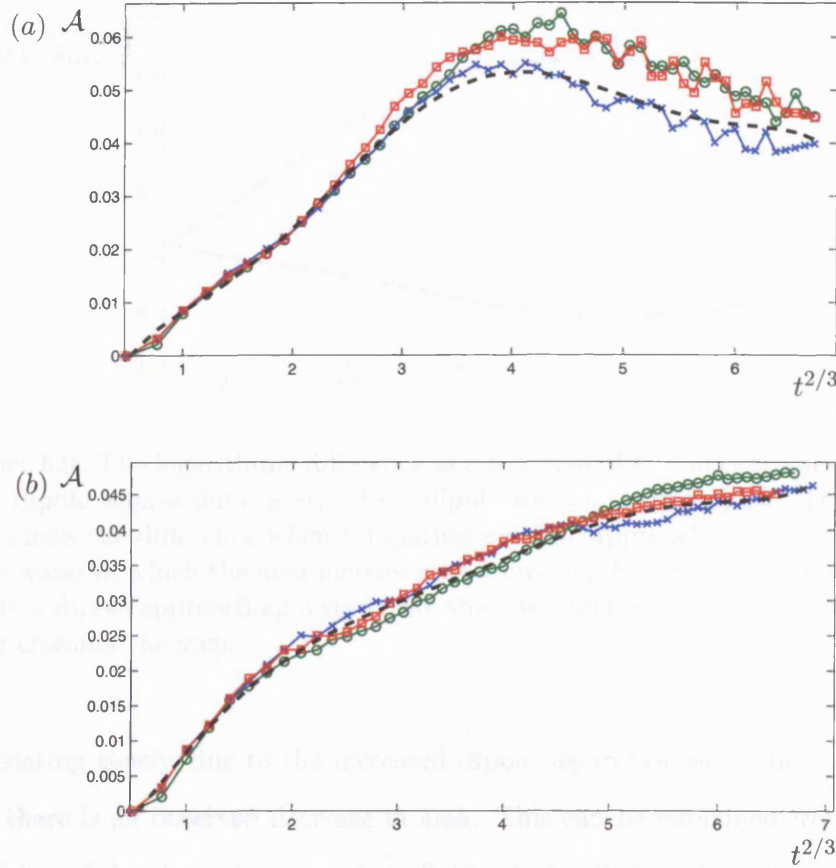


Figure 8.8: The area of the whole dipole as a function of $t^{2/3}$ ($s^{2/3}$) for a dipole approaching a step at normal incidence with (a) $\gamma = 1/2$ and the dipole approaches from deep water and (b) $\gamma = 3/2$ where a dipole approaches from shallow water. Each coloured line represents an experiment with an identical configuration with the black dashed line showing the curve which represents the whole set of experiments.

it translates in shallow water. Figure 8.8(a) gives strong evidence for this behaviour. For $t^{2/3} = 0 - 2s^{2/3}$ the region is characterized by the turbulent jet settling into a dipole structure entirely located in deep water. Then, between $t^{2/3} = 2 - 3s^{2/3}$, the dipole crosses the step from deep into shallow water, and there is a notable increase in the gradient of the line, indicating a sharp increase in dipole area. Then at $t^{2/3} = 4 - 6s^{2/3}$ the dipole is now

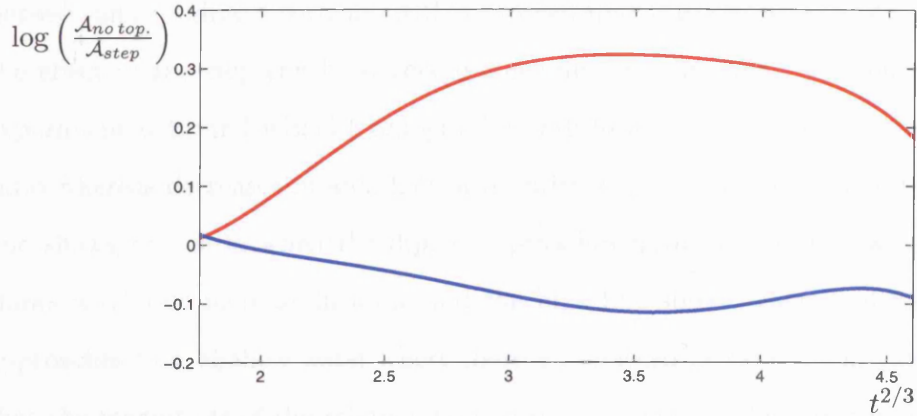


Figure 8.9: The logarithmic difference as a function of $t^{2/3}$ between the area of a dipole approaching a step to a dipole without topography. The red line shows the difference when comparing a dipole approaching a step from deep water in which the area increases after crossing the step. The blue line shows a dipole approaching a step from shallow water and its area decreases after crossing the step.

translating slowly, due to the increased dipole separation in shallow water and there is an observed decrease in area. This can be explained from the diffusion of dye into the anomalous fluid. A detailed explanation of this phenomenon is given in Appendix K.

Figure 8.8(b) shows how the area of a dipole varies with time $t^{2/3}$ when a dipole crosses a step from shallow water with $\gamma = 3/2$. It is expected that the dipole will have a smaller area after crossing the step. Similar to the previous case, the region $t^{2/3} = 0 - 2s^{2/3}$ is characterized by the creation of the dipole, this time wholly located in shallow water. Then at $t^{2/3} \approx 2^{2/3}$ the dipole crosses the step into deep water, with an accompanying decrease in the rate of increase of area. The area of the dipole then continues to increase at a constant rate as the dipole translates in deeper water.

Figure 8.9 compares the above examples to the area of a dipole which translates without variable topography. By taking the logarithm of the ratio

between an experiment with and without topography (i.e. $\log(\mathcal{A}_{no\ top.}/\mathcal{A}_{step})$) the effect of the step can be observed since increases in area (between an experiment with and without topography) will have a positive logarithmic ratio whereas decreases in area have a negative logarithmic ratio. The red line shows this ratio when the dipole approaches from deep water, which shows a relative increase in area, and the blue line shows where a dipole approaches from shallow water where there is a marked decrease area. Note that the magnitude of the relative difference is not symmetrical, this is because the depth ratio for the deep to shallow water experiment ($\gamma = 1/2$) is not the reciprocal of the shallow to deep experiment ($\gamma = 3/2$). Also note that the effect of the topography is always present not just when the dipole crosses the step. This is due to the partial images owing to the step which are able to influence the dipole at a distance.

8.3.2 Vorticity decay

Unlike the inviscid theory of the previous chapters the experimentally generated dipoles are subjected to viscous effects and entrainment. Figure 8.10 shows the vorticity of both positive vorticity patch, drawn with a red line, and the negative vorticity patch, the magnitude of which is drawn with a blue line, as functions of time for two experiments: (a) for figure 8.2 i.e. a dipole approaching from deep water with normal incidence and $\gamma = 4/5$, and (b) for figure 8.7 i.e. a dipole approaching from shallow water with incident angle $3\pi/8$ and $\gamma = 7/10$. Details on how the vorticity of the dipole was computed are given in Appendix K. Figure 8.10(a) shows that initially away from the step in deep water the dipole's vorticity decays with time. However, at around 6s into its evolution, when the dipole crosses the escarpment, there is a sudden increase in the rate at which vorticity is

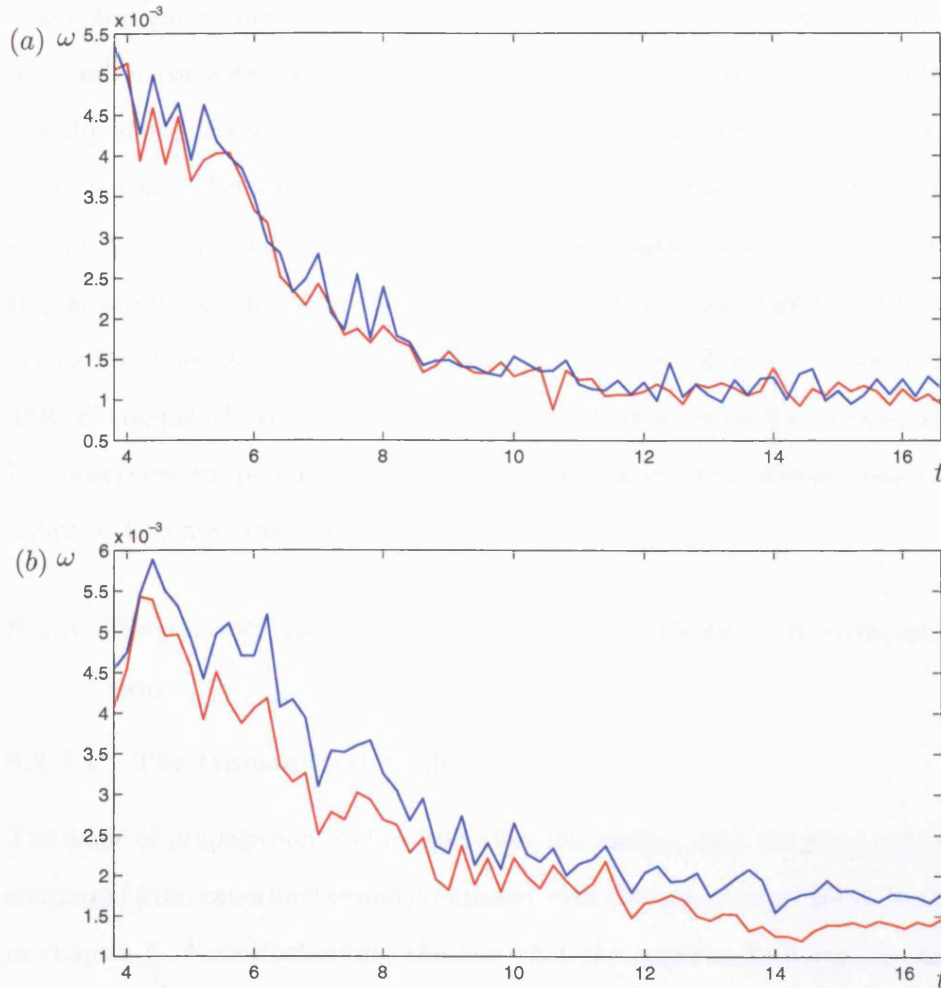


Figure 8.10: The vorticity of a patch as a function of time for two experiments: (a) same as figure 8.2 i.e. a dipole approaching from deep water with normal incidence and $\gamma = 4/5$. (b) same as figure 8.7 i.e. a dipole approaching from shallow water with incident angle $3\pi/8$ and $\gamma = 7/10$. The red line is the vorticity of the positively signed vortex, and the blue line is the magnitude of vorticity of the negatively signed vortex.

lost. This may be explained from the conservation of potential vorticity: when the dipole crosses into a smaller depth, its vorticity decreases so that ω/H remains constant. As the dipole continues to translate away from the step its vorticity continues to decrease at an exponential rate owing to vis-

cosity and entrainment (where an increase in vortex patch area leads to a decrease in vorticity owing to the circulation conservation). Figure 8.10(b) initially shows the dipole emerging from the turbulent jet with the vorticity increasing. Then as the dipole translates toward the step, its vorticity decays due to viscous effects. The dipole then starts to interact with the step at around 6s. In doing so, as shown in figure 8.7, the negatively signed vortex straddles the escarpment (unlike the positive vortex) as it performs TIR. Consequently this straddling (negative) vortex increases its vorticity by conserving its potential vorticity whereas the positive vortex does not (since it does not cross the step).

8.3.3 Experimental results and inviscid theory: a comparison

8.3.3.1 The transmitted angle

The angle of propagation (before and after interacting with the step) can be computed from experiments and compared with analytical expressions found in chapter 5. Notwithstanding the fact that the experimental vortices are different dynamically owing to (i) viscosity, (ii) entrainment and (iii) non-uniform vorticity. Following the trajectory of the dipole (for typically 5 computed centroid points) before colliding with the step, a mean incident angle can be computed using linear regression. Similarly, after the dipole has either crossed the step or performed TIR, another set of computed centroid points are used to find the mean transmitted angle. Theoretically, given an initial angle and the depth ratio, the transmitted angle can be computed using (5.8) and then compared with actual experimental results.

Figure 8.11 compares the experimentally computed transmitted angle with the exact expression found by (5.8). Comparisons are divided into the

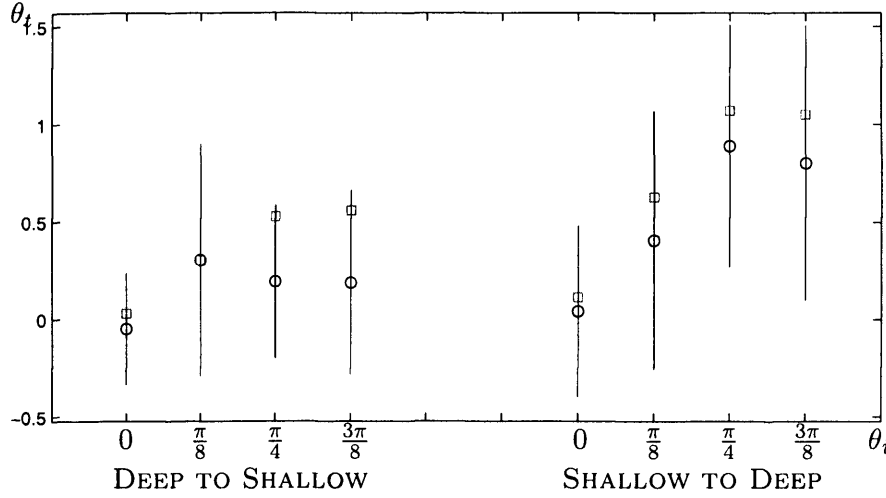


Figure 8.11: Transmitted angle computed from experiment. Experiments are divided according to whether a dipole approaches from deep water (on the left) or shallow water (on the right). Each topographic case is divided further by grouping experiments with the same incident angle taking values $\theta_i = 0, \pi/8, \pi/4, \pi/8$. Circles represent the theoretically predicted transmitted value for each data set with error bars drawn. Squares represent the theoretically predicted angle expected from (5.8).

two cases of a dipole approaching the step from deep water (on the left) and a dipole approaching from shallow water (on the right). Each topographic case is further divided by collating experiments with the same incident angles with each data set representing at least 7 experiments. Comparisons for dipoles approaching from deep water are good when the incident angle is small, and are less accurate when the nozzle angle increases where inviscid theory overestimates the actual transmitted angle. For dipoles approaching from shallow water, comparisons are still favourable and for small incident angles the comparison is good. However, for larger incident angles the variance of the data set is large and the comparison is less accurate. For some experiments this is a consequence of dipoles performing TIR when inviscid theory would predict the dipole to cross the step.

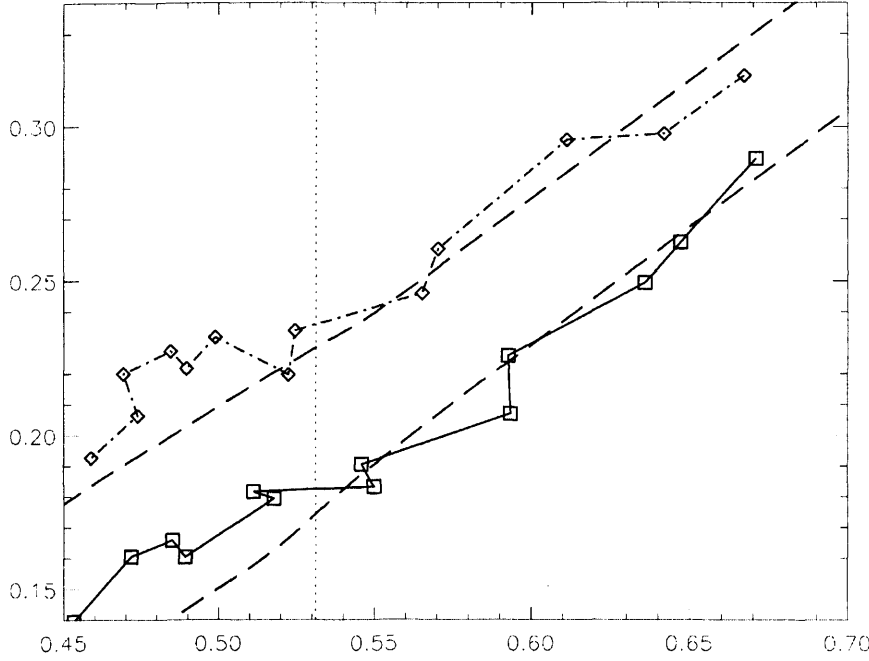


Figure 8.12: A comparison between experimental and a computed vortex patch trajectory found using contour dynamics (dashed line) for a pair approaching a step from deep water at an angle of 0.69 to a step with $\gamma = 4/5$.

8.3.3.2 Dipole Trajectories

Trajectories from two experiments are compared with equivalent (in terms of its incident angle and separation) vortex patch trajectories, computed using contour dynamics. Figure 8.12 shows the case of a dipole approaching a step with depth ratio $\gamma = 4/5$ at an angle (computed from the experimental trajectory using linear regression) of $\theta_i = 0.69$. Vortex patch trajectories are drawn with long dashed lines and are initialized away from the escarpment. The two sets of trajectories compare well: experimental trajectories are found to have increased separation after crossing the step and translate at an almost constant transmitted angle, although greater than predicted by inviscid theory. Figure 8.13 gives another comparison between a dipole that approaches a step with $\gamma = 6/5$ from shallow water at an angle $\theta_i = 0.95$.

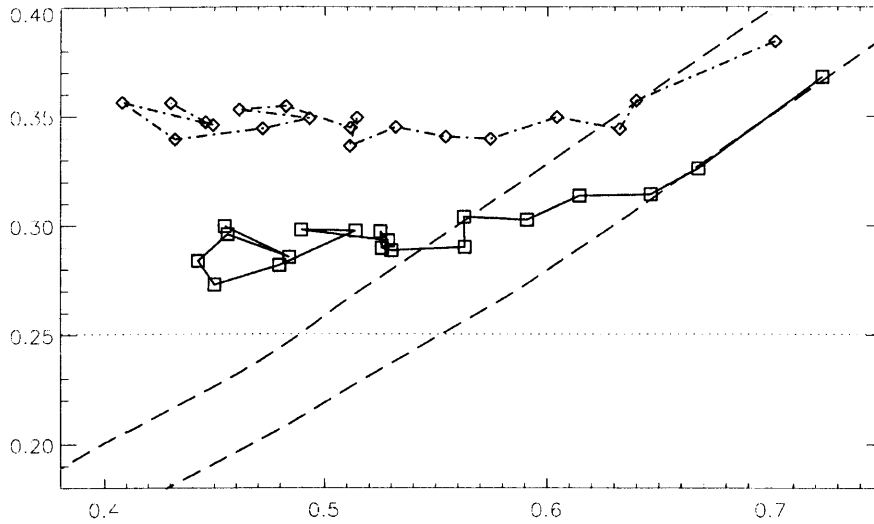


Figure 8.13: A comparison between experimental and a computed vortex patch trajectory found using contour dynamics (dashed line) for a pair approaching a step from shallow water at an angle of 0.95 to a step with $\gamma = 6/5$.

This example shows where a dipole would be expected, from inviscid theory, to cross the step where it will shed vorticity (not shown) since it lies in the debris region, but instead the dipole performs TIR.

8.4 Conclusions

Laboratory experiments for a two-dimensional dipole propagating toward a step change in depth in shallow water have been carried out. Experimental dipoles are considered: (i) approaching the step from deep water and (ii) approaching the step from shallow water. For each case, experiments were carried out for three different depth ratios and for each depth ratio four different incident angles were examined. Qualitative observations confirm theoretical predictions that the dipolar separation will increase when crossing from deep water and decrease for a dipole crossing from shallow

water. For obliquely incident dipoles it was observed that the transmitted angle (normal to the topography) increased as the dipole crossed from deep water and decreased when crossing from shallow water in accordance to the theory prescribed in chapter 5. Further, for dipoles approaching a step from shallow water with large incident angle total internal reflection was observed and in one example, a dipole translated parallel to the step for a significant time before crossing back into shallow water, again confirming theoretical predictions (see figure 5.7). However, there were some experiments which were contrary to theoretical predictions. For example, it was observed that a dipole approaching the step from deep water could perform total internal reflection, suggesting the existence of a critical depth ratio such that below this ratio, a dipole would be reflected at the escarpment and continue to translate in deep water. In fact, similar behaviour has been found for dipoles approaching a wall at normal incidence, from numerical computations by Orlandi (1990) and by laboratory experiments by van Heijst & Flór (1989*b*). In these studies, as a dipole approaches the wall an intense thin layer of vorticity is induced at the wall which rolls up to form secondary vorticity, which in turn, causes a dipole to rebound from the wall. While this behaviour is clearly a viscous effect it is unclear how dipoles would react approaching at oblique incidence or whether this phenomenon could be observed with finite height topography.

A measure of the rate of entrainment was found and it was predicted that the area of the whole dipole varied as a function of time to the power two-thirds which was supported by experimental observations. Next, the magnitude of the vorticity for each vortex comprising the dipole was computed from the experimental data. Observations of the relative vorticity increasing when crossing a step from shallow water and decreasing when

crossing from deep water were made, again in accordance to the theoretical predictions.

Direct comparisons with inviscid theory were made for the transmitted angle. There was reasonable agreement despite real fluid effects (viscosity, entrainment and non-uniform viscosity), improving when a dipole approached at small incident angles. However, in the main theoretical analysis over predicted the observed transmitted angle.

Trajectories were compared with vortex patch trajectories computed using contour dynamics. These agreed well for a dipole approaching a step from deep water, but was less favourable for dipoles crossing from shallow water, where dipoles which were predicted to cross the step did not, but instead performed TIR. This suggests that viscous effects allow dipoles to perform TIR more than would be expected from inviscid theory. This might be explained in a similar way to dipoles which rebound after approaching a step from deep water.

Chapter 9

Conclusions and Future Work

The dynamics of coastal vortices near piecewise flat topography has been studied using analytical, numerical and experimental methods.

The presentation of this research has been divided according to the choice of topography: chapters 3, 4, 5, 8 considered an infinitely long step change in depth, whereas chapters 6 and 7 considered a circular step change in fluid depth. The principal effect of finite height topography is that vortices are subjected to partial, topographic images resulting from the boundary conditions. These images are virtual in the sense where they do not actually exist and no extra vorticity is required to account for the presence of the step and are termed ‘partial’ since they have smaller magnitude than that of the real vortex. However, by describing vortex motion in terms of image vorticity, otherwise complex interactions can be simply explained. For a step change in depth, the effect of the topography can take two forms: first, when a vortex is located in relatively deep water, the partial image is of opposite-sign; second when the vortex is located in relatively shallow water, the partial im-

age takes the same-sign as the vortex. In this case the topography has been called an ‘anti-wall’ by Johnson & McDonald (2004). A consequence of the partial image effect is that a monopolar vortex will not remain stationary in the presence of a step, but will translate in the same direction regardless of being in deep or shallow water and in a direction parallel to the topography.

The difference from being in relatively deep or shallow water is perhaps most striking when monopolar vortex patches (computed using contour dynamics) are near to piecewise flat topography. When wholly contained in deep water, the patch is subjected to an image of opposite-sign flattening the patch along its edge closest to the step, with a shape similar to one half of an equal and oppositely signed vortex pair (Wu *et al.*, 1984; Saffman & Tanveer, 1982; Pierrehumbert, 1980). For patches in shallow water, the image is of the same-sign as the patch which draws vorticity closer to the step. The resultant shape being similar to one of two vortices having the same-sign circulation (Dritschel, 1995). These steadily translating, without deformation in shape, monopolar patches of vorticity called V-states were computed for rectilinear topography in chapter 3 and circular topography in chapter 6.

Previous studies have demonstrated that in coastal regions vortex structures are ubiquitous and are frequently found to interact with each other (see, for example Peregrine, 1998; Bühler & Jacobson, 2001; Özkan-Haller & Kirby, 1999). Motivated by these observations chapter 4 examined the general two vortex-vortex interaction problem near rectilinear step topography. By considering point vortices, trajectories were obtained explicitly in terms of the Hamiltonian and the conserved quantities of circulation, impulse and energy. Trajectories could be classified into distinct families, including, interestingly, steadily translating two vortex equilibrium states (i.e. V-states).

These states could be found in relative distance space at either hyperbolic points or at centres. Analogous equilibrium states for two vortex patches were computed and were found to be robust configurations when located at equivalent (in terms of their conserved quantities) point vortex equilibrium points at centres and unstable when situated at hyperbolic points of the Hamiltonian in parameter space.

Dipolar vortices (consisting of equal and opposite vorticity) are known to be generally more robust than their monopolar counterparts (Gorshkov *et al.*, 2000) and are likely to be important features of coastal regions. The scattering of vortex pairs was examined for rectilinear topography in chapter 5. By considering the motion of obliquely incident vortex patch pairs only, it was found that approaching a rectilinear step from deep water, pairs will always cross the step and translate in shallow water. In contrast, if approaching from shallow water a vortex pair will either cross the step and translate in deeper water or, instead, be reflected at the escarpment and continue to translate in shallow water at a propagation angle equal to the incident angle. This scattering phenomenon might be a significant feature of vortex pairs translating near sharp ledges (e.g. wide sand bars).

The scattering of vortex pairs by circular topography was studied in chapter 7. Trajectories of pairs were found to be significantly deflected from both seamounts (i.e. shallow islands which do not extend through the whole fluid depth) and wells (i.e. a circular depression). Similar to rectilinear topography, equilibrium states were found for both point vortices where exact trajectories could be found using Hamiltonian techniques and for vortex patches computed using contour dynamics. Equilibrium states for pairs near a seamount were found to translate steadily around the seamount along constant radial lines, however, pairs near a well were stationary, held motionless

by the topography.

Many of the theoretical predictions for vortex motion near rectilinear topography were verified by a series of laboratory experiments in chapter 8. In particular, vortex pairs were observed to perform TIR if approaching from shallow water and having a sufficiently large incident angle. The transmitted angle at which the dipole propagated from experimental data was compared with inviscid theory from chapter 5 with reasonable agreement. This suggests that the main dynamical features of shallow water vortices are captured by considering idealized vortices in shallow inviscid water.

Other, more realistic, choices of topography would yield even better understanding of the dynamics surf zone vortices. Typically surf zone regions have continuously varying depth and it is common to find beaches with submerged sand bars (occasionally separated by gaps) and it would be desirable to understand the dynamics of vortices near such topography. It is likely that numerical methods such as CASL (Dritschel & Ambaum, 1997) would be necessary to study such choices of topography. It would also be of interest to consider the weakly rotating problem such that $1 < Ro < \infty$, in contrast to the case $Ro = \infty$ considered here and the $Ro \ll 1$ which has been well studied theoretically and experimentally (see McDonald, 2000; Tenreiro, Zavala Sansón & van Heijst, 2006). The presence of rotation and variable topography inevitably gives rise to the possibility of waves (Rossby waves) and the coupled motion of waves and vortices presents a challenging mathematical problem. In addition, experimental results from chapter 8 suggest that viscous effects are significant for large times and require further investigation.

Appendix A

V-State Centres Of Vorticity And Propagation Speeds

Frame number (from left to right)	Depth ratio					
	$\gamma = 1/2$		$\gamma = 1/3$		$\gamma = 1/5$	
	y_c	U	y_c	U	y_c	U
1	2.16	0.0385	2.14	0.0583	2.11	0.0785
2	0.994	0.0805	0.934	0.125	0.864	0.172
3	0.611	0.109	0.619	0.158	0.609	0.206
4	0.403	0.119	0.460	0.169	0.501	0.214
5	0.278	0.122	0.361	0.172	0.431	0.217
6	0.0241	0.122	0.140	0.172	0.266	0.218
7	-0.404	0.110	-0.303	0.158	-0.112	0.205
8	-1.57	0.0550	-2.02	0.0651	-2.73	0.0649
9	-2.48	0.0338	-3.08	0.409	-4.03	0.0417

Table A.1: V-State Centres Of Vorticity And Propagation Speeds. Note here that in the calculations it was taken that $\omega = 1$ with $\gamma < 1$ so that deep water exists in the $y > 0$ half-plane.

Appendix B

Analytical Approximation to V-States near Rectilinear Topography

Consider, following Johnson (1978), a vortex patch in deep water with boundary $\partial\mathcal{V}$ and volume πH^+ so that the V-state has unit radius. Take the centre of the V-state to be $(x, y) = (0, y_c)$ so that the vortex is not straddling the step. An approximation to the shape of the V-state can be found by expanding in terms of ϵ where $\epsilon = y_c^{-1} \ll 1$. Let the boundary of the V-state to be $z = iy_c + R(\theta)e^{i\theta}$ where $R(\theta)$ is given by

$$R(\theta) = 1 + \epsilon^2 F_2(\theta) + \epsilon^3 F_3(\theta) + \mathcal{O}(\epsilon^4). \quad (\text{B.1})$$

The Green's function (3.10) consists of a vortex and an image contribution, giving an image and a vortex contribution to the expression for the stream-function on the boundary of the V-state. For the V-state to be steadily propagating these two terms must sum, with a term giving a uniform back-

ground flow, to a constant on $\partial\mathcal{V}$. The image contribution follows from integrating \bar{z} around $\partial\mathcal{V}$ as

$$\psi^{\mathcal{I}} = -\frac{\alpha Q H^+}{2\pi} \int_0^{2\pi} \int_0^{R(\theta')} \log |R(\theta)e^{i\theta} + iy_c - (r'e^{-i\theta'} - iy_c)| r' dr d\theta. \quad (\text{B.2})$$

Evaluating these integrals and taking the real part of the streamfunction including the uniform background flow, $\psi^{\mathcal{B}} = -\lambda(\epsilon)y$ (where $\lambda(\epsilon) = \epsilon\lambda_1 + \epsilon^2\lambda_2 + \epsilon^3\lambda_3 + \mathcal{O}(\epsilon^4)$) gives

$$\begin{aligned} \psi^{\mathcal{I}+\mathcal{B}} = & -\frac{\alpha Q H^+}{2} \left\{ \log |2y_c| + \frac{\epsilon \sin \theta}{2} + \frac{\epsilon^2 \cos 2\theta}{8} + \epsilon^3 \left[\frac{F_2 \sin \theta}{2} - \frac{\sin 3\theta}{24} \right] \right. \\ & + \int_0^{2\pi} [\epsilon^2 F_2(\theta') + \epsilon^3 F_3(\theta')] \log |2y_c| + 1/2\epsilon^3 (\sin \theta + \sin \theta') F_2(\theta') d\theta' \Big\} \\ & - \{ (\epsilon\lambda_1 + \epsilon^2\lambda_2 + \epsilon^3\lambda_3)(y_c + \sin \theta) + \epsilon^3(\lambda_1 F_1 \sin \theta) \} + \mathcal{O}(\epsilon^4). \quad (\text{B.3}) \end{aligned}$$

The vortex contribution to the streamfunction is

$$\psi^{\mathcal{V}} = -\frac{QH^+}{2\pi} \int_0^{2\pi} \int_0^{R(\theta')} \log |R(\theta)e^{i\theta} - r'e^{i\theta'}| r' dr' d\theta'. \quad (\text{B.4})$$

$$\begin{aligned} = & -\frac{QH^+}{4\pi} \left\{ 2\pi[\epsilon^2 F_2(\theta) + \epsilon^3 F_3(\theta)] + \right. \\ & \left. \int_0^{2\pi} [\epsilon^2 F_2(\theta') + \epsilon^3 F_3(\theta')] \log |2[1 - \cos(\theta - \theta')]| d\theta' \right\} + \mathcal{O}(\epsilon^4), \quad (\text{B.5}) \end{aligned}$$

Equating coefficients of ϵ in $\psi^{\mathcal{V}}$ and $\psi^{\mathcal{I}+\mathcal{B}}$ gives

$$\epsilon^1 : 0 = -\frac{\alpha Q H^+}{4} \sin \theta - \lambda_1 \sin \theta, \quad (\text{B.6})$$

$$\begin{aligned} \epsilon^2 : & -\frac{QH^+}{2} F_2(\theta) - \frac{QH^+}{4\pi} \int_0^{2\pi} F_2(\theta') \log |2[1 - \cos(\theta - \theta')]| d\theta' \\ & = -\frac{\alpha Q H^+}{16} \cos 2\theta - \lambda_2 \sin \theta, \quad (\text{B.7}) \end{aligned}$$

$$\begin{aligned} \epsilon^3 : & -\frac{QH^+}{2} F_3(\theta) - \frac{QH^+}{4\pi} \int_0^{2\pi} F_3(\theta') \log |2[1 - \cos(\theta - \theta')]| d\theta' \\ & = -(\lambda_1 F_1 + \lambda_3) \sin \theta - \frac{\alpha Q H^+}{4} F_2(\theta) \sin \theta + \frac{\alpha Q H^+}{48} \sin 3\theta. \quad (\text{B.8}) \end{aligned}$$

These integral equations have exact solutions of form $F_2 = A_2 \cos 2\theta$ and $F_3 = A_3 \sin 3\theta$, for constants A_2 and A_3 , yielding the boundary expansion (3.16) with background flow $\lambda(\epsilon) = -(1/4)\epsilon\alpha QH^+$

If the V-state is on the shallow side the radius $R(\theta)$ follows by replacing α by $-\alpha$, scaling by $\gamma^{-1/2}$ to conserve volume, and the background field follows by replacing H^+ with H^- so

$$R(\theta) = \gamma^{-1/2} \left(1 - \frac{\epsilon^2 \alpha}{4} \cos 2\theta + \frac{\epsilon^3 \alpha}{16} \sin 3\theta \right), \quad (\text{B.9})$$

$$\lambda(\epsilon) = -\frac{\epsilon\alpha QH^-}{4}. \quad (\text{B.10})$$

Appendix C

Straddling V-State Model

This section presents a model that gives a smooth transition from a touching V-state in deep water, through the range of straddling V-states to a touching V-state in shallow water. The straddling V-state is modelled, as shown in figure C.1, by taking it to consist in $y > 0$ of a segment of the ellipse given by (3.16) that just touches the step from $y > 0$ and to consist in $y < 0$ of a segment of the corresponding ellipse given by (3.16) that just touches the step from $y < 0$. The total volume of the V-state is fixed and so the shape, for a given centre of vorticity, is completely determined. The translational velocity of the V-state can then be estimated by taking the entire vorticity of each segment to be concentrated at its centroid to give, in effect, a vortex pair. Two quantities determine the speed: first the area of each segment giving the circulation of each segment, and second, the centroid of each segment giving the position of the concentrated vorticity. Once these quantities are known calculating the translational velocity is straight forward. If the segment on the deep side $y > 0$ has strength Γ_d and centroid position c_d , and the segment on the shallow side $y < 0$ has strength

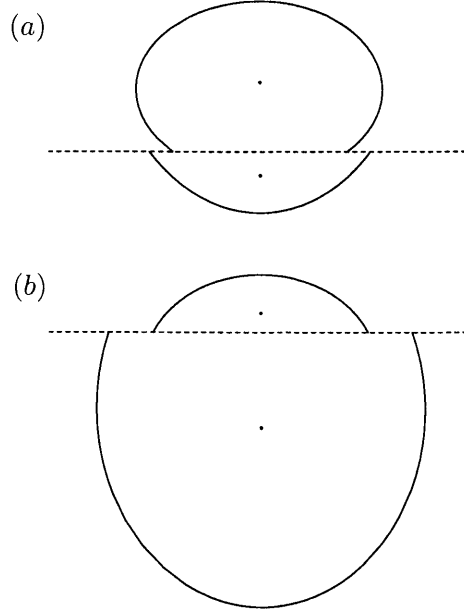


Figure C.1: The elliptical segment model with depth ratio $\gamma = 1/3$. Dots mark segment centroids. (a) A vortex mainly on the deep side. (b) A vortex mainly on the shallow side.

Γ_s and centroid position c_s the velocity of the segments can be written

$$u_d = -\frac{\alpha\Gamma_d}{4\pi c_d} + \frac{\beta\gamma^{-1}\Gamma_s}{2\pi(c_d + c_s)}, \quad u_s = \frac{\alpha\Gamma_s}{4\pi c_s} - \frac{\beta\Gamma_d}{2\pi(c_d + c_s)}. \quad (\text{C.1})$$

A translational velocity and center of vorticity for the V-state as a whole follows from the circulation-weighted averages

$$u_{tot} = (\Gamma_d u_d + \Gamma_s u_s) / (\Gamma_d + \Gamma_s), \quad Y(y_{tot}) = \mathcal{I} / (\Gamma_d + \Gamma_s), \quad (\text{C.2})$$

where \mathcal{I} is the total impulse of the patch.

To find the area of each segment first take each of the two segments to

be circular, i.e. consider a truncated circle,

$$x^2 + y^2 \leq r^2, \quad y > h, \quad (\text{C.3})$$

where h is the distance from the origin to the chord dividing the circle into a segment (note that in the y -plane h has the range $-r < h < r$). The area A_c of a circular segment is

$$A_c(h/r) = \cos^{-1}(h/r) - (h/r)\sqrt{1 - (h/r)^2} \quad (\text{C.4})$$

and the centroid position of the circular segment, c_c , is by,

$$c_c(h/r) = \frac{2(1 - (h/r)^2)^{3/2}}{3A_c(h/r)} - \text{sgn}(h)\frac{h}{r}. \quad (\text{C.5})$$

Let h_d be the distance from the origin of the deep sided circle to the escarpment then h_s , the distance from the origin of the shallow sided circle to the escarpment follows from volume conservation i.e. $h_s = \sqrt{1/\gamma}h_d$. Thus all parameters are known, i.e. the area of each segment from (C.4) and the centroid positions of both segments from (C.5).

The circulation of each segment is found by considering the area of the appropriate segment i.e. $\Gamma_i = A_i\omega_i$, $i = d, s$ where ω_i are defined from the conservation of potential vorticity such that,

$$\omega_d = 1, \quad \omega_s = \gamma. \quad (\text{C.6})$$

To return to the elliptical model transform from circular coordinates (x, y) to elliptical coordinates (x', y') through,

$$x \rightarrow \frac{x'}{a}, \quad y \rightarrow \frac{y'}{b}. \quad (\text{C.7})$$

The elliptical segment has area

$$A_e = \frac{ab}{r^2} A_c. \quad (\text{C.8})$$

For the elliptical and circular segments to have the same area, $ab/r^2 = 1$. The other constraint on a and b follows from the pre-determined aspect ratio of the ellipse, $\Delta = b/a$, derived from (3.16) for V-states touching the escarpment.

Appendix D

Point Vortex Trajectories near Step Topography: detailed point vortex trajectories

In chapter 4, section 4.3, trajectories of two point vortices near stepped topography were presented. Trajectories have been divided into four regimes depending on the placement of vortices in either deep or shallow water and for brevity only one example trajectory was given. For certain regimes it was found that point vortex trajectories can be divided further into trajectories which are periodic or aperiodic. For completeness, this Appendix presents examples of possible trajectories which were not given in the main body of the presentation.

This Appendix is divided into two parts: when the vortices have the same-sign and when they have opposite-sign. Where the vortices have the

same-sign, a system with negative impulse and both vortices existing in shallow water, [shallow,shallow] is presented, figure D.1. Second, where the vortices have opposite-sign two cases are examined; first when the vortices exist in a [deep,deep] configuration, figure D.2 and second when they exist in a [shallow,deep] configuration, figure D.3. Each figure labels the different types of motion in (ξ, η) or (ξ, δ) -space by roman numerals with example trajectories in (x, y) -space given.

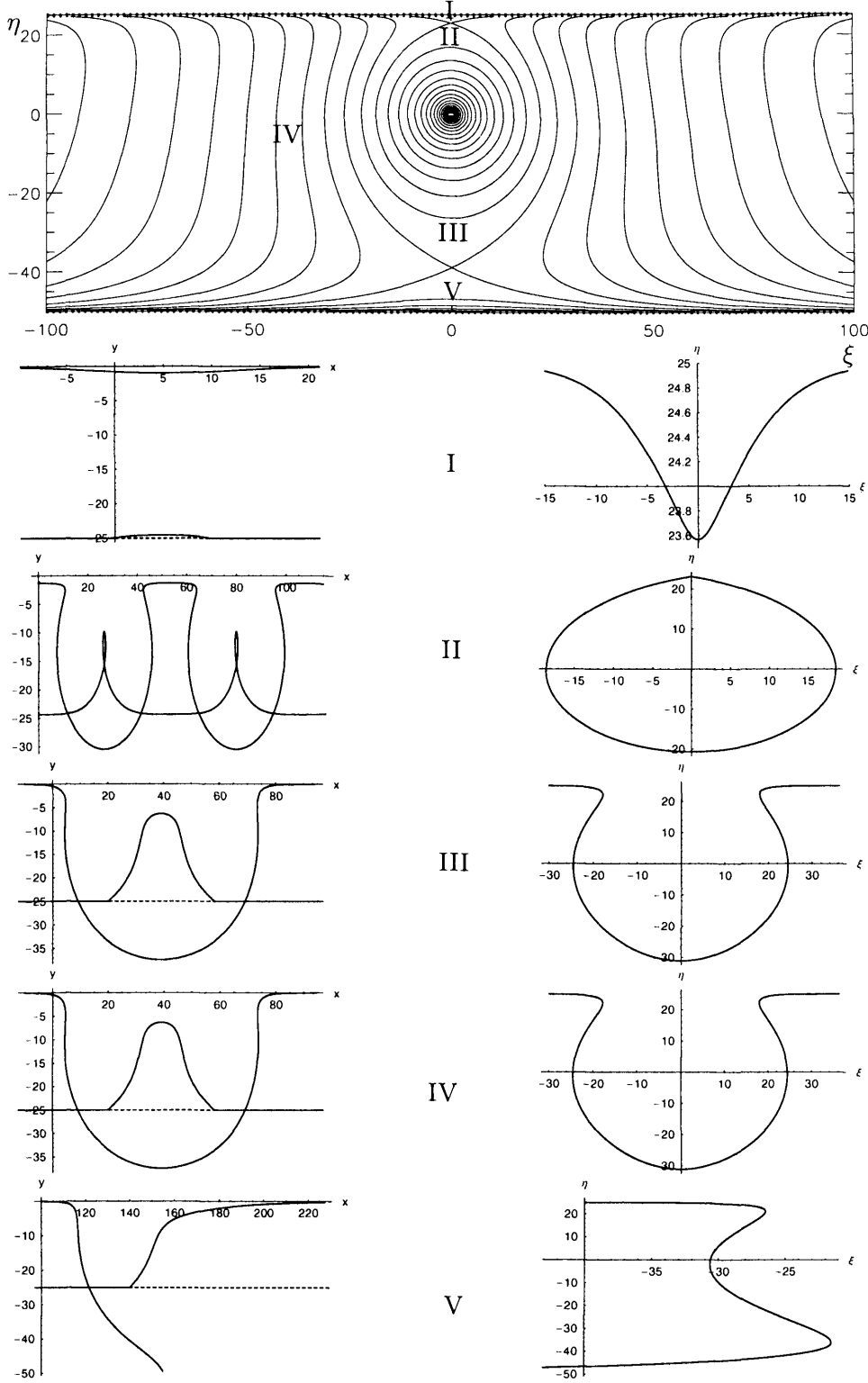


Figure D.1: A description of point vortex trajectories for two vortices where both vortices exist in shallow water having same-sign. Owing to two dipole equilibrium states there are five distinct types of motion. Figures on the left show the physical (x, y) plane where figures on the right show the trajectories in (ξ, δ) -space. A dashed line shows the region where physical motion for vortex can exist in.

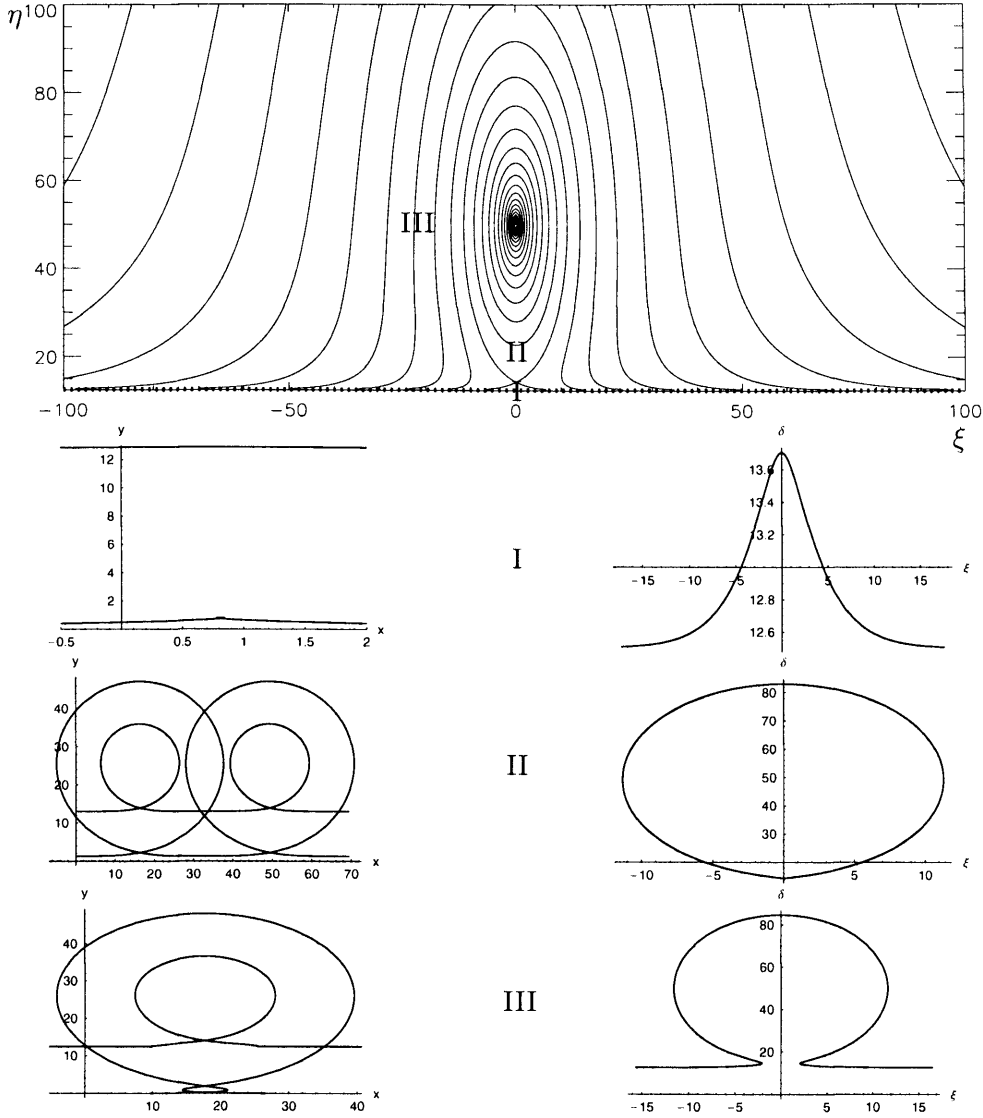


Figure D.2: A description of point vortex trajectories for two vortices where both vortices exist in deep water having opposite-sign. Owing to the dipole equilibrium states there are three distinct types of motion. Figures on the left show the physical (x, y) plane where figures on the right show the trajectories in (ξ, η) -space. A dashed line shows the region where physical motion for vortex can exist in.

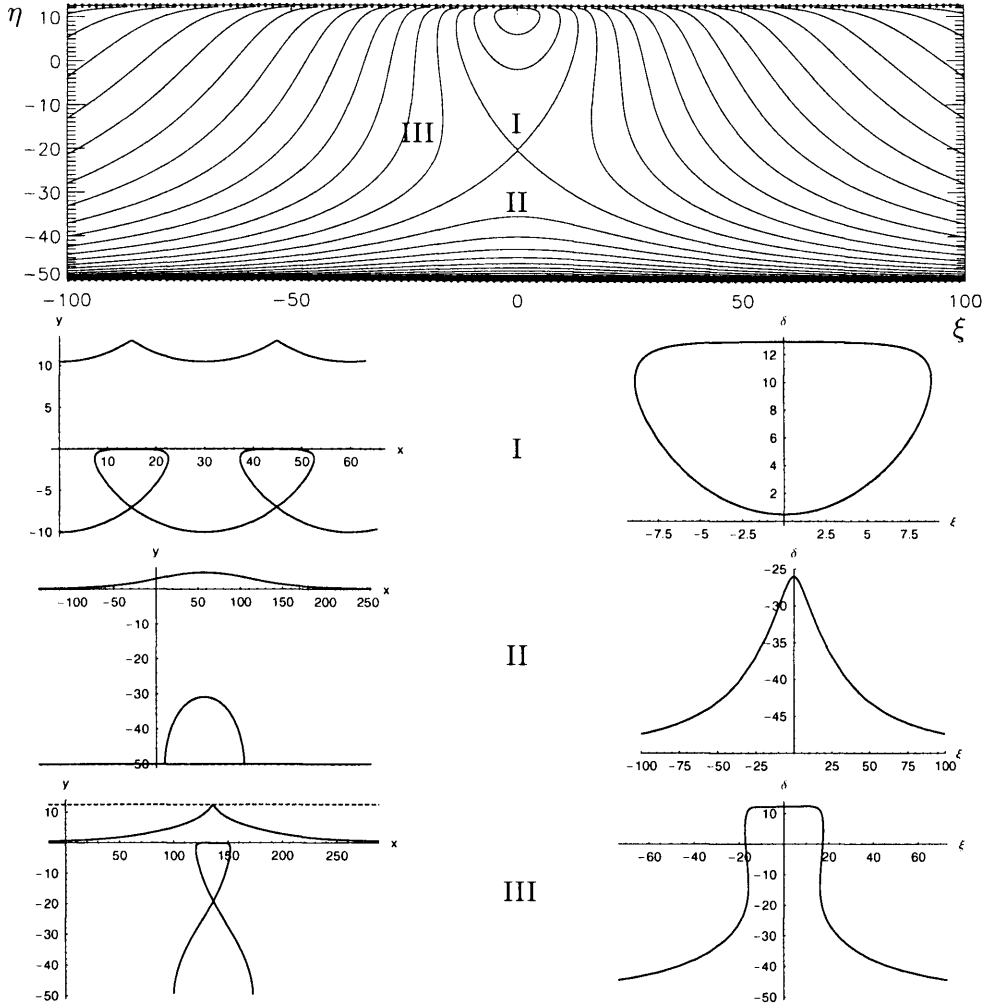


Figure D.3: A description of point vortex trajectories for two vortices where both vortices exist in deep water having opposite-sign. Owing to the dipole equilibrium states there are three distinct types of motion. Figures on the left show the physical (x, y) plane where figures on the right show the trajectories in (ξ, η) -space. A dashed line shows the region where physical motion for vortex can exist in.

Appendix E

Calculating Two-Vortex Equilibrium States for Rectilinear Topography

Dipole equilibrium states are defined such that each vortex in the pair translates parallel to the step. To find dipole equilibrium states equate the horizontal velocity for each vortex and solve for their y positions with $\eta = x_1 - x_2 = 0$ and the impulse, $\mathcal{I} = \Gamma_1 H_1 y_1 + \Gamma_2 H_2 y_2$.

Assume the dipole comprises of two vortices with strengths $\Gamma_{1,2}$ and positions $z_{1,2}$. Using the Green's function, (3.10), the horizontal velocity acting on one of the vortices of the dipole can be found,

$$u_{d,d} = -\frac{1}{2\pi} \left(\frac{\Gamma_1}{z_1 - z_2} + \frac{\alpha\Gamma_1}{z_1 - \bar{z}_1} + \frac{\alpha\Gamma_1}{z_1 - \bar{z}_2} \right), \quad (\text{E.1})$$

$$u_{d,s} = -\frac{1}{2\pi} \left(\frac{\alpha\Gamma_1}{z_1 - \bar{z}_1} + \frac{\beta\Gamma_2}{H_1(z_1 - \bar{z}_2)} \right), \quad (\text{E.2})$$

for both vortices existing in deep water or one vortex out of the pair lying in shallow water. First assume both vortices are in deep water then it

is required that the horizontal velocity of both vortices is the same i.e.

$u_{d,d}^1 = u_{d,d}^2$, hence solve

$$\frac{\alpha}{2}(y_1^2 - y_2^2)(\Gamma_2 y_1 - \Gamma_1 y_2) = (\Gamma_1 + \Gamma_2)(y_1 + y_2)y_1 y_2 + \alpha(y_1 - y_2)y_1 y_2(\Gamma_1 - \Gamma_2), \quad (\text{E.3})$$

along with the impulse, $\mathcal{I} = \Gamma_1 H^+ y_1 + \Gamma_2 H^+ y_2$. For the case where both vortices exist in shallow water replace α to $-\alpha$ in the above expression. For vortices existing on both sides of the step, say vortex 1 in deep water solve,

$$-\frac{\alpha}{2}(y_1^2 - y_2^2)(\Gamma_2 y_1 + \Gamma_1 y_2) = \beta \left(\Gamma_2 + \frac{\Gamma_1}{\gamma} \right) y_1 y_2, \quad (\text{E.4})$$

again along with the impulse. If vortex 1 is in shallow water solve the above with subscripts 1 and 2 swapped.

Appendix F

Energy of a Vortex Patch near Step Topography

The energy of dipolar vortex patches near a rectilinear step is known (Johnson & McDonald, 2004). For non symmetrical circulation configurations further analysis is required. Following a discussion given in Batchelor (1967) the form of the kinetic energy will be described for vortex patches near an escarpment.

The kinetic energy per unit mass of a patch of vorticity contained within an area \mathcal{D} with boundary $\partial\mathcal{D}$ is,

$$\mathcal{E} = \frac{1}{2} \int_{\mathcal{D}} (u^2 + v^2) dx dy = \frac{1}{2} \int_{\mathcal{D}} \psi \omega dx dy - \frac{1}{2} \oint_{\partial\mathcal{D}} \psi \mathbf{u} \cdot d\mathbf{r}, \quad (\text{F.1})$$

where symbols take their usual meanings. The first of these two integrals converges as $\mathcal{D} \rightarrow \infty$, the second does not. However assuming that for sufficiently large distances away from the vortex

$$\psi(x, y) = -\frac{1}{2\pi} \log r \int_{\mathcal{D}} \omega dx dy + \mathcal{O}(r^{-1}), \quad (\text{F.2})$$

where $r = (x^2 + y^2)^{1/2}$. Therefore (F.1) can be rewritten as

$$\mathcal{E} = \frac{1}{2} \int_{\mathcal{D}} \psi \omega dx dy - \frac{1}{4\pi} \log r \left(\int_{\mathcal{D}} \omega dx dy \right)^2. \quad (\text{F.3})$$

This shows that the second integral holds no information on the dynamical nature of the vortices. Therefore it is possible to define the conserved quantity

$$\mathcal{W} = \frac{1}{2} \int_{\mathcal{D}} \psi \omega dx dy. \quad (\text{F.4})$$

\mathcal{W} can be considered the kinetic energy of a vortex patch which wholly depends on the configuration of the vorticity. Although it cannot be regarded strictly as the kinetic energy of the system, it is only required to observe conserved quantities in dynamical motion it is sufficient to use \mathcal{W} as the energy.

The stream function of a vortex patch of radius a and strength QH can be written as,

$$\psi = \begin{cases} -(QH/2\pi)[\frac{1}{2}(R/a)^2 - \frac{1}{2}] & y > 0, \\ -(QH/2\pi) \log(R/a) & y < 0, \end{cases} \quad (\text{F.5})$$

with R defined as the radial point from the center. For [deep, deep] configuration, the energy of a pair of vortices is a sum of self interacting energies and cross interacting energies such that,

$$\mathcal{E}_{d,d} = -\frac{(H^+)^3}{4\pi} \left\{ Q_1 Q_2 (\log |R_s^2/a_1 a_2| + \alpha \log |R_s'^2/a_1 a_2|) + \alpha Q_1^2 \log |2y_1/a_1| + \alpha Q_2^2 \log |2y_2/a_2| + \pi(Q_1^2 + Q_2^2)/4 \right\}, \quad (\text{F.6})$$

where R_s is the radial separation of the vortices, $R_s' = |z_1 - \bar{z}_2|$ and $a_{1,2}$ is the radius of the each vortex respectively. This is the form of the Hamiltonian

for a point vortex in [deep,deep] configuration with similar expressions being derived for the remaining regimes.

Appendix G

Numerical Method For Calculating V-States near Circular Topography

Steady vortex patches rotating with constant angular velocity about an arbitrary point can be found efficiently by using a combination of contour dynamics to compute the velocity field and an algorithm which adjusts the contour toward a state such that the boundary is tangential to the local velocity (Wu *et al.*, 1984). Vortex patches that translate or rotate with constant angular momentum about its centroid have already been found by Wu *et al.* (1984). Since the vortex patches studied here rotate about a point other than the centroid of the patch itself the algorithm must be modified slightly. Essentially, if the vortex patch were to rotate with angular velocity Ω , then we find the contour that would remain invariant in a background solid body rotation with speed Ω . Therefore on the boundary of the vortex patch we demand

$$\Psi(r, \theta) + \frac{\Omega}{2} r^2(\theta) = c, \quad (\text{G.1})$$

where Ψ is the streamfunction of the vortex induced flow and (r, θ) are polar coordinates from the centre of the topography (and here the centre of rotation) to the boundary of the vortex. After differentiating (G.1), discretizing with N nodes yields

$$u_{k+1/2}\Delta y_k - v_{k+1/2}\Delta x_k + (\Omega/2)\Delta(r_k^2) = 0, \quad 1 \leq k \leq N \quad (\text{G.2})$$

where the subscript $k + 1/2$ is the mean value of the quantity at node k , i.e. $u_{k+1/2} = (u_k + u_{k+1})/2$. It is possible to find Ω at each iteration by computing the velocity at each node and summing (G.2) over the N nodes.

To iterate the vortex boundary closer to a V-state choose polar coordinates $(R(\Theta), \Theta)$ centred at an appropriate point, (\tilde{x}, \tilde{y}) such that $R(\Theta)$ remains single valued for $0 \leq \Theta \leq \pi$ since every V-state has a line of symmetry. Then following Wu *et al.* (1984), (G.2) can be written as

$$r_k - f_{k+1/2}r_{k+1} = 0, \quad 1 \leq k \leq N, \quad \text{or,} \quad r_k - f_{k-1/2}^{-1}r_{k-1} = 0, \quad 2 \leq k \leq N+1, \quad (\text{G.3})$$

where $f_{k+1/2}$ is defined as

$$f_{k+1/2} \equiv \frac{u_{k+1/2} \sin \Theta_{k+1} - v_{k+1/2} \cos \Theta_{k+1} + \Omega(2R_{k+1} + \tilde{y} \sin \Theta_{k+1} + \tilde{x} \cos \Theta_{k+1})}{u_{k+1/2} \sin \Theta_k - v_{k+1/2} \cos \Theta_k + \Omega(2R_k + \tilde{y} \sin \Theta_k + \tilde{x} \cos \Theta_k)}, \quad (\text{G.4})$$

this reduces to the form of the translating vortex near a wall when $\sqrt{\tilde{x}^2 + \tilde{y}^2} \rightarrow \infty$ and the rotating vortex when $\sqrt{\tilde{x}^2 + \tilde{y}^2} \rightarrow 0$. It is simple to arrange (G.3) into a tri-diagonal system and solve for $R_k, k = 1, \dots, N$.

Appendix H

Computing the Velocity near the Origin of a Circular Domain

From (6.18), when $|z| < 1$, $|z_0| < 1$, two singularities of equal and opposite strength exist at $z = 0$. Here an alternative formulation in terms of an expansion that is valid for all $|z| < 1$, $|z_0| < 1$. The image term in (6.15) can be expanded as

$$\frac{\alpha H^-}{2\pi} \log |1 - z\bar{z}_0| = \frac{\alpha H^-}{2\pi} \operatorname{Re} \sum_1^{\infty} \frac{(z\bar{z}_0)^n}{n}, \quad (\text{H.1})$$

giving on differentiating and taking the complex conjugate,

$$u + iv = \frac{\alpha H^-}{2\pi} \sum_1^{\infty} \bar{z}^{n-1} \int \int_{\mathcal{A}} z_0^n dx_0 dy_0 = \frac{\alpha H^-}{2\pi} \sum_1^{\infty} \frac{\bar{z}^{n-1}}{n+1} \oint_{\partial\mathcal{A}} z_0^{n+1} dy_0, \quad (\text{H.2})$$

by Green's theorem (since $\partial z_0/\partial x_0 = 1$). Now

$$\oint_{\partial\mathcal{A}} z_0^{n+1} dz_0 = 0, \quad (\text{H.3})$$

as the integrand is entire. Combining real and imaginary parts of (H.2) and (H.3) gives on taking the complex conjugate,

$$u - iv = -\frac{i\alpha H^-}{4\pi} \sum_1^\infty \frac{z^{n-1}}{n+1} \oint_{\partial\mathcal{A}} \bar{z}_0^{n+1} dz_0, \quad (\text{H.4})$$

a power series expansion for the velocity near $z = 0$.

Appendix I

V-state Centres of Vorticity and Initial Mean Radius

Frame	1		2		3	
	r_{cv}	R	r_{cv}	R	r_{cv}	R
	0.100	0.270	0.240	0.228	0.380	0.186
	0.100	0.450	0.240	0.380	0.380	0.310
	0.100	0.630	0.240	0.532	0.380	0.434
	0.100	0.810	0.240	0.684	0.380	0.558
	0.100	0.878	0.240	0.741	0.380	0.605
Frame	4		5		6	
	r_{cv}	R	r_{cv}	R	r_{cv}	R
	0.520	0.144	0.660	0.102	0.800	0.060
	0.520	0.240	0.660	0.170	0.800	0.100
	0.520	0.336	0.660	0.238	0.800	0.140
	0.520	0.432	0.660	0.306	0.800	0.180
	0.520	0.475	0.660	0.337	0.800	0.198

Table I.1: Centres Of Vorticity, r_{cv} , and mean radius, R, for monopolar V-States given in figure 6.3(a), which are interior to circular topography. Frames are taken from left to right.

Frame	1		2		3	
	r_{cv}	R	r_{cv}	R	r_{cv}	R
	1.200	0.060	1.500	0.150	2.000	0.300
	1.200	0.100	1.500	0.250	2.000	0.500
	1.200	0.140	1.500	0.350	2.000	0.700
	1.200	0.180	1.500	0.450	2.000	0.900
	1.200	0.195	1.500	0.488	2.000	0.975
Frame	4		5		6	
	r_{cv}	R	r_{cv}	R	r_{cv}	R
	3.000	0.600	0.300	1.320	0.600	1.620
	3.000	1.000	0.300	1.400	0.600	1.750
	3.000	1.400	0.300	1.550	0.600	2.000
	3.000	1.800	0.300	1.800	0.600	2.250
	3.000	1.980	0.300	2.000	0.600	2.500

Table I.2: Centres Of Vorticity, r_{cv} , and mean radius, R for monopolar V-States given in figure 6.3(b), which are exterior to circular topography. Frames are taken from left to right.

Appendix J

Calculating Two-Vortex Equilibrium States for Circular Topography

In chapter 7 it was possible to find vortex pairs near circular topography in a steadily translating configuration such that the frequency of each vortex comprising the pair was the same. To compute this frequency, Υ first find the frequency $\Upsilon = ru_\theta$, of each vortex, from (6.15)

$$\Upsilon_1 = -\frac{\alpha\Gamma_1}{r_1^2(r_1^2 - 1)} + \frac{\Gamma_2(r_2 \cos(\theta_1 - \theta_2) - r_1)}{r_1(r_1^2 - 2r_1r_2 \cos(\theta_1 - \theta_2) + r_2^2)} + \frac{\alpha\Gamma_2(r_1r_2 \cos(\theta_1 - \theta_2) - 1)}{r_1^2(r_1^2r_2^2 - 2r_1r_2 \cos(\theta_1 - \theta_2) + 1)},$$

(J.1a)

$$\Upsilon_2 = -\frac{\alpha\Gamma_2}{r_2^2(r_2^2 - 1)} + \frac{\Gamma_1(r_1 \cos(\theta_2 - \theta_1) - r_2)}{r_2^2(r_2^2 - 2r_2r_1 \cos(\theta_2 - \theta_1) + r_1^2)} + \frac{\alpha\Gamma_1(r_2r_1 \cos(\theta_2 - \theta_1) - 1)}{r_2^2(r_2^2r_1^2 - 2r_2r_1 \cos(\theta_2 - \theta_1) + 1)}.$$

(J.1b)

Then to find an equilibrium point, set the frequencies of both vortices equal to each other with $\phi = \theta_1 - \theta_2 = 0$ for a seamount and $\phi = \pi$ for a well. Then solve for r_1, r_2 simultaneously along with the energy or impulse of the

pair.

Appendix K

Experimental Data Analysis

In this Appendix the techniques used to process the experimental data from chapter 8 are described.

K.1 MatPIV

Particle image velocimetry (PIV) can essentially be looked upon as an application of pattern matching in experiments. MatPIV is one of a variety of different computer codes available written specifically for this purpose. Specific details of the algorithm are not given here and the interested reader is referred to <http://www.math.uio.no/~jks/matpiv/> for further details. However, the fundamentals of how the code works is as follows. Assume two successive images (I_1 and I_2) have been taken from the experiment. Each image is divided into smaller regions called sub-windows whose size is a function of the resolution. Each sub-window in the second image is then tested to each sub-window first image for correlation, i.e. each sub-window in the second image is associated with a sub-window in the first image for which it compares most favourably. If $I_{i,j}^{1,2}$ represents sub-window i, j in the first image and second image respectively then this comparison is calculated

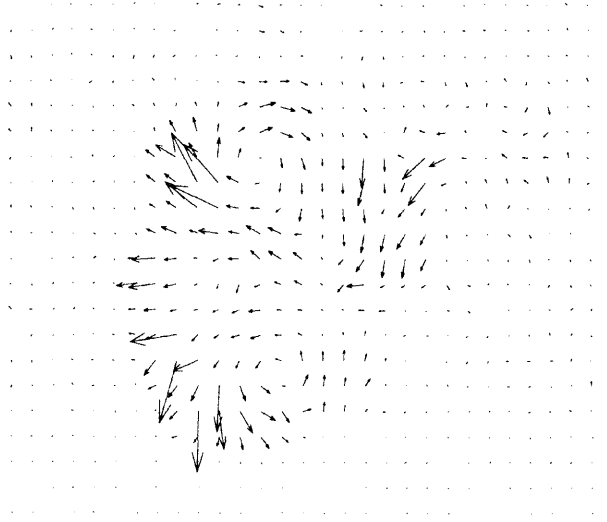


Figure K.1: An example velocity field computed using MatPIV, arrows show the direction of the velocity at that point with the size indicating the magnitude.

by

$$C_{i,j} = \sum_m \sum_n (I_{i,j}^1 - I_{m,n}^2)^2. \quad (\text{K.1})$$

Then by evaluating the distance between sub-windows a two-dimensional velocity for at each grid point (i.e. sub-window) can be calculated such that a velocity field can be drawn (see figure K.1)

With knowledge of the velocity at grid points it is possible to calculate the associated vorticity at that point by calculating

$$\omega_{i,j} = \frac{\partial v_{i,j}}{\partial x_i} - \frac{\partial u_{i,j}}{\partial y_j}. \quad (\text{K.2})$$

Several numerical schemes can be implemented to evaluate $\omega_{i,j}$. MatPIV

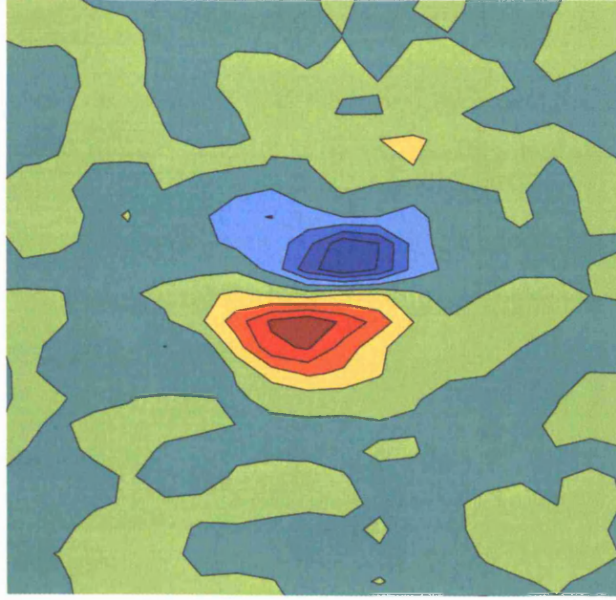


Figure K.2: An example vorticity contour map field computed using Mat-PIV. Blue regions show areas of equivalent negative vorticity where red regions show areas of equivalent positive vorticity.

uses the least squares method namely,

$$\omega_{i,j} = \frac{1}{10\Delta x}(2v_{i+2,j} + v_{i+1,j} - v_{i-1,j} - v_{i-2,j}) - \frac{1}{10\Delta y}(2u_{i,j+2} + u_{i,j+1} - u_{i,j-1} - u_{i,j-2}), \quad (\text{K.3})$$

for constant grid spaces only. Contouring similar values of vorticity will lead to a vorticity map similar to figure K.2.

K.2 Dipole trajectories

The trajectories of a dipole are found by following vortex patch centroids. The procedure to compute each patch comprising the dipole is as follows:

1. From the vorticity contour map, separate the domain into regions of

positive vorticity $\omega_{i,j}^+$ and negative vorticity $\omega_{i,j}^-$.

2. For each set (i.e. positive and negative) evaluate the mean vorticity, $\bar{\omega}^+$ for the positive vorticity only and $\bar{\omega}^-$ for the negative vorticity only.
3. Remove the background vorticity so that only the significant vortical motions remain by evaluating

$$\hat{\omega}_{i,j} = \omega_{i,j} - \bar{\omega}, \quad (\text{K.4})$$

for both the positive and negative vorticity.

4. Now set any value that is less than zero for the positive vorticity or greater than zero for the negative vorticity to be equal to zero.
5. To define the centroid evaluate

$$(x_c, y_c) = \frac{\sum_i \sum_j \omega_{i,j}(x_i, y_j)}{\sum_i \sum_j (x_i, y_j)}, \quad (\text{K.5})$$

which can then be calibrated to have dimensions m .

By taking successive images at specific time intervals the evolution of the dipole can be computed. To complete a thorough investigation, a total of 155 experiments were undertaken. Evaluating trajectories for each experiment is computationally intensive; accordingly, approximately 10 – 15 intervals are taken for each experiment which leads the trajectories taking a slightly jagged appearance.

K.3 Dipole area

The area of the dipole was computed in a similar fashion to the previously described procedure:

1. Start by considering a ‘base’ image, i.e. an image which captures the anomalous fluid and equipment. Discretize this image by associating value, $\mathcal{B}_{i,j}$, which represents the colour at that point (with the colour black being equal to 0).
2. Do the same to a single image at a prescribed time during the experiment. Define $\mathcal{C}_{i,j}$ to represent the colour values for the comparison image.
3. Define, $\mathcal{D}_{i,j}$, by

$$\mathcal{D}_{i,j} = \log \left(\frac{\mathcal{B}_{i,j}}{\mathcal{C}_{i,j}} \right), \quad (\text{K.6})$$

such that $\mathcal{D}_{i,j} > 0$ for regions where there is an increase in dye concentration.

4. Remove any background concentrations of dye by subtracting the mean level of concentration such that only the regions of significant dye concentrations remain.
5. Now define $D_{i,j}$ such that

$$D_{i,j} = \begin{cases} 1 & \text{for } \mathcal{D}_{i,j} > 0, \\ 0 & \text{otherwise,} \end{cases} \quad (\text{K.7})$$

so that no negative concentrations exist and to filter the considered dipole area so that any entrained fluid (having smaller dye concentrations) will have the same weighting as the main dipole.

6. The area of the dipole can then be calculated by

$$\mathcal{A} = \sum_i \sum_j D_{i,j}, \quad (\text{K.8})$$

which can then be calibrated to have dimensions m^2 .

Figure 8.8(a) shows how the area of a dipole which approaches a step at normal incidence varies with $t^{2/3}$. For later times there is a decrease in the area, this can be explained by the dye being dissipated into the anomalous fluid. As the dipole entrains an increasing amount of fluid its mean dye concentration decreases. For sufficiently large times the mean dye concentration of the dipole is comparable to the mean concentration from the whole tank. Therefore from step 4 in the above procedure, some of the dipole may be considered part of the anomalous fluid which results in an apparent decrease in area.

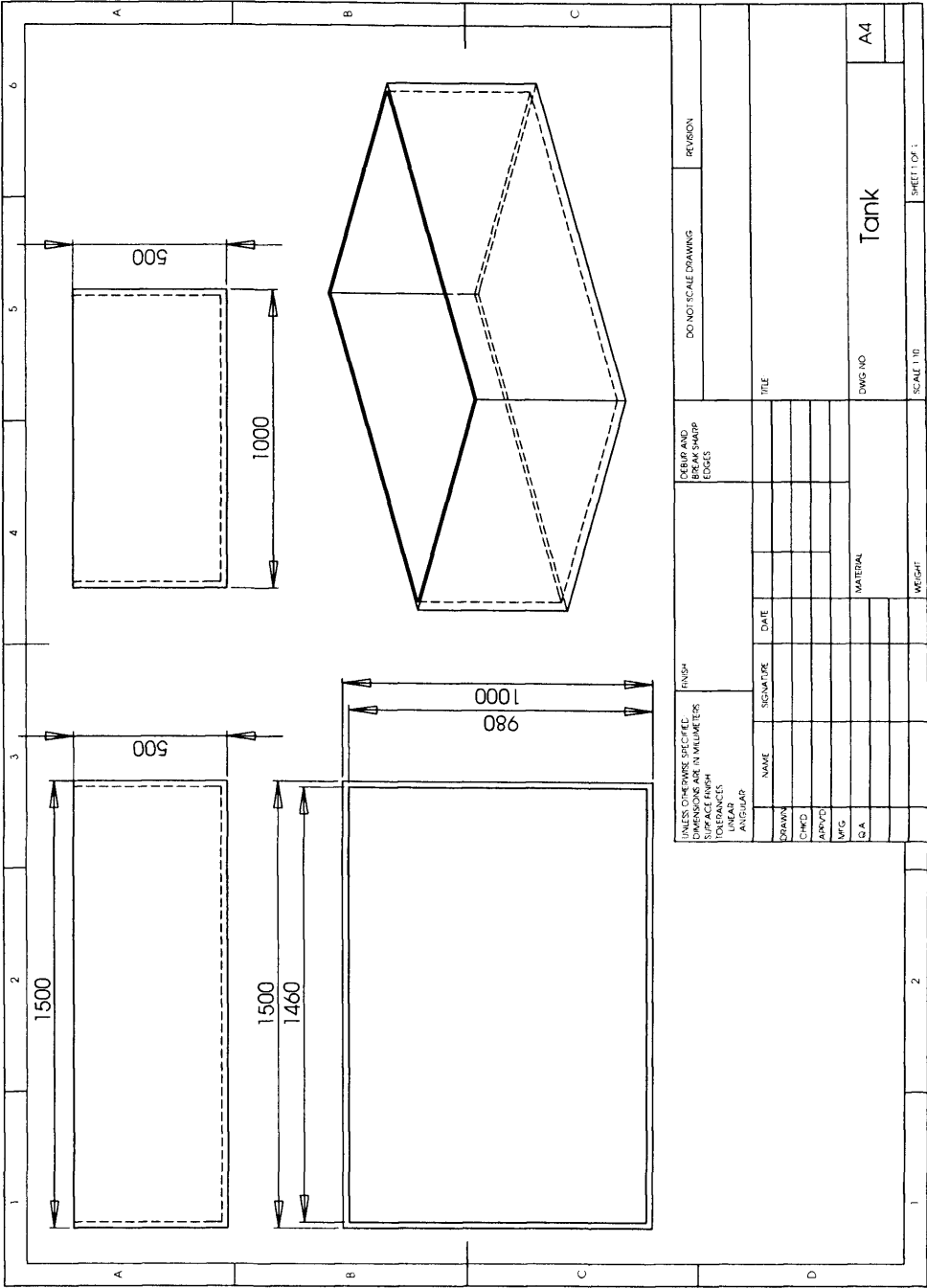
K.4 Incident and transmitted angle

The incident and transmitted angles for an experiment are found from the computed dipole trajectories. Incident angles are found by dividing trajectories into those which are incident to the step (x_i, y_i) , and those which have crossed the step (x_t, y_t) . For dipoles which perform TIR, trajectories are divided by the point which comes closest to the step. Using linear regression on the mid-points of these vectors, an angle can be defined by taking the inverse tangent of the gradient.

Appendix L

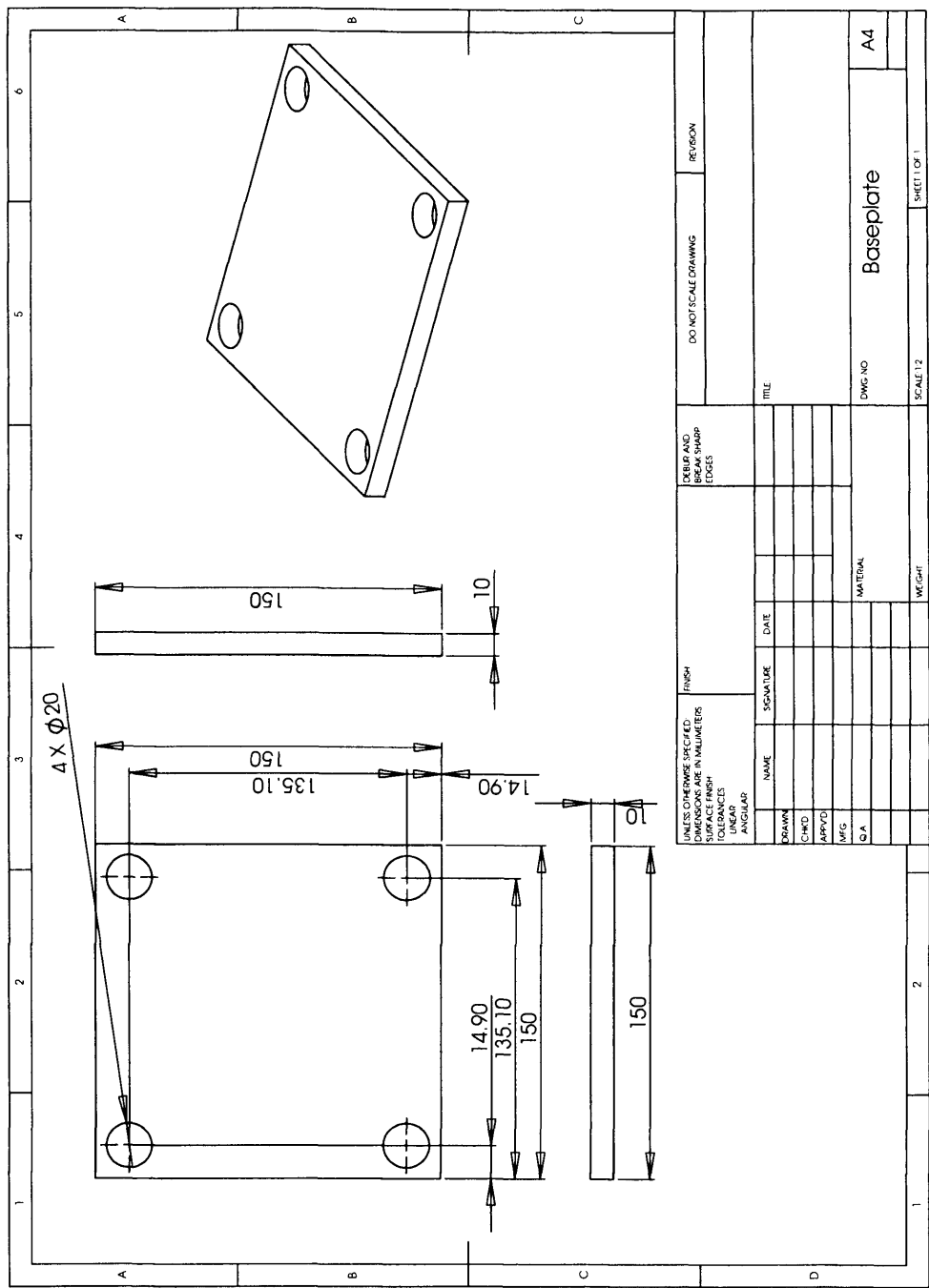
Technical Drawings of Experiment Apparatus

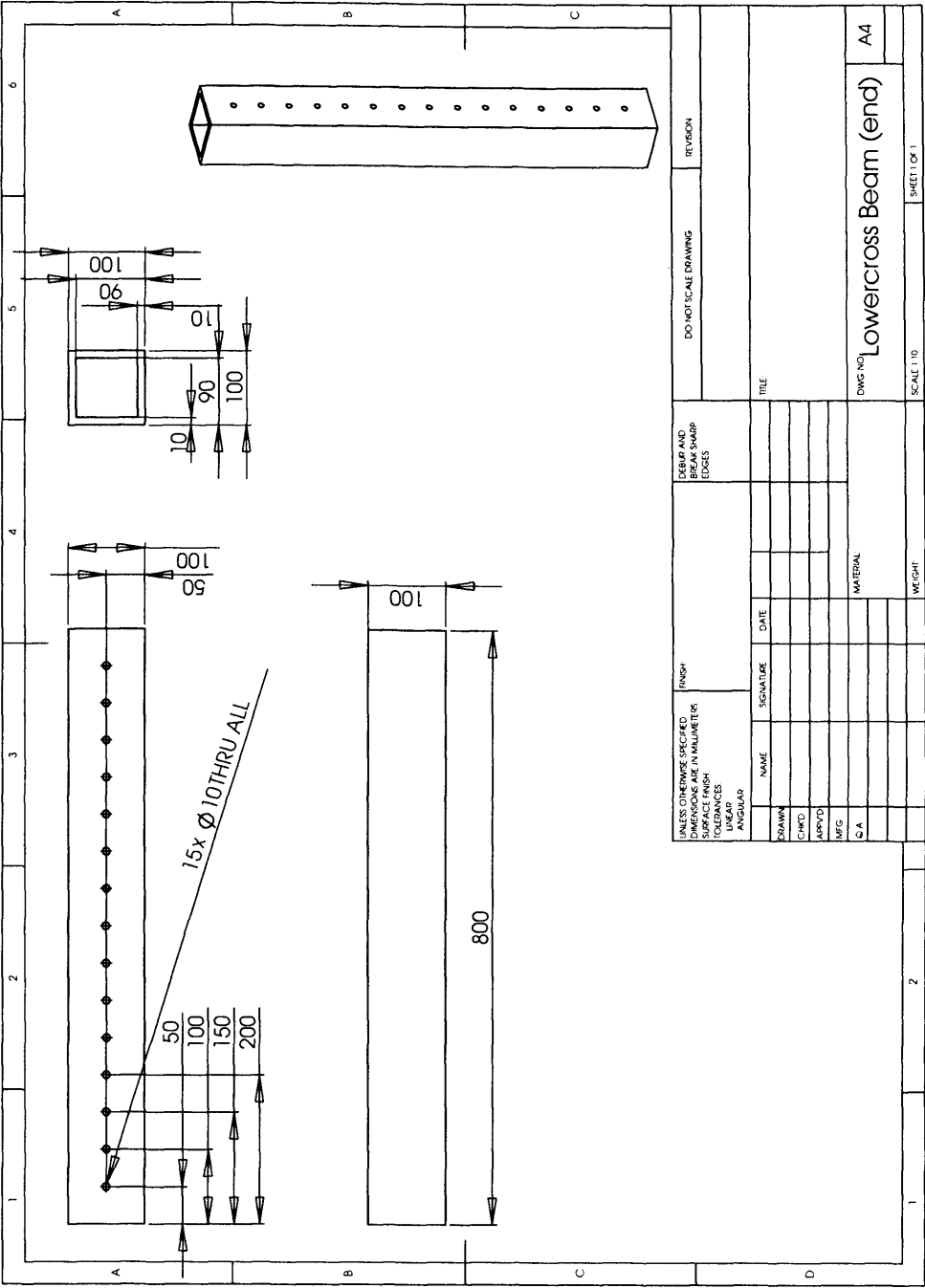


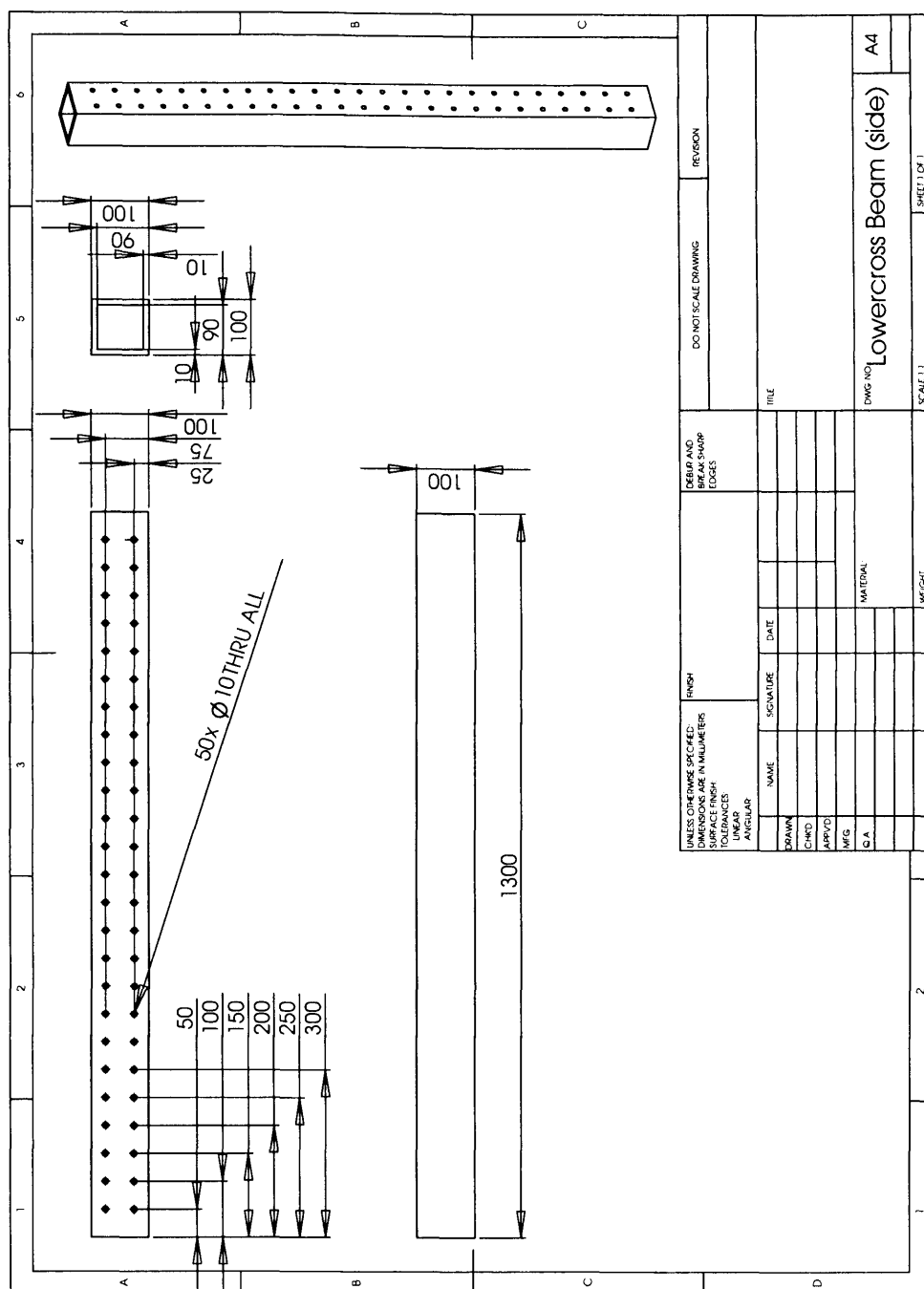


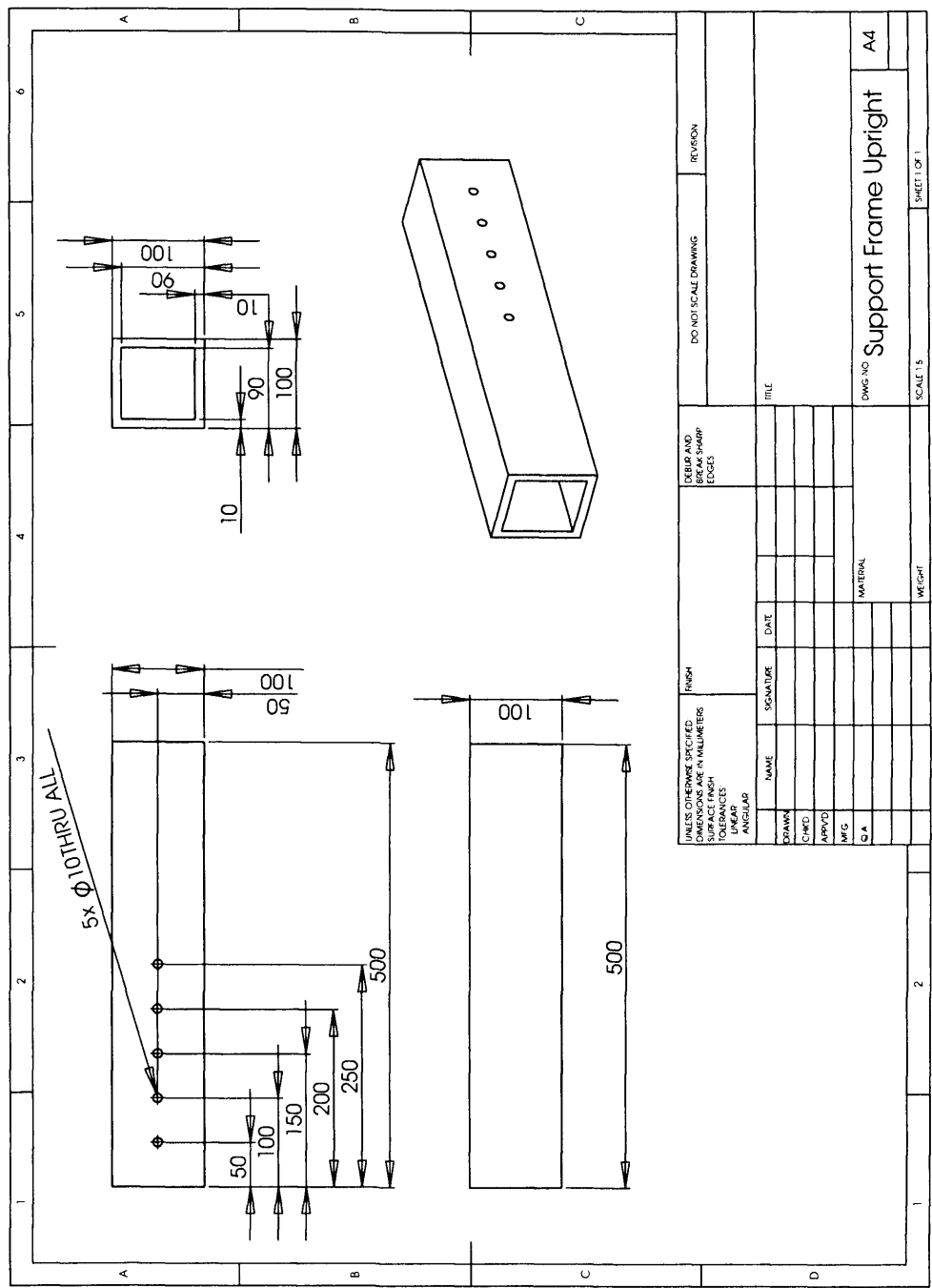
Part I

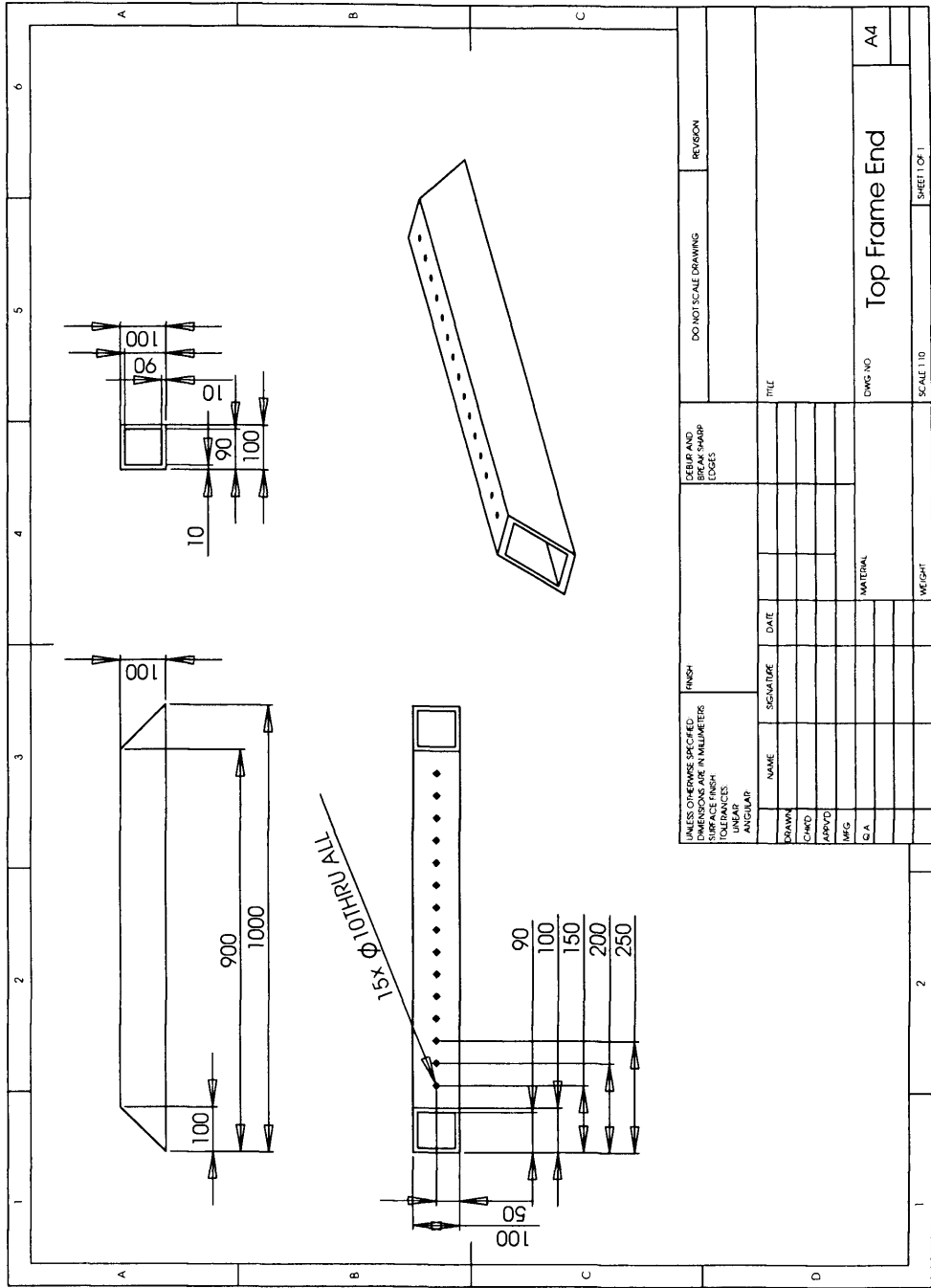
Stand Design

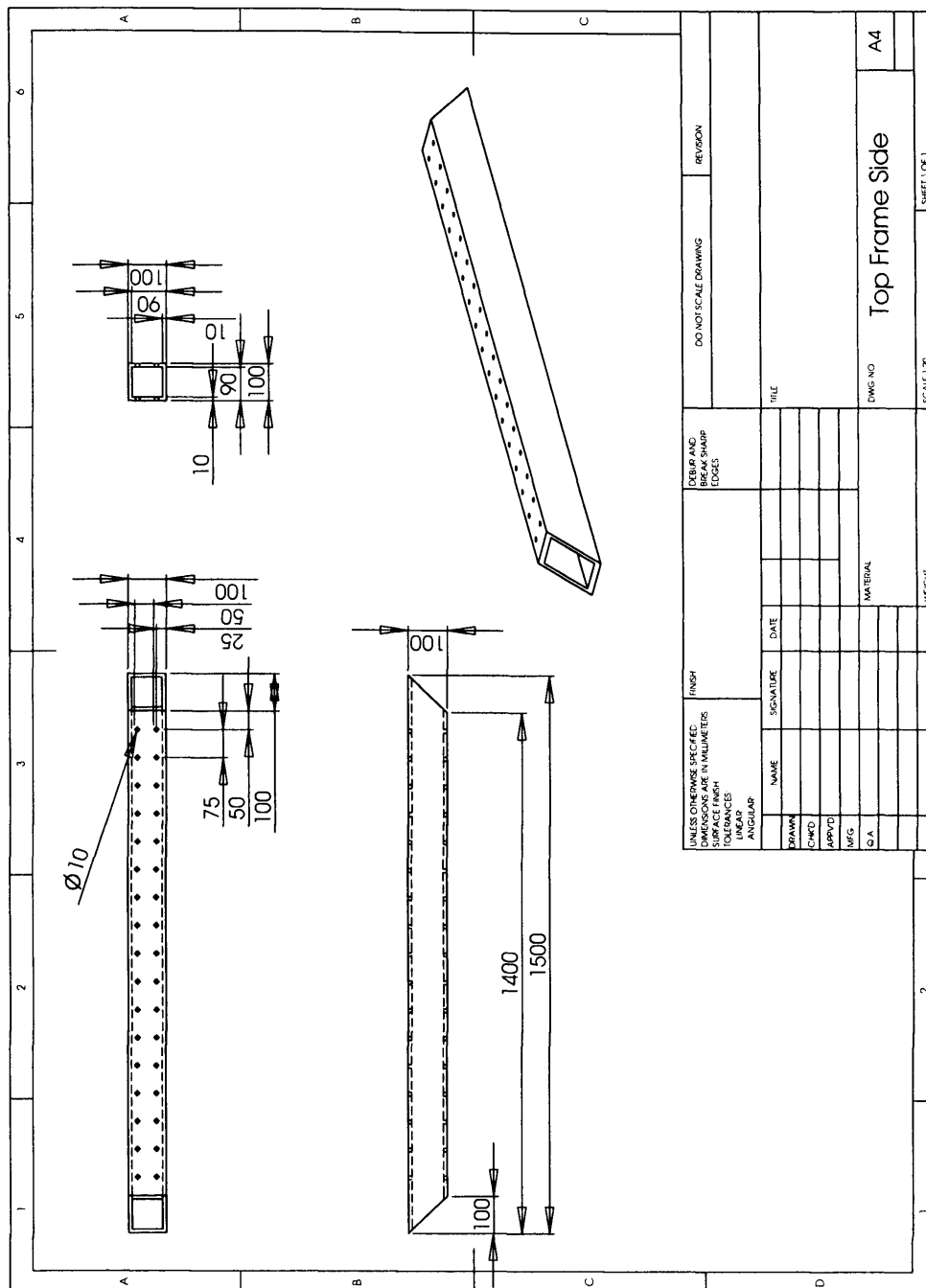


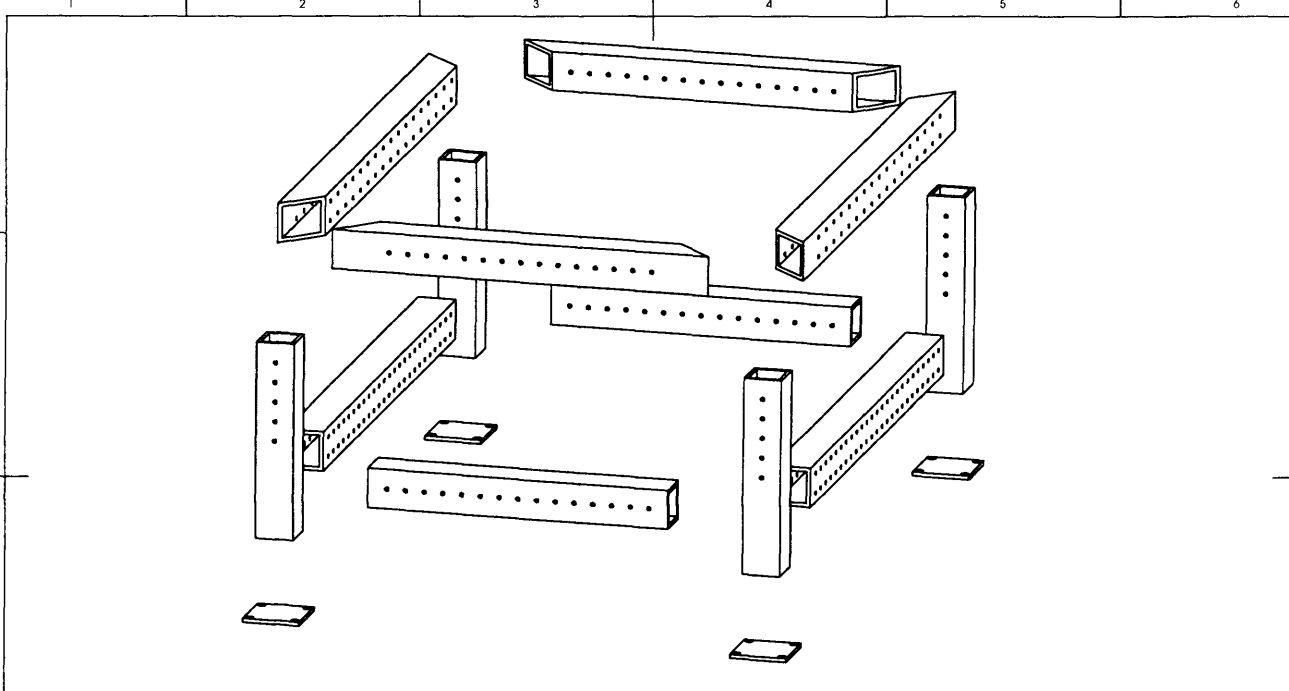






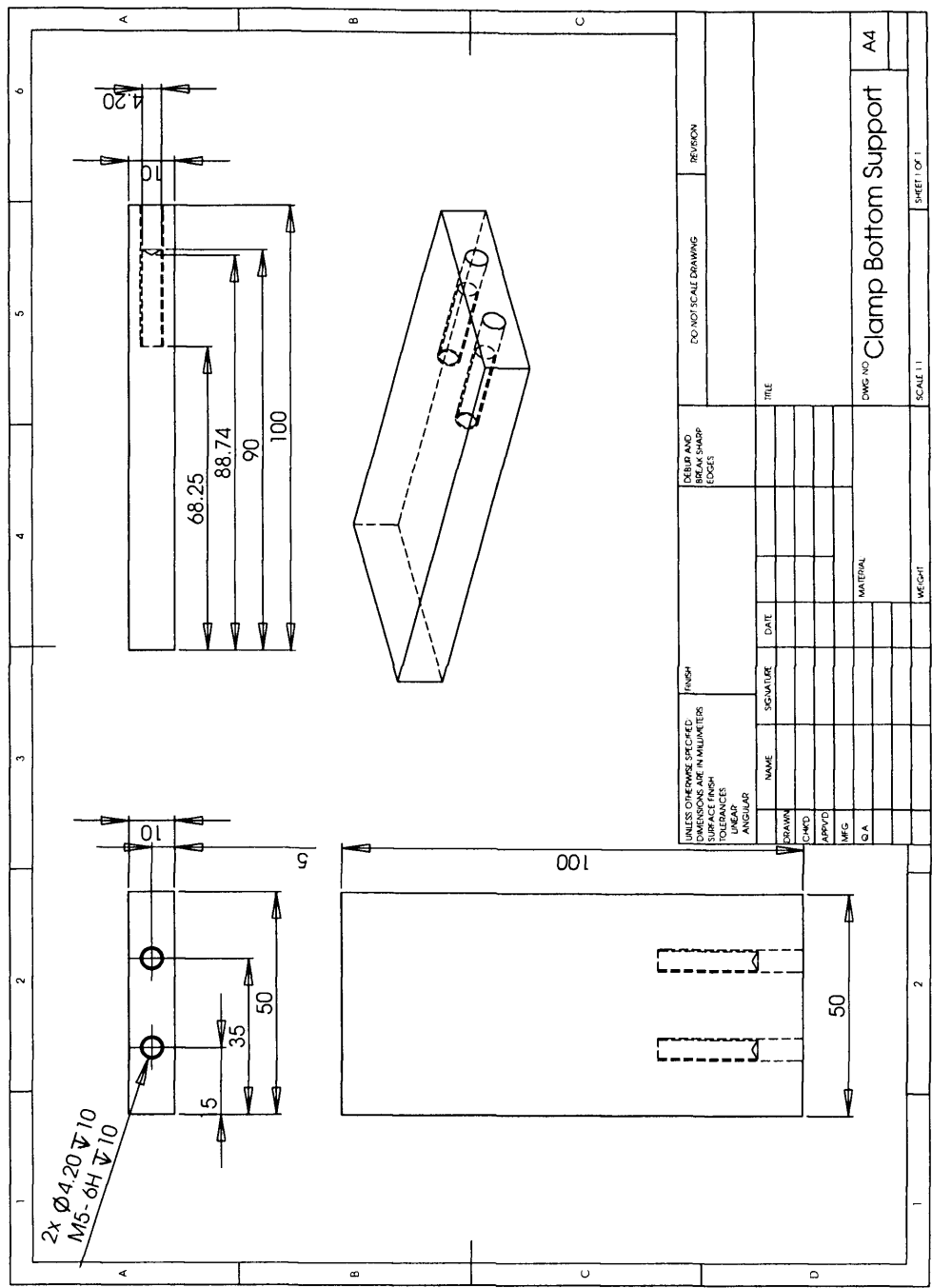


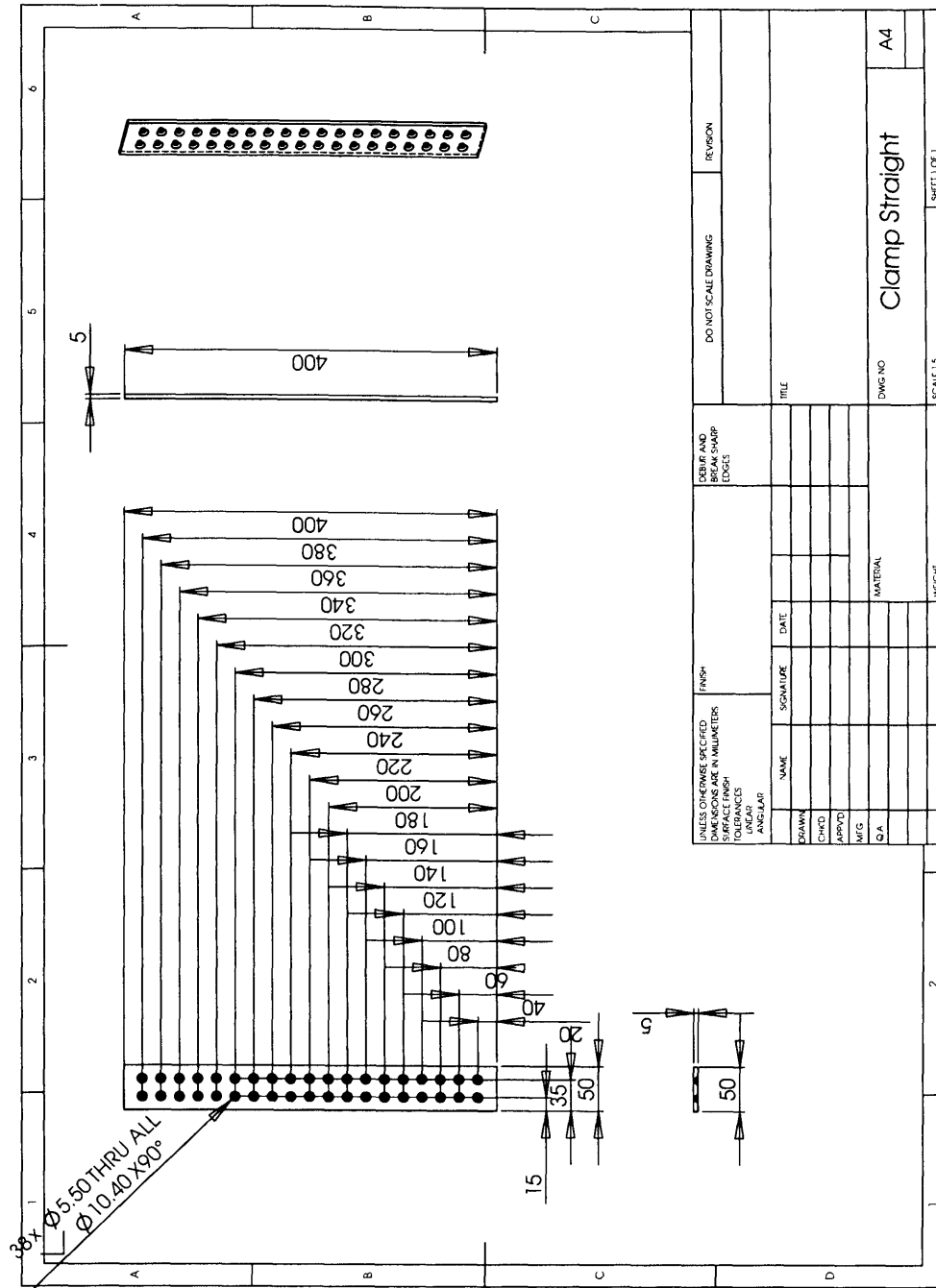


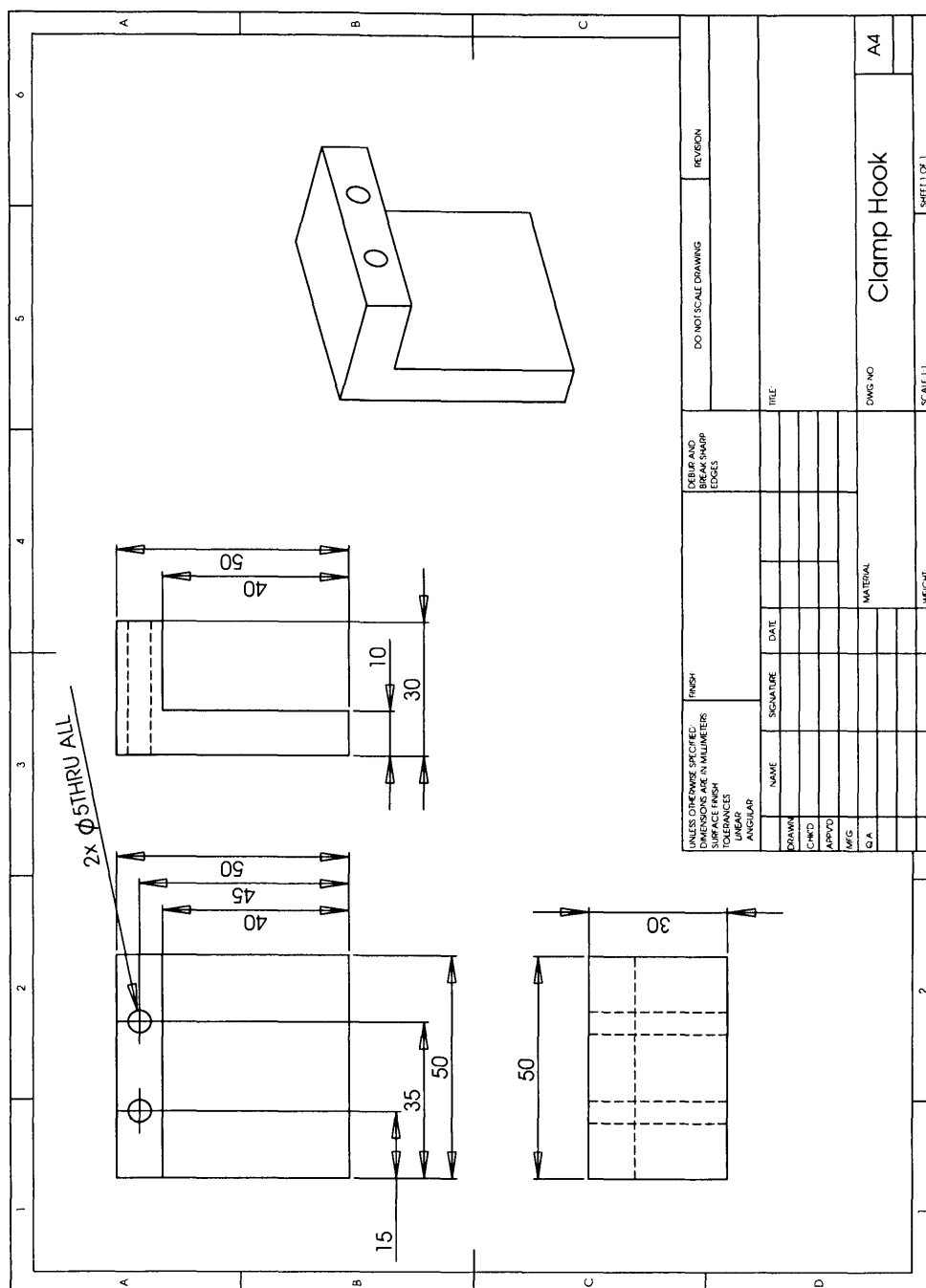
1		2		3		4		5		6	
A											A
B											B
C											C
D											D
UNLESS OTHERWISE SPECIFIED: DIMENSIONS ARE IN MILLIMETERS SURFACE FINISH TOLERANCES LINEAR: ANGULAR				FINISH		DEBUR AND BREAK SHARP EDGES		DO NOT SCALE DRAWING		REVISION	
NAME		SIGNATURE		DATE				TITLE			
DRAWN								Frame Assembly Explode		A4	
CHK'D											
APP'D											
MFG											
Q.A.						MATERIAL		DWG. NO.			
								WEIGHT		SCALE 1:20	
1		2								SHEET 1 OF 1	

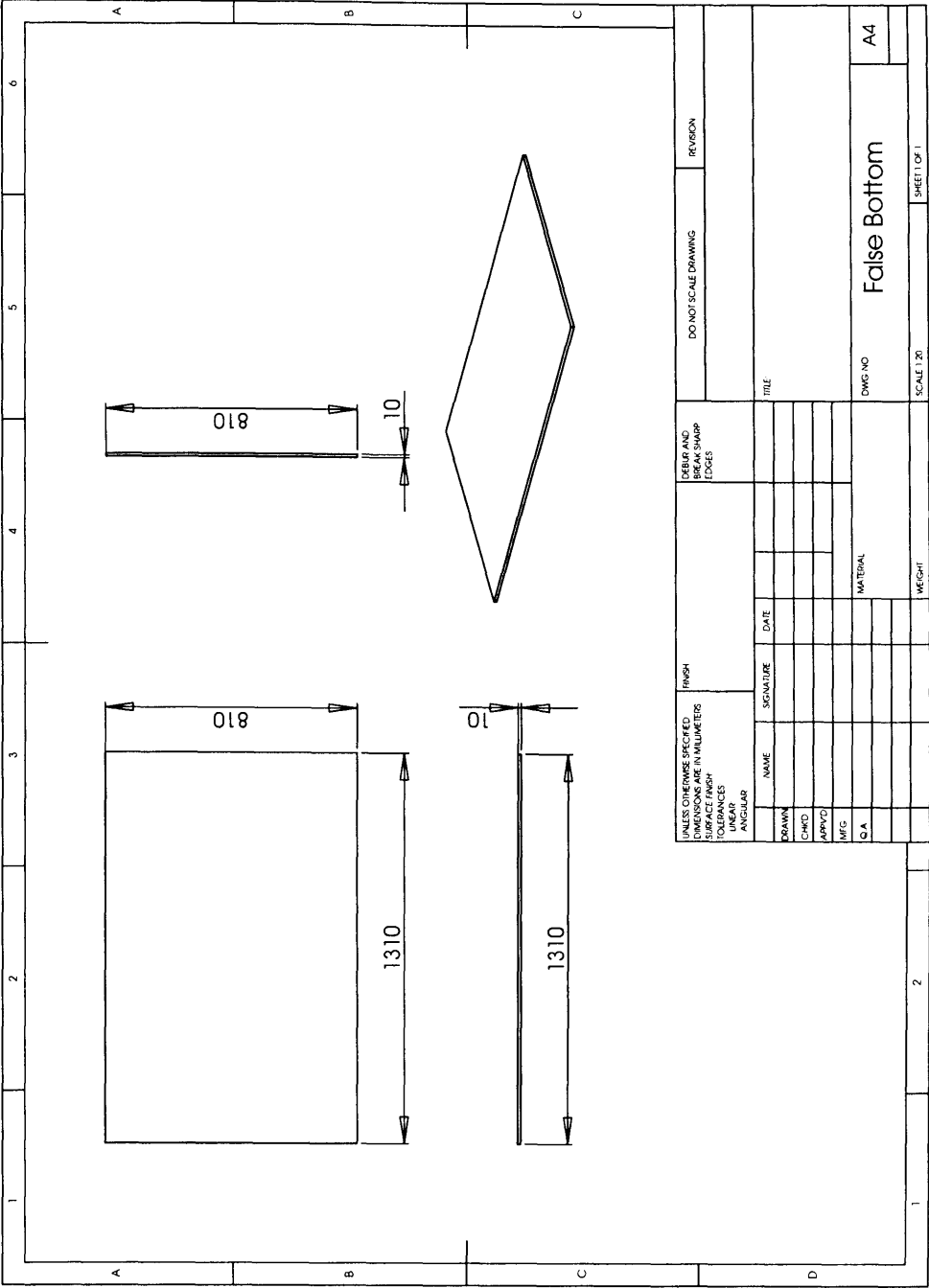
Part II

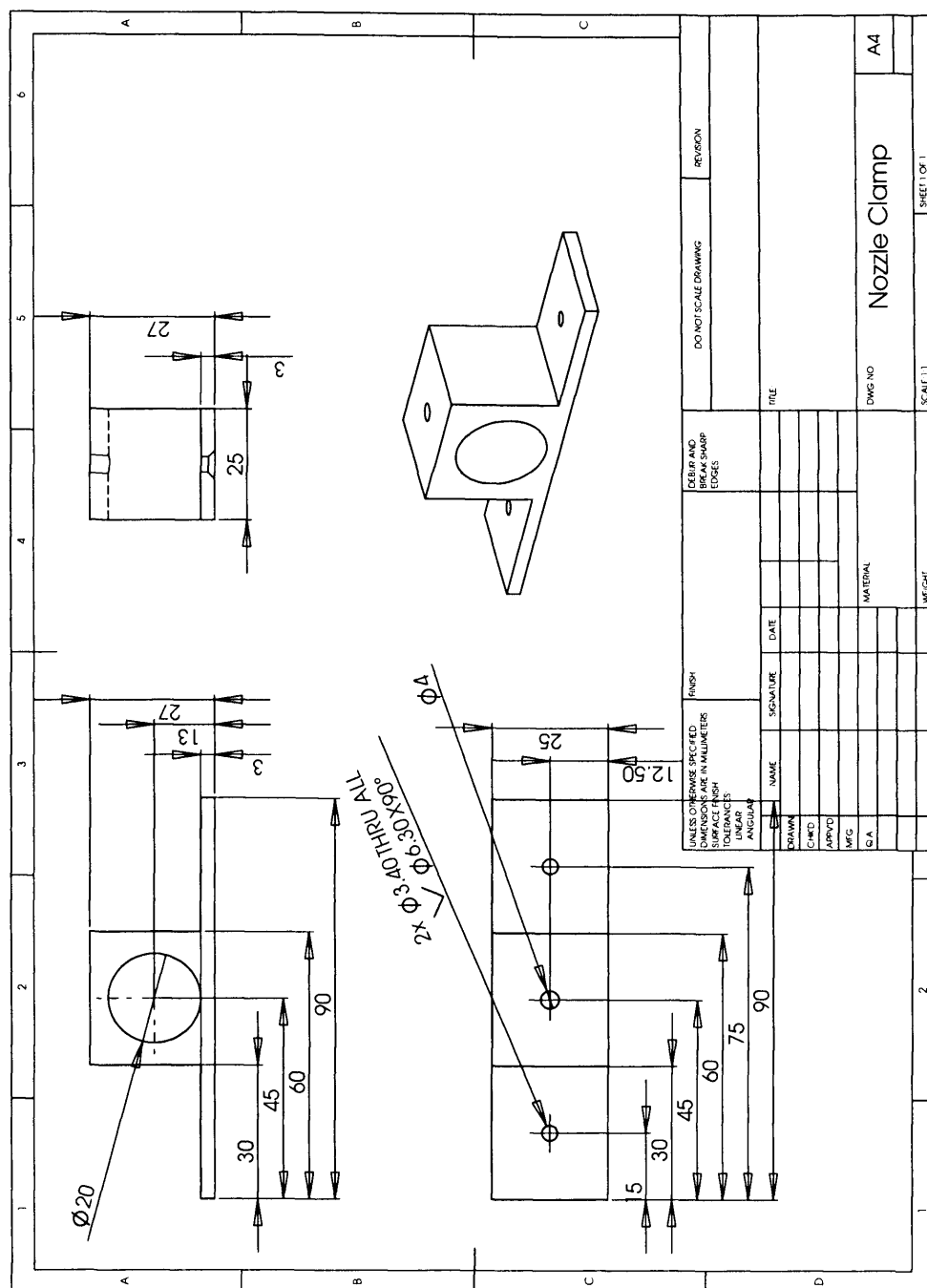
Tank Interior

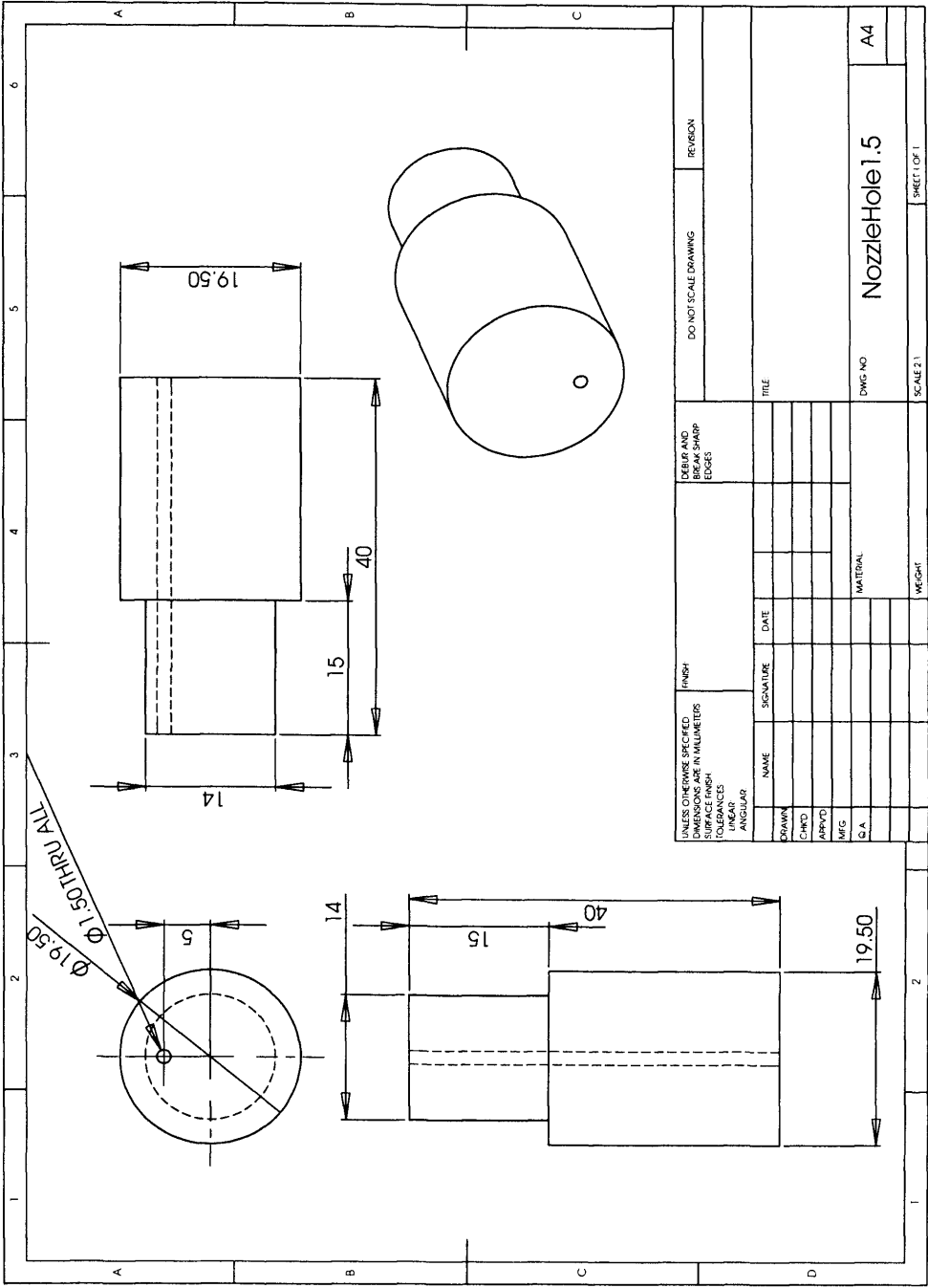


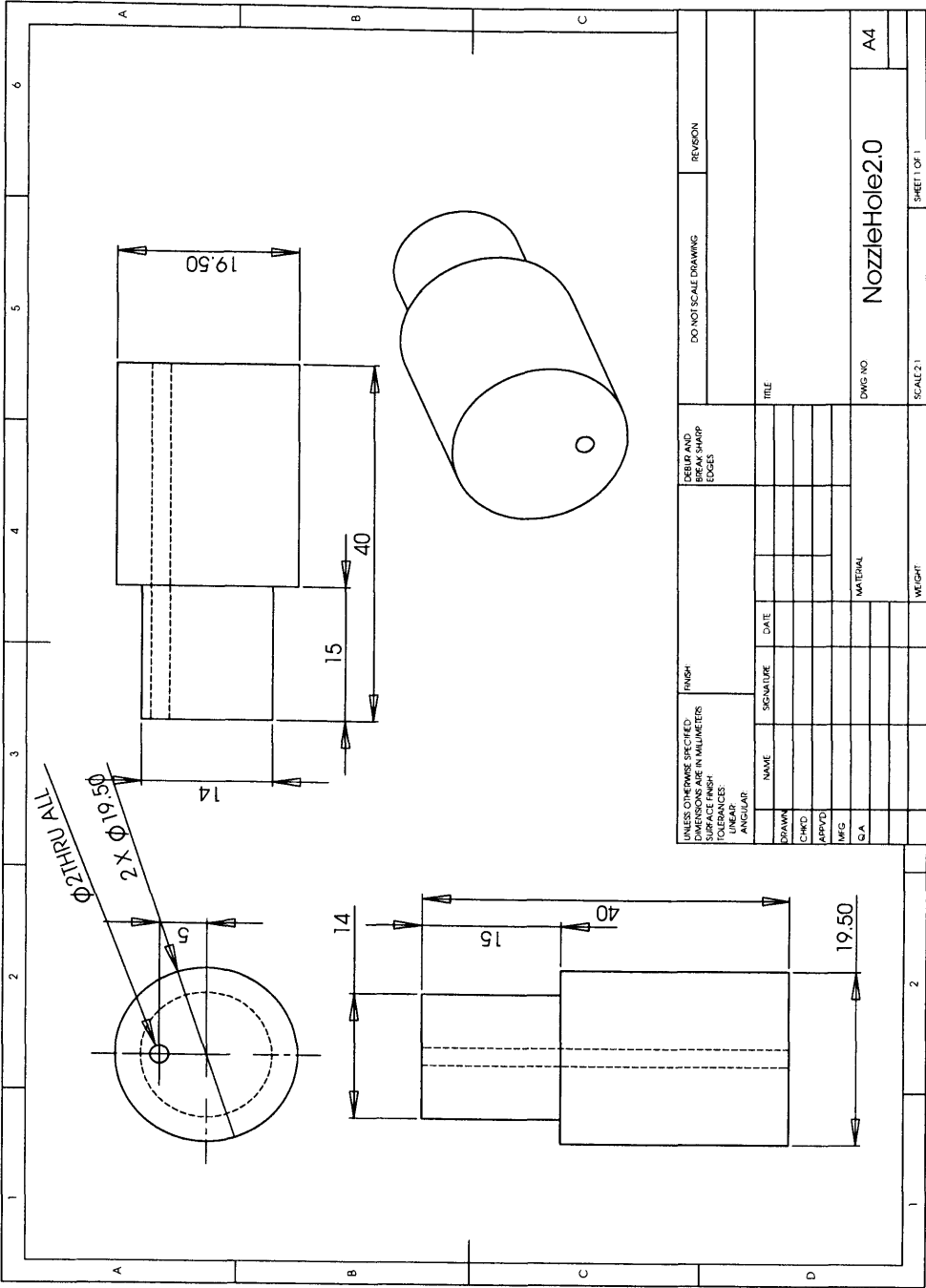


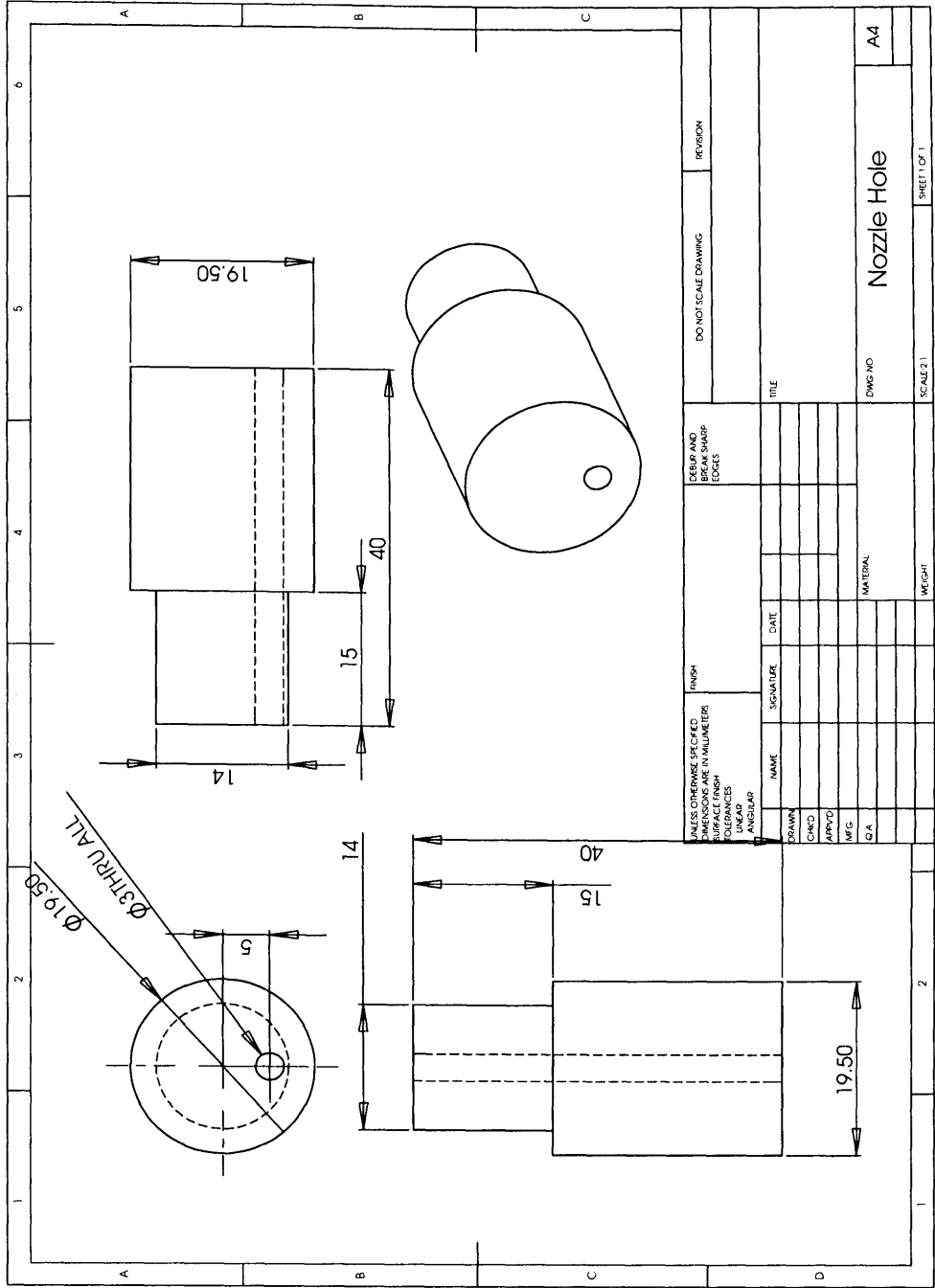






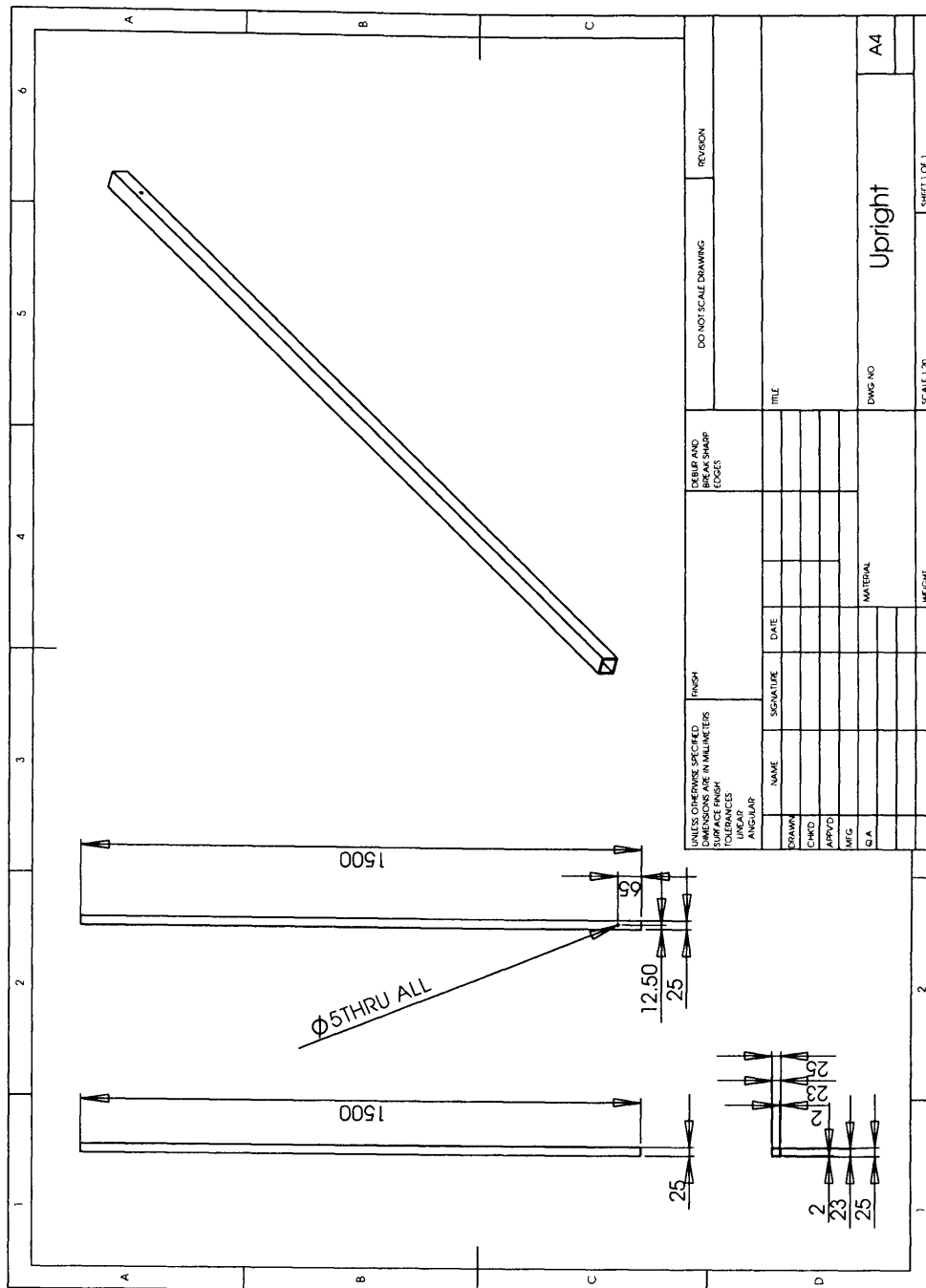


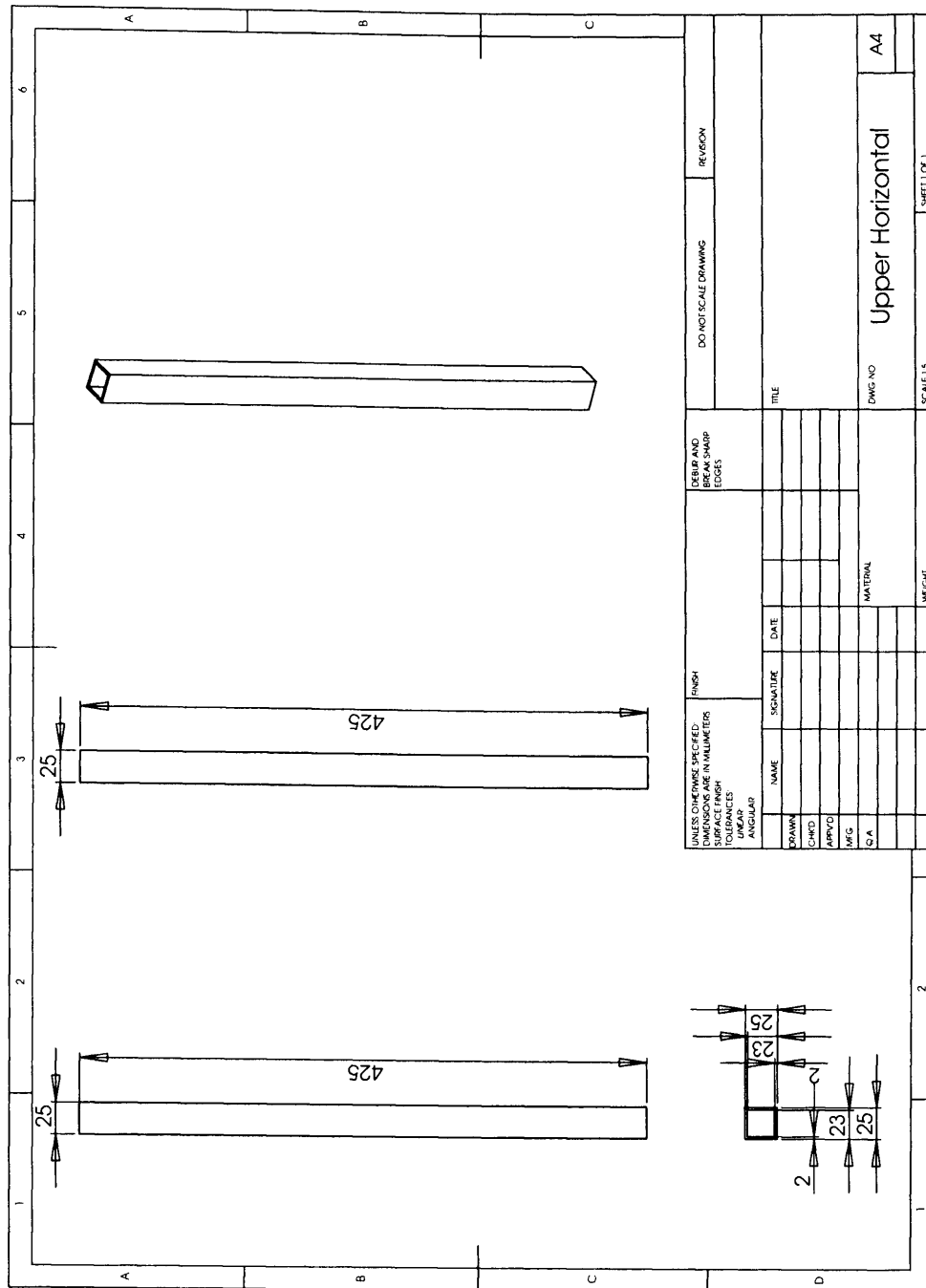


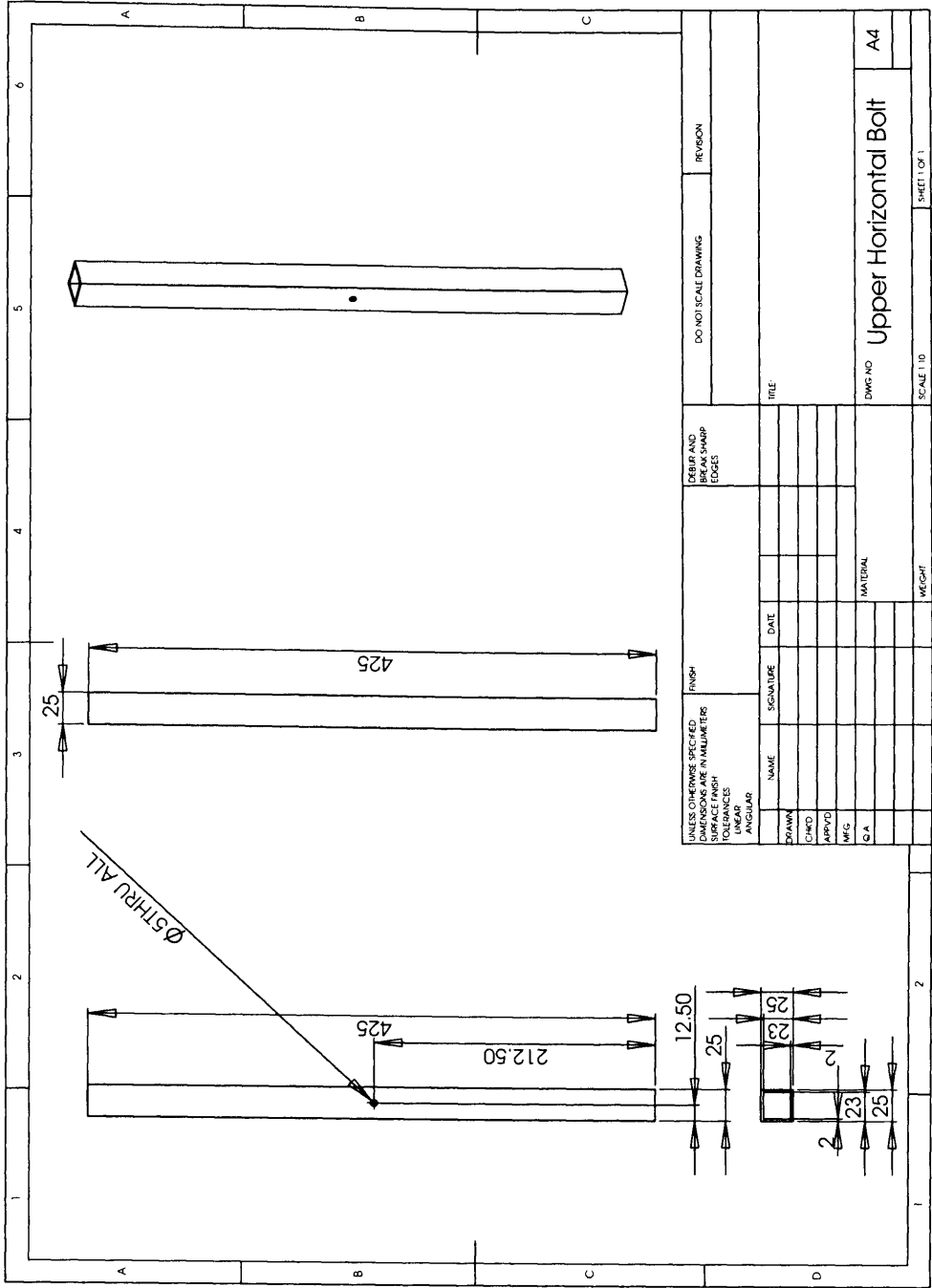


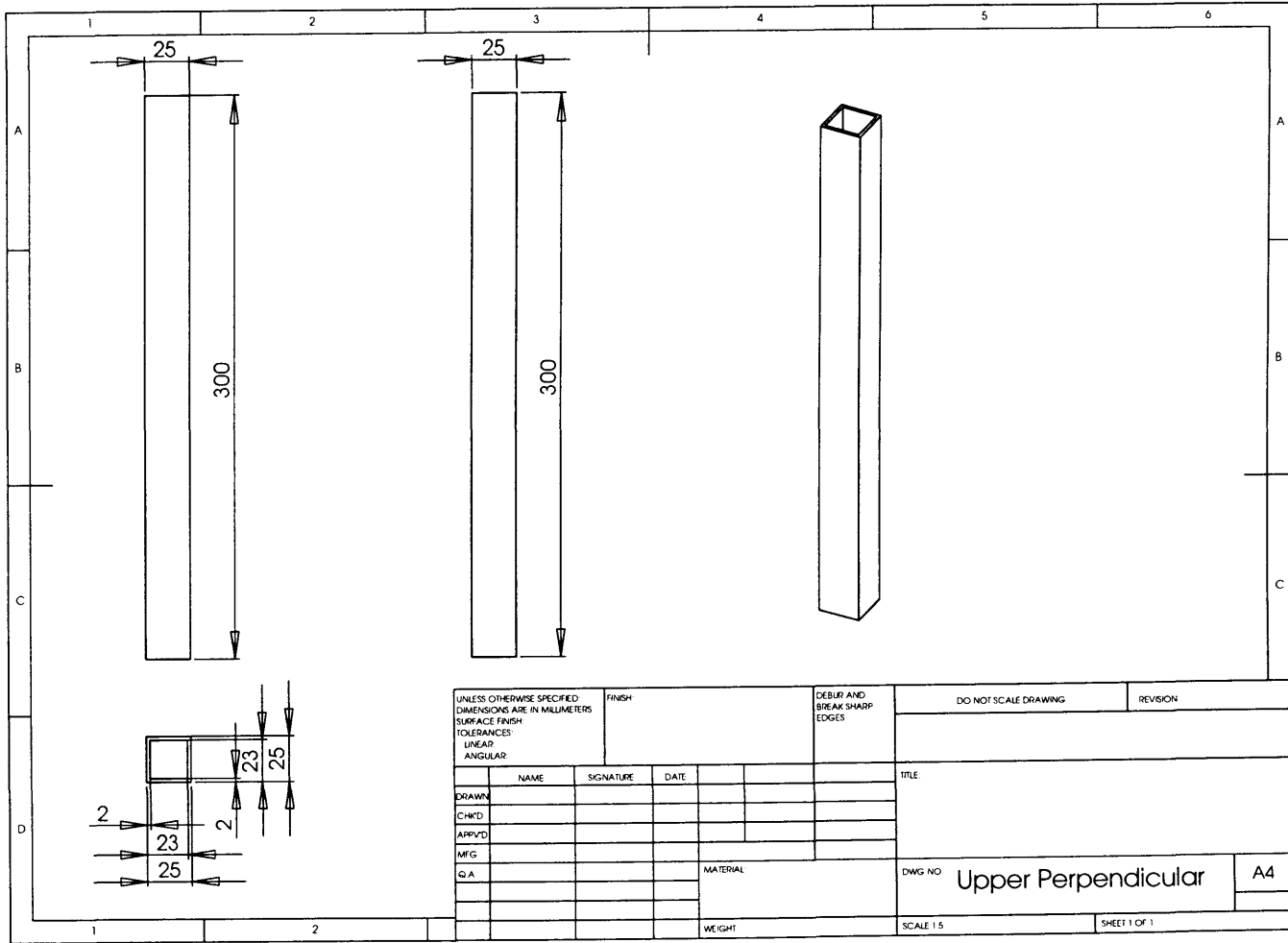
Part III

Camera Stand





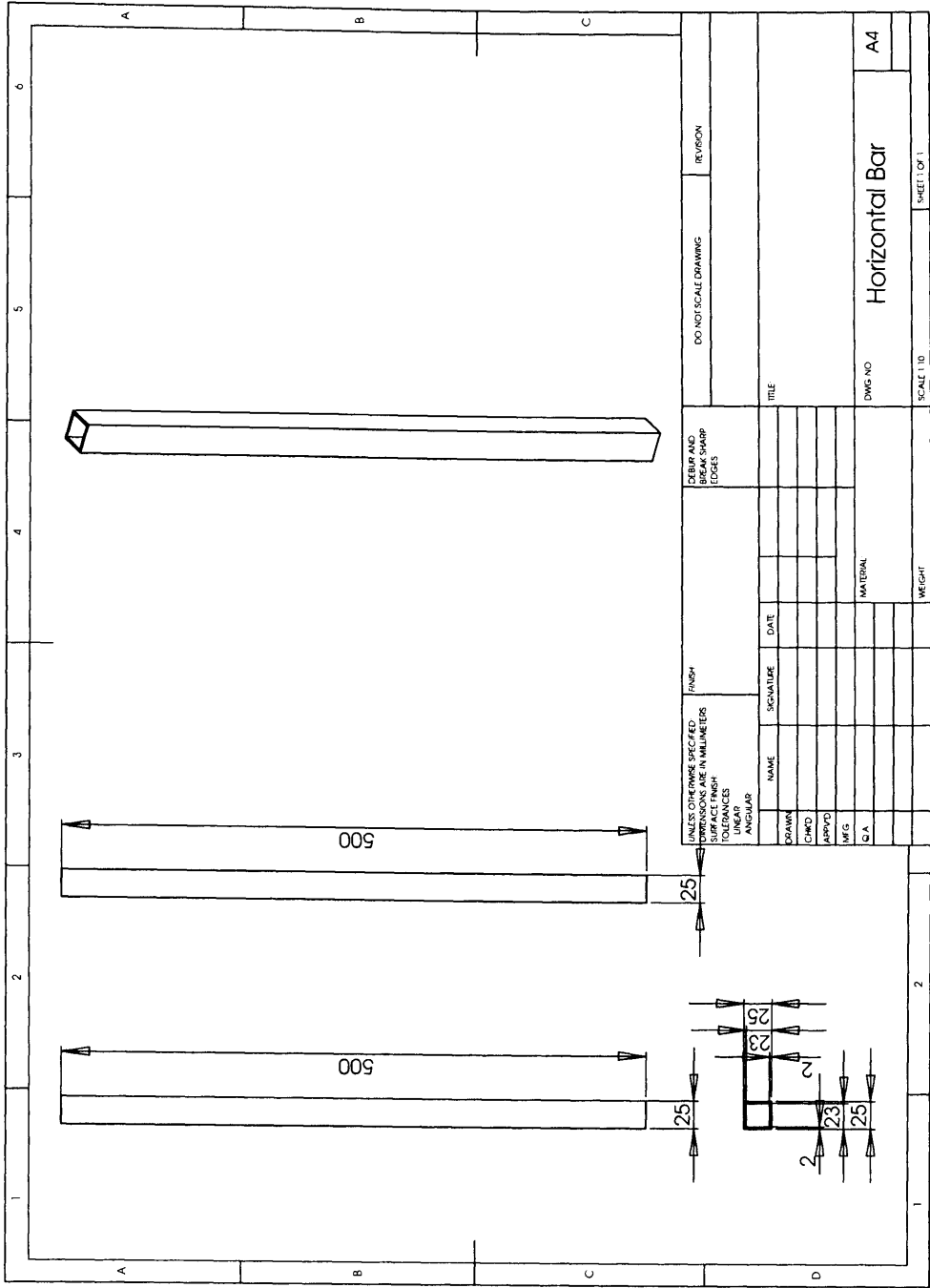


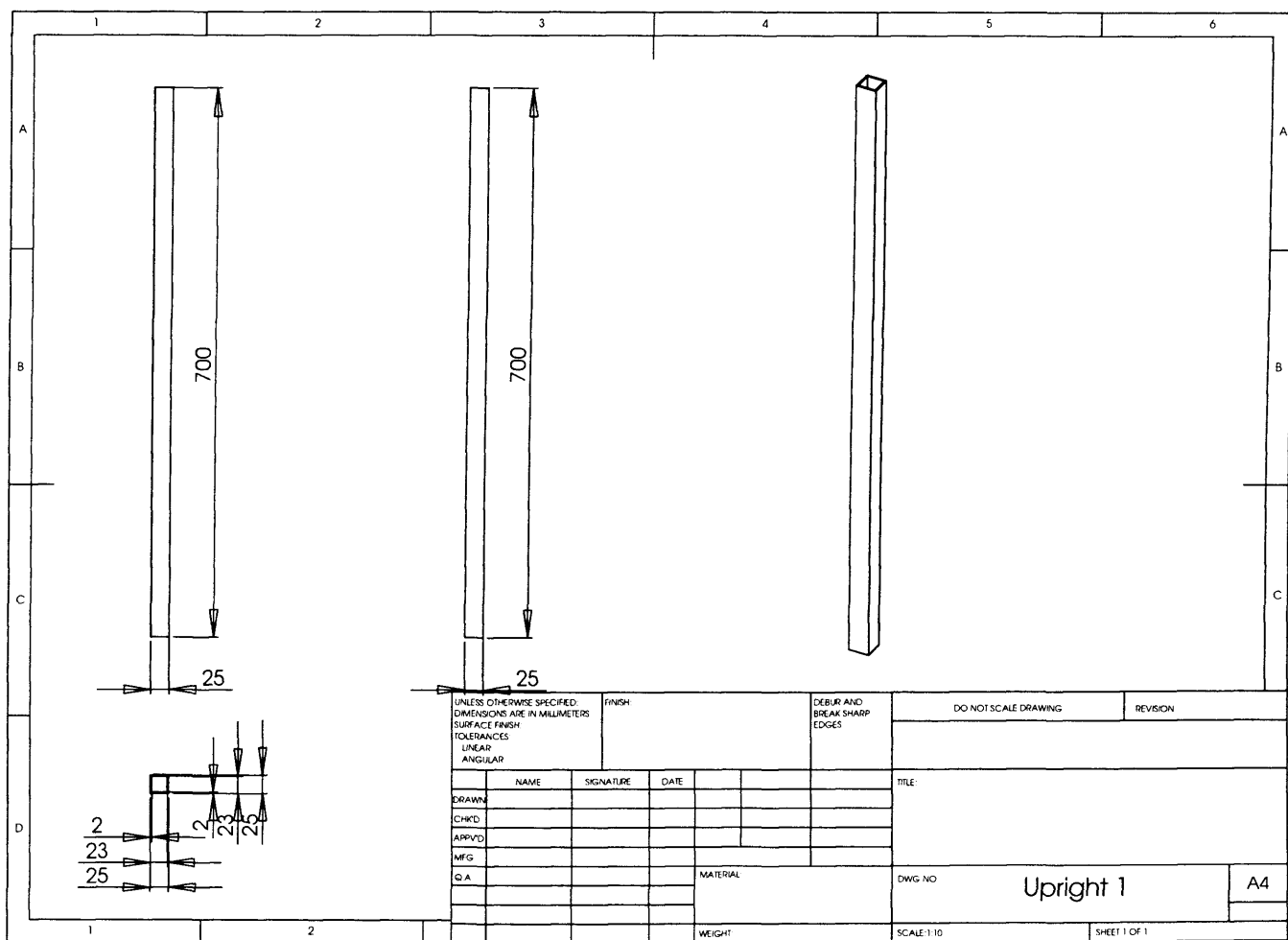


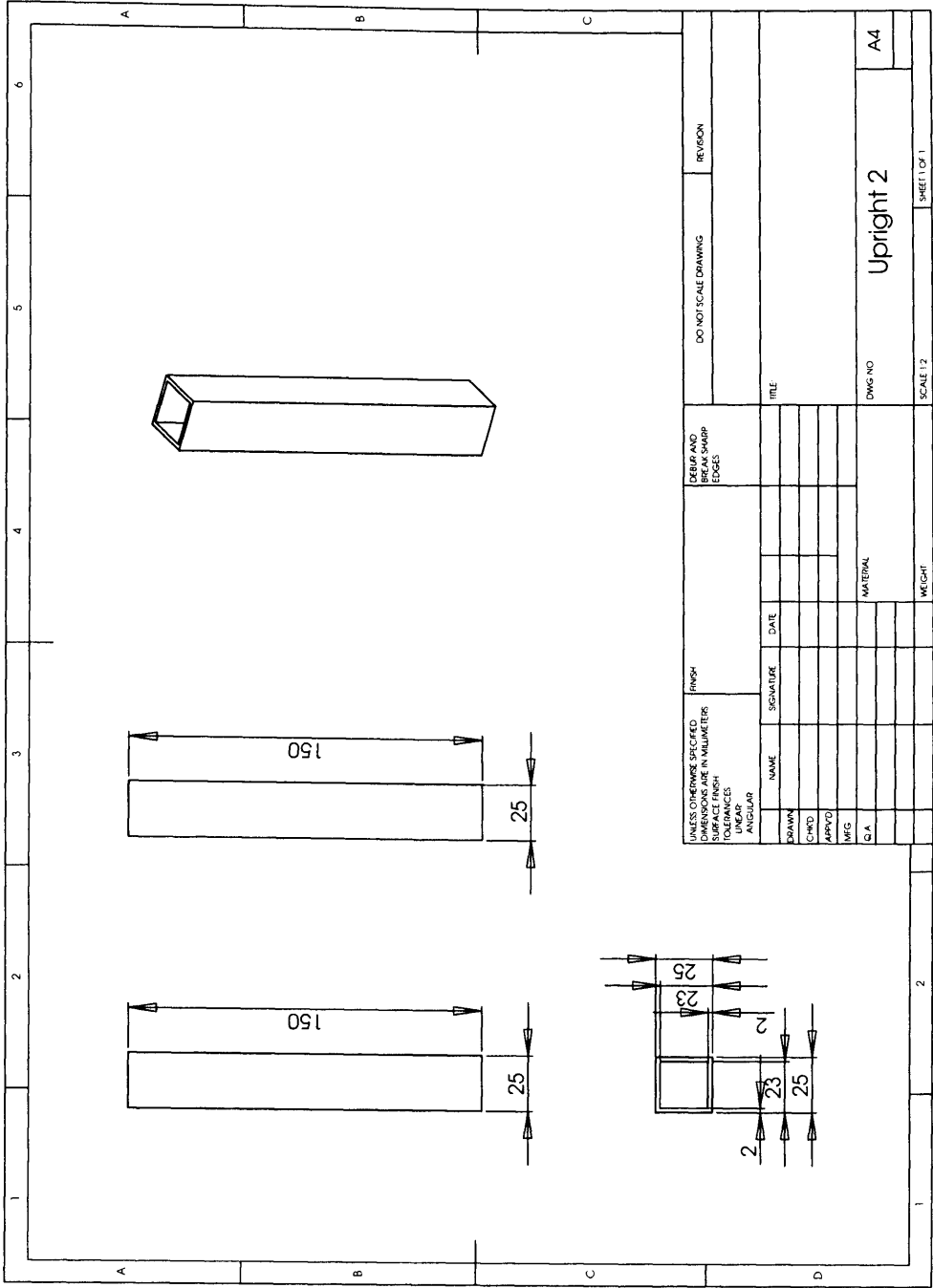
Exploded view drawing of a camera stand assembly. The drawing shows a central column with a base, a middle section, and a top section. The base is a rectangular plate with four mounting holes. The middle section is a long, thin rectangular plate with two mounting holes. The top section is a long, thin rectangular plate with two mounting holes. The drawing is labeled with dimensions and tolerances. The title block on the right contains the following information: DWG NO. A4, Camera Stand Explode, SCALE 1:1, SHEET 1 OF 1.

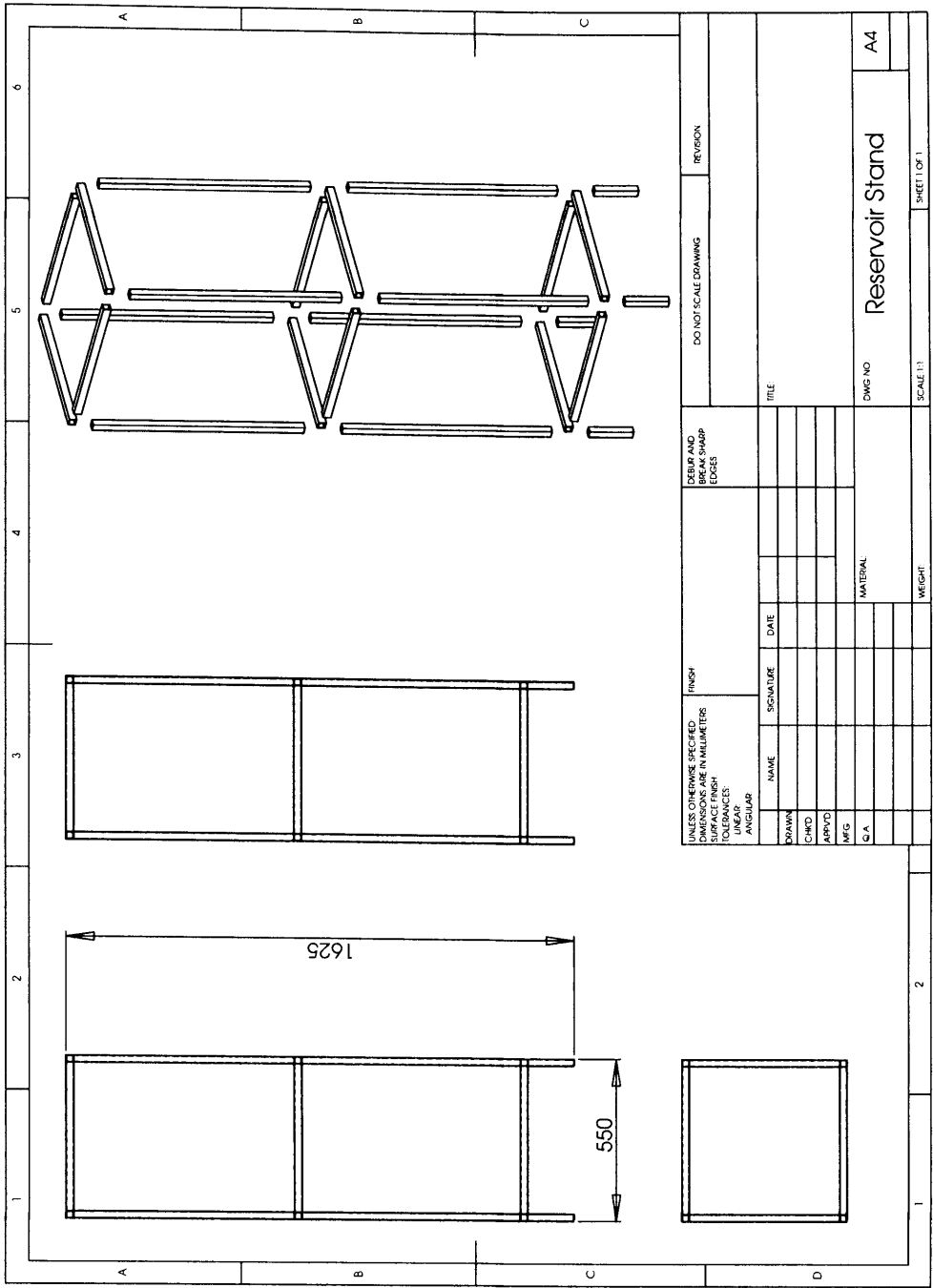
Part IV

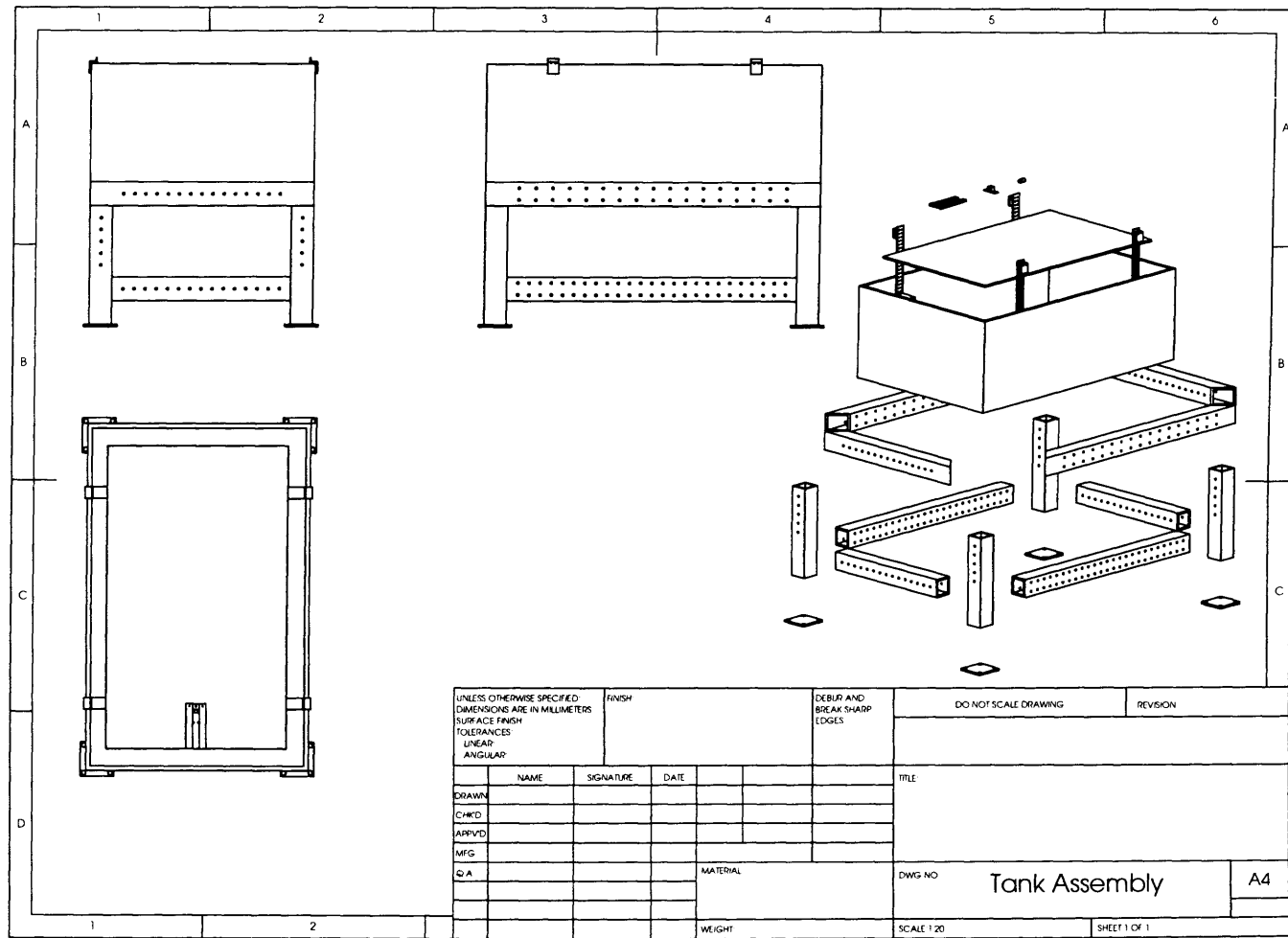
Reservoir Stand











Bibliography

- ACHESON, D. J. 2000 “Instability of vortex leap-frogging”. *Eur. J. Phys.* **21**, 269.
- AREF, H. 1978 “Motion of three vortices”. *Phys. Fluids* **22**, 393.
- AREF, H. 1982 “Point vortex motions with a center of symmetry”. *Phys. Fluids* **25**, 2183.
- AREF, H. 1983*a* “Integrable, Chaotic and Turbulent Vortex Motion in Two-Dimensional Flows”. *Ann. Rev. Fluid Mech.* **15**, 345.
- AREF, H. 1983*b* “Integrable, chaotic and turbulent vortex motion in two-dimensional flows”. *Ann. Rev. Fluid Mech.* **15**, 345.
- AREF, H. & STREMLER, M. A. 1999 “Four-vortex motion with zero total circulation and impulse”. *Phys. Fluids* **11**, 3704.
- BARKER, S.J. & CROW, S.C. 1977 “The motion of two-dimensional vortex pairs in a ground effect”. *J. Fluid Mech.* **82**, 659.
- BATCHELOR, G. K. 1967 *An Introduction to Fluid Dynamics*. Cambridge University Press.
- BATTJES, J. A. 1988 “Surf-zone Dynamics”. *Ann. Rev. Fluid Mech.* **20**, 257.

- BIDLOT, J.R. & STERN, M.E. 1994 "Maintenance of continental boundary-layer shear through counter-gradient vorticity flux in a barotropic model". *J. Fluid Mech.* **271**, 55.
- BÜHLER, O. & JACOBSON, T. E. 2001 "Wave-driven currents and vortex dynamics on barred beaches". *J. Fluid Mech.* **449**, 313.
- CENTURIONI, L.R. 2002 "Dynamics of vortices on a uniformly shelving beach". *J. Fluid Mech.* **472**, 211.
- CHEN, Q., DALRYMPLE, R. A., KIRBY, J. T., KENNEDY, A. B. & HALLER, M. C. 1999 "Boussinesq modelling of a rip current system.". *J. Geophys. Res.* **104**, 20617.
- COUDER, Y. & BASDEVANT, C. 1986 "Experimental and numerical study of vortices couples in two-dimensional flows". *J. Fluid Mech.* **173**, 225.
- CROWDY, D. G. & MARSHALL, J. S. 2005 "The motion of a point vortex around multiple circular islands". *Phys. Fluids* **17**, 566.
- DEEM, G.S. & ZABUSKY, N.J. 1978 "Stationary 'V-states', interactions, recurrence and breakings". *Phys. Rev. Lett.* **40**, 859.
- DEWAR, W. K. 2002 "Baroclinic Eddy Interaction with Isolated Topography". *J. Phys. Oceanogr.* **32**, 2789.
- DRITSCHEL, D.G. & AMBAUM, M.H.P. 1997 "A contour-advective semi-Lagrangian numerical algorithm for simulating fine-scale conservative dynamical fields". *Quarterly Journal of the Royal Meteorological Society* **123**, 1097.

- DRITSCHER, D. G. 1988 "Contour surgery: a topological reconnection scheme for extended integrations using contour dynamics". *J. Comput. Phys.* **77**, 240.
- DRITSCHER, D. G. 1995 "A general-theory for 2-dimensional vortex interactions". *J. Fluid Mech.* **293**, 269.
- FLÓR, J.B. & VAN HEIJST, G.J.F. 1994 "An experimental study of dipolar vortex structures in a stratified fluid". *J. Fluid Mech.* **279**, 101.
- FLÓR, J.B., VAN HEIJST, G.J.F. & DELFOS, R. 1995 "Decay of dipolar vortex structures in a stratified fluid". *Phys. Fluids* **7**, 374.
- FRATANTONI, D. M. & JOHNS, W. E. 1995 "Rings of the North Brazil Current: Their structure and behavior inferred from observations and a numerical simulation". *J. Geophys. Res.* **100**, 10633.
- GORSHKOV, K.A., OSTROVSKY, L.A. & SOUSTOVA, I.A. 2000 "Perturbation theory for Rankine vortices". *J. Fluid Mech.* **404**, 1.
- HAYNES, P. H., JOHNSON, E. R. & HURST, R. G. 1978 "A simple model of Rossby-wave hydraulic behaviour". *J. Fluid Mech.* **86**, 209.
- VAN HEIJST, G.J.F. Viewed on 7th November 2006 "Self-Organization of Two-Dimensional Flows". <http://www.fluid.tue.nl/WDY/2Dturb/ntvn/selforg.html>.
- VAN HEIJST, G.J.F. & FLÓR, J.B. 1989a "Dipole formation and collisions in a stratified fluid". *Nature* **340**, 212.
- VAN HEIJST, G.J.F. & FLÓR, J.B. 1989b *Mesoscale/Synoptic Coherent Structures in Geophysical Turbulence*. Elsevier.

- HINDS, A. K., JOHNSON, E. R. & McDONALD, N. R. 2007 "Vortex scattering by step topography". *J. Fluid Mech.* **571**, 495.
- HOMA, J., LUCAS, M. & ROCKWELL, D. 1988 "Interaction of impulsively generated vortex pairs with bodies". *J. Fluid Mech.* **197**, 571.
- HOPFINGER, E.J. & VAN HEIJST, G.J.F. 1993 "Vortices in rotating fluids". *J. Fluid Mech.* **25**, 241.
- JACKSON, J. D. 1998 *Classical Electrodynamics*, 3rd edn. Wiley.
- JOHNSON, D. & PATTIARATCHI, C. 2004 "Transient rip currents and nearshore circulation on a swell beach". *J. Geophys. Res.* **109**, 1798.
- JOHNSON, D. & PATTIARATCHI, C. 2006 "Boussinesq modelling of transient rip currents". *Coast. Eng.* **53**, 419.
- JOHNSON, E. R. 1978 "Trapped vortices in rotating flow". *J. Fluid Mech.* **86**, 209.
- JOHNSON, E. R. & CLARKE, S. R. 1998 *Numerical Methods for Fluid Dynamics*, , vol. 7. Oxford University Press.
- JOHNSON, E. R., HINDS, A. K. & McDONALD, N. R. 2005 "Steadily translating vortices near step topography". *Phys. Fluids* **17**, 6601.
- JOHNSON, E. R. & McDONALD, N. R. 2004 "Surf zone vortices over stepped topography". *J. Fluid Mech.* **511**, 265.
- JOHNSON, E. R. & McDONALD, N. R. 2004a "The motion of a vortex near a gap in a wall". *Phys. Fluids* **16**, 462.
- JOHNSON, E. R. & McDONALD, N. R. 2004b "The motion of a vortex near two circular cylinders". *Proc. R. Soc. Lond.* **460**, 939.

- KIRCHOFF, G.R. 1876 *Vorlesungen über Matematische Physik*, , vol. 1. Leipzig:Teubner.
- LAMB, H. 1932 *Hydrodynamics*, 6th edn. Cambrige University Press.
- LIN, C. C. 1941 "On the motion of vortices in two dimensions. I. Existence of the Kirchhoff-Routh function". *Proc. Natl. Acad. Sci. USA* **27**, 570.
- LONGUET-HIGGINS, M.S. 1970a "Longshore currents generated by obliquely incident waves, 1.". *J Geophys. Res.* **75**, 6778.
- LONGUET-HIGGINS, M.S. 1970b "Longshore currents generated by obliquely incident waves, 2.". *J Geophys. Res.* **75**, 6790.
- LONGUET-HIGGINS, M.S. & STEWART, R.W. 1964 "Radiation stresses in water waves; a physical discussion, with applications". *Deep Sea Res.* **11**, 529.
- LOVE, A. E. H. 1894 "On the motion of paired vortices with a common axis". *Proc. London Math. Soc.* **25**, 185.
- MACMAHAN, J.H., THORNTON, E.B. & RENIERS, J.H.M 2006 "Rip current review". *Coast. Eng.* **53**, 191.
- MCDONALD, N. R. 1999 "The motion of geophysical vortices". *Phil. Trans. R. Soc. Lond.* **357**, 3427.
- MCDONALD, N. R. 2000 "The interaction of two baroclinic geostrophic vortices on the β -plane". *Phil. Trans. R. Soc. Lond.* **459**, 1029.
- MCWILLIAMS, J. C. 1984 "The emergence of isolated coherent vortices in turbulent flow". *J. Fluid Mech.* **146**, 21.
- MILNE-THOMSON, L.M. 1955 *Theoretical Hydrodynamics*. Macmillan.

- MORTON, B.R., TAYLOR, G. & TURNER, J.S. 1956 "Turbulent Gravitational Convection from Maintained and Instantaneous Sources". *Proc. Roy. Soc.* **234**, 1.
- MUNK, W.H. 1949 "Surf Beats". *Trans. Amer. Geophys. Union* **30**, 849.
- NGUYEN DUC, J.M. & SOMMERIA, J. 1988 "Experimental characterization of steady two-dimensional vortex couples". *J. Fluid Mech.* **192**, 175.
- ORLANDI, P. 1990 "Vortex dipole rebound from a wall". *Phys. Fluids* **8**, 1429.
- ORLANDI, P. 1993 "Vortex dipoles impinging on circular cylinders". *Phys. Fluids* **5**, 2196.
- OVERMAN, E. A. & ZABUSKY, N. J. 1982 "Coaxial scattering of Euler-equation translating V-states via contour dynamics". *J. Fluid Mech.* **125**, 187.
- ÖZKAN-HALLER, H. T. & KIRBY, J. T. 1999 "Nonlinear evolution of the longshore current: A comparison of observations and computations". *J. Geophys. Res.* **104**, 25953.
- PEDLOSKY, J.P. 1987 *Geophysical Fluid Dynamics*, 2nd edn. Springer.
- PEREGRINE, D. H. 1998 "Surf zone currents". *Theoret. Comput. Fluid. Dyn.* **10**, 295.
- PEREGRINE, D. H. 1999 "Large-scale vorticity generation by breakers in shallow and deep water". *Eur. J. Mech. B/Fluids* **18**, 403.
- PIERREHUMBERT, R.T. 1980 "A family of steady, translating vortex pairs with distributed vorticity". *J. Fluid Mech.* **99**, 129.

- PULLIN, D.I. 1992 "Contour dynamics methods". *Ann. Rev. Fluid Mech.* **24**, 89.
- RICHARDSON, G. 2000 "Vortex motion in shallow water with varying bottom topography and zero Froude number". *J. Fluid Mech.* **411**, 351.
- RICHARDSON, P. L. & TYCHENSKY, A. 1993-1995 "Meddy trajectories in the Canary Basin measured during the seamount experiment". *J. Geophys. Res.* **103**, 25029.
- SAFFMAN, P.G. 1979 "The approach of a vortex pair to a plane surface in inviscid fluid". *J. Fluid Mech.* **92**, 497.
- SAFFMAN, P.G. & TANVEER, S. 1982 "The touching pair of equal and opposite uniform vortices". *Phys. Fluids* **25**, 1929.
- SAFFMAN, P. G. 1992 *Vortex Dynamics*. Cambridge University Press.
- SHEPARD, F. P., EMERY, K. O. & LA FOND, E. C. 1941 "Rip currents: a process of geological importance.". *J. Geol.* **49**, 337.
- SLINN, D. N., ALLEN, J. S., NEWBERGER, P. A. & HOLMAN, R. A. 1998 "Nonlinear shear instabilities of alongshore currents over barred beaches.". *J. Geophys. Res.* **103**, 18357.
- SMITH, J. A. & LARGIER, J. L. 1995 "Observations of nearshore circulation: Rip currents.". *J. Geophys. Res.* **100**, 10967.
- SOUS, D., BONNETON, N. & SOMMERIA, J. 2005 "Transition from deep to shallow water layer: formation of vortex dipoles". *Eur. J. Mech. B/Fluids* **24**, 19.
- STERN, M. E. 1999 "Scattering of an eddy advected by a current towards a topographic obstacle". *J. Fluid Mech.* **402**, 211.

- TENREIRO, M., ZAVALA SANSÓN, L. & VAN HEIJST, G.J.F. 2006 "Interaction of dipolar vortices with a step-like topography". *Phys. Fluids* **18**, 056603.
- THORPE, S. A. & CENTURIONI, L. R. 2000 "On the use of the method of images to investigate nearshore dynamical processes". *J. Mar. Res.* **58**, 779.
- TURNER, J.S. 1973 *Buoyancy Effects in Fluids*. Cambridge University Press.
- VELASCO, O.U. & VAN HEIJST, G.J.F. 1994 "Experimental study of dipolar vortices on a topographic β -plane". *J. Fluid Mech.* **259**, 79.
- VERZICCO, R., FLÓR, J.B., VAN HEIJST, G.J.F. & ORLANDI, P. 1995 Numerical and experimental study of the interaction between a vortex dipole and a circular cylinder. *Exp. Fluids* **18**, 153.
- VOROPAEV, S.I. & AFANAS'EV, I.D. 1992 "Two-dimensional vortex-dipole interactions in a stratified fluid". *J. Fluid Mech.* **236**, 665.
- WU, H. M., OVERMAN, E. A. & ZABUSKY, N. J. 1984 "Steady-State Solutions to the Euler Equations in Two Dimensions: Rotating and Translating V-States with Limiting Cases. I. Numerical Algorithms and Results". *J. Comput. Phys.* **77**, 53.
- YAMADA, H. & MATSUI, T. 1978 "Preliminary study of mutual slip-through of a pair of vortices". *Phys. Fluids* **21**, 292.
- YEH, P. 1998 *Optical Waves in Layered Media*. Wiley.